

TIAGO FERNANDES MOHERDAUI

The Virtual Element Method for Wheel-Rail Contact Problems

São Paulo

2021

TIAGO FERNANDES MOHERDAUI

The Virtual Element Method for Wheel-Rail Contact Problems

Corrected Version

Dissertation submitted to the Polytechnic School of the University of São Paulo in partial fulfillment of the requirements for the degree of Master of Science in Engineering.

Concentration area: Structural Engineering

Supervisor: Prof. Dr. Alfredo Gay Neto

São Paulo

2021

Autorizo a reprodução e divulgação total ou parcial deste trabalho, por qualquer meio convencional ou eletrônico, para fins de estudo e pesquisa, desde que citada a fonte.

Este exemplar foi revisado e corrigido em relação à versão original, sob responsabilidade única do autor e com a anuência de seu orientador.

São Paulo, 24 de Setembro de 2021

Assinatura do autor: 

Assinatura do orientador: 

Catálogo-na-publicação

Moherdai, Tiago Fernandes
The Virtual Element Method for Wheel-Rail Contact Problems / T. F.
Moherdai -- versão corr. -- São Paulo, 2021.
226 p.

Dissertação (Mestrado) - Escola Politécnica da Universidade de
São Paulo. Departamento de Engenharia de Estruturas e Geotécnica.

1.Métodos Numéricos 2.Método dos Elementos Finitos 3.Mecânica
dos Sólidos 4.Ferrovias I.Universidade de São Paulo. Escola Politécnica.
Departamento de Engenharia de Estruturas e Geotécnica II.t.

I dedicate this work to my grandmother Aida.

ACKNOWLEDGEMENTS

There are many people without whom this work would not have happened, and to whom I express my deepest gratitude:

To my family, for their support and incentive throughout this adventure.

To professor Alfredo Gay Neto, for excellent supervising experience, for introducing me to the Virtual Element Method and Computational Contact Mechanics, for the many opportunities and the valuable lessons on being a researcher. And to the many other teachers I have had during this period, each one an inspiration in their own way.

To my colleagues and friends at the Laboratório de Mecânica Computacional (LMC), for the companionship and the many coffee breaks that have helped fuel this work.

To the graduate program (PPGEC), the Department of Structural and Geotechnical Engineering (PEF), and University of São Paulo (USP), not only for the structure and support throughout the course, but for the instruction on the administrative aspects involved in doing research.

Last, but not least, I would like to thank the colleagues at the Wheel-Rail Chair, as well as Vale S.A. for the financial support through the Wheel-Rail Chair project.

RESUMO

O método dos elementos virtuais foi apresentado pela primeira vez em 2012, e desde então tem sido explorado em uma ampla gama de aplicações. O método consiste em uma generalização do método dos elementos finitos através de uma sistematização da construção dos espaços das funções interpoladoras para elementos de formatos poligonais genéricos. Estes espaços são deliberadamente construídos para conter um subespaço polinomial completo (que determina a ordem do elemento) e funções adicionais não-polinomiais. A definição do espaço é feita com base em um conjunto de graus de liberdade padronizado, de modo que a construção da forma fraca e matriz de rigidez associada é possível sem conhecimento direto das funções não-polinomiais. A utilização da projeção destas funções no subespaço polinomial e uma aproximação dos termos resultantes do resíduo desta projeção, são suficientes para garantir a consistência e estabilidade do método, respectivamente. Desta maneira o método se concretiza como uma versão mais versátil do método dos elementos finitos com relação à geometria dos elementos. Este trabalho busca prospectar este método como ferramenta para lidar com problemas de contato na interface roda-trilho. Isto é feito através de diversas aplicações em contextos de complexidade crescente, visando explorar suas características em comparação com o método dos elementos finitos. A primeira aplicação busca comparar as características de convergência dos métodos para um problema de um campo escalar. A segunda busca uma comparação dos métodos em um contexto de elasticidade linear plana. A terceira introduz o método *Node-to-Segment* de discretização de contato e faz uma comparação entre os métodos e com a solução analítica, para um problema de contato regido pela teoria de Hertz. Por fim, a quarta aplicação compara ambos os métodos para um problema simples de contato roda-trilho.

Palavras-chave: Método dos elementos virtuais. Método dos elementos finitos. Mecânica do contato. Mecânica computacional. Interface roda-trilho.

ABSTRACT

The virtual element method was first published in 2012 and has since been explored for a wide range of applications. The method consists of a generalization of the finite element method for general polygonal elements by introducing a novel procedure to define the interpolation function spaces. These spaces are designed to contain a full polynomial subspace (which defines the element's order), along with additional nonpolynomial functions. This space is built upon a determined set of degrees of freedom, deliberately devised so that the problem's weak form and stiffness matrix are computable without full knowledge of the nonpolynomial functions. The projection of those onto the polynomial subspace and an approximation for terms arising from said projection's residual are enough to ensure the method's consistency and stability. Thus, leading to a more versatile method regarding element geometry. The present work prospects the virtual element method as a tool for wheel-rail contact problems. This is achieved through a series of applications of increasing complexity, aiming to compare the method to the finite elements' in different scenarios. The first application compares both methods' convergence characteristics using a scalar field problem. The second compares them for plane linear elasticity, a two-component vector field problem. The third introduces the Node-to-Segment contact discretization technique, comparing both methods, and the analytic solution, for a Hertzian contact problem. Finally, the fourth application compares both methods for a simple wheel-rail contact problem.

Keywords: Virtual element method. Finite element method. Contact mechanics. Computational mechanics. Wheel-rail interface.

LIST OF FIGURES

Figure 1. Desired contact configuration for (a) tangent track, (b) smooth curve and (c) narrow curve.....	23
Figure 2. Descriptive illustration of the notation used for the reference configuration and current configuration.....	29
Figure 3. Descriptive illustration of the notation used for the unique configuration of linear elasticity.....	41
Figure 4. Schematic illustration of contact interaction between two bodies. Reference configuration (a), current configuration (b), and pressure distribution (c).	47
Figure 5. Illustration of nonconformal contact. Starts at a point (a); displacements and penetration if contact were not considered (b); detail on contact surface (c).....	51
Figure 6. Rod of generic cross-section subject to pure twisting moment.....	55
Figure 7. Displacement according to Coulomb's (a) and St. Venant's (b) theories.....	56
Figure 8. Normal (\mathbf{n}), tangent ($\boldsymbol{\tau}$) and projection of position vector on the cross-section plane (\mathbf{r}).	58
Figure 9. Basis functions for the space associated with a simple mesh (4 elements) for linear polynomials.....	65
Figure 10. Basis functions for the space associated with a simple mesh (4 elements) for quadratic polynomials.....	66
Figure 11. Barycentric coordinates as the ratio of areas.	71
Figure 12. Finite elements T3 and T6 and their shape functions.....	72
Figure 13. Examples of Escher-based elements, Pegasus and Bulldog.	78
Figure 14. Notation for the virtual element.	80
Figure 15. Boundary and internal degrees of freedom for $nv = 5$ and k from 1 to 3.	82
Figure 16. Ordering of the degrees of freedom illustrated for the 3 rd -order element.....	83
Figure 17. Original Delaunay triangulation.	92
Figure 18. Generation of Voronoi mesh from the Delaunay mesh.....	92
Figure 19. Geometric interpretation of Newton-Raphson method.	98
Figure 20. Contact kinematics for a node-segment pair.	103
Figure 21. Local contact problem solution.....	104

Figure 22. Equivalent nodal forces for the master segment. Linear (a) and Quadratic (b).	113
Figure 23. Interpretation of the Penalty method as springs.	113
Figure 24. Bed of springs interpretation of the penalty parameter (a) and equivalent spring for node B (b).	115
Figure 25. Slave node and uniform pressure inequivalence. Corner node (a), uniform mesh exception (b), and general case (c).	115
Figure 26. Integration scheme proposed by Zavarise and De Lorenzis (a), mechanical equivalence on segment level (b) and on the level of each integration point influence width (c).	116
Figure 27. Problem of wrongful force transmission illustrated. (a) Normal case, (b) problematic case: its incurred force transfer (c) and the ideal force transfer (d).....	117
Figure 28. Nodal forces equivalent to constant pressure. Linear element (a) and quadratic element (b).	117
Figure 29. Cross-section geometries.....	120
Figure 30. Domain partitions of different geometries and sizes.....	121
Figure 31. Mesh codification example.	121
Figure 32. FEM approximated warping functions for the square cross-section.	124
Figure 33. FEM approximated warping function for triangle cross-section.	125
Figure 34. VEM approximated warping function for square cross-section.....	126
Figure 35. VEM approximated warping function for triangle cross-section.....	127
Figure 36. FEM approximated Prandtl's function for square cross-section.....	128
Figure 37. FEM approximated Prandtl's function for triangle cross-section.....	129
Figure 38. VEM approximated Prandtl's function for square cross-section.	130
Figure 39. VEM approximated Prandtl's function for triangle cross-section.....	131
Figure 40. Vector plots of VEM stresses.	132
Figure 41. Vector plots of FEM stresses.	133
Figure 42. Tangential stress norm colormaps for VEM.	134
Figure 43. Tangential stress norm colormaps for FEM.....	135
Figure 44. Convergence curve, for element size, of square cross-section and St. Venant's formulation.....	141

Figure 45. Convergence curve, for element size, of triangle cross-section and St. Venant's formulation.....	141
Figure 46. Convergence curve, for element size, of square cross-section and Prandtl's formulation.....	142
Figure 47. Convergence curve, for element size, of triangle cross-section and St. Venant's formulation.....	142
Figure 48. Convergence curve, for number of degrees of freedom, of square cross-section and St. Venant's formulation.	143
Figure 49. Convergence curve, for number of degrees of freedom, of triangle cross-section and St. Venant's formulation.	143
Figure 50. Convergence curve, for number of degrees of freedom, of square cross-section and Prandtl's formulation.....	144
Figure 51. Convergence curve, for number of degrees of freedom, of triangle cross-section and Prandtl's formulation.....	144
Figure 52. Illustrative example of the codification for the simulations of (a) the patch test and (b) Cook's membrane.....	146
Figure 53. Patch test configuration.....	147
Figure 54. Cook's membrane problem configuration.....	148
Figure 55. Mesh for the overkilled solution using ABAQUS Standard 2018.....	148
Figure 56. Patch test results for FDPTO1 and VVPTO1 in kN/cm^2	149
Figure 57. Cook's membrane solutions with linear finite elements for the meshes: (a) M1, (b) M2, (c) M3, and (d) M4, in kN/cm^2	150
Figure 58. Cook's membrane solutions with quadratic finite elements for the meshes: (a) M1, (b) M2, (c) M3, and (d) M4, in kN/cm^2	151
Figure 59. Cook's membrane solutions with linear virtual elements for the meshes: (a) M1, (b) M2, (c) M3, and (d) M4, in kN/cm^2	152
Figure 60. Cook's membrane solutions with quadratic virtual elements for the meshes: (a) M1, (b) M2, (c) M3, and (d) M4, in kN/cm^2	153
Figure 61. Cook's membrane results for (a) ABAQUS, (b) FCM4O2, (c) VCM4O2, in kN/cm^2	154
Figure 62. Contact patch tests. Original version (a) and modified version (b).	155

Figure 63. Influence width for each type of slave node: Linear elements (a) and quadratic elements (b).	156
Figure 64. Contact patch test configuration, dimensions in <i>cm</i>	157
Figure 65. Codification for simulations of the contact patch test.....	158
Figure 66. Hertz problem configuration. Colors in boundary refer to the triangulation algorithm's element-size parameter. Dimensions in <i>cm</i>	159
Figure 67. Codification for simulations of Hertz's problem.	160
Figure 68. Edge refinement illustration. Original mesh (a), linear refined mesh (b) and quadratic refined mesh (c). Finite elements in blue, virtual elements in green.	161
Figure 69. Illustration of triangular mesh (a), generated Voronoi mesh (b), and manually fixed Voronoi mesh (c).	162
Figure 70. Contact forces [<i>kN</i>] detail for: (a) FPTM3O1, (b) FPTM3O2, (c) VPTM3O1, and (d) VPTM3O2.	165
Figure 71. Estimated contact pressure [<i>kN/cm²</i>] for Linear (a) and Quadratic (c) Finite Elements, and for Linear (b) and Quadratic (d) Virtual Elements.	166
Figure 72. Contact patch test results [<i>kN/cm²</i>] for linear finite elements: M1 (a), M2 (b) and M3 (c). The bottom box is the master surface, and the top box is the slave one...	167
Figure 73. Contact patch test results [<i>kN/cm²</i>] for linear virtual elements: M1 (a), M2 (b) and M3 (c). The bottom box is the master surface, and the top box is the slave one...	168
Figure 74. Contact patch test results [<i>kN/cm²</i>] for quadratic finite elements: M1 (a), M2 (b) and M3 (c). The bottom box is the master surface, and the top box is the slave one.	169
Figure 75. Contact patch test results [<i>kN/cm²</i>] for quadratic virtual elements: M1 (a), M2 (b) and M3 (c). The bottom box is the master surface, and the top box is the slave one.	170
Figure 76. Contact pressure estimates [<i>kN/cm²</i>] for all configurations along with Hertz theoretic reference. Linear FEM (a), Linear VEM with polygons (b), Quadratic FEM (c), Quadratic VEM with polygons (d) and triangles (e), and the Hybrid approach with edge refined mesh (f).	172

Figure 77. Contact pressure estimates [kN/cm^2] based on master-surface forces. Quadratic FEM (a), Quadratic VEM with polygons (b) and triangles (c), and the Hybrid approach with edge refined mesh (d).	173
Figure 78. Vertical normal stress (σ_y [kN/cm^2]) results along the symmetry line coordinate ζ [cm].	175
Figure 79. Horizontal normal stress (σ_x [kN/cm^2]) results along the symmetry line coordinate ζ [cm].	176
Figure 80. Maximum shear stress (τ_1 [kN/cm^2]) results along symmetry line coordinate ζ [cm].	177
Figure 81. Reference stress results from ABAQUS, in kN/cm^2 .	178
Figure 82. Stress results for linear FEM meshes (FDO1), in kN/cm^2 .	180
Figure 83. Stress results for linear VEM with polygonal meshes (VVO1), in kN/cm^2 ...	181
Figure 84. Stress results for quadratic FEM meshes (FDO2), in kN/cm^2 .	182
Figure 85. Stress results for quadratic VEM with polygonal meshes (VVO2), in kN/cm^2 .	183
Figure 86. Stress results for quadratic VEM with triangular meshes (VDO2), in kN/cm^2 .	184
Figure 87. Stress results for the hybrid approach in the edge-refined meshes (HEO2), in kN/cm^2 .	185
Figure 88. Comparison of Minimum Principal Stresses [kN/cm^2] on the contact surface for quadratic methods. FEM (a), VEM with polygonal meshes (b), VEM with triangular meshes (c), and Hybrid approach with Edge refinement (d).	186
Figure 89. Geometry illustration for tangent configuration (no superelevation).	192
Figure 90. Geometry for (a) Tangent and (b) Curve configurations.	193
Figure 91. Codification for wheel-rail contact simulations.	195
Figure 92. Tangent: Delaunay (a) and Voronoi (b). Curve: Delaunay (c) and Voronoi (d).	195
Figure 93. Linear FEM results for Tangent situation. Von Mises stress (a), maximum shear stress (b), minimum principal (c) with left (d) and right (e) zooms, in kN/cm^2 . Contact forces (f) with left (g) and right (h) zooms, in kN .	199

Figure 94. Linear VEM results for Tangent situation. Von Mises stress (a), maximum shear stress (b), minimum principal (c) with left (d) and right (e) zooms, in kN/cm^2 . Contact forces (f) with left (g) and right (h) zooms, in kN	200
Figure 95. Quadratic FEM results for Tangent situation. Von Mises stress (a), maximum shear stress (b), minimum principal (c) with left (d) and right (e) zooms, in kN/cm^2 . Contact forces (f) with left (g) and right (h) zooms, in kN	201
Figure 96. Quadratic VEM results for Tangent situation. Von Mises stress (a), maximum shear stress (b), minimum principal (c) with left (d) and right (e) zooms, in kN/cm^2 . Contact forces (f) with left (g) and right (h) zooms, in kN	202
Figure 97. Linear FEM results for Curve situation. Von Mises stress (a), maximum shear stress (b), minimum principal (c) with left (d) and right (e) zooms, in kN/cm^2 . Contact forces (f) with left (g) and right (h) zooms, in kN	205
Figure 98. Linear VEM results for Curve situation. Von Mises stress (a), maximum shear stress (b), minimum principal (c) with left (d) and right (e) zooms, in kN/cm^2 . Contact forces (f) with left (g) and right (h) zooms, in kN	206
Figure 99. Quadratic FEM results for Curve situation. Von Mises stress (a), maximum shear stress (b), minimum principal (c) with left (d) and right (e) zooms, in kN/cm^2 . Contact forces (f) with left (g) and right (h) zooms, in kN	207
Figure 100. Quadratic VEM results for Curve situation. Von Mises stress (a), maximum shear stress (b), minimum principal (c) with left (d) and right (e) zooms, in kN/cm^2 . Contact forces (f) with left (g) and right (h) zooms, in kN	208
Figure 101. Overlap of GIRAFFE's result over: (a) Linear FEM, (b) Linear VEM, (c) Quadratic FEM, and (d) Quadratic VEM.....	209

LIST OF TABLES

Table 1. The importance of iron ore in the Brazilian exports and railway transport system. (*) Values of 2019 available until October.	22
Table 2. Determination of contact pressure field for parallel cylinders based on different supplied quantities.....	52
Table 3. Mesh parameters.....	122
sTable 4. Torsion constant results for square cross-section in St. Venant's formulation.	136
Table 5. Torsion constant results for triangle cross-section in St. Venant's formulation.	137
Table 6. Torsion constant results for square cross-section in Prandtl's formulation.	138
Table 7. Torsion constant results for triangle cross-section in Prandtl's formulation. ...	139
Table 8. Numerical method used relative to element shape and order.	160
Table 9. Mesh element-size parameters.	162
Table 10. Penalty parameters [kN/cm].	163
Table 11. Reference results for the Hertz problem.....	171
Table 12. Minimum of the Minimum Principal Stress ($\min\sigma_3$) in kN/cm^2	179
Table 13. Maximum of Maximum Shear Stress ($\max\tau_1$) in kN/cm^2	179
Table 14. Maximum of Von Mises Stress ($\max\sigma_{vm}$) in kN/cm^2	179
Table 15. Boundary conditions and errors for Tangent situation.	197
Table 16. Boundary conditions and errors for Curve situation.....	203

CONTENTS

ACKNOWLEDGEMENTS.....	5
RESUMO.....	6
ABSTRACT	7
LIST OF FIGURES.....	8
LIST OF TABLES	14
CONTENTS.....	15
1. Introduction	20
1.1. Mechanics and contact.....	21
1.2. Contact in rail transport	22
1.3. Objective	25
1.4. Outline.....	26
2. Mathematical formulation	27
2.1. Notation.....	27
2.2. Finite elasticity.....	28
2.2.1. Boundary Conditions	29
2.2.2. Kinematics	30
2.2.3. Stresses.....	32
2.2.4. Constitutive law.....	34
2.2.5. Balance Equations.....	35
2.2.6. Differential formulation.....	36
2.2.7. Weak formulation.....	36
2.3. Linear Elasticity	40
2.3.1. Linearization procedure	40
2.3.2. Hypotheses.....	41

2.3.3.	Boundary conditions	41
2.3.4.	Kinematics	42
2.3.5.	Stresses.....	42
2.3.6.	Constitutive law.....	43
2.3.7.	Balance equations	43
2.3.8.	Differential formulation.....	43
2.3.9.	Weak formulation.....	44
2.4.	Plane strain problem	45
2.5.	Contact constraint	46
2.6.	Hertz contact theory	49
2.6.1.	Hypotheses.....	50
2.6.2.	Description for parallel cylinders	51
2.7.	St. Venant torsion theory.....	53
2.7.1.	Problem and hypotheses	54
2.7.2.	Development and differential formulation	55
2.7.3.	Weak formulation.....	58
2.7.4.	Prandtl's solution	59
2.7.5.	Torsion constant	61
3.	Numerical methods	62
3.1.	A historical perspective	62
3.2.	Finite element method (FEM).....	64
3.2.1.	Meshes and function spaces	64
3.2.2.	The finite element approximation.....	66
3.2.3.	Finite elements	69
3.2.4.	Convergence curves.....	73

3.2.5.	Mesh generation	73
3.2.6.	Adaptations for plane linear elasticity	73
3.3.	Virtual element method (VEM)	76
3.3.1.	The virtual element	79
3.3.2.	Orthogonality condition	83
3.3.4.	Consistency and stability terms	88
3.3.5.	Load term and L2-projector.....	89
3.3.6.	Mesh generation	91
3.3.7.	Adaptations for plane linear elasticity	94
3.4.	Newton-Raphson method.....	97
3.4.1.	Procedure for one real variable.....	97
3.4.2.	Generalization for more variables	98
3.5.	Node-to-Segment contact discretization.....	99
3.5.1.	Kinematics	102
3.5.2.	Local contact problem.....	103
3.5.3.	Weak formulation	104
3.5.4.	Consistent linearization.....	105
3.5.5.	Linear element formulation	107
3.5.6.	Quadratic element formulation.....	108
3.5.7.	Solution algorithm	109
3.5.8.	Inherent problems and alternate interpretations	113
4.	First application – St. Venant torsion.....	118
4.1.	Goals.....	118
4.2.	Methodology.....	118
4.2.1.	Torsion constant error.....	119

4.2.2.	Formulation.....	119
4.2.3.	Cross-section geometry.....	119
4.2.4.	Element geometry, size, and order.....	120
4.2.5.	Meshes and simulations.....	121
4.3.	Results.....	123
4.3.1.	Warping function.....	124
4.3.2.	Prandtl's function.....	127
4.3.3.	Stress distribution.....	131
4.3.4.	Torsion constant error.....	136
4.4.	Conclusions.....	145
5.	Second application – Plane strain linear elasticity.....	146
5.1.	Goals.....	146
5.2.	Methodology.....	146
5.2.1.	Patch test.....	147
5.2.2.	Cook's membrane.....	147
5.3.	Results.....	148
5.3.1.	Patch test.....	148
5.3.2.	Cook's membrane.....	149
5.4.	Conclusions.....	154
6.	Third application – Contact benchmarks.....	155
6.1.	Goals.....	156
6.2.	Methodology.....	156
6.2.1.	Contact patch test.....	157
6.2.2.	Hertz problem.....	158
6.3.	Results.....	164

6.3.1. Contact patch test.....	164
6.3.2. Hertz problem	170
Conclusion	186
7. Fourth application – Wheel-Rail contact problem.....	190
7.1. Goals.....	191
7.2. Methodology.....	191
7.2.1. Mechanical and geometric aspects.....	191
7.2.2. Numerical aspects	194
7.3. Results	196
7.3.1. Tangent situation	197
7.3.2. Curve situation.....	203
7.4. Conclusions.....	209
8. Final considerations	211
8.1. Further work	213
9. References.....	215

1. Introduction

In the history of science, Mechanics has always played a lead role. Turning the spotlight to the field celestial mechanics, one can watch the scientific revolution unfold. Copernicus sets up the heliocentric stage for Kepler's laws and Galilei's systematic observations. Newton's Principia synthesizing his laws of motion close the act: the birth of classical mechanics and modern science. Both have led to profound impacts not only on science, but on society as a whole.

Besides the scientific relevance, the study of motion has remarkable technological significance. One can refer to the immediate impacts of Galileo's and Newton's works to the field of ballistics, introducing the idea of compound motion and the mathematical tools to predict trajectories. The advancements in ballistics were cornerstone for modern and postmodern warfare technologies. A less grim example of impacts arising from advancements in mechanics is its association with thermodynamics, enabling the development of engines and machines. These set up the first two industrial revolutions, drastically changing society.

Mechanics not only transforms technology, but is also changed by it. The advent and popularization of the computer have produced lasting changes to the technological aspect of mechanics. Many problems previously required relying on restrictive simplifications, or creative adaptations from the scarce geometries for which analytical solutions were available. Computation provided the means to make high volume of calculations with incredible speed, allowing for the development of new numerical methods which exploit these new capabilities. Many problems, previously unsolvable due to their complexity, can now be approximated up to the desired precision. This has led to a field called Computational Mechanics, that is concerned with computer-based methods for the solution of problems governed by mechanics.

This work aspires to delve into a tiny facet on the boundaries of this colossal body of knowledge and, perhaps, leave a contribution to those that will help further expand them.

1.1. Mechanics and contact

Almost every real-world mechanical interaction involves contact. Whenever two bodies tend to occupy the same space at the same time, the contact interaction forms an action-reaction pair of pressure fields, one on each side of the contact surface (intersection of the surfaces of both bodies), keeping the bodies from penetrating each other.

In the most basic form of contact, the pressure field is normal to the contact surface at each point. This is called the frictionless or normal contact component. Its complementary aspect is friction, which for rough surfaces is generally associated with the normal contact between their asperities. Friction adds a tangential component to this contact traction field and is termed tangential contact.

The contact interaction presents most of its complexity at a local scale. The determination of the point/line/surface where contact will begin, as well as the pressure field that balances the forces that would instigate the penetration of the bodies, are heavily dependent on the geometry of the surfaces involved. The class of problems that examine these quantities is that of contact problems.

On a more global scale, the contact interaction is a means of force transmission between the two bodies. When modeling problems where the location and total force involved are known, it is simpler to represent it as a load. For contact problems where the focus is on the location and total force transmitted, a rigid-body framework is usually adopted. This is usually the approach of the field of multibody dynamics, e.g., Shabana [1]. However, when the traction field and the associated stresses are important, then it is a contact problem in the framework of deformable solid mechanics.

The problem investigated in this work is of the latter type. The study of the wheel-rail contact interaction is interested in detecting where contact will occur, as well as the stresses associated with it. For this, a characterization of the pressure field developed in the contact interaction is of great importance. The contact problem must be solved in the context of deformable solid mechanics.

1.2. Contact in rail transport

Iron ore is one of the main export products of Brazil, representing 11.4% of all exports in 2019, a close third place after Oil seeds (12.5%) and Mineral fuels (13.1%); averaging roughly 10% of the total Brazilian exports over the last decade, about US\$20 billion per year, according to the Brazilian Ministry of Industry, Foreign Trade and Services (MDIC)¹. Almost all iron ore production, including that for the internal market, is transported via the railway system. The transport of this product is approximately 75% of everything that is transported via railway, according to statistic of the National Land Transportation Agency (ANTT)². This information is summarized in Table 1.

Table 1. The importance of iron ore in the Brazilian exports and railway transport system. (*) Values of 2019 available until October.

Year	Brazilian Exports				Railway transport		
	Total [US\$ FOB]	Iron Ore [US\$ FOB]	%	Iron Ore [Tonnes]	Total [Tonnes]	Iron Ore [Tonnes]	%
2006	\$ 137,708,096,759.00	\$ 8,948,871,317.00	6.5%	2.43E+08	3.89E+08	2.82E+08	72.4%
2007	\$ 160,521,882,755.00	\$ 10,557,911,454.00	6.6%	2.69E+08	4.15E+08	3.07E+08	74.1%
2008	\$ 197,778,858,085.00	\$ 16,538,542,577.00	8.4%	2.82E+08	4.27E+08	3.16E+08	74.2%
2009	\$ 152,910,580,383.00	\$ 13,239,763,470.00	8.7%	2.66E+08	3.79E+08	2.78E+08	73.3%
2010	\$ 201,788,337,035.00	\$ 28,867,719,633.00	14.3%	3.11E+08	4.35E+08	3.25E+08	74.6%
2011	\$ 255,936,306,857.00	\$ 41,817,213,855.00	16.3%	3.31E+08	4.54E+08	3.43E+08	75.5%
2012	\$ 242,277,307,190.00	\$ 30,989,292,517.00	12.8%	3.27E+08	4.53E+08	3.43E+08	75.6%
2013	\$ 241,967,561,759.00	\$ 32,491,530,731.00	13.4%	3.30E+08	4.51E+08	3.41E+08	75.7%
2014	\$ 224,974,401,228.00	\$ 25,819,090,176.00	11.5%	3.44E+08	4.65E+08	3.57E+08	76.7%
2015	\$ 190,971,087,339.00	\$ 14,037,103,623.00	7.4%	3.65E+08	4.92E+08	3.78E+08	76.9%
2016	\$ 185,232,116,301.00	\$ 13,289,341,907.00	7.2%	3.74E+08	5.04E+08	3.97E+08	78.8%
2017	\$ 217,739,218,466.00	\$ 19,199,154,200.00	8.8%	3.84E+08	5.39E+08	4.16E+08	77.3%
2018	\$ 239,263,992,681.00	\$ 20,220,359,405.00	8.5%	3.90E+08	5.70E+08	4.41E+08	77.4%
2019*	\$ 185,521,705,661.00	\$ 18,567,905,412.00	10.0%	2.83E+08	3.71E+08	2.72E+08	73.2%

Source: MDIC and ANTT.

The costs of railway infrastructure are usually classified as either the capital for the installation of the infrastructure and acquisition of equipment, or costs relative to the maintenance of the system during its operation. For a specific railroad to be financially sustainable, the income generated for the transport services minus the maintenance costs

¹ <http://www.mdic.gov.br/index.php/comercio-exterior/estatisticas-de-comercio-exterior/balanca-comercial-brasileira-acumulado-do-ano>

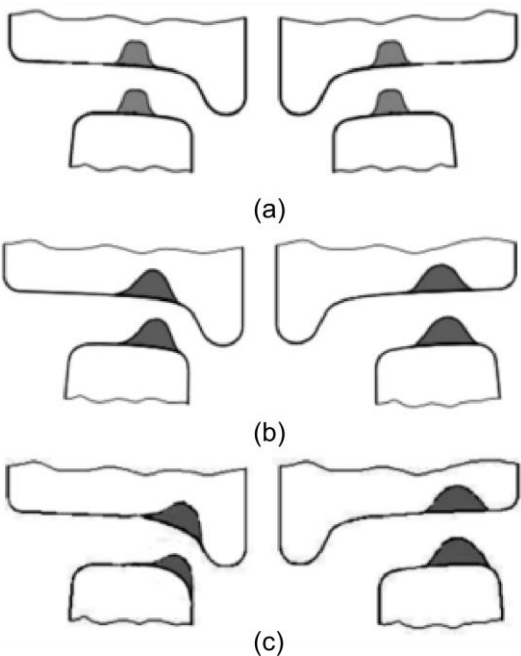
² http://www.antt.gov.br/ferrovias/arquivos/Anuario_Estatistico.html

must, over time, pay off the capital investment, ensuring profitable operations in the long run.

The transport of large quantities of bulk cargo, such as iron ore, are denoted heavy haul railway operations. This kind of operation leads to high maintenance costs as the heavy loads borne by the wagons are transferred to the rails through small contact patches, leading to high pressures in the contact between the wheel and rail. A good reference regarding the role of Wheel-Rail interface in the maintenance for heavy haul operations is the guide published by the International Heavy Haul Association (IHHA) [2].

The characterization of the contact between the wheel and rail is highly dependent on the geometry of both elements, the geometry of the track (tangents and curves leading to different contact situations, as shown in Figure 1), the weight and speed of the train. Another aggravating factor is the propensity of the wheel's and rail's geometries to change over time due the wear inherent to this form of interaction. In addition, each rail section interacts with multiple different wheels, and each wheel rolls over many different rail sections. This aggravates the complexity of the problem.

Figure 1. Desired contact configuration for (a) tangent track, (b) smooth curve and (c) narrow curve.



Source: Adapted from IHHA [2].

There are many different phenomena that can damage both elements during the operation, these are still not fully comprehended and comprise an open area of study. One important (and complex) phenomenon is the rolling contact fatigue (RCF), a comprehensive work on which can be found in Magel [3]. Another phenomenon is wear itself, especially in narrow curves, where it is intensified as consequence of the lateral friction necessary to change the train's direction. Therefore, the adequate modelling of the wheel-rail contact, especially regarding the stresses, is of paramount importance for comprehending the phenomena involved in the degradation of the system during the operation; for designing better wheels, rails, and maintenance procedures; and overall reduction of maintenance costs.

The role of contact mechanics in helping to understand the phenomena on the wheel-rail interface has been brought to light by Magel and Kalousek [4]. The modeling of the interaction of both bodies constitutes a contact problem of elasticity, as it seeks the location, pressure distribution and stresses derived from the contact interaction. The methodology for pummeling analysis proposed in Magel and Kalousek's work treats both objects as rigid bodies. Their work finds the positions and forces associated with each contact interaction and associates, with each contact point, the analytic pressure distributions provided by Hertz theory on nonconformal (initially pointwise) contact. This theory can be found in Johnson [5], and the formulation for contact between aligned cylinders is presented in section 2.6.2.

The author participates in a research group focused on the computational modelling of the wheel-rail contact. Recent efforts by Higa, Kina, and Gay Neto [6] have developed a procedure of accumulated contact pressure evaluation based on Magel and Kalousek's pummeling methodology, using Refachinho de Campos and Gay Neto's [7] rigid body formulation and Gay Neto and Wriggers' [8] master-master approach to contact. One caveat of this approach is that all contacts are treated as pointwise, both the contact pressure and stress evaluation are taken from Hertz theory. Although powerful, this theory yields good results for isolated pointwise contacts, whereas in wheel-rail interaction there might be conformal contact, as well as more than one pointwise contact close enough to question the theory's validity. The present work seeks to explore the solution of the contact

problem in the framework of the theory of elasticity, providing the means to find pressure distributions and stress fields for the more general case.

The usual numerical method for problems in the theory of elasticity is the finite element method. Recently, however, Wriggers, Rust, and Reddy [9] have presented a new strategy for contact problems based on the (novel) virtual element method. The paper proposed a methodology based on the virtual element's geometric versatility. This initial paper focused on 2D problems, compared the proposed methodology with the node-to-segment contact approach (with the finite element method), and achieved promising results for both conformal and nonconformal contact.

1.3. Objective

The general objective of this work is to explore the Virtual Element Method (VEM) for contact problems in two dimensions. The specific objective is to use the VEM to obtain solutions for non-conformal and conformal contact problems and, in particular, to problems involving wheel and rail geometries.

To achieve this, smaller goals are provided as steppingstones. These are organized as different applications with increasing complexity, building up to the general objective. In each application the author's own implementation of VEM is compared to their implementation of the Finite Element Method (FEM) and to a reference external solution, either an analytic solution or reliable software.

The first application is a general study of St. Venant's uniform torsion theory. This application provides a simpler background (the interpolated field is scalar) to explore the convergence of the method. The goals for this application are:

- First successful implementation of the Virtual Element Method.
- Explore both Dirichlet and Neumann boundary conditions.
- Show that the convergence properties are like those of the Finite Element Method.

The second application revolves around plane strain linear elasticity. The goals for this application are:

- Successfully implement the method for the interpolation of a two-component vector field (displacements in the plane).
- Use common benchmarks to ensure the implementation's adequacy (Patch test and Cook's membrane).
- Validate the solution via analytic solution (Patch test) and commercial software (Cook's membrane).

The third application extends the method for contact problems, using the Node-to-Segment contact discretization. The goals for this application are:

- Successfully implement the node-to-segment (frictionless) contact strategy with the Virtual Element Method and Finite Element Method.
- Use common benchmarks to evaluate the methods used (Contact patch test and Hertz problem)
- Validate the solutions with analytic results and commercial software.

The fourth application applies the method for a problem borrowed from the context of the wheel-rail interface. The goals for this application consist of:

- Simulate the two typical situations: tangent and curve.
- Evaluate the results in the light of the previous section.
- Compare with those from a rigid-body approach with the software GIRAFFE.

1.4. Outline

This dissertation is organized in the following manner. Section 2 introduces the mathematical formulation for the problems explored in this work. Section 3 addresses the computational methods (FEM, VEM, and others) that are used to obtain approximated solutions for the proposed problems. The next four sections are the consecutive applications employing the methods to the problems of earlier sections. Section 4 is the first application, based on St. Venant's torsion theory. In it convergence aspects of both methods are compared; Section 5 is the second application, focusing on plane linear elasticity; Section 6 is the third application, consisting of benchmark contact problems; Section 7, the fourth application, comprised of two wheel-rail contact problems. Section 8 contains the final considerations and possible future works.

2. Mathematical formulation

This section presents and explores the mathematical formulation for the theories and models to be explored. All of these are static problems of the Theory of Elasticity, which is itself a topic inside Continuum Mechanics; there are many good references on this subject, such as Reddy [10] and Lai, Krempl, and Rubin [11]. The starting point is finite elasticity, or nonlinear elasticity, which is the more general formulation. In the sequence, the approximations necessary for linear elasticity are introduced, leading to its formulation. Furthermore, the hypotheses for plane strain state are presented for both finite and linear elasticity. Then, a general perspective on the contact constraint is presented, followed by a brief glance over Hertz contact theory for nonconformal contact in linear elasticity. To close the section, St. Venant torsion theory is presented as a special case of linear elasticity.

2.1. Notation

In this work's notation, scalars are denoted by plain italic letters (e.g., i, α, u_i, P_{ij}), vectors by lowercase bold italic letters (e.g., $\boldsymbol{x}, \boldsymbol{u}$), second-order tensors by uppercase bold italic letters (e.g., $\boldsymbol{F}, \boldsymbol{P}$) and fourth-order tensors by blackboard bold uppercase letters (e.g., \mathbb{G}, \mathbb{D}).

The usual scalar product between vectors, i.e., the dot product, is represented by “ \cdot ” (e.g., $\boldsymbol{\sigma} \cdot \boldsymbol{\varepsilon} = \sigma_i \varepsilon_i$). Einstein's summation convention is adopted when index notation is shown. The cross product between two vectors is denoted by “ \times ” (e.g., $\boldsymbol{e}_1 \times \boldsymbol{e}_2 = \boldsymbol{e}_3$). The usual scalar product between two second-order tensors is “ $:$ ” (e.g., $\boldsymbol{P}:\boldsymbol{F} = P_{ij}F_{ij}$). The tensor product is denoted by “ \otimes ”, be it the dyadic product of two vectors (e.g., $\boldsymbol{P} = \boldsymbol{\tau}_i \otimes \boldsymbol{e}_i = \boldsymbol{\tau}_i \boldsymbol{e}_i^T$), or the usual tensor product between two second-order tensors (e.g., $\mathbb{D} = \boldsymbol{A} \otimes \boldsymbol{B} \therefore \mathbb{D}(\boldsymbol{X}) = (\boldsymbol{B}:\boldsymbol{X})\boldsymbol{A}$).

The symbol δ_{ij} is the Kronecker delta and ε_{ijk} is the Levi-Civita symbol.

The notation regarding the position with respect to each coordinate axis is sometimes presented in index notation (x_1, x_2, x_3) , other times in the usual notation (x, y, z) . There is always direct correspondence $x_1 = x; x_2 = y; x_3 = z$.

If certain entity can be represented as a function of another entity, this function representation is marked with “($\hat{\cdot}$)” (e.g., $\mathbf{t}^R = \hat{\mathbf{t}}^R(\mathbf{x}^R)$).

Partial derivatives of a quantity may be represented using a subscript with a comma indicating the variable with respect to which it is derived (e.g., $\frac{\partial \theta}{\partial x_3} = \theta_{,3}$). Directional derivatives will be presented with the direction inside brackets, e.g., $\frac{\partial f}{\partial \mathbf{u}}(\bar{\mathbf{u}})[\Delta \mathbf{u}]$ is the directional derivative of the function f defined over a vector variable \mathbf{u} at the point $\bar{\mathbf{u}}$ in the direction of $\Delta \mathbf{u}$.

2.2. Finite elasticity

Static problems in elasticity are generally concerned with the configuration of an elastic solid subject to certain external loads under kinematic restrictions. The solution to the problem is the configuration of the solid in which the stresses balance the external loads, while kinematic restrictions are obeyed. This is called the current configuration. The sought configuration is, by definition, not known *a priori*; the solution must then be expressed relative to another configuration.

This known configuration is called the reference configuration. The solution is the transformation that the reference configuration must undergo to become the current configuration. It is usually expressed in the form of a vector field of displacements (\mathbf{u}). The notation described in the following paragraphs is illustrated in Figure 2. This is known as a total Lagrangian description.

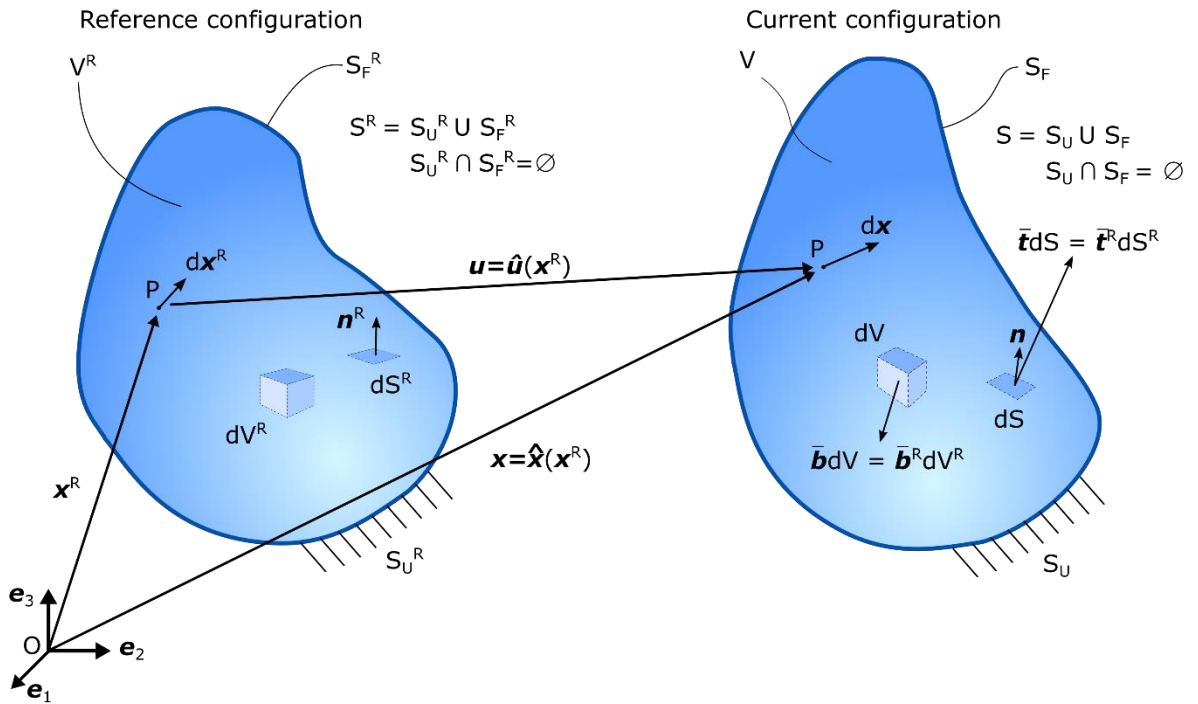
Let there be a tridimensional solid on which there are no loads (of any kind) acting; this is adopted as the reference configuration and mark all symbols that refer to this configuration with the superscript $(\cdot)^R$. The solid can be seen as a set of points in \mathbb{R}^3 that occupy its volume V^R ; to each point P corresponds a position vector $\mathbf{x}^R(P)$ with respect to the origin of a coordinate system $(O, \mathbf{e}_1, \mathbf{e}_2, \mathbf{e}_3)$. The boundary of V^R is the surface S^R , to each point on which corresponds an external unit normal vector \mathbf{n}^R .

The transformation takes each material point P in the reference configuration, herein represented by its position vector (\mathbf{x}^R), into its corresponding position vector in the current configuration (\mathbf{x}). This transformation is denoted by $\mathbf{x} = \hat{\mathbf{x}}(\mathbf{x}^R): V^R \rightarrow V$, and is one-to-one

and onto, therefore bijective. The volume of the solid in the current configuration is denoted by V and bounded by the surface S , to each point of which corresponds an external unitary normal vector \mathbf{n} . The transformation can also be expressed in terms of the displacement field ($\mathbf{u} = \hat{\mathbf{u}}(\mathbf{x}^R): V^R \rightarrow \mathbb{R}^3$) as

$$\hat{\mathbf{x}}(\mathbf{x}^R) = \mathbf{x}^R + \hat{\mathbf{u}}(\mathbf{x}^R). \quad (2.1)$$

Figure 2. Descriptive illustration of the notation used for the reference configuration and current configuration.



Source: Author.

2.2.1. Boundary Conditions

Considering the boundary conditions: the kinematic restrictions are valid on the subset S_U^R of S^R , which corresponds to the subset S_U of S in the current configuration, these are called the *Dirichlet boundary conditions* of the problem; when expressed in general form, as in

$$\hat{\mathbf{u}}(\mathbf{x}^R) = \bar{\mathbf{u}}, \quad \mathbf{x}^R \in S_U^R, \quad \bar{\mathbf{u}} \in \mathbb{R}^3, \quad (2.2)$$

they are called heterogeneous or prescribed displacements; when expressed as in

$$\hat{\mathbf{u}}(\mathbf{x}^R) = \mathbf{0}, \quad \mathbf{x}^R \in S_U^R, \quad (2.3)$$

homogeneous. For this model, the external loads are divided into either body forces ($\bar{\mathbf{b}}$), which are expressed as force per current configuration volume (dV); or surface forces ($\bar{\mathbf{t}}$), which are expressed as force per current configuration area (dS); they only exist in the current configuration. As the current configuration is not yet known, there are reference configuration counterparts defined as $\bar{\mathbf{b}}^R$ and $\bar{\mathbf{t}}^R$, which are expressed by volume, and area of the latter configuration, dV^R and dS^R respectively. The Neumann boundary condition is associated with the local balance on the surface; it is presented in

$$\mathbf{t}^R = \hat{\mathbf{t}}^R(\mathbf{x}^R) = \bar{\mathbf{t}}^R, \quad \mathbf{x}^R \in S_F^R, \quad (2.4)$$

and states that the stresses (\mathbf{t}^R) must balance the external forces imposed on the surface ($\bar{\mathbf{t}}^R$).

2.2.2. Kinematics

The Jacobian matrix of the transformation is the deformation gradient (\mathbf{F}); it is a second-order tensor which characterizes the local deformation. It is presented in tensor notation, index notation, and column vector notation, respectively, in

$$\begin{aligned} \mathbf{F} &= \nabla \mathbf{x} = \mathbf{I} + \nabla \mathbf{u}, \\ F_{ij} &= \frac{\partial x_i}{\partial x_j^R} = \delta_{ij} + \frac{\partial u_i}{\partial x_j^R}, \\ \mathbf{F} &= \mathbf{f}_i \otimes \mathbf{e}_i, \quad \text{where } \mathbf{f}_i = \frac{\partial \mathbf{x}}{\partial x_i^R}. \end{aligned} \quad (2.5)$$

It relates the differentials $d\mathbf{x}$ and $d\mathbf{x}^R$ as

$$d\mathbf{x} = \mathbf{F}d\mathbf{x}^R. \quad (2.6)$$

The tensor \mathbf{F} can also be written in terms of the displacement gradient (\mathbf{L})

$$\begin{aligned} \nabla \mathbf{u} = \mathbf{L} &= \boldsymbol{\gamma}_i \otimes \mathbf{e}_i, \quad \text{where } \boldsymbol{\gamma}_i = \frac{\partial \mathbf{u}}{\partial x_i^R}, \\ \mathbf{f}_i &= \boldsymbol{\gamma}_i + \mathbf{e}_i. \end{aligned} \quad (2.7)$$

The determinant of \mathbf{F} is a notable scalar denominated the Jacobian (J), it mediates the relationship between the infinitesimal volumes in the current and reference configurations, according to Euler's relation:

$$dV = JdV^R. \quad (2.8)$$

The cofactor matrix of the deformation gradient (\mathbf{G}), defined as:

$$\mathbf{G} = J\mathbf{F}^{-T} = \mathbf{g}_i \otimes \mathbf{e}_i, \text{ where } \mathbf{g}_i = \frac{1}{2} \epsilon_{ijk} \mathbf{f}_j \times \mathbf{f}_k, \quad (2.9)$$

mediates the relationship between areas in both configurations according to Nanson's relation:

$$n dS = \mathbf{G} \mathbf{n}^R dS^R. \quad (2.10)$$

There are many possible strain measures that can be useful for different contexts; all of them are related to the stretch ratio (λ) given by

$$\lambda = \frac{\|\mathbf{dx}\|}{\|\mathbf{dx}^R\|} = \frac{\|\mathbf{F} \mathbf{dx}^R\|}{\|\mathbf{dx}^R\|}. \quad (2.11)$$

The right Cauchy-Green tensor ($\mathbf{C} = \mathbf{F}^T \mathbf{F}$) represents a quadratic form that associates the square of the stretch ratio to the direction characterized by a generic unitary vector (\mathbf{v})

$$\lambda^2(\mathbf{v}) = \mathbf{v} \cdot \mathbf{C} \mathbf{v} = \mathbf{v}^T \mathbf{C} \mathbf{v}. \quad (2.12)$$

The strain measure adopted for the purposes of this work (most usual for engineering applications) is the Green strain (ε), as defined in:

$$\varepsilon = \frac{1}{2}(\lambda^2 - 1). \quad (2.13)$$

The strain tensor associated with this unidimensional strain is the Green-Lagrange tensor (\mathbf{E}), which can be written in terms of the deformation gradient (or the right Cauchy-Green tensor)

$$\mathbf{E} = \frac{1}{2}(\mathbf{F}^T \mathbf{F} - \mathbf{I}) = \frac{1}{2}(\mathbf{C} - \mathbf{I}); \quad (2.14)$$

it represents a quadratic form that associates the Green strain with the direction characterized by a generic unitary vector

$$\varepsilon(\boldsymbol{v}) = \boldsymbol{v} \cdot \boldsymbol{E} \boldsymbol{v} = \boldsymbol{v}^T \boldsymbol{E} \boldsymbol{v}. \quad (2.15)$$

2.2.3. Stresses

The stresses are the internal forces due to strain in the material; they are responsible for balancing out the external forces. The stresses are associated with a point and a direction. Only present in the current configuration, their most intuitive representation is that of the Cauchy stress tensor (\boldsymbol{T}), which associates the stress (\boldsymbol{t}), as force per unit of current configuration area (dS), to the unitary direction vector in current configuration as exemplified in

$$\boldsymbol{T} \boldsymbol{n} = \boldsymbol{t}. \quad (2.16)$$

To be able to express this in terms of the reference configuration one needs the introduction of two stress tensors: the first and second Piola-Kirchhoff stress tensors, \boldsymbol{P} and \boldsymbol{S} respectively. The first tensor associates the stress in terms of reference configuration area and direction, analog to the Cauchy stress tensor

$$\boldsymbol{P} \boldsymbol{n}^R = \boldsymbol{t}^R. \quad (2.17)$$

The two tensors relate to the Cauchy stress tensor and each other through the deformation gradient

$$\boldsymbol{P} = \boldsymbol{J} \boldsymbol{T} \boldsymbol{F}^{-T} = \boldsymbol{T} \boldsymbol{G} = \boldsymbol{F} \boldsymbol{S}. \quad (2.18)$$

The first and second Piola-Kirchhoff stress tensors are energetically conjugated to the deformation gradient and the Green-Lagrange strain tensor, respectively. This means that the internal power (P_{int}) of the solid can be written as the integral over the solid of the scalar product between the stress tensor and the time derivative of the conjugate tensor

$$P_{int} = \int_{V^R} \boldsymbol{P} : \dot{\boldsymbol{F}} \, dV^R = \int_{V^R} \boldsymbol{S} : \dot{\boldsymbol{E}} \, dV^R. \quad (2.19)$$

The interpretation and visualization of stresses is important for most elasticity problems. Although tensors are mathematical quantities independent of the choice of coordinate system, their assessment is usually through their matrix representation. This representation is tied to a choice of basis. There are some ways to circumvent this.

One such way is to do a principal component analysis. At each point there is an orthonormal basis for which there are only normal stresses. This is reflected in a diagonalized matrix representation of the stress tensor for this choice of basis. These are known as the principal stresses and are usually ordered such that $\sigma_1 \geq \sigma_2 \geq \sigma_3$. Put another way, the intensity of the principal stresses are the eigenvalues of the matrix representation of the stress tensor, and the associated basis are the eigenvectors. Another interesting result from this analysis is to find the maximum shear stress τ_{max} . At each point there is another basis that leads to no normal stresses, only shearing. Interpreting the stress tensor with Mohr's circle one can find the following expression for the maximum shear stress

$$\tau_{max} = \frac{\sigma_1 - \sigma_3}{2}. \quad (2.20)$$

A different approach to representing stresses independently from the choice of basis is by using the tensor's invariants. One important stress-related quantity that arises from this approach is the von Mises stress (σ_{vm}), commonly used in plasticity problems as the quantity evaluated in a yield criterion. This stress is computed from the Cauchy stress tensor (\mathbf{T}), which is split into its spherical ($\mathbf{T}^{sph} = \frac{1}{3}tr(\mathbf{T})\mathbf{I}$) and deviatoric ($\mathbf{T}^{dev} = \mathbf{T} - \mathbf{T}^{sph}$) components. The von Mises stress is the second invariant of the deviatoric stress tensor, which is the determinant of any of its matrix representations ($\sigma_{vm} = \det \mathbf{T}^{dev}$). It can also be expressed in terms of the generic components of the stress tensor

$$\sigma_{vm} = \sqrt{\frac{1}{2}[(T_{11} - T_{22})^2 + (T_{22} - T_{33})^2 + (T_{33} - T_{11})^2] + 3(T_{12}^2 + T_{23}^2 + T_{31}^2)}. \quad (2.21)$$

2.2.4. Constitutive law

The relationship between the stresses and strains is given by the constitutive law. According to Truesdell and Noll [12], there are three general principles that must be satisfied for a valid constitutive law. The first is the *principle of frame-indifference*, which affirms that the material behavior should not change for different observers; the second is the *principle of determinism*, which asserts that the stress state of a material point should be determined by the history of former states; and the *principle of local action*, which asserts that only the states of a small neighborhood around a particle influences its state. Ogden [13] presents what are called Cauchy elastic materials, which are models where the stress state of a particle depends only on its own current deformation state, not on history or neighboring states; these materials automatically observe the principles of determinism and local action. There is one special subclass of Cauchy elastic material which are called Green elastic or hyperelastic; these are materials for which an *elastic potential energy function*, henceforth called *strain-energy function*, exists; thus, it is a class of conservative constitutive laws.

The law adopted as example in this section is the Simo-Ciarlet Neo-Hookean material. This constitutive law is isotropic and hyperelastic, defined by a strain energy function

$$\psi = \hat{\psi}(\mathbf{F}, J) = \frac{\Lambda}{2} \left[\frac{1}{2} (J^2 - 1) - \ln J \right] + \frac{\mu}{2} [\text{tr}(\mathbf{F}^T \mathbf{F}) - 3 - 2 \ln J]; \quad (2.22)$$

where Λ and μ are material constants (in the context of linear elasticity Λ is the bulk modulus, and μ is the shear modulus); two elastic moduli are sufficient to fully characterize an isotropic material. This strain-energy function satisfies the conditions set by Ball [14] for polyconvexity, i.e., ψ is a function of \mathbf{F} and J ; and is convex for both these parameters, this implies the existence of solutions for the problem of nonlinear elasticity, as shown in the same paper. The first Piola-Kirchhoff stress tensor is the derivative of the strain energy function with respect to the deformation gradient

$$\mathbf{P} = \hat{\mathbf{P}}(\mathbf{F}) = \frac{\partial \psi}{\partial \mathbf{F}} = \left[\frac{\Lambda}{2} (J^2 - 1) - \mu \right] \mathbf{F}^{-T} + \mu \mathbf{F}. \quad (2.23)$$

This establishes the relationship between the transformation given by a displacement field and the stresses generated.

2.2.5. Balance Equations

The balance equations for the dynamics of solids are Euler's laws of motion. The first law regards the conservation of linear momentum, i.e., the change of linear momentum in time is equal to the sum of the external forces; for static problems the inertial term is neglected, and this balance can be expressed only in terms of the external forces, either in the current

$$\mathbf{f}_{ext} = \int_V \bar{\mathbf{b}} dV + \int_S \bar{\mathbf{t}} dS = \mathbf{0}, \quad (2.24)$$

or reference configuration

$$\mathbf{f}_{ext} = \int_{V^R} \bar{\mathbf{b}}^R dV^R + \int_{S^R} \bar{\mathbf{t}}^R dS^R = \mathbf{0}. \quad (2.25)$$

The equations in current and reference configuration are both further explored by applying the divergence theorem and introducing (2.16) and (2.17), respectively, leading to

$$\mathbf{f}_{ext} = \int_V (\bar{\mathbf{b}} + \text{div } \mathbf{T}) dV = \mathbf{0} \quad (2.26)$$

in the current configuration, and

$$\mathbf{f}_{ext} = \int_{V^R} (\bar{\mathbf{b}}^R + \text{div } \mathbf{P}) dV^R = \mathbf{0} \quad (2.27)$$

in the reference configuration; this must be valid for any arbitrary part of the solid, therefore, the conservation of linear momentum implies

$$\text{div } \mathbf{T}(\hat{\mathbf{x}}(\mathbf{x}^R)) + \bar{\mathbf{b}}(\hat{\mathbf{x}}(\mathbf{x}^R)) = \mathbf{0}, \quad \forall \mathbf{x}^R \in V^R, \text{ and} \quad (2.28)$$

$$\text{div } \mathbf{P}(\mathbf{x}^R) + \bar{\mathbf{b}}^R(\mathbf{x}^R) = \mathbf{0}, \quad \forall \mathbf{x}^R \in V^R \quad (2.29)$$

must hold, each in their respective configuration. The second law states the conservation of angular momentum, this is equivalent to requiring the symmetry of the Cauchy stress tensor, which can also be written in terms of the First Piola-Kirchhoff stress tensor

$$\mathbf{P}\mathbf{F}^T = (\mathbf{P}\mathbf{F}^T)^T; \quad (2.30)$$

the expression in (2.23) satisfies this condition.

2.2.6. Differential formulation

The static problem of elasticity can be entirely formulated in terms of the displacement field using (2.29), (2.23), (2.5), and the boundary conditions (2.2) and (2.4); this formulation configures the Boundary Value Problem (BVP) summarized in the system of partial differential equations (PDE)

Find $\mathbf{u}(\mathbf{x}^R)$ such that:

$$\begin{cases} \operatorname{div} \mathbf{P} + \bar{\mathbf{b}}^R = \mathbf{0}, & \mathbf{x}^R \in V^R \\ \mathbf{P}\mathbf{n}^R = \bar{\mathbf{t}}^R, & \mathbf{x}^R \in S_F^R \\ \mathbf{u} = \bar{\mathbf{u}}, & \mathbf{x}^R \in S_U^R \end{cases} . \quad (2.31)$$

The problem is presented formulated relative to the reference configuration because it is the one known *a priori*. This is called the differential formulation of the problem.

In this formulation, the displacement field must be known up to second derivatives. Therefore, admitting $\bar{\mathbf{b}}^R$ as continuous, \mathbf{u} must be an element of $(C^2(V^R))^3$, the space of continuous vector-valued functions with continuous first and second derivatives in V^R . This system of partial differential equations is nonlinear, due to geometrical (displacement-strain relationship is nonlinear, as well as admitting large displacements and rotations) and physical nonlinearity (stresses are nonlinear with respect to the strains).

Analytic solutions to this kind of problem are usually regarded as unattainable or, at least, impractical. This is because of the nonlinearity, and possible intricacy of the domain, in practical applications. There is a recently developed area of study called nonconvex analysis that focuses on analytic solutions for this sort of problem. It is, however, outside the scope of this work. For a general overview of this one can refer to Gao, et al. [15], and for problem of elasticity in large deformations specifically, to Gao [16].

2.2.7. Weak formulation

The problem can be reformulated to admit a different kinds of solutions, called weak solutions; these must hold only when considered along with certain weight functions, called test functions. The advantage of this is a drop in the regularity requirement of the problem, rendering the weak solutions easier to find. For most practical purposes, the

lesser regularity of the weak solution is not a drawback. More in-depth information regarding partial differential equations can be found in Evans [17]. The weak formulation is obtained by integrating the residual of the differential equations over the domain, weighted by a test function (in this case a test vector) $\delta \mathbf{u}$,

$$\int_{V^R} (\operatorname{div} \mathbf{P} + \bar{\mathbf{b}}^R) \cdot \delta \mathbf{u} \, dV^R = \int_{V^R} \operatorname{div} \mathbf{P} \cdot \delta \mathbf{u} \, dV^R + \int_{V^R} \bar{\mathbf{b}}^R \cdot \delta \mathbf{u} \, dV^R = 0. \quad (2.32)$$

Using the divergence theorem,

$$\int_{V^R} \operatorname{div} \mathbf{P} \cdot \delta \mathbf{u} \, dV^R = - \int_{V^R} \mathbf{P} : \nabla \delta \mathbf{u} \, dV^R + \int_{S^R} (\mathbf{P} \mathbf{n}^R) \cdot \delta \mathbf{u} \, dS^R, \quad (2.33)$$

and applying the boundary conditions,

$$\int_{S^R} (\mathbf{P} \mathbf{n}^R) \cdot \delta \mathbf{u} \, dS^R = \int_{S_U^R} (\mathbf{P} \mathbf{n}^R) \cdot \delta \mathbf{u} \, dS^R + \int_{S_F^R} (\mathbf{P} \mathbf{n}^R) \cdot \delta \mathbf{u} \, dS^R = \int_{S_F^R} \bar{\mathbf{t}}^R \cdot \delta \mathbf{u} \, dS^R, \quad (2.34)$$

one obtains the weak formulation:

$$\int_{V^R} \mathbf{P} : \nabla \delta \mathbf{u} \, dV^R - \int_{V^R} \bar{\mathbf{b}}^R \cdot \delta \mathbf{u} \, dV^R - \int_{S_F^R} \bar{\mathbf{t}}^R \cdot \delta \mathbf{u} \, dS^R = 0. \quad (2.35)$$

This formulation is also called the *principle of virtual work* (PVW). This is due to the test function being interpreted as a virtual displacement field. The positive integral is interpretable as the work done by the stresses for that virtual displacement field, i.e., the internal virtual work; while the negative integrals represent the work done by the external forces for that same virtual displacement, i.e., the external virtual work. The principle states that, for the solution to be balanced, the difference between internal and external virtual works should be zero for arbitrary virtual displacement fields $\delta \mathbf{u}$.

Looking at the requirements: $\bar{\mathbf{b}}^R$ and $\bar{\mathbf{t}}^R$ need to be integrable functions, while \mathbf{u} and $\delta \mathbf{u}$ must have integrable first derivatives. There are specific function vector spaces that satisfy each of these requirements. The space $L^2(\Omega)$, over a domain Ω , is known as the vector space of square-integrable functions; it has an associated inner product, which will be

denoted³ as $(f, g)_{0,\Omega} = \int_{\Omega} f g \, d\Omega$, and the induced norm: $\|f\|_0 = \left(\int_{\Omega} |f|^2 \, d\Omega \right)^{\frac{1}{2}}$. The space $H^1(\Omega)$ is the Sobolev space $W^{1,2}(\Omega)$, which is the vector space of functions of $L^2(\Omega)$ with all first derivatives in $L^2(\Omega)$; this space also has an associated inner product $(f, g)_{1,\Omega} = \int_{\Omega} (fg + \nabla f \cdot \nabla g) \, d\Omega$, the induced norm $\|f\|_1 = \left(\int_{\Omega} (|f|^2 + \nabla f \cdot \nabla f) \, d\Omega \right)^{\frac{1}{2}}$, and also a semi-norm $|f|_1 = \left(\int_{\Omega} (\nabla f \cdot \nabla f) \, d\Omega \right)^{\frac{1}{2}}$. Additionally, the subspace $H_0^1(\Omega)$ of $H^1(\Omega)$ is that of those functions that satisfy the homogeneous Dirichlet boundary conditions ($f = 0$ in S_U^R). The terms $\bar{\mathbf{b}}^R$ and $\bar{\mathbf{t}}^R$ belong to $(L^2(V^R))^3$, as they are vectors with three components, each of which belong to $L^2(\Omega)$; whereas the displacement field (\mathbf{u}) belongs to $(H^1(V^R))^3$, and the test vector ($\delta\mathbf{u}$) to $(H_0^1(V^R))^3$.

In this formulation, the problem becomes to find \mathbf{u} , which satisfies the Dirichlet boundary condition (2.2), and for which (2.35) holds for every $\delta\mathbf{u}$.

$$\begin{aligned} & \text{Find } \mathbf{u} \in \left(H^1(V^R) \right)^3 \text{ such that, for all } \delta\mathbf{u} \in \left(H_0^1(V^R) \right)^3 : \\ & \left\{ \begin{array}{l} \int_{V^R} \mathbf{P} : \nabla \delta\mathbf{u} \, dV^R - \int_{V^R} \bar{\mathbf{b}}^R \cdot \delta\mathbf{u} \, dV^R - \int_{S_F^R} \bar{\mathbf{t}}^R \cdot \delta\mathbf{u} \, dS^R = 0 \\ \mathbf{u} = \hat{\mathbf{u}}, \mathbf{x}^R \in S_U^R \end{array} \right. \end{aligned} \quad (2.36)$$

2.2.7.1. Potential formulation

The weak formulation just presented was obtained from purely mathematical manipulations, without much consideration for the physical interpretation behind the results. This is the more general way to arrive at this formulation.

There is another way to formulate the problem which provides a physical meaning. This connection to the physical world is important for the proof of existence of solutions for conservative problems.

³ The index 0 is adopted because $L^2(\Omega)$ can be thought of as $H^0(\Omega)$, the vector space of functions whose 0th derivatives (i.e., themselves) belong to $L^2(\Omega)$.

Let $\bar{\mathbf{b}}^R$ and $\bar{\mathbf{t}}^R$ be conservative loads. This means that there exist external potential energy density functions associated with each, ψ_V and ψ_S , respectively. They are defined such that $\bar{\mathbf{b}}^R = -\frac{\partial \psi_V}{\partial \mathbf{u}}$, and $\bar{\mathbf{t}}^R = -\frac{\partial \psi_S}{\partial \mathbf{u}}$.

The total mechanical energy of the problem E is the sum of kinetic T and the total potential energy $U = U_{int} + U_{ext}$. The kinetic energy is zero, for the herein considered static or quasi-static problems. Therefore, the total mechanical energy is the total potential energy.

$$E = U = U_{int} + U_{ext}. \quad (2.37)$$

The internal potential energy is given by the integral of the strain-energy function, assuming a hyperelastic material,

$$U_{int} = \int_{V^R} \psi dV^R; \quad (2.38)$$

whereas the external potential energy is the integral of the external potential energy density functions:

$$U_{ext} = \int_{V^R} \psi_V dV^R + \int_{S^R} \psi_S dS^R. \quad (2.39)$$

The total potential energy is a functional on the displacement field \mathbf{u} :

$$E = U = \hat{U}(\mathbf{u}) = \int_{V^R} \psi dV^R + \int_{V^R} \psi_V dV^R + \int_{S^R} \psi_S dS^R. \quad (2.40)$$

The solution for the problem is given by a stationary point of the total mechanical energy, in this case the total potential energy; furthermore, for stable solutions the stationary point must correspond to a point of minimum. Equating the first variation to zero leads to:

$$\begin{aligned} \delta E = \delta U &= \int_{V^R} \frac{\partial \psi}{\partial \mathbf{u}} \cdot \delta \mathbf{u} dV^R + \int_{V^R} \frac{\partial \psi_V}{\partial \mathbf{u}} \cdot \delta \mathbf{u} dV^R + \int_{S^R} \frac{\partial \psi_S}{\partial \mathbf{u}} \cdot \delta \mathbf{u} dS^R \\ &= \int_{V^R} \mathbf{P} : \nabla \delta \mathbf{u} dV^R - \int_{V^R} \bar{\mathbf{b}}^R \cdot \delta \mathbf{u} dV^R - \int_{S^R} \bar{\mathbf{t}}^R \cdot \delta \mathbf{u} dS^R = 0. \end{aligned} \quad (2.41)$$

Which is the same equation as the weak formulation (obtained by the weighted integral of the residual), but now restricted to conservative loads (those for which the potentials

shown in (2.39) exist). The existence of solutions for the minimization of the energy functional is related to the polyconvexity of the strain-energy function.

2.3. Linear Elasticity

Finite elasticity is useful for modeling a wide range of problems; it is capable of handling both small and large strains, displacements, and rotations. Nonetheless, the ensuing system of partial differential equations is nonlinear, thus requiring iterative techniques to solve. Many problems in engineering do not require such powerful formulation of elasticity; most problems involving structural applications deal with small strains, displacements, and rotations. The formulation for Linear Elasticity results from the linearization of kinematic and constitutive relations around the solution $\bar{\mathbf{u}} = \mathbf{0}$, which yields a linear system of partial differential equations. This linearized version is applicable for situations where a set of hypotheses are valid.

2.3.1. Linearization procedure

The procedure consists of taking the linear terms in the Taylor series expansion of the quantity being linearized. This is exemplified for a generic function $f = \hat{f}(\mathbf{u})$ expanded around $\mathbf{u} = \bar{\mathbf{u}}$ leads to:

$$f(\bar{\mathbf{u}} + \Delta\mathbf{u}) = f(\bar{\mathbf{u}}) + \frac{\partial f}{\partial \mathbf{u}}(\bar{\mathbf{u}}) \cdot \Delta\mathbf{u} + R. \quad (2.42)$$

The term containing the gradient is equivalent to the directional derivative of f at the point $\bar{\mathbf{u}}$ in the direction of $\Delta\mathbf{u}$. The linearization of f around $\bar{\mathbf{u}}$ can therefore be presented as:

$$\Delta(f)|_{\mathbf{u}=\bar{\mathbf{u}}} = f(\bar{\mathbf{u}}) + \frac{\partial f}{\partial \mathbf{u}}(\bar{\mathbf{u}})[\Delta\mathbf{u}]. \quad (2.43)$$

In the case of a vector valued function $\mathbf{f} = \hat{\mathbf{f}}(\mathbf{u})$:

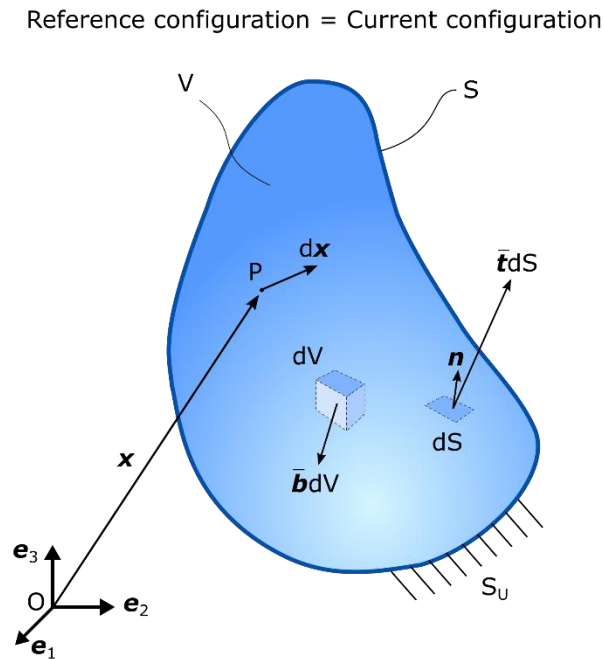
$$\mathbf{f}(\bar{\mathbf{u}} + \Delta\mathbf{u}) = \mathbf{f}(\bar{\mathbf{u}}) + \frac{\partial \mathbf{f}}{\partial \mathbf{u}}(\bar{\mathbf{u}}) \cdot \Delta\mathbf{u} + \mathbf{R} = \mathbf{f}(\bar{\mathbf{u}}) + \nabla \mathbf{f}(\bar{\mathbf{u}}) \cdot \Delta\mathbf{u} + \mathbf{R}, \quad (2.44)$$

$$\Delta(\mathbf{f})|_{\mathbf{u}=\bar{\mathbf{u}}} = \mathbf{f}(\bar{\mathbf{u}}) + \nabla \mathbf{f}(\bar{\mathbf{u}})[\Delta\mathbf{u}]. \quad (2.45)$$

2.3.2. Hypotheses

As the linear problem derives from a linearization around a configuration where $\mathbf{u} = \mathbf{0}$, two hypotheses are introduced: those of *small displacements* and *small rotations*. As consequence, the separation into reference and current configurations is not needed, as the difference between them is negligible (with respect to balance equations). Due to this, the problem can be formulated in the current configuration, as illustrated in Figure 3. To account for geometrical linearity, the strain relations must be linearized, requiring the *small strain hypothesis*. And for material linearity the constitutive law is also linearized, which is consistent with the last hypothesis.

Figure 3. Descriptive illustration of the notation used for the unique configuration of linear elasticity.



Source: Author.

2.3.3. Boundary conditions

The boundary conditions remain the same as previously explained in section 2.2.1; the Dirichlet boundary condition, homogeneous Dirichlet boundary condition, and Neumann boundary condition, are expressed as in (2.2), (2.3), and (2.4), respectively, with the exception that the superscript $(\cdot)^R$ is dropped, as they are all written in the current configuration.

2.3.4. Kinematics

The strain tensor used is called the infinitesimal strain tensor (E^l); this tensor is derived by linearizing E around $\bar{\mathbf{u}} = \mathbf{0}$ (where $E|_{\mathbf{u}=\mathbf{0}} = \mathbf{0}$ and $F|_{\mathbf{u}=\mathbf{0}} = \mathbf{I}$):

$$E^l = \Delta E[\mathbf{u}] = E|_{\mathbf{u}=\mathbf{0}} + \frac{1}{2}(F^T|_{\mathbf{u}=\mathbf{0}}\nabla\mathbf{u} + \nabla\mathbf{u}^T F|_{\mathbf{u}=\mathbf{0}}) = \frac{1}{2}(\nabla\mathbf{u} + \nabla\mathbf{u}^T), \quad (2.46)$$

obtaining what is, effectively, the symmetric part of the displacement gradient.

Due to this symmetric nature of the tensor, there are only six independent terms; the infinitesimal strain tensor can be represented as a column vector ($\boldsymbol{\varepsilon}$) of dimension 6, which can be expressed using the notation of tensors,

$$\boldsymbol{\varepsilon} = \{E_{11}^l, E_{22}^l, E_{33}^l, 2E_{12}^l, 2E_{23}^l, 2E_{31}^l\}^T, \quad (2.47)$$

or the one adopted by Timoshenko, which is common in the literature, and will be adopted for the section on St. Venant's theory:

$$\boldsymbol{\varepsilon} = \{\varepsilon_{11}, \varepsilon_{22}, \varepsilon_{33}, \gamma_{12}, \gamma_{23}, \gamma_{31}\}^T. \quad (2.48)$$

This vector representation is used for Voigt's notation.

2.3.5. Stresses

Due to geometric linearity, the stress tensor used is Cauchy's. Which is energetically conjugated with Green-Lagrange strain tensor, or in this case, with the infinitesimal strain tensor. This tensor is symmetric due to the conservation of angular momentum, as explained in section 2.2.5; because of this symmetry, this tensor can also be written as a column vector ($\boldsymbol{\sigma}$) of dimension 6, for Voigt's notation. This column vector can also be written in tensor notation

$$\boldsymbol{\sigma} = \{T_{11}, T_{22}, T_{33}, T_{12}, T_{23}, T_{31}\}^T, \quad (2.49)$$

or Timoshenko's notation

$$\boldsymbol{\sigma} = \{\sigma_{11}, \sigma_{22}, \sigma_{33}, \tau_{12}, \tau_{23}, \tau_{31}\}^T. \quad (2.50)$$

2.3.6. Constitutive law

Due to physical linearity, the constitutive law degenerates into a linear law. The relationship between the stress and strain tensors is mediated by a constant 4th-order tensor (\mathbb{D})

$$\mathbf{T} = \mathbb{D}\mathbf{E}^I. \quad (2.51)$$

In the case of isotropic material, this 4th-order tensor can be fully determined by two elastic constants (in this case the Young modulus, E , and Poisson ratio, ν). However, adopting Voigt's notation, this 4th-order tensor can be represented by a 6-dimensional 2nd-order tensor (\mathbf{D}),

$$\mathbf{D} = \frac{E}{(1+\nu)(1-2\nu)} \begin{bmatrix} 1-\nu & \nu & \nu & & & \\ \nu & 1-\nu & \nu & & & \\ \nu & \nu & 1-\nu & & & \\ & & & \frac{1-2\nu}{2} & 0 & 0 \\ & & & 0 & \frac{1-2\nu}{2} & 0 \\ & & & 0 & 0 & \frac{1-2\nu}{2} \end{bmatrix}. \quad (2.52)$$

In this notation the relationship expressed in (2.51) becomes

$$\boldsymbol{\sigma} = \mathbf{D}\boldsymbol{\varepsilon}. \quad (2.53)$$

2.3.7. Balance equations

The balance equations remain the same, only now written in the unique configuration. Conservation of linear momentum becomes

$$\text{div } \mathbf{T} + \bar{\mathbf{b}} = \mathbf{0}, \text{ in } V; \quad (2.54)$$

and conservation of angular momentum

$$\mathbf{T} = \mathbf{T}^T. \quad (2.55)$$

2.3.8. Differential formulation

The differential formulation of the problem is written as

Find \mathbf{u} such that:

$$\begin{cases} \operatorname{div} \mathbf{T} + \bar{\mathbf{b}} = \mathbf{0}, & \mathbf{x} \in V \\ \mathbf{T}\mathbf{n} = \bar{\mathbf{t}}, & \mathbf{x} \in S_F \\ \mathbf{u} = \bar{\mathbf{u}}, & \mathbf{x} \in S_U \end{cases} \quad (2.56)$$

The requirements are analog to those described in section 2.2.6: $\mathbf{u} \in (C^2(V))^3$ if $\bar{\mathbf{b}} \in (C^0(V))^3$. Analytic solutions can be found in the literature for simple geometries, usually for plane problems; Timoshenko [18] presents some, Johnson [5] presents Hertz's analytic solution for non-conformal contact, Roark's [19] present a compendium of solutions.

2.3.9. Weak formulation

The weak formulation for linear elasticity is derived using the same process described in section 2.2.7,

Find $\mathbf{u} \in (H^1(V))^3$ such that, for all $\delta\mathbf{u} \in (H_0^1(V))^3$:

$$\begin{cases} \int_V \mathbf{T} : \delta\mathbf{E}^l \, dV - \int_V \bar{\mathbf{b}} \cdot \delta\mathbf{u} \, dV - \int_{S_F} \bar{\mathbf{t}} \cdot \delta\mathbf{u} \, dS = 0, \\ \mathbf{u} = \hat{\mathbf{u}}, & \mathbf{x} \in S_U \end{cases} \quad (2.57)$$

where the virtual infinitesimal strain tensor is

$$\delta\mathbf{E}^l = \frac{1}{2}(\nabla\delta\mathbf{u} + \nabla\delta\mathbf{u}^T). \quad (2.58)$$

The change when using Voigt's notation is:

$$\int_V \mathbf{T} : \delta\mathbf{E}^l \, dV = \int_V \boldsymbol{\sigma} \cdot \delta\boldsymbol{\varepsilon} \, dV. \quad (2.59)$$

The potential formulation for linear elasticity is basically the same, performing the suitable substitution for linearized quantities.

2.4. Plane strain problem

Plane strain problems are a set of problems in elasticity where the displacement in one direction is restricted. This is achieved due to characteristics of the geometry, load and boundary conditions; and leads to a decoupling in the system of partial differential equations, allowing for a three-dimensional problem to be solved using a two-dimension framework, effectively simplifying it. This applies to both Finite and Linear elasticity.

These problems are associated with prismatic solids, therefore inducing the existence of an axis, along which all cross-sections share the same geometry. The boundary conditions regarding directions orthogonal to the axis are the same through all cross-sections, and the displacement in the direction of the axis is bound at the extremities. The usual example presented in textbooks for this class of problems is the analysis of dams: the shoulders provide the displacement restrictions, the geometry is usually prismatic, and the load provided by the water pressure on the wall is shared by all cross-sections.

For the purposes of this work, the axis associated with \mathbf{e}_3 will be adopted as aligned with the axis of the prismatic object in question, therefore the remaining two-dimensional problem is associated with the planes parallel to the one defined by \mathbf{e}_1 and \mathbf{e}_2 . This plane strain problem can be expressed as the kinematic restriction: $\boldsymbol{\gamma}_3 = \mathbf{0} \rightarrow \mathbf{f}_3 = \mathbf{e}_3$.

This restriction implies that there are no out-of-plane strains ($\varepsilon_{33} = \gamma_{23} = \gamma_{31} = 0$). This leads to the associated shear stresses being null ($\tau_{23} = \tau_{31} = 0$) and the out-of-plane normal stress reflecting the Poisson effect of the other two stresses - $\sigma_{33} = \nu(\sigma_{11} + \sigma_{22})$.

Another consequence on the formulations presented in earlier sections is that: for tensor notation, all vectors (and tensors), which were 3-dimensional can now be treated as 2-dimensional by collapsing the dimension associated with \mathbf{e}_3 , e.g.

$$\mathbf{E} = \begin{bmatrix} E_{11} & E_{12} & E_{13} \\ E_{21} & E_{22} & E_{23} \\ E_{31} & E_{32} & E_{33} \end{bmatrix} \rightarrow \begin{bmatrix} E_{11} & E_{12} \\ E_{21} & E_{22} \end{bmatrix}. \quad (2.60)$$

Whereas for Voigt's notation, the 6-dimensional vectors/tensors can be treated as 3-dimensional, e.g.

$$\boldsymbol{\varepsilon} = \{\varepsilon_{11}, \varepsilon_{22}, \varepsilon_{33}, \gamma_{12}, \gamma_{23}, \gamma_{31}\}^T \rightarrow \{\varepsilon_{11}, \varepsilon_{22}, \gamma_{12}\}^T. \quad (2.61)$$

The formulation for the von Mises stress can be simplified to

$$\sigma_{vm} = \sqrt{(1 - \nu + \nu^2)\sigma_{11}^2 + (1 - \nu + \nu^2)\sigma_{22}^2 - (1 + 2\nu - 2\nu^2)\sigma_{11}\sigma_{22} + 3\tau_{12}^2}. \quad (2.62)$$

2.5. Contact constraint

The formulation of elasticity problems is easily adapted for a system of more than one body (V_i), as illustrated in Figure 4(a). For the weak formulation this is a matter of adding for each term the contribution of each body:

$$\sum_i \int_{V_i^R} \mathbf{P} : \nabla \boldsymbol{\delta u} \, dV^R - \sum_i \int_{V_i^R} \bar{\mathbf{b}}^R \cdot \boldsymbol{\delta u} \, dV^R - \sum_i \int_{S_{F,i}^R} \bar{\mathbf{t}}^R \cdot \boldsymbol{\delta u} \, dS^R = 0. \quad (2.63)$$

This can also be interpreted as a global volume, defined by the union of the individual volumes:

$$\int_{\cup_i V_i^R} \mathbf{P} : \nabla \boldsymbol{\delta u} \, dV^R - \int_{\cup_i V_i^R} \bar{\mathbf{b}}^R \cdot \boldsymbol{\delta u} \, dV^R - \int_{\cup_i S_{F,i}^R} \bar{\mathbf{t}}^R \cdot \boldsymbol{\delta u} \, dS^R = 0, \quad (2.64)$$

which, as $V^R = \cup_i V_i^R$ and $S_F^R = \cup_i S_{F,i}^R$, is equal to (2.35).

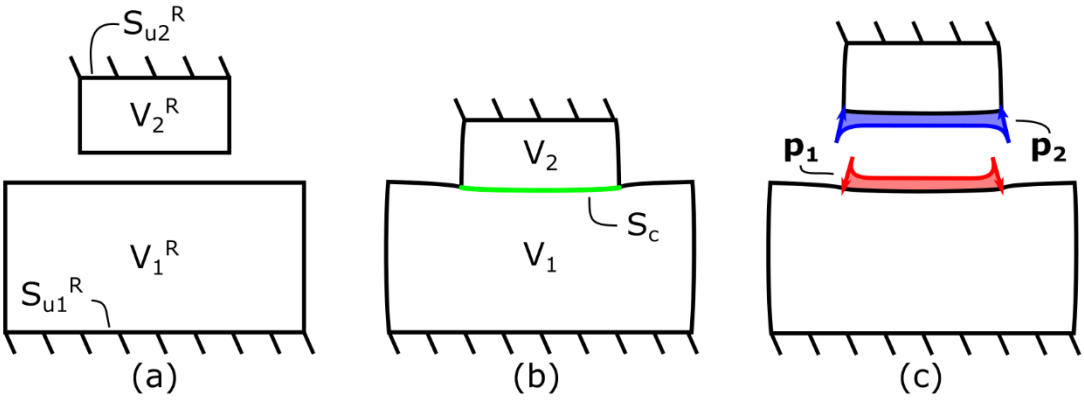
When contact occurs a new kind of boundary becomes relevant, the contact surface - $S_c = \cap_i V_i$, which is the intersection of the individual volumes (where there is contact). This is illustrated in Figure 4(b). With this new type of surface composing the boundary partition, the equality in the weak formulation stated above becomes invalid. The contact pressure must also be considered to fully balance the energy involved. This leads to the variational inequality:

$$\int_{\cup_i V_i^R} \mathbf{P} : \nabla \boldsymbol{\delta u} \, dV^R - \int_{\cup_i V_i^R} \bar{\mathbf{b}}^R \cdot \boldsymbol{\delta u} \, dV^R - \int_{\cup_i S_{F,i}^R} \bar{\mathbf{t}}^R \cdot \boldsymbol{\delta u} \, dS^R \geq 0 \quad (2.65)$$

This can be interpreted as the internal virtual work being greater than the external virtual work of the known body and surface forces because it must also balance the contact pressure, not known *a priori*, illustrated in Figure 4(c).

It bears noting that this contact pressure (p) is related to the penetration that would happen, if allowed, and is either compressive (when there is contact) or null (no contact) ($p \leq 0$). This model does not consider adhesion. This penetration is evaluated using the normal gap (g_n), the dot product of the distance to a point in the other body with the external normal at this point. A negative normal gap means there is penetration, which is not allowed ($g_n \geq 0$). The normal gap is expanded upon in section 3.5. The contact pressure is only non-zero when the normal gap is closed, otherwise it is null. This can be expressed as what is called the complementarity condition: $g_n p = 0$. The first two inequalities along with the complementarity condition describe the contact constraint as a Karush-Kuhn-Tucker condition: $p \leq 0$, $g_n \geq 0$, $g_n p = 0$. This type of condition is usual in constrained optimization problems.

Figure 4. Schematic illustration of contact interaction between two bodies. Reference configuration (a), current configuration (b), and pressure distribution (c).



Source: Author.

The problem can be solved by adopting a term for the contact contribution in the weak formulation. Normal contact can be treated as conservative (assuming no dissipation occurs), and therefore a potential can be provided to represent its contribution, adopting the framework of the potential formulation discussed in section 2.2.7.1. This potential arises from a minimization problem (total potential energy) subject to a constraint (no penetration), therefore the mathematical methods used to formulate it are borrowed from the area of constrained optimization.

There are many different methods to enforce constraints, a more comprehensive overview (in the context of contact problems) can be found in Wriggers [20]. Describing some of the usual methods:

- Lagrange multipliers enforce the constraint exactly, at the cost of introducing new degrees of freedom. These new degrees of freedom represent the contact pressure (if treated continuously) or contact forces (if treated discretely). The problem becomes of mixed nature, as a pressure/force is treated as a variable along with the displacements. The problem also turns into finding a Saddle point, as the solution must minimize the first three terms (internal and external virtual work), while maximizing the fourth one (virtual work of contact forces).
- The Mortar method uses a continuous form of the Lagrange multipliers to satisfy the contact restriction in a weak sense. Its mathematical formalism is much more elaborated, being adapted to contact contexts from its original purpose of handling mesh-tying problems. The careful choice of basis functions allows the condensation of variables, leading to smaller linear systems. However, the correct integration leads to a much more computationally expensive method. This is currently considered the state-of-the-art of contact methods where the contact forces are treated as continuous.
- The Nitsche method introduces a new boundary term in the weak formulation and does not introduce new degrees of freedom. It also treats the constraint in continuous form. However, this term leads to a more complex formulation, especially when material nonlinearity is involved.
- The Penalty method does not enforce the constraint exactly, and is usually adopted with discretized pairs, as mentioned in the Lagrange multipliers. It introduces a new parameter (the penalty coefficient), which effectively works as a spring for the penetration in each pair. The amount of persisting penetration is inversely proportional to this parameter. It requires no new degrees of freedom.
- The Augmented Lagrange method (Uzawa's algorithm) combines both the Lagrange multipliers and penalty method, usually for discretized contact pairs. It uses the penalty solution to update the Lagrange multipliers, therefore requiring no new degree of freedom, but enforcing the constraint exactly. The cost is the

introduction of a new loop to transform forces from penalty formulation into Lagrange multipliers, which runs at linear time (inefficient compared to quadratic-convergence methods such as Newton's).

The Penalty method is selected for this work. This is because of its simple formulation and physical interpretation. The discretization adopted is the Node-to-Segment discretization, which is the topic of section 3.5.

Revisiting the potential formulation of the problem, the new term representing the potential associated with the contact interaction (U_c) can be introduced in (2.37):

$$U(\mathbf{u}) = U_{int}(\mathbf{u}) + U_{ext}(\mathbf{u}) - U_c(\mathbf{u}). \quad (2.66)$$

This new term is expressed in terms of the penalty parameter (ϵ) and the normal gap (g_n) as:

$$U_c = \int_{S_c} \frac{1}{2} \epsilon g_n^2(\mathbf{u}) dS. \quad (2.67)$$

Performing the variation of this term gives

$$\delta U_c = \epsilon \int_{S_c} g_n \frac{\partial g_n}{\partial \mathbf{u}} [\delta \mathbf{u}] dS = \epsilon \int_{S_c} g_n \delta g_n dS. \quad (2.68)$$

This term is included in the weak formulation, allowing the equality again:

$$\int_{V^R} \mathbf{P} : \nabla \delta \mathbf{u} \, dV^R - \int_{V^R} \bar{\mathbf{b}}^R \cdot \delta \mathbf{u} \, dV^R - \int_{S_F^R} \bar{\mathbf{t}}^R \cdot \delta \mathbf{u} \, dS^R - \epsilon \int_{S_c} g_n \delta g_n dS = 0. \quad (2.69)$$

2.6. Hertz contact theory

This section contains a very brief introduction to Hertz contact theory, mainly focusing on the more relevant aspects for validating the contact model in the third application (section 6). This theory gives local analytical solutions for nonconformal frictionless contact (starting at a point or line; without friction) and its use is widespread. The main reference used for this section is Johnson's [5] book on Contact Mechanics.

2.6.1. Hypotheses

The theory assumes that the contact starts at a point (or line, in the special case of aligned cylinders). The configuration of the problem consists of both bodies touching at this one point, which is the origin of the coordinate system. The direction perpendicular to both surfaces at this point is elected as the z -axis. Each body (V_i) is approximated by a quadric surface around a small neighborhood of the point of contact, i.e., there is an equation $z = Ax^2 + By^2 + Cxy + Dx + Ey + F$, that describes each the approximated quadric. Each quadric has two principal curvatures around the origin, here denoted by the associated radii: the maximum (R'_i) and minimum (R''_i). The directions associated with these principal curvatures are individual to each body, here represented by index coordinates in the quadric surface equation: $z^{(i)} = \frac{1}{2R'_i} x_i^2 + \frac{1}{2R''_i} y_i^2$. The gap, $g = z^{(1)} - z^{(2)}$, between the surfaces is also a quadric and has principal curvatures denoted by the associated radii: R' and R'' . The directions associated with the principal directions for this quadric approximation of the gap are chosen as the x and y directions for our reference system.

In the general case, the contact area has an elliptic shape centered around the initial contact point. The ellipse is characterized by its two semi-axes (a, b). These, along with the maximum contact pressure (p_0) and some information on the stresses are fully determined by the principal radii of both surfaces and the total force transferred through the contact.

Another important information is that this theory relies on the principle of local action (presented in section 2.2.4). Each body is treated as an elastic half-space, this assumes that its other representative dimensions, here represented by l , are large enough for the validity of this treatment.

With these quantities established, the set of hypotheses is the following:

- i. The surfaces are continuous and nonconforming: $a \ll R'$, $b \ll R''$.
- ii. The strains are small: (Linear Elasticity) and $a \ll R'$, $b \ll R''$.
- iii. Each solid can be considered an elastic half-space: $a \ll R'_i, R''_i, l$.
- iv. The contact interaction is frictionless.

2.6.2. Description for parallel cylinders

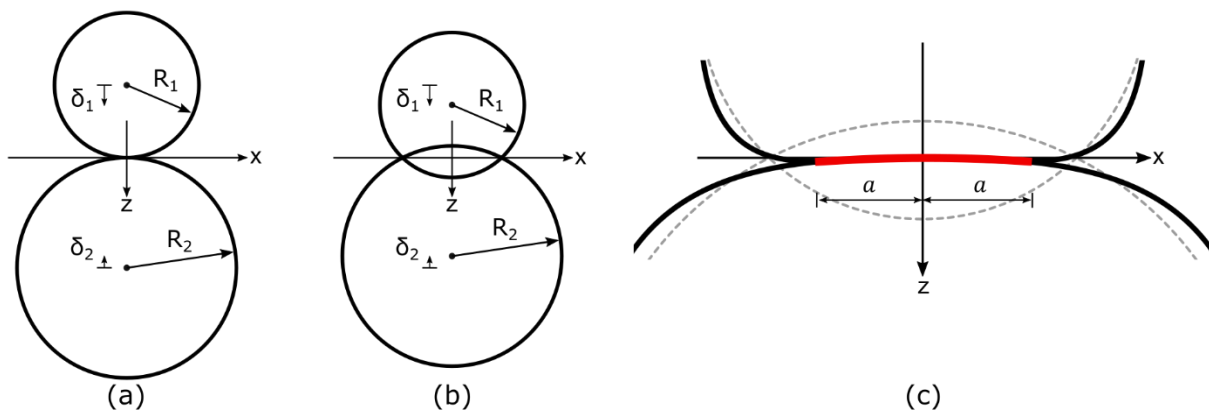
The special case of Hertz theory that is of interest for this work is that of two parallel cylinders, also known as line contact. It is treated as a plane strain problem, leading to a two-dimensional analysis involving the cylinders cross-sections, i.e., two circles.

A cylinder has its principal curvatures, and their directions, well defined. The maximum curvature radius is infinite ($R'_i = \infty$) and corresponds to the direction of the axis of the cylinder. Whereas the minimum curvature radius is the radius of its cross-section ($R''_i = R_i$). The gap, thus, has one infinite curvature radius and one non-infinite principal radius (R), this last one is the one of interest to determine the contact area and pressure, and is determined with the following expression:

$$R = \left(\frac{1}{R_1} + \frac{1}{R_2} \right)^{-1}. \quad (2.70)$$

In the case of cylinders, the contact area is a rectangle, and its width is associated with the semi-axis (a). The starting and final configurations of the contact between two cylinders are illustrated in Figure 5. In this figure, the contact is initiated at a point (a), the displacements of both cylinders accumulate to a total displacement of $\delta = \delta_1 + \delta_2$, which would lead to penetration if contact were not considered (b). The contact develops into its final configuration with the contact area in red (c). The width of the contact area is twice the semi-axis a .

Figure 5. Illustration of nonconformal contact. Starts at a point (a); displacements and penetration if contact were not considered (b); detail on contact surface (c).



Source: Author.

The interaction is also dependent on the elastic properties of both bodies. This is considered in the equivalent elastic parameter E^* :

$$E^* = \left(\frac{1-\nu_1^2}{E_1} + \frac{1-\nu_2^2}{E_2} \right)^{-1}. \quad (2.71)$$

Although displacements were used to illustrate the development of the contact, it is a quantity of global nature, whereas this theory is of a more local nature. The implication is that knowledge of the penetration that would happen if contact were not considered is not enough to determine the contact interaction. To fully determine the contact pressure field one of the following three quantities must be supplied: the total transferred load (P), which is the resultant force of the contact pressure field; the maximum pressure (p_0); or the semi-width/axis of the contact area (a). Each one can determine the other two, as is shown in Table 2.

Table 2. Determination of contact pressure field for parallel cylinders based on different supplied quantities.

Independent quantity	$P =$	$a =$	$p_0 =$
P	P	$\sqrt{\frac{4PR}{\pi E^*}}$	$\sqrt{\frac{PE^*}{\pi R}}$
a	$\frac{\pi a^2 E^*}{4R}$	a	$\frac{aE^*}{2R}$
p_0	$\frac{\pi R p_0}{E^*}$	$\frac{2R p_0}{E^*}$	p_0

Source: Author.

The contact pressure distribution is given by:

$$p(x) = \frac{p_0}{a} \sqrt{a^2 - x^2}. \quad (2.72)$$

For this case, expressions for the stresses (σ_z, σ_x) and maximum shear stress (τ_1) along the symmetry line of the contact pressure (z -axis) are supplied:

$$\sigma_z(z) = -\frac{p_0 a}{\sqrt{a^2 + z^2}}; \quad (2.73)$$

$$\sigma_x(z) = -\frac{p_0}{a} \left(\frac{a^2 + 2z^2}{\sqrt{a^2 + z^2}} - 2z \right); \quad (2.74)$$

$$\tau_1(z) = -\frac{p_0}{a} \left(z - \frac{z^2}{\sqrt{a^2+z^2}} \right). \quad (2.75)$$

2.7. St. Venant torsion theory

Torsion is relevant for many structural applications. Either as the most relevant load, e.g., torque transmission elements such as axles connecting rotors and turbines; or as undesired effect of eccentrically applied loads, as is usual in steel-framed structures due to the restraints of practical construction. Its study dates back a long time, the first known theory is attributed, according to Timoshenko [18], to French physicist Charles-Augustin de Coulomb; his theory, however, was only applicable to prismatic rods of circular cross-sections, such as the electric wires he was working with. For generic cross-sections there is another phenomenon at play: warping. The first theory that takes warping into consideration is that of French mathematician Adhémar Jean Claude Barré de Saint Venant. His theory concerns free-to-warp linear-elastic prismatic rods under uniform torsion. One important development is the formulation of a system of partial differential equations for the warping function of a given cross-section geometry; this function determines the shape the cross-section will take when warping. Another important contribution is the introduction of the torsion constant (I_T), the quantity associated with the cross-section's geometry which mediates, alongside the shear modulus (G), the relationship between the twisting moment (M_T) and the rod's rate of twist (θ') for his theory.

$$\frac{M_T}{GI_T} = \theta' \quad (2.76)$$

Later theories have further developed the study of torsion. Vlasov's theory [21] on thin-walled beams, also under linear elasticity, takes into consideration the effects of warping restriction and non-uniform torsion; in this theory the structural response is comprised of two components: one associated with uniform torsion and the other with warping torsion. The former is that of St. Venant's theory, and the latter takes only the effects of warping restrictions into consideration. The proportion of each in the total response is dependent on the cross-section's geometry. In this theory there is another geometrical quantity of great importance: the warping constant (I_w), which corresponds to the integral, over the

cross-section, of St. Venant's warping function squared. This quantity, as well as the torsion constant, is recurring in current works that cover non-uniform torsion, e.g., Trahair's [22] work on nonlinear elastic nonuniform torsion, and Sapountzakis' and Tsipira's [23] on nonlinear inelastic uniform torsion. St. Venant's theory, however simple, is still of great relevance for this field.

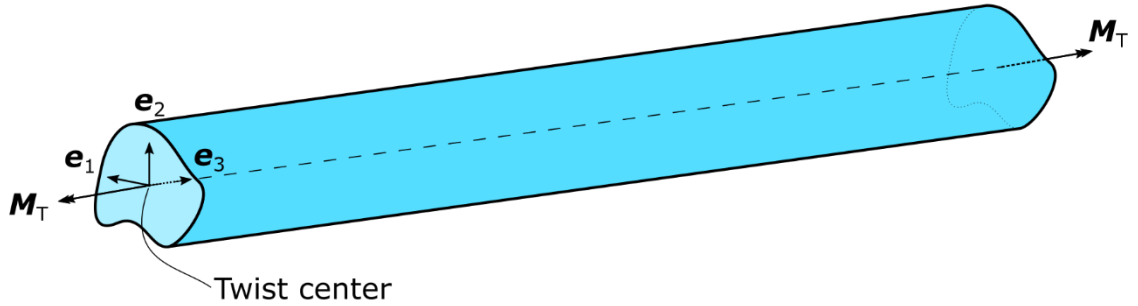
2.7.1. Problem and hypotheses

The theory developed by St. Venant (circa 1855) is constructed using the semi-inverse method, i.e., a displacement field is proposed (under a set of hypotheses) and shown to be a solution to the equations of linear elasticity. It is formulated based on a prismatic rod of general cross-section; made of a linear-elastic material with constant shear modulus (G); experiencing, exclusively, a pure twisting moment (M_T); whose length is aligned with the coordinate axis e_3 , and the origin is located at the twist center⁴ of the cross-section (which coincides with the shear center for homogeneous isotropic beams, according to Romano, Barretta and Barretta [24]), at one end of the rod; as illustrated in Figure 6. The set of hypotheses upon which the theory is constructed is the following:

- I. Each individual cross-section ($x_3 = \text{constant}$) rotates as a rigid body by an angle $\theta = \hat{\theta}(x_3)$;
- II. The rate of twist ($\theta' = \theta_{,3}$) is constant (uniform torsion);
- III. The cross-sections are free to warp. However, the warping is the same for all of them;
- IV. Small rotations ($\theta \ll 1$);
- V. Linear elastic material ($\sigma_{ij} = G\gamma_{ij}$, $i \neq j$).

⁴ If the same BVP is formulated using another point as the origin of the system, the resulting solution is a linear combination of the warping function and a first order polynomial.

Figure 6. Rod of generic cross-section subject to pure twisting moment.



Source: Author.

2.7.2. Development and differential formulation

Based on (I), applying a rigid body rotation of angle θ only the first two coordinates, then the corresponding terms of the displacement field can be expressed as

$$\begin{cases} u_1 = x_1(\cos \theta - 1) - x_2 \sin \theta \\ u_2 = x_1 \sin \theta + x_2(\cos \theta - 1) \end{cases} \quad (2.77)$$

The small rotations hypothesis (IV) justifies the linearization of the sine and cosine functions

$$\theta \ll 1 \therefore \begin{cases} \cos \theta \approx 1 \\ \sin \theta \approx \theta \end{cases} \quad (2.78)$$

and of θ , by taking the first term of its Taylor expansion around 0:

$$\theta \approx \frac{d\theta}{dx_3} x_3 = \theta' x_3. \quad (2.79)$$

With these approximations and writing the warping (u_3) as the warping function $\psi = \hat{\psi}(x_1, x_2)$ times the rate of twist, in accordance with (III), yields the proposed displacement field

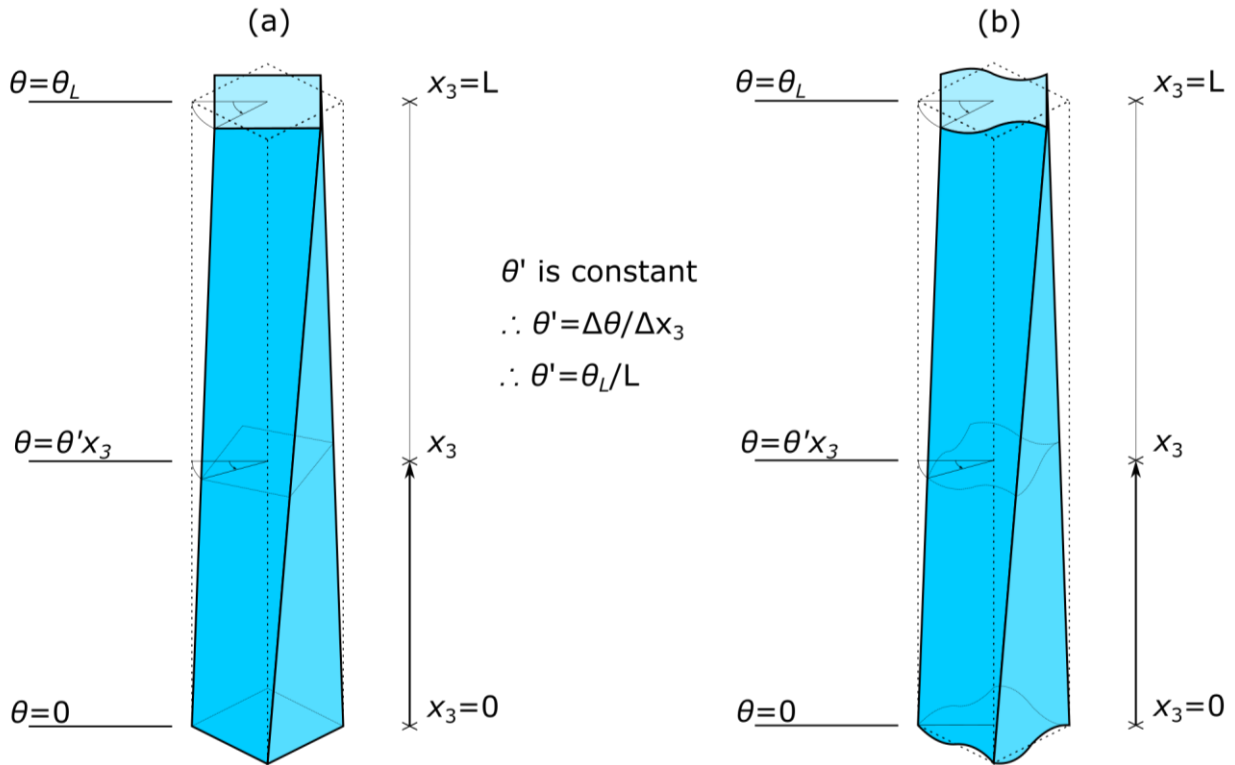
$$\begin{cases} u_1 = -\theta' x_2 x_3 \\ u_2 = +\theta' x_1 x_3 \\ u_3 = \theta' \psi(x_1, x_2) \end{cases} \quad (2.80)$$

This displacement field is illustrated in Figure 7, where (a) represents the displacement of Coulomb's theory, i.e., with no warping, and (b) the displacement field for St. Venant's theory. The displacements are exaggerated to illustrate the differences.

The components of the linearized Green-Lagrange tensor, in Voigt's notation, are derived from this field

$$\begin{aligned} \varepsilon_{11} = \varepsilon_{22} = \varepsilon_{33} = \gamma_{12} &= 0 \\ \gamma_{13} &= \theta'(\psi_{,1} - x_2) \\ \gamma_{23} &= \theta'(\psi_{,2} + x_1) \end{aligned} \quad (2.81)$$

Figure 7. Displacement according to Coulomb's (a) and St. Venant's (b) theories.



Source: Author.

Using the linear elastic constitutive law (V) the components of the Cauchy stress tensor are obtained

$$\begin{aligned} \sigma_{11} = \sigma_{22} = \sigma_{33} = \tau_{12} &= 0 \\ \tau_{13} &= G\theta'(\psi_{,1} - x_2) \\ \tau_{23} &= G\theta'(\psi_{,2} + x_1) \end{aligned} \quad (2.82)$$

The balance equations for linear elasticity (2.54) result in only one non-trivial equation

$$G\theta'(\psi_{,11} + \psi_{,22}) = G\theta'\Delta\psi = 0, \quad (2.83)$$

which is satisfied if

$$\Delta\psi = 0, \quad (2.84)$$

the Laplace equation in two dimensions, holds for the whole of the cross-section. The cross-section is now the domain of a BVP whose solution is the warping function; herein this domain will be denoted Ω , and its boundary $\partial\Omega$. The Neumann boundary condition, second equation in (2.56), in the absence of an imposed surface force, results in only one non-trivial equation

$$\mathbf{T}\mathbf{n} = \mathbf{0} \rightarrow \tau_{13}n_1 + \tau_{23}n_2 = 0. \quad (2.85)$$

Substituting the stresses from (2.82) leads to

$$G\theta'[(\psi_{,1} - x_2)n_1 + (\psi_{,2} + x_1)n_2] = 0, \quad (2.86)$$

which can be rewritten as

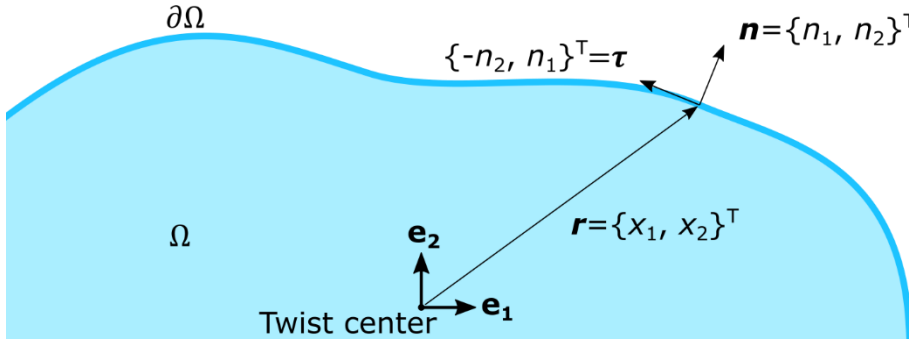
$$\psi_{,1}n_1 + \psi_{,2}n_2 = -x_1n_2 + x_2n_1, \quad (2.87)$$

or, in vector notation:

$$\nabla\psi \cdot \mathbf{n} = \mathbf{r} \cdot \boldsymbol{\tau}, \quad (2.88)$$

where \mathbf{n} is the external normal unit vector, $\boldsymbol{\tau}$ is the tangential unit vector (both defined for every point on the boundary), and \mathbf{r} is the position vector relative to the twist center, as illustrated in Figure 8.

Figure 8. Normal (\mathbf{n}), tangent ($\boldsymbol{\tau}$) and projection of position vector on the cross-section plane (\mathbf{r}).



Source: Author.

Therefore, the boundary value problem for the warping function ψ is presented in its differential form

Find $\psi = \hat{\psi}(\mathbf{r})$ such that:

$$\begin{cases} \Delta\psi = 0, & \mathbf{r} \in \Omega \\ \nabla\psi \cdot \mathbf{n} = \mathbf{r} \cdot \boldsymbol{\tau}, & \mathbf{r} \in \partial\Omega \end{cases} \quad (2.89)$$

As the function is only represented in this formulation by derivatives, the solution is determined up to a constant; the missing constant is that which makes the integral of this function over the domain equal to zero.

In this formulation the requirement for ψ is that its Laplacian is constant and equal to zero, therefore defined for the whole domain. Ergo, the sought function must belong to the space $C^2(\Omega)$.

The problem (in this formulation) has analytical solutions for a few simple geometries in the literature. Some are presented in the work of Timoshenko. Another interesting work exploring analytical solutions for simple geometries is that of Silva [25].

2.7.3. Weak formulation

As with the other BVPs, the same process of integrating the residual, weighed by an arbitrary test function ($\delta\psi$), is applied

$$\int_{\Omega} \Delta\psi \delta\psi d\Omega = 0. \quad (2.90)$$

Using Green's first identity and rearranging the terms:

$$\int_{\Omega} \nabla\psi \cdot \nabla\delta\psi d\Omega = \int_{\partial\Omega} \delta\psi (\nabla\psi \cdot \mathbf{n}) d\partial\Omega. \quad (2.91)$$

Substituting the Neumann boundary condition (2.88),

$$\int_{\Omega} \nabla\psi \cdot \nabla\delta\psi d\Omega = \int_{\partial\Omega} \delta\psi (\mathbf{r} \cdot \boldsymbol{\tau}) d\partial\Omega. \quad (2.92)$$

The problem can then be formulated as

$$\text{Find } \psi \in H^1(\Omega) \text{ such that, for all } \delta\psi \in H^1(\Omega): \quad (2.93)$$

$$\int_{\Omega} \nabla\psi \cdot \nabla\delta\psi d\Omega = \int_{\partial\Omega} \delta\psi (\mathbf{r} \cdot \boldsymbol{\tau}) d\partial\Omega.$$

In this form both ψ and $\delta\psi$ belong to $H^1(\Omega)$.

2.7.4. Prandtl's solution

In the times before computers (and computational methods) were invented, solving for the warping function becomes a real challenge for geometries more intricate than the elementary shapes. One inventive way to circumvent this problem was proposed by German physicist Ludwig Prandtl, around 1903. He proposed an alternative way to formulate the problem, in which a new function, called Prandtl's function (ϕ), is related to the tangential stresses,

$$\begin{cases} \phi_{,1} = -\tau_{23} \\ \phi_{,2} = \tau_{13} \end{cases}. \quad (2.94)$$

With this function, the non-trivial balance equation from earlier becomes automatically satisfied due to Clairaut-Schwartz's theorem ($\phi_{,12} = \phi_{,21}$). The equation that needs to be satisfied is obtained by taking the Laplacian of said function, and substituting the stresses definition from (2.82):

$$\Delta\phi = G\theta'(\psi_{,21} - \psi_{,12} - 2) = -2G\theta', \text{ in } \Omega. \quad (2.95)$$

The boundary equation (2.88) can be written, in terms of ϕ , as

$$\nabla\phi \cdot \boldsymbol{\tau} = \frac{\partial\phi}{\partial\tau} = 0, \text{ in } \partial\Omega; \quad (2.96)$$

Which translates to ϕ being constant along the boundary. This constant is arbitered as 0. This way the boundary condition of Neumann type (2.96) becomes a Dirichlet type condition:

$$\phi = 0, \text{ in } \partial\Omega. \quad (2.97)$$

Therefore, St. Venant's torsion is formulated in terms of Prandtl's function as

$$\begin{cases} \Delta\phi = -2G\theta', \text{ in } \Omega \\ \phi = 0, \text{ in } \partial\Omega \end{cases} \quad (2.98)$$

As this formulation does not involve the coordinates in the BVP, this problem does not require the origin to be at the twist center.

This BVP is remarkable because it represents a formulation of the uniform torsion problem like that of the displacement of an elastic membrane, covering a cross-section-shaped hole, supported at the edges and subject to uniform pressure. This inspired what is called the membrane analogy, which allows the physical modelling of membranes to obtain results regarding torsion properties of the cross-section, such as the torsion constant and a qualitative estimate of the stresses distribution.

2.7.4.1. Weak Formulation

Applying the same process done for the formulation based on the warping function, using $\delta\phi$ as test function:

$$\int_{\Omega} \nabla\phi \cdot \nabla\delta\phi d\Omega = -2G\theta' \int_{\Omega} \delta\phi d\Omega. \quad (2.99)$$

Leads to:

Find $\psi \in H^1(\Omega)$ such that, for all $\delta\psi \in H^1(\Omega)$:

$$\begin{cases} \int_{\Omega} \nabla\phi \cdot \nabla\delta\phi d\Omega = -2G\theta' \int_{\Omega} \delta\phi d\Omega \\ \phi = 0, \text{ in } \delta\Omega \end{cases} \quad (2.100)$$

2.7.5. Torsion constant

This geometric property of the cross-section helps mediate the relation between the twisting moment and the twist rate, as shown in (2.76). Defining the twisting moment in terms of the tangential stresses

$$M_T = \int_{\Omega} (\tau_{23}x_1 - \tau_{13}x_2)d\Omega, \quad (2.101)$$

and expressing the stresses in terms of the warping function

$$M_T = \int_{\Omega} G\theta'(x_1\psi_{,2} + x_2\psi_{,1} + x_1^2 + x_2^2)d\Omega; \quad (2.102)$$

introducing this definition of the twisting moment in (2.76) and solving for the torsion constant:

$$I_T = \int_{\Omega} (x_1\psi_{,2} + x_2\psi_{,1} + x_1^2 + x_2^2)d\Omega, \quad (2.103)$$

Whereas, substituting the definition of Prandtl's function (2.94) in (2.101):

$$M_T = \int_{\Omega} (-\phi_{,1}x_1 - \phi_{,2}x_2)d\Omega, \quad (2.104)$$

integrating by parts gives

$$M_T = 2 \int_{\Omega} \phi d\Omega; \quad (2.105)$$

finally, substituting in (2.76), an expression for the torsion constant in terms of Prandtl's function is found:

$$I_T = \frac{2}{G\theta'} \int_{\Omega} \phi d\Omega; \quad (2.106)$$

Once again, note the non-dependency on the choice of origin for this formulation.

3. Numerical methods

This section presents the numerical methods used to obtain solutions for the formulations stated previously. Two problem-discretization methods are presented: the Finite Element Method in section 3.2 and the Virtual Element Method in section 3.3, comparison between them is present at every application in this work. The two methods are enough on their own to solve problems that are linear and without more complicated boundary condition (such as contact problems). They are used to solve problems of this type in the first two applications, in sections 4 and 5. Problems involving contact require the introduction of a contact discretization, in this case the Node-to-Segment procedure is used. It is presented in section 3.5. Contact problems are inherently nonlinear, and to solve nonlinear problems the Newton-Raphson method is adopted. This method is presented in section 3.4. The following is a brief review on the historical development of the Finite Element Method.

It might be worth remarking that all the methods shown here have been implemented by the author in his own code.

3.1. A historical perspective

Numerical approximations are as old as mathematics. It is hard to pinpoint an origin for a field so wide, ranging from ideas as intuitive as linear interpolations to those as abstract (for the author, at least) as vector spaces of functions. In order not to stray from the subject at hand, this comment on numerical methods will be restrained to those of the same family, or historically related, to the Finite Element Method. Although this includes the Virtual Element Method, its review is presented in a separate section.

Thomeé [26] presents a great overview of the historical development of the numerical analysis of partial differential equations with Finite Difference Method (FDM): The chosen starting point was a paper by Courant, Friedrichs and Lewy [27] (originally published in 1928), this paper proves the existence of solutions with this method, and states the CFL-condition; this condition must be observed to ensure stable convergence of finite difference method. Subsequent papers explored other facets of the method, such as: error bounds for elliptic problems, it uses for parabolic and hyperbolic PDE's.

The origin of variational formulations for boundary value problems is attributed to Lord Rayleigh (1894) and Ritz (1908), the Rayleigh-Ritz method is usually employed to solve for eigenmodes of physical systems; it consists in choosing a finite function space, writing the solution as a linear combination of the basis functions and solving for the combination coefficients that minimize the functional.

To Galerkin (1915) is attributed the idea of treating the solution as a projection problem; Galerkin's method works by choosing a finite function space, writing the approximate solution as a combination of the basis elements and stating that the residual must be orthogonal to that space. Dispensing a variational formulation of the problem. This method is more general and is equivalent to Rayleigh-Ritz's, according to Singer [28], when applied to an equilibrium equation resulting from the variation of the total potential energy. The orthogonality condition, when expressed in terms of the full vector space of admissible test functions, is the weak formulation of the problem.

The Finite Element Method is a direct application of Galerkin's. The origins and early history of the method are presented on lectures given by Clough [29] and Zienkiewicz [30] during the Fifth World Congress on Computational Mechanics held in Vienna in 2002, and later published. The first publication it appeared on was Turner, Clough, Martin, and Topp [31], in the context of aircraft structures; the method was an extension of the *direct stiffness method*, usual for reticulate structures, for the representation of continua.

Ever since its invention, great progress has been accomplished regarding the finite element method. The mathematical background has been established, regarding proof of existence and uniqueness of solutions for weakly formulated problems; proof of, and conditions for, the convergence of the method; as well as *a priori* and *a posteriori* error estimates; for more on this topic the author recommends the works of Ciarlet [32], and Brenner and Scott [33]. There are references in the literature that present the method from a more practical point of view, such as those by Bathe, Wriggers, and Zienkiewicz, Taylor and Zhu [34]–[36]. Other methods have been developed taking the finite element method as basis, e.g., the generalized finite element method, more on Strouboulis, Babuška, and Copps [37]; the extended finite element method, more on Khoei [38]; mixed finite element method, more on Boffi, Brezzi, and Fortin [39]; to mention a few.

During this maturing period, other classes of methods appeared, such as the finite volume method, more on Wesseling [40]; the discontinuous Galerkin methods, more on Brezzi, et al. [41]; and even a series of meshfree methods, e.g., smoothed particles hydrodynamics and the material point method; these last two methods are widely used in the field of Computer Graphics, as can be seen in this state of the art review by Ihmsen, et al. [42], and the work of Stomakhin, et al. [43] about the snow simulation for the Disney movie Frozen.

Some recent advances in the Finite Element Method include: the use of automatic differentiation software to automate the formulation of such methods, as presented in the works by Korelc and Wriggers [44], associated with the software AceGen and AceFEM; and by Logg, Mardal and Wells [45], associated with the FeniCS project; the integration with artificial intelligence and machine learning, as exemplified with the works by Oishi and Yagawa [46], and Caputo and Rimoli [47]; and processing-time enhancement procedures, such as the use of graphic processors proposed in Cecka, Lew and Darve [48].

3.2. Finite element method (FEM)

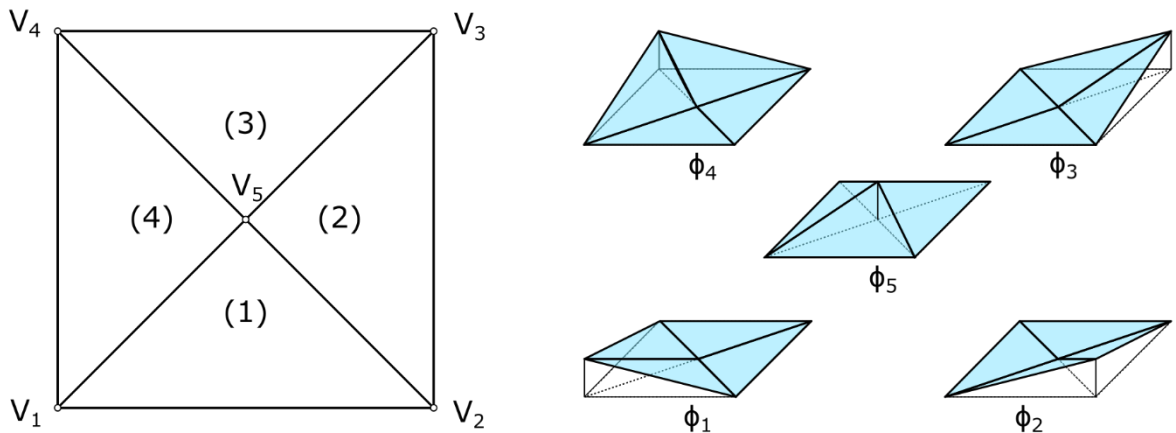
As stated earlier, the Galerkin method consists in defining a finite-dimensional vector space of functions and finding the element of this space that best approximates the solution for the problem, i.e., find the projection of the solution in that space. The finite element method is a procedure for generating finite-dimensional spaces of compactly supported piecewise-polynomial functions, based on a partition of the domain (a mesh input) and a choice of polynomial space (defining the element's order); and formulating the orthogonality condition that yields the approximate solution.

3.2.1. Meshes and function spaces

The procedure established by the finite element method is to partition the domain into subdomains of basic shapes: usually triangles and quadrilaterals for 2D domains; tetrahedra, pyramids, triangular prisms, or hexahedra for 3D domains. This partition is referred to as the mesh and is a basic input for this method. In this work, all the finite elements used are of triangular geometry. Taking this into consideration, this section takes for granted that the chosen mesh is a triangulation.

The mesh can be interpreted as a set of nodes (corresponding to the vertices of the triangles) and elements (the triangles themselves). To each node is associated one piecewise polynomial function with compact support, i.e., a function that is a polynomial on each triangle that shares said node and assumes the constant value 0 on all other triangles. Specifying even more, inside each triangle where the function is a polynomial, it is the uniquely defined polynomial that is evaluated as 1 at the associated node, and 0 on all other nodes shared by said triangle. This is illustrated in Figure 9, where the basis functions for the space associated with a simple mesh, comprised of $n_e = 4$ elements - (1) to (4) - and 5 nodes - V_1 to V_5 , constructed with linear polynomials, are shown. In Figure 10, the basis of the associated space for the same triangulation is shown for quadratic polynomials, the same 4 elements are used, but 13 nodes are necessary. The number of nodes per element must increase for quadratic elements, as there are more degrees of freedom to uniquely define a quadratic polynomial rather than a linear polynomial. The number of nodes per element is associated with the dimension of the polynomial space defined inside each element.

Figure 9. Basis functions for the space associated with a simple mesh (4 elements) for linear polynomials.

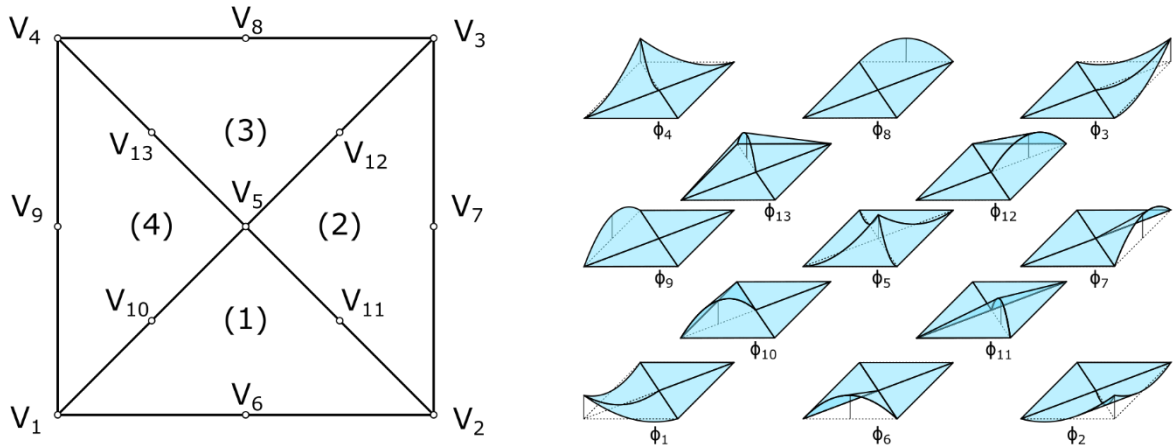


Source: Author.

There are two important parameters associated with the mesh that are used in other sections to characterize them and establish comparison between results of different meshes. The first is the element-size parameter (h), which is a global measure of how refined the mesh is. For each triangle, define its size as the length of its longest edge. The

element-size parameter associated with the mesh is the maximum of the sizes of its elements.

Figure 10. Basis functions for the space associated with a simple mesh (4 elements) for quadratic polynomials.



Source: Author.

The second parameter is the number of degrees of freedom (n_{dof}). To each node there will be assigned one degree of freedom for each field being interpolated, e.g., for 3D elasticity, there are 3 fields being interpolated, i.e., the three displacements; for 2D elasticity there are 2 fields; whereas for St. Venant's torsion there is only one field, either the warping function or Prandtl's function. For conformal elements, category in which all elements used in this work belong, the total number of degrees of freedom of the mesh is equal to the number of fields times the number of nodes; it is a measure of the size of the linear systems that will need to be solved (once or multiple times) to find the solution. For other problems there may be formulations where non-conformal elements are used, i.e., different nodes may present different quantities of degrees of freedom.

3.2.2. The finite element approximation

The chosen way to present the approximation is via illustrative example; in this case, Poisson's equation with homogeneous Dirichlet boundary conditions⁵

⁵ Note that this equation is analog to Prandtl's solution to St. Venant's torsion, where $f = -2G\theta'$, employing the notation presented in item 2.5.

$$\begin{cases} \Delta u = f, & \text{in } \Omega \\ u = 0, & \text{in } \partial\Omega \end{cases} \quad (3.1)$$

The exact solution for (3.1), u , is a member of $H_0^1(\Omega)$, as $H_0^1(\Omega) \supset C_0^2(\Omega)$. The finite element method provides a way to produce a finite subspace $V_h(\Omega) \subset H_0^1(\Omega)$. The approximate solution, u_h , is the projection of the exact solution in that subspace.

The projection is found by stating that the residual $(\Delta u_h - f)$ is orthogonal to that subspace. This implies that the inner product between the residual and any function in that space must be zero. Taking the $L^2(\Omega)$ inner product, presented in section 2.2.7, with a generic function ($\delta u \in V_h$):

$$(\Delta u_h - f, \delta u)_{0,\Omega} = \int_{\Omega} (\Delta u_h - f) \delta u \, d\Omega = 0, \quad (3.2)$$

introducing Green's first identity yields:

$$\int_{\Omega} \nabla u_h \cdot \nabla \delta u \, d\Omega - \int_{\Omega} f \delta u \, d\Omega = 0, \quad (3.3)$$

which must hold for all $\delta u \in V_h(\Omega)$.

Therefore, the orthogonality condition is like the weak formulation of the problem, except that the function spaces for the approximate solution and test functions are the finite-dimensional space associated with the mesh, instead of the infinite-dimensional general space established by the requirements of the weak form (H^1 for all the weak formulations presented in section 2). The approximate solution is a linear combination of the basis functions

$$u_h = u_i \phi_i. \quad (3.4)$$

The scalar value associated with each basis function is the value of the approximate solution at that node by construction, due to each basis evaluating 1 at the associated node and 0 at all others. This scalar value is the *degree of freedom* associated with that node. This decomposition is expressed as the covector field (\mathbf{h}), whose components are basis functions,

$$\mathbf{h} = \{\phi_1, \dots, \phi_n\}, \quad (3.5)$$

acting on the constant vector (\mathbf{u}), whose components are the degrees of freedom

$$\mathbf{u} = \{u_1, \dots, u_n\}^T; \quad (3.6)$$

this is written as

$$u_h = \mathbf{h}\mathbf{u}. \quad (3.7)$$

The degrees of freedom are the variables of the problem. For the generic test function δu , the same covector field acts on its degrees of freedom represented by the constant value vector $\delta\mathbf{u}$, analog to \mathbf{u} :

$$\delta u = \mathbf{h}\delta\mathbf{u}. \quad (3.8)$$

Substituting these decompositions into the orthogonality condition:

$$\int_{\Omega} (\nabla\mathbf{h})\mathbf{u} \cdot (\nabla\mathbf{h})\delta\mathbf{u}d\Omega - \int_{\Omega} f\mathbf{h}\delta\mathbf{u}d\Omega = \delta\mathbf{u}^T \left(\int_{\Omega} \nabla\mathbf{h}^T\nabla\mathbf{h}d\Omega \mathbf{u} - \int_{\Omega} \mathbf{h}^T f d\Omega \right) = 0, \quad (3.9)$$

The degrees of freedom of the test function $\delta\mathbf{u}$ are arbitrary. The expression on the right-hand side holds for all $\delta\mathbf{u}$ if, and only if, the inside of the parenthesis is zero:

$$\int_{\Omega} \nabla\mathbf{h}^T\nabla\mathbf{h}d\Omega \mathbf{u} - \int_{\Omega} \mathbf{h}^T f d\Omega = 0. \quad (3.10)$$

Because of the origins of the method tracing back to structural applications, the first integral is denominated tangent stiffness matrix (\mathbf{K}_T), the second is the load vector (\mathbf{f}). Therefore (3.10) is written as

$$\mathbf{K}_T\mathbf{u} = \mathbf{f}. \quad (3.11)$$

Both of these terms are integrals, those can be split into the sum of integrals over each subdomain, i.e., over each element; e.g., for the stiffness matrix:

$$\mathbf{K}_T = \int_{\Omega} \nabla\mathbf{h}^T\nabla\mathbf{h}d\Omega = \sum_e^{n_e} \int_{\Omega_e} \nabla\mathbf{h}^T\nabla\mathbf{h}d\Omega_e. \quad (3.12)$$

As the basis functions have compact support, the stiffness matrix is sparse. Only the basis function associated with the nodes of a given element (\mathbf{h}_e) will contribute to the integral

over its domain. This allows the stiffness matrix, and load vector, to be assembled from each element's local stiffness matrices (\mathbf{K}_T^e)

$$\mathbf{K}_T = \Lambda_e^{n_e} \mathbf{K}_T^e = \Lambda_e^{n_e} \int_{\Omega_e} \nabla \mathbf{h}_e^T \nabla \mathbf{h}_e d\Omega_e; \quad (3.13)$$

the same formulation in terms of the assembly operation, denoted by $\Lambda_e^{n_e}(\cdot)$, and local counterparts is applicable to the load term.

$$\mathbf{f} = \Lambda_e^{n_e} \mathbf{f}^e = \Lambda_e^{n_e} \int_{\Omega_e} \nabla \mathbf{h}_e^T f d\Omega_e. \quad (3.14)$$

As the shape functions are polynomials, the integral for the local stiffness matrix can be computed exactly using numerical integration techniques, in this work the Gaussian quadrature is used.

This formulation of the global problem as the assembly of smaller counterparts is the essence of the finite element method. One can shift the focus, from global to local, and reimagine the basis functions shown in Figure 9 and Figure 10 as the coordinated combination of a set of shape functions associated, in similar manner, with each finite element. The formulation of the finite elements used in this work are the topic of the next section.

3.2.3. Finite elements

Ciarlet defines a finite element as the association of: a domain with piecewise smooth boundary (Ω_e), a finite-dimensional space of functions on that domain, also called the local finite element space ($V_h^e(\Omega_e)$), the chosen basis of which are the element's *shape functions*; and its dual space (V_h^{e*})⁶, the induced basis of which, correspond to the elements degrees of freedom.

The elements used in this work are all two-dimensional and represent triangular subdomains of the problem. The geometry is fully characterized by the coordinates of its

⁶ The dual space (V^*) associated with a vector space of functions (V), is the space of linear functionals from that space into the base field, in this case the real numbers. $u \in V^*, u: V \rightarrow \mathbb{R}$.

three vertices. One advantage of using simplices for geometry is the barycentric coordinates, based on which the shape functions are constructed.

3.2.3.1. Barycentric coordinates and the shape functions

Let a generic triangle T formed by the vertices V_i ($i = 1,2,3$), with the coordinates $x_1(V_i) = x_i$ and $x_2(V_i) = y_i$. The area of this triangle corresponds the following determinant:

$$A = \frac{1}{2} \begin{vmatrix} x_1 & y_1 & 1 \\ x_2 & y_2 & 1 \\ x_3 & y_3 & 1 \end{vmatrix}. \quad (3.15)$$

For any internal point P with coordinate pair (x, y) , the original triangle can be split into three sub-triangles T_i ($i = 1,2,3$); each new triangle generated by the edge opposite to the vertex of same index connected with the new point. The area of each sub-triangle is expressed as:

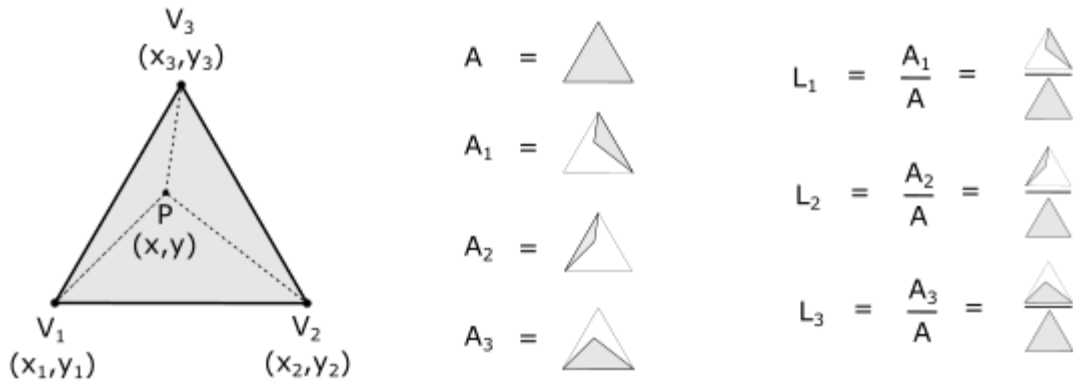
$$A_i = \frac{\epsilon_{ijk}}{4} \begin{vmatrix} x & y & 1 \\ x_j & y_j & 1 \\ x_k & y_k & 1 \end{vmatrix}. \quad (3.16)$$

The barycentric coordinate $L_i(x, y)$ of P associated with the vertex V_i is the following ratio (as illustrated in Figure 11):

$$L_i(x, y) = \frac{A_i(x, y)}{A}. \quad (3.17)$$

These coordinates are three linear functions over the domain of the triangle. Each coordinate will evaluate to 1 if the point corresponds to the associated vertex and 0 if it is located at the edge opposite to that vertex. They form a basis for the space of linear polynomials over that domain, $P_1(\Omega_e)$.

Figure 11. Barycentric coordinates as the ratio of areas.



Source: Author.

3.2.3.2. The elements T3 and T6

A Linear triangular element (T3) can be formulated using these functions as shape functions $\phi_i = L_i, i = 1,2,3, (V_h^e = P_1)$. For this, a set of degrees of freedom is required, such that they form a basis for the dual space. In order to check that some set of linear functionals form a basis for that space, it is necessary that: if all evaluate 0 for a given function, then this implies that said function is the constant function equal to 0. Taking the values at the vertices as a set of degrees of freedom:

$$dof_i(v) = v(x_i, y_i). \quad (3.18)$$

It is known that three points fully characterize a plane, i.e., a linear function over a 2-dimensional domain. Therefore, if the function at all vertices evaluates to 0, then the function must be constant and equal to 0. Furthermore, this choice of shape functions and degrees of freedom has another nice property

$$dof_i(\phi_j) = \delta_{ij}. \quad (3.19)$$

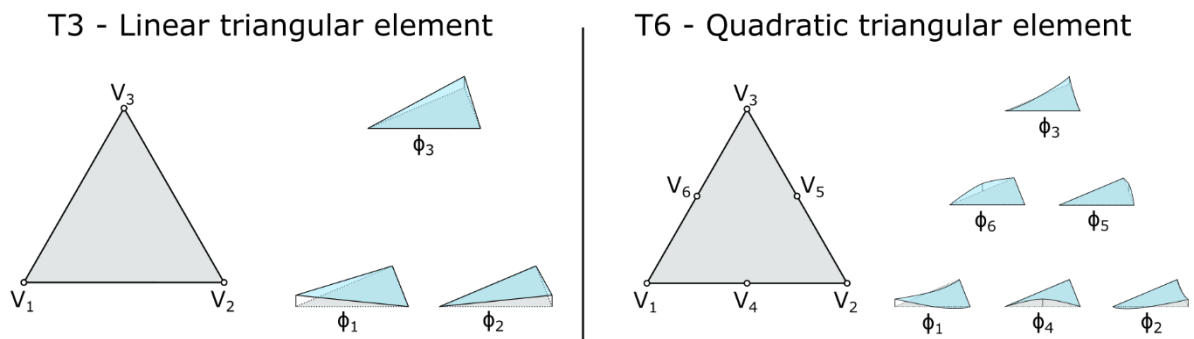
A basis for the space of quadratic polynomials, $P_2(\Omega_e)$, is determinable in terms of these coordinates:

$$\begin{cases} Q_i = 2L_i^2 - L_i, & i = 1,2,3. \\ Q_{i+3} = 2\epsilon_{ijk}L_jL_k \end{cases} \quad (3.20)$$

Taking this basis as the shape functions and adopting the values at the three vertices and at the center of the edges as the degrees of freedom, the quadratic triangular element (T6) is obtained.

The points at which the functions are evaluated for the degrees of freedom are called *nodes*. Extending the nomenclature adopted for the vertices at the beginning of the section to the nodes, the two elements and their shape functions are presented in Figure 12.

Figure 12. Finite elements T3 and T6 and their shape functions.



Source: Author.

3.2.3.3. Elements of other shapes

The triangular elements are easily formulated in terms of the barycentric coordinates, as shown in the previous section; other shaped elements generally use the isoparametric formulation, where a mapping from a reference element to the real one is used. The nodes, for triangular geometry, are evenly distributed and in sufficient number and disposition to fully determine full polynomial spaces. For elements of other shapes this may not be possible.

Another common geometry for 2-dimensional elements is quadrilateral. The linear quadrilateral element (Q4) has 4 nodes, one for each vertex; this implies that the element space must have dimension 4, $V_h^{Q4} = span(\{1, x_1, x_2, x_1x_2\})$, to preserve a directional symmetry. This quadratic element can be formulated in usual form Q9 (9 nodes) or in serendipity form Q8 (8 nodes), either way, monomials from higher order polynomial spaces are needed: $V_h^{Q8} = span(\{1, x_1, x_2, x_1^2, x_1x_2, x_2^2, x_1^2x_2, x_1x_2^2\})$ and $V_h^{Q9} = span(\{1, x_1, x_2, x_1^2, x_1x_2, x_2^2, x_1^2x_2, x_1x_2^2, x_1^2x_2^2\})$.

3.2.4. Convergence curves

The method is said to converge, for a given problem, if there exists a sequence of spaces V_h (u_h being the approximated solution for that space), such that the following limit holds:

$$\lim_{h \rightarrow 0} \|u - u_h\| = 0. \quad (3.21)$$

Ciarlet shows that the error of the approximate solution is exponentially related to the element-size parameter h as

$$\|u - u_h\| \leq Ch^p, \quad (3.22)$$

where C is a constant independent of h , and p is called the *rate of convergence*, has to do with the order of the largest full polynomial space used in the shape functions and the norm relative to which the error is measured.

One important result for the analysis of a problem using the finite element method is the convergence curve. It is a plot of the estimated error, for a sequence of solutions, against the element-size parameter of their meshes. This plot is presented in logarithmic scale, this way the curve(s) should appear as straight lines; the slope being related to the rate of convergence. Curves representing solutions using elements of different orders should present different slopes.

3.2.5. Mesh generation

All the triangular meshes used in this work were generated using the software GMSH by Geuzaine and Remacle [49]. The mesh is generated using a Delaunay triangulation algorithm, and the input is given in the form of a geometry and point-wise information on the desired element size.

3.2.6. Adaptations for plane linear elasticity

Until now, the method has been explored for Poisson's problem (3.3). The weak formulation for plane linear elasticity in Voigt's notation is:

$$\text{Find } \mathbf{u} \in (H^1(V))^2 \text{ such that, for all } \delta \mathbf{u} \in (H_0^1(V))^2: \quad (3.23)$$

$$\begin{cases} \int_V \boldsymbol{\sigma} : \boldsymbol{\delta \varepsilon} \, dV - \int_V \bar{\mathbf{b}} \cdot \boldsymbol{\delta \mathbf{u}} \, dV - \int_{S_F} \bar{\mathbf{t}} \cdot \boldsymbol{\delta \mathbf{u}} \, dS = 0, \\ \mathbf{u} = \hat{\mathbf{u}}, \quad \mathbf{x} \in S_U \end{cases};$$

The key differences are: the interpolated field is now two-dimensional (displacement in two directions); and instead of a product of gradients, there is a product of symmetric parts of the gradient (linearized strain tensor) (2.58).

The finite element approximation for two dimensions is like the one shown in (3.7), but $\mathbf{u}_h = \{u_h, v_h\}^T$ is now a 2-dimensional vector; the covector field of the interpolating functions \mathbf{h} , formerly given by (3.5), is now

$$\mathbf{h} = \{\phi_1 \mathbf{I}, \dots, \phi_n \mathbf{I}\}, \quad (3.24)$$

\mathbf{I} being the 2×2 identity matrix. And the vector with the degrees of freedom, previously shown in (3.6), is now structured as

$$\mathbf{u} = \{u_1, v_1, \dots, u_n, v_n\}^T; \quad (3.25)$$

where there is a correspondence between even and odd degrees of freedom and the direction of the displacement it refers to.

The strain vector $\boldsymbol{\varepsilon}$ is formulated as

$$\boldsymbol{\varepsilon} = \boldsymbol{\partial} \mathbf{u}_h = \boldsymbol{\partial} \mathbf{h} \mathbf{u} = \mathbf{B} \mathbf{u}. \quad (3.26)$$

with help from the operator matrix $\boldsymbol{\partial}$ defined as:

$$\boldsymbol{\partial} = \begin{bmatrix} \frac{\partial}{\partial x} & 0 \\ 0 & \frac{\partial}{\partial y} \\ \frac{\partial}{\partial y} & \frac{\partial}{\partial x} \end{bmatrix}. \quad (3.27)$$

As shown in (3.26), the product $\boldsymbol{\partial} \mathbf{h}$ is denoted by the matrix \mathbf{B} . The same is done for the virtual displacements.

With the constitutive equation given by (2.53), and observing the reductions from the plane strain formulation, the main equation of the weak formulation is written in discrete form as

$$\int_V \delta \mathbf{u}^T \mathbf{B}^T \mathbf{D} \mathbf{B} \mathbf{u} \, dV - \int_V \delta \mathbf{u}^T \mathbf{h}^T \bar{\mathbf{b}} \, dV - \int_{S_F} \delta \mathbf{u}^T \mathbf{h}^T \bar{\mathbf{t}} \, dS = 0. \quad (3.28)$$

As the degrees of freedom for the virtual displacements ($\delta \mathbf{u}$) and displacements (\mathbf{u}) are constants, they can be taken out of the integrals, resulting in

$$\delta \mathbf{u}^T \left(\int_V \mathbf{B}^T \mathbf{D} \mathbf{B} \, dV \mathbf{u} - \int_V \mathbf{h}^T \bar{\mathbf{b}} \, dV - \int_{S_F} \mathbf{h}^T \bar{\mathbf{t}} \, dS \right) = 0. \quad (3.29)$$

As this must be valid for any $\delta \mathbf{u}$, the solution is that for which the parenthesis is zero, leading to the plane linear elasticity equivalent for (3.10):

$$\int_V \mathbf{B}^T \mathbf{D} \mathbf{B} \, dV \mathbf{u} - \int_V \mathbf{h}^T \bar{\mathbf{b}} \, dV - \int_{S_F} \mathbf{h}^T \bar{\mathbf{t}} \, dS = \mathbf{0}. \quad (3.30)$$

The left-hand side of the equation above is termed the total unbalanced force \mathbf{R}_u in nonlinear problems, it is the difference between the total internal force \mathbf{R}_{int} and total external force \mathbf{R}_{ext} . The former is defined as:

$$\mathbf{R}_{int} = \int_V \mathbf{B}^T \boldsymbol{\sigma} \, dV, \quad (3.31)$$

and the latter as:

$$\mathbf{R}_{ext} = \int_V \mathbf{h}^T \bar{\mathbf{b}} \, dV + \int_{S_F} \mathbf{h}^T \bar{\mathbf{t}} \, dS. \quad (3.32)$$

The expression in (3.30) is the same as the linear system in (3.11). The tangent stiffness matrix \mathbf{K}_T is defined as:

$$\mathbf{K}_T = \int_V \mathbf{B}^T \mathbf{D} \mathbf{B} \, dV, \quad (3.33)$$

and the load term \mathbf{f} is the same as the total external force \mathbf{R}_{ext} .

Note that for linear problems the total internal force coincides with the product of the stiffness matrix and the vector of degrees of freedom $\mathbf{R}_{int} = \mathbf{K}_T \mathbf{u}$, this is not the case when any nonlinearity is involved (e.g., contact problems).

3.3. Virtual element method (VEM)

The virtual element method provides a similar, yet different, scheme for producing a finite-dimensional function space associated with a discretization of the problem's domain. Through a crafty construction of local function space and choice of degrees of freedom, the elements admit generic polytope shapes, i.e., polygons in 2D and polyhedra in 3D. This is done by constructing a local element space containing the full polynomial space for a chosen order, along with non-polynomial functions. These additional functions receive the adjective virtual because the choice of degrees of freedom is designed so that the orthogonality condition does not require knowledge of these functions. Each element of this space is split into two contributions: its projection onto the associated polynomial space (via the projection operator) and the residual of that projection. The stiffness matrix is, therefore, separated into two terms: a consistency term (which requires only polynomial integrals) and a stability term (which is approximated, needing only behavior similar to the exact term).

The introductory paper for the VEM was published in 2012 by Beirão da Veiga, et al. [50]. Its development originated from a reformulation of the recent advancements of the mimetic finite differences' method into the Galerkin framework. In this paper the main idea for the method is presented; An abstract framework is established in the context of the Poisson's problem (3.1), for which a series of theorems regarding the convergence, consistency, and stability, are proved. In that same year two other papers were also published: one presenting the method's application for linear elasticity, by Beirão da Veiga, Brezzi and Marini [51], and the other paper explored the method for designing H^2 -conforming elements, i.e., with continuous first-order derivatives, in the specific context of plate-bending problems, by Brezzi and Marini [52].

Ever since, many works have helped further explore the methods capabilities. Briefly summarizing some of the advancements: Brezzi presented a paper [53] at the International Congress of Mathematicians, displaying method's ability to interpolate solutions from the usual functions spaces for classical problems ($L^2(\Omega)$, $H(\mathit{div}; \Omega)$, $H(\mathit{curl}; \Omega)$, and $H(\mathit{grad}; \Omega) = H^1(\Omega)$), this was further explored by Beirão da Veiga, et al. [54]; Beirão da Veiga, et al. [55] formulated the method for the general second-order

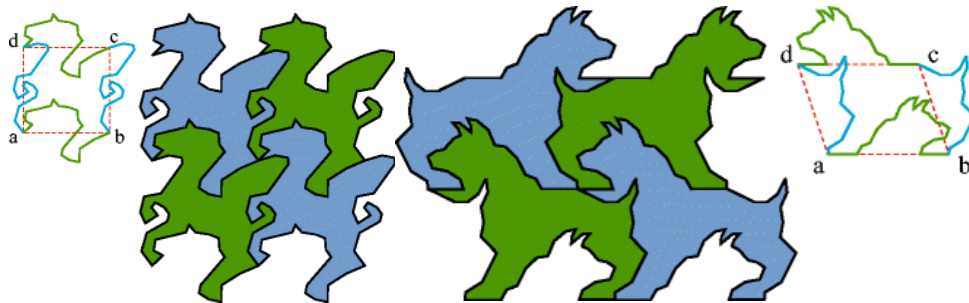
elliptic problem, while Vacca and Beirão da Veiga [56] did the same for the parabolic problem, and Vacca [57] for the hyperbolic problem. Brezzi, Falk and Marini [58] presented the basic principles for the mixed formulation of the virtual element method, which was formulated for the general second-order elliptic problem by Beirão da Veiga, Brezzi, Marini and Russo [59]. Beirão da Veiga, Brezzi, Marini and Russo, have also expanded on Serendipity virtual elements in a series of papers, one together with Dassi [60]–[62]. Beirão da Veiga and Manzini [63] expanded on the idea of solutions with different regularity requirements and presented a procedure to generate virtual elements with arbitrary regularity; Recently, Beirão da Veiga, Russo and Vacca [64] have presented how to handle elements with curved edges, a generalization has been presented by Wriggers, Hudobivnik, and Aldhakeel [65], along with applications for 2D solid mechanics by Artioli, Beirão da Veiga, and Dassi [66]. Ahmad, et al. [67] presented the equivalence of projectors for lower polynomial orders, which simplify the computations while retaining the same convergence properties. Beirão da Veiga, Lovadina and Russo [68] have further explored the stability of the method while discarding the internal degrees of freedom from the stabilization term, as well as with small edges, a topic which Brenner and Sung have also explored [69]. Mascotto [70] also explored alternatives to handle ill-conditioned problems, possible consequence of high-order methods or small edges, proposing the use of orthogonal polynomials as basis instead of the scaled monomials, the same solution was proposed by Berrone and Borio [71] in the context of badly shaped elements. High-order three-dimensional virtual elements were explored by both Beirão da Veiga, Dassi and Russo [72], and Dassi and Mascotto [73]. Brenner, Guan and Sung [74], as well as Chen and Huang [75], Beirão da Veiga and Manzini [76], Cangiani, et al. [77], Berrone and Borio [78], Artioli, et al. [79], D’Altri, et al. [80], Guo, Xie, and Zhao [81], have explored gradient or stress recovery schemes and *a posteriori* error estimations for the method. Still in the theme of gradient recovery procedures, this works author would like to acknowledge the work by Chi, Beirão da Veiga, and Paulino [82] for its clarity and descriptiveness. The author and advisor have published a conference paper on the virtual functions, their projections and residuals [83].

Other works have focused on presenting the method from a more pragmatic approach, formulating it in a more friendly manner for computational implementation. The paper

which has certainly been the most influent in guiding the author of this work is The Hitchhiker's Guide to the Virtual Element Method [84], by Beirão da Veiga, Brezzi, Marini and Russo; the guide provides a friendly matrix-based framework for the stiffness matrix and load term, in the context of Poisson's problem; shows numerical examples for validation of intermediary matrices; how to obtain the mass matrix for the problems in which it might be relevant; and a preamble on what changes when considering three-dimensional problems. Sutton [85] published their Matlab implementation of linear virtual elements for this same problem. Artioli, et al. [86] and Mengolini, Benedetto, and Aragón [87] have both presented different friendly matrix-based frameworks for linear elasticity.

There is a myriad of works exploring the method's application for specific contexts. One paper that truly explored the method's geometric versatility is that of Paulino and Gain [88], in which topology optimization was performed in meshes inspired by the work of M.C. Escher, Figure 13; these meshes have become the paramount example of the method's flexibility regarding the element geometry.

Figure 13. Examples of Escher-based elements, Pegasus and Bulldog.



Source: Adapted from Paulino and Gain [88].

Considering applied publications that are certainly providing basis for the eventual continuity of this work, the author cites the works of Beirão da Veiga, Lovadina, and Mora [89], Wriggers, Reddy, Rust, and Hudobivnik [90], de Bellis, Wriggers, and Hudobivnik [91], and van Huyssteen and Reddy [92] for the application of the method in nonlinear elasticity. As well as the work by Wriggers, Rust, and Reddy [9], on a formulation for a virtual element method for normal contact, which initially inspired the present work; as well as the advancement including frictional contact, by Wriggers and Rust [93], and now including curvilinear virtual elements by Aldhakeel, et al. [94].

3.3.1. The virtual element

The following 2D virtual element introduction is an adaptation to that found on the Hitchhiker's guide [84], with additional commentary; the notation adopted for this introduction is very similar to the guide's, some differences remain for the sake of consistency with what has been presented earlier. Although virtual elements can assume non-convex shapes, the present work is restricted to convex polygons.

Let there be a polygonal virtual element of n_v sides (as illustrated in Figure 14) its vertices are denoted by V_i ($i = 0, 1, \dots, n_v - 1$), ordered counterclockwise, and have coordinates (x_i, y_i) ; its edges⁷ are denoted by e_i ($i = 0, 1, \dots, n_v - 1$), with the i^{th} edge starting at V_i and ending at V_{i+1} . The domain of the element is Ω_e , its measure $|\Omega_e|$ corresponds to the area enclosed by the polygon, which is calculated using Gauss's area formula

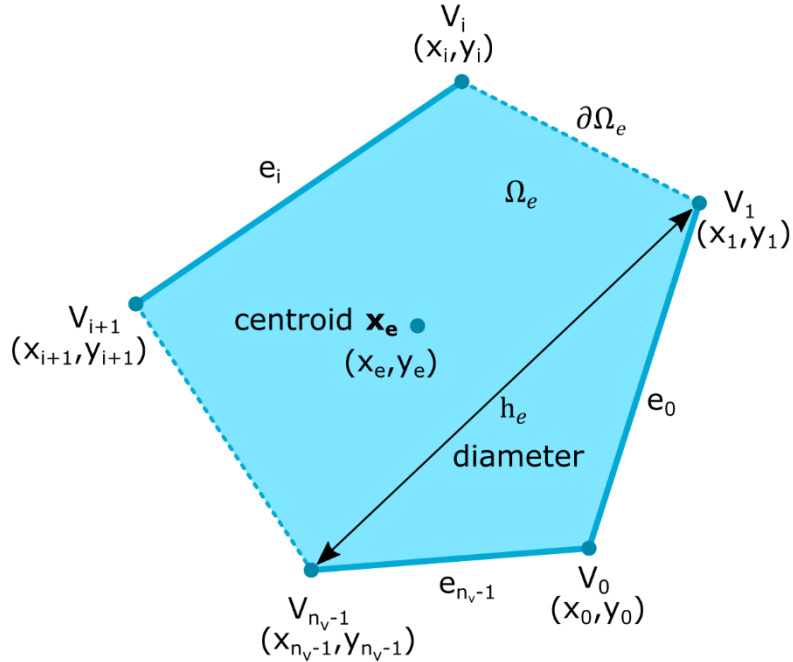
$$|\Omega_e| = \frac{1}{2} \left| \sum_{i=0}^{n_v-2} (x_i y_{i+1} - x_{i+1} y_i) + x_{n_v-1} y_0 - x_0 y_{n_v-1} \right|; \quad (3.34)$$

its diameter h_e is the largest distance between two points in the domain, for convex polygons this corresponds to the largest distance between vertices. The centroid $\mathbf{x}_e = (x_e, y_e)$ is computed using a weighted version of Gauss's area formula

$$\begin{aligned} x_e &= \frac{1}{6|\Omega_e|} \left[\sum_{i=0}^{n_v-2} (x_i + x_{i+1})(x_i y_{i+1} - x_{i+1} y_i) + (x_{n_v-1} + x_0)(x_{n_v-1} y_0 - \right. \\ &\quad \left. x_0 y_{n_v-1}) \right], \\ y_e &= \frac{1}{6|\Omega_e|} \left[\sum_{i=0}^{n_v-2} (y_i + y_{i+1})(x_i y_{i+1} - x_{i+1} y_i) + (y_{n_v-1} + y_0)(x_{n_v-1} y_0 - \right. \\ &\quad \left. x_0 y_{n_v-1}) \right]. \end{aligned} \quad (3.35)$$

⁷ There is no problem for a vertex to share two colinear edges, i.e., no hanging node problems.

Figure 14. Notation for the virtual element.



Source: Author.

Let $P_k(\Omega_e)$ be the space of polynomials of degree less than or equal to k in Ω_e . Then the dimension of that space (n_k) is defined as

$$n_k = \dim P_k(\Omega_e) = \frac{(k+1)(k+2)}{2}. \quad (3.36)$$

One important basis for this space is that of the *scaled monomials*. For their introduction, the multi-index notation, usual for texts in mathematics, should first be presented: boldface Greek letter in this context means a multi-index: $\alpha = (\alpha_1, \alpha_2)$, with the norm $|\alpha| = \alpha_1 + \alpha_2$. Representing the spacial variables in this notation $\mathbf{x} = (x_1, x_2) = (x, y)$, then $\mathbf{x}^\alpha = x_1^{\alpha_1} x_2^{\alpha_2}$. The scaled monomial associated with the multi-index α has degree equal to $|\alpha|$ and is defined by

$$m_\alpha = \left(\frac{\mathbf{x} - \mathbf{x}_e}{h_e} \right)^\alpha = \left(\frac{x - x_e}{h_e} \right)^{\alpha_1} \left(\frac{y - y_e}{h_e} \right)^{\alpha_2}. \quad (3.37)$$

The set of scaled monomials of degree less than or equal to k over the element's domain is denoted by $\mathcal{M}(\Omega_e) = \{m_\alpha \mid 0 \leq |\alpha| < k\}$, and forms a basis for the space $P_k(\Omega_e)$.

Henceforth, the non-bold Greek letter α will indicate a one-dimensional index (starting at 0) with natural correspondence to the two-dimensional multi-index $\boldsymbol{\alpha}$, as

$$0 \leftrightarrow (0,0), 1 \leftrightarrow (1,0), 2 \leftrightarrow (0,1), 3 \leftrightarrow (2,0), 4 \leftrightarrow (1,1), \dots; \quad (3.38)$$

a useful correspondence between these two notations was derived through the course of this work, to facilitate the computational implementation:

$$\begin{cases} \alpha_1 = k + n_{(k-1)} - \alpha \\ \alpha_2 = \alpha - n_{(k-1)} \end{cases}. \quad (3.39)$$

For each polygon Ω_e the local virtual element space is denoted $V_k(\Omega_e)$. This space contains the polynomial space $P_k(\Omega_e)$, this guarantees the convergence, plus other (virtual) functions, which are required to be polynomials of degree up to k on each edge. Any function of this space ($v_h \in V_k(\Omega_e)$) is defined by the following properties:

1. v_h is a polynomial of degree up to k on each edge e of $\partial\Omega_e$, i.e., $v_h|_e \in P_k(e)$;
2. v_h on $\partial\Omega_e$ is globally continuous, i.e., $v_h|_{\partial\Omega_e} \in C^0(\partial\Omega_e)$;
3. Δv_h is a polynomial of degree $k - 2$ in Ω_e , i.e., $\Delta v_h \in P_{k-2}(\Omega_e)$.

The degrees of freedom are the following:

- the value of v_h at the vertices of Ω_e : n_v degrees;
- on each edge e , the value of v_h at the $k - 1$ internal points of the $(k + 1)$ -point Gauss-Lobatto rule on e : $n_v(k - 1)$ degrees;
- the moments up to order $k - 2$ of v_h on Ω_e :

$$\frac{1}{|\Omega_e|} \int_{\Omega_e} v_h m_\alpha d\Omega_e, \quad \alpha = 1, \dots, n_{(k-2)}. \quad (3.40)$$

where the scaled monomials m_α are defined in (3.37), and $n_{(k-2)}$ in (3.36).

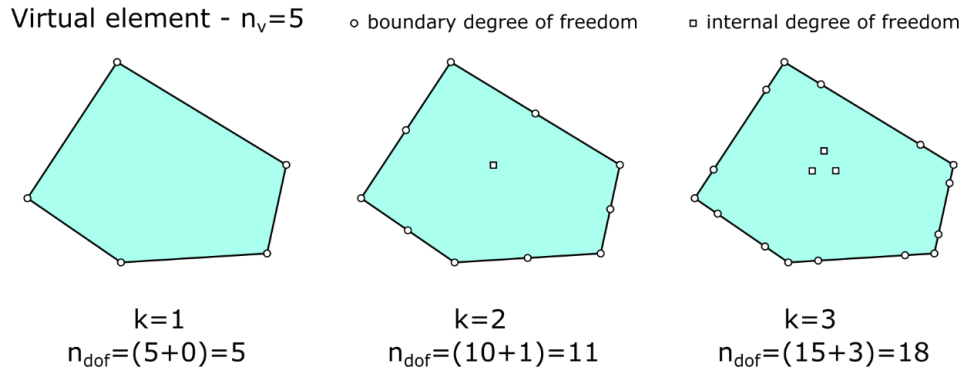
The dimension of $V_k(\Omega_e)$ is n_{dof} :

$$n_{dof} = \dim V_k(\Omega_e) = n_v k + \frac{(k-1)k}{2}. \quad (3.41)$$

The first and second set (bullet points) of degrees of freedom are associated with values at the boundary, whereas the third set is composed of internal degrees of freedom. The

degrees of freedom for a virtual element with $n_v = 5$ and $k = 1, 2, 3$, are illustrated in Figure 15. This choice of degrees of freedom for the boundary, along with properties 1 and 2, allow virtual elements to be used along with finite elements, sharing nodes, granting continuity of the functions in the divide of neighbor elements. This coincidence of boundary nodes for typical Lagrangian finite elements and virtual elements occurs naturally for first and second order elements, whereas for third order and on the position of the boundary degrees of freedom for the finite element must be changed to match the Gauss-Lobatto quadrature, to remain compatible with virtual elements.

Figure 15. Boundary and internal degrees of freedom for $n_v = 5$ and k from 1 to 3.



Source: Author.

The $(k+1)$ -point Gauss-Lobatto rule is a quadrature rule for 1-dimension that includes the extremities of the interval, integrating exactly polynomials of degree up to $2k - 1$. The ingenuity of the choice of degrees of freedom is that any integral in the form $(\nabla v_h, \nabla w_h)_{0, \Omega_e} = \int_{\Omega_e} \nabla v_h \cdot \nabla w_h d\Omega_e$, which will be recurrent for all problems in this work, can be manipulated, using Green's first identity, into

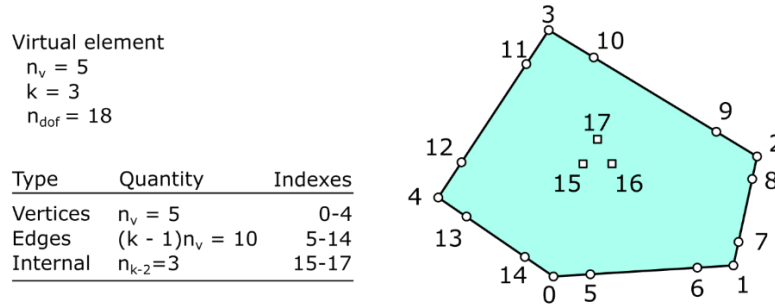
$$(\nabla v_h, \nabla w_h)_{0, \Omega_e} = - \int_{\Omega_e} \Delta v_h w_h d\Omega_e + \int_{\partial\Omega_e} \frac{\partial v_h}{\partial n} w_h d \partial\Omega_e. \quad (3.42)$$

As $\Delta v_h \in P_{k-2}(\Omega_e)$, the first integral is equal to the measure of the element's domain ($|\Omega_e|$) times a linear combination of the internal degrees of freedom of w_h . The second integral is a boundary integral of a polynomial of degree $2k - 1$, as $\frac{\partial v_h}{\partial n} \in P_{k-1}(\partial\Omega_e)$ and $w_h \in P_k(\partial\Omega_e)$, which is exactly integrable using the Gauss-Lobatto rule points at which both

functions are known, as they are degrees of freedom. Therefore, any integral of that type for functions of that space is exactly integrable using only the degrees of freedom.

The canonical basis for the space $V_k(\Omega_e)$ is composed of the functions ϕ_i , where i ranges from 0 to $n_{dof} - 1$ and each basis function satisfies $dof_i(\phi_j) = \delta_{ij}$, i.e., each basis function has its associated degree of freedom valued 1, and all other degrees valued 0. This extends the definition of $dof_i(v_h)$ from the one presented in (3.18), in compliance with the new set of degrees of freedom, i.e., the first n_v degrees of freedom correspond to the evaluation of the function at the corresponding vertices, the following $(k - 1)n_v$ correspond to the evaluation at the Gauss-Lobatto nodes, and the last $\frac{k(k-1)}{2}$ degrees of freedom correspond to the internal moments of the function. The ordering of the degrees of freedom is illustrated for the 3rd-order element, as shown in Figure 16.

Figure 16. Ordering of the degrees of freedom illustrated for the 3rd-order element.



Source: Author.

3.3.2. Orthogonality condition

Taking Poisson's equation in two dimensions as illustrative example, the orthogonality condition is formulated by integrating the residual weighted by the arbitrary test function, as was already introduced in section 3.2.2. This ultimately leads to the formulation of the element-wise contribution to the stiffness matrix and loading term. Another way to express the element's local stiffness matrix is

$$(\mathbf{K}_T^e)_{ij} = (\mathbf{K}^e)_{ij} = (\nabla\phi_i, \nabla\phi_j)_{0, \Omega_e}, \quad (3.43)$$

which is equivalent to K_T^e as presented in (3.13). As this specific problem is linear, the subscript $(\cdot)_T$, which denotes the tangent characteristic, is dropped to alleviate the notation, with no detriment to the understanding.

The functions that form the canonical basis are not known. This problem is handled by splitting them into their projection onto the associated polynomial space and the residue,

$$v_h = \Pi_{\Omega_e, k}^\nabla v_h + (I - \Pi_{\Omega_e, k}^\nabla)v_h, \quad (3.44)$$

where I in this context is the identity map. This projection is performed by the projection operator

$$\Pi_{\Omega_e, k}^\nabla: V_k(\Omega_e) \rightarrow P_k(\Omega_e), \quad (3.45)$$

whose symbol is abbreviated Π^∇ for notational relief; this operator is used only internally to each virtual element. Therefore, the associated domain (Ω_e) , and the degree of polynomial space are those associated with such element. This operator is associated with the gradient operator (∇) because orthogonality is written for the product of the gradients of the functions as

$$\left(\nabla p_k, \nabla((I - \Pi^\nabla)v_h) \right)_{0, \Omega_e} = 0, \forall p_k \in P_k(\Omega_e), \quad (3.46)$$

or, in terms of the scaled monomials basis

$$\left(\nabla m_\alpha, \nabla((I - \Pi^\nabla)v_h) \right)_{0, \Omega_e} = 0, \alpha = 0, \dots, n_k - 1; \quad (3.47)$$

this is done reflecting the structure of the problem's weak formulation, preserving this important characteristic of the solution.

This orthogonality condition defines the projection up to a constant, i.e., for $\alpha = 0$, this condition is trivially satisfied. To circumvent the kernel, an additional projection operator into constants

$$P_0: V_k(\Omega_e) \rightarrow P_0(\Omega_e), \quad (3.48)$$

must be prescribed, such that

$$P_0(\Pi^\nabla v_h - v_h) = 0. \quad (3.49)$$

The operator presented in the Hitchhiker's guide was adopted for this work:

$$\begin{cases} P_0 v_h = \frac{1}{n_v} \sum_{i=0}^{n_v-1} v_h(V_i), & \text{for } k = 1 \\ P_0 v_h = \frac{1}{|\Omega_e|} \int_{\Omega_e} v_h d\Omega_e, & \text{for } k \geq 2 \end{cases} \quad (3.50)$$

With the split form of the canonical basis functions, the stiffness matrix is rewritten as

$$\begin{aligned} (\mathbf{K}^e)_{ij} &= \left(\nabla(\Pi^\nabla \phi_i + (I - \Pi^\nabla)\phi_i), \nabla(\Pi^\nabla \phi_j + (I - \Pi^\nabla)\phi_j) \right)_{0, \Omega_e} \\ &= \left(\nabla(\Pi^\nabla \phi_i), \nabla(\Pi^\nabla \phi_j) \right)_{0, \Omega_e} + \left(\nabla((I - \Pi^\nabla)\phi_i), \nabla((I - \Pi^\nabla)\phi_j) \right)_{0, \Omega_e} \\ &= (\mathbf{K}_c^e)_{ij} + (\mathbf{K}_s^e)_{ij}, \end{aligned} \quad (3.51)$$

where \mathbf{K}_c^e is called the consistency term of the stiffness matrix, which is responsible for the convergence, and can be exactly computed as it only involves polynomials; and \mathbf{K}_s^e is the stability term, which is not known but can be approximated and still confer stability to the method. The approximation adopted is presented later in the text.

3.3.3. Projection operator

The projection $\Pi^\nabla v_h$, being a polynomial, can be expressed as a linear combination of the scaled monomials basis, using Einstein's summation convention,

$$\Pi^\nabla v_h = s_\beta m_\beta; \quad (3.52)$$

or in terms of the canonical basis

$$\Pi^\nabla v_h = s_\beta \text{dof}_i(m_\beta) \phi_i. \quad (3.53)$$

Writing it in terms of the monomial basis, the orthogonality condition (3.47) is rewritten as

$$s_\beta \left(\nabla m_\alpha, \nabla m_\beta \right)_{0, \Omega_e} = \left(\nabla m_\alpha, \nabla v_h \right)_{0, \Omega_e}, \quad \alpha = 0, \dots, n_k - 1; \quad (3.54)$$

this can be expressed in matrix form

$$\mathbf{G}\mathbf{s} = \mathbf{b}. \quad (3.55)$$

Writing the matrices more explicitly:

$$\mathbf{G} = \begin{bmatrix} P_0 m_0 & P_0 m_1 & \cdots & P_0 m_{n_k-1} \\ 0 & (\nabla m_1, \nabla m_1)_{0, \Omega_e} & \cdots & (\nabla m_1, \nabla m_{n_k-1})_{0, \Omega_e} \\ \vdots & \vdots & \ddots & \vdots \\ 0 & (\nabla m_{n_k-1}, \nabla m_1)_{0, \Omega_e} & \cdots & (\nabla m_{n_k-1}, \nabla m_{n_k-1})_{0, \Omega_e} \end{bmatrix}, \quad (3.56)$$

and

$$\mathbf{b} = \begin{bmatrix} P_0 v_h \\ (\nabla m_1, \nabla v_h)_{0, \Omega_e} \\ \vdots \\ (\nabla m_{n_k-1}, \nabla v_h)_{0, \Omega_e} \end{bmatrix}. \quad (3.57)$$

Each element $v_h \in V_k(\Omega_e)$ is associated with a vector that holds its degrees of freedom $\mathbf{v}_h^{(i)}$ associated with the canonical basis; polynomials $p_k \in P_k(\Omega_e)$, are also associated with a vector that holds the degrees of freedom with respect to the scaled monomials basis $\mathbf{p}_k^{(\alpha)}$.

The projection of a single element, just presented, can be generalized considering every element of V_k , which can be written in terms of the canonical basis as

$$v_h = \text{dof}_i(v_h) \phi_i; \quad (3.58)$$

the projection (3.55) can be extended for all the basis functions and reorganized as

$$\mathbf{G}\mathbf{\Pi}_*^\nabla = \mathbf{B}; \quad (3.59)$$

where the matrix form $(\mathbf{\Pi}_*^\nabla)$ holds, as column vectors, the projections of the canonical basis functions written in terms of the scaled monomial basis; and

$$\mathbf{B} = \begin{bmatrix} P_0\phi_0 & P_0\phi_1 & \cdots & P_0\phi_{n_{dof}-1} \\ (\nabla m_1, \nabla\phi_0)_{0,\Omega_e} & (\nabla m_1, \nabla\phi_1)_{0,\Omega_e} & \cdots & (\nabla m_1, \nabla\phi_{n_{dof}-1})_{0,\Omega_e} \\ \vdots & \vdots & \ddots & \vdots \\ (\nabla m_{n_k-1}, \nabla\phi_0)_{0,\Omega_e} & (\nabla m_{n_k-1}, \nabla\phi_1)_{0,\Omega_e} & \cdots & (\nabla m_{n_k-1}, \nabla\phi_{n_{dof}-1})_{0,\Omega_e} \end{bmatrix}. \quad (3.60)$$

Therefore, the matrix form $\mathbf{\Pi}_*^\nabla$ of the projection operator is responsible for taking a vector of degrees of freedom in the canonical basis and outputting the monomial basis coordinate vector for the projection of that function:

$$\mathbf{\Pi}_*^\nabla \mathbf{v}_h^{(i)} = (\mathbf{\Pi}^\nabla \mathbf{v}_h)^{(\alpha)}; \quad (3.61)$$

and is defined as:

$$\mathbf{\Pi}_*^\nabla = \mathbf{G}^{-1} \mathbf{B}. \quad (3.62)$$

The associated polynomial space into which the projection maps, is a subspace of the virtual element space; the projection operator can, thus, be interpreted as a map of V_k into itself ($\mathbf{\Pi}^\nabla: V_k(\Omega_e) \rightarrow V_k(\Omega_e)$). The matrix form $\mathbf{\Pi}^\nabla$ that corresponds to this interpretation is obtained via the relation with the degrees of freedom of the scaled monomials, as expressed in (3.53); it is related to the other matrix form,

$$\mathbf{\Pi}^\nabla = \mathbf{D} \mathbf{\Pi}_*^\nabla = \mathbf{D} \mathbf{G}^{-1} \mathbf{B}, \quad (3.63)$$

by the matrix \mathbf{D} that holds said degrees of freedom

$$(\mathbf{D})_{i\alpha} = dof_i(m_\alpha). \quad (3.64)$$

This form operates in similar way to (3.61), but resulting in the degrees of freedom in the canonical basis instead:

$$\mathbf{\Pi}^\nabla \mathbf{v}_h^{(i)} = (\mathbf{\Pi}^\nabla \mathbf{v}_h)^{(i)}; \quad (3.65)$$

There is another relationship between the matrices presented in this section, which is useful for validation purposes:

$$\mathbf{G} = \mathbf{B} \mathbf{D}; \quad (3.66)$$

there is a demonstration for this in the Hitchhiker's guide, conducted by expanding the product in index notation and showing that it corresponds to the integrals that define \mathbf{G} .

3.3.4. Consistency and stability terms

In the paper on the basic principles of the method, the existence and uniqueness of the solution for the weak formulation of Poisson's problem is shown as consequence of the coercivity and boundedness of the associated continuous bilinear form $a(u, v) = \int_{\Omega_e} \nabla u \cdot \nabla v d\Omega_e$. The convergence properties for this problem are based on two conditions that imply that the discrete bilinear form $a_h(u_h, v_h) = \int_{\Omega_e} \nabla u_h \cdot \nabla v_h d\Omega_e$ behaves like the continuous form: consistency and stability.

The first states that the solution should be exact for polynomials of degree less than or equal to that of the space associated with the element. This is achieved using the projection onto the space of polynomials and the circumvention of the kernel in the projection. Therefore, any polynomial solution should have no residue in the projection, and the exactness with which the consistency term of the stiffness matrix is computed guarantees this property.

The stability condition is that there exist two positive constants α_* and α^* such that

$$\alpha_* a(v_h, v_h) \leq a_h(v_h, v_h) \leq \alpha^* a(v_h, v_h); \quad (3.67)$$

there is not upper or lower limit for these constants, they just have to exist. Therefore, the bilinear form must scale like the continuous form. As the consistency term is not the problem, the stability term must be chosen carefully to ensure both convergence and its expected properties, which are the same as the finite element method.

Resuming from (3.51), and expanding the consistency term:

$$(\mathbf{K}_c^e)_{ij} = \left(\nabla(\Pi^\nabla \phi_i), \nabla(\Pi^\nabla \phi_j) \right)_{0, \Omega_e} = (\mathbf{\Pi}^\nabla)_{\alpha i} (\mathbf{\Pi}^\nabla)_{\beta j} (\nabla m_\alpha, \nabla m_\beta)_{0, \Omega_e}. \quad (3.68)$$

Introducing the matrix $\tilde{\mathbf{G}}$, which is \mathbf{G} without the addition of P_0 to circumvent the kernel, i.e., it coincides with \mathbf{G} for all terms, except the first row, which is comprised of zeros. The consistency term can be written in matrix form as

$$\mathbf{K}_c^e = (\boldsymbol{\Pi}_*^{\nabla})^T \tilde{\mathbf{G}} (\boldsymbol{\Pi}_*^{\nabla}). \quad (3.69)$$

The exact stabilization term,

$$S^{\Omega_e}(\phi_i, \phi_j) = \left(\nabla \left((I - \boldsymbol{\Pi}^{\nabla}) \phi_i \right), \nabla \left((I - \boldsymbol{\Pi}^{\nabla}) \phi_j \right) \right)_{0, \Omega_e} \quad (3.70)$$

is not knowable without knowledge of the virtual functions. It can, however, be approximated so long as it behaves like the continuous form would. This is still a topic of research regarding the virtual element method. For the Poisson problem, the stabilization term that follows works well. However, for nonlinear elasticity, a stabilization term that works for some problems might not work for others.

The approximation for this term suggested in Beirão da Veiga, Brezzi, Marini, and Russo [84] is

$$S^{\Omega_e} \approx \mathbf{K}_s^e = (\mathbf{I} - \boldsymbol{\Pi}^{\nabla})^T (\mathbf{I} - \boldsymbol{\Pi}^{\nabla}), \quad (3.71)$$

where \mathbf{I} is the $n_{dof} \times n_{dof}$ identity matrix.

3.3.5. Load term and L^2 -projector

The original projector Π_k^{∇} is associated with the gradient operator because of the structure of the bilinear form; this is reflected in the required orthogonality condition (3.46). The linear form $f(\delta u) = \int_{\Omega_e} f \delta u d\Omega_e$ associated with the load term, however, does not involve the gradient of the test function. Ahmad, et al. [67] proposed another way to design the virtual element space, such that everything that was presented still holds, and the L^2 -projector Π_k^0 is possible; this is done by considering a larger space with the desired properties and defining the new virtual element space as a subspace; more details are found in the original work.

The L^2 -projector is defined as

$$\Pi_k^0 = \Pi_{\Omega_e, k}^0: V_k(\Omega_e) \rightarrow P_k(\Omega_e), \quad (3.72)$$

by requiring the orthogonality condition

$$(m_\alpha, (I - \Pi^0)v_h)_{0,\Omega_e} = 0 \text{ for } \alpha = 0, \dots, n_k - 1, \quad (3.73)$$

to hold. Manipulating this, and substituting (3.52)

$$s_\beta(m_\alpha, m_\beta)_{0,\Omega_e} = (m_\alpha, v_h)_{0,\Omega_e} \text{ for } \alpha = 0, \dots, n_k - 1, \quad (3.74)$$

leads a system similar to that of (3.55),

$$\mathbf{H}\mathbf{s} = \mathbf{c}. \quad (3.75)$$

The same process for obtained the matrix forms of the original projector is performed, obtaining

$$\mathbf{\Pi}_*^0 = \mathbf{H}^{-1}\mathbf{C}, \quad (3.76)$$

and

$$\mathbf{\Pi}^0 = \mathbf{D}\mathbf{H}^{-1}\mathbf{C}; \quad (3.77)$$

where

$$(\mathbf{H})_{\alpha\beta} = (m_\alpha, m_\beta)_{0,\Omega_e}, \quad (3.78)$$

and

$$(\mathbf{C})_{\alpha i} = \begin{cases} (m_\alpha, \phi_i)_{0,\Omega_e} & \text{if } 1 \leq \alpha \leq n_{k-2} \\ (m_\alpha, \Pi^\nabla \phi_i)_{0,\Omega_e} & \text{if } n_{k-2} < \alpha \leq n_k \end{cases}. \quad (3.79)$$

There is a useful correspondence in cases $k = 1$ and $k = 2$:

$$\Pi_{k=1,2}^\nabla = \Pi_{k=1,2}^0; \quad (3.80)$$

with this the load term \mathbf{f} is written as

$$(\mathbf{f})_i = \int_{\Omega_e} f \Pi_k^0 \phi_i. \quad (3.81)$$

This concludes the illustrative example on how the virtual element method works.

3.3.6. Mesh generation

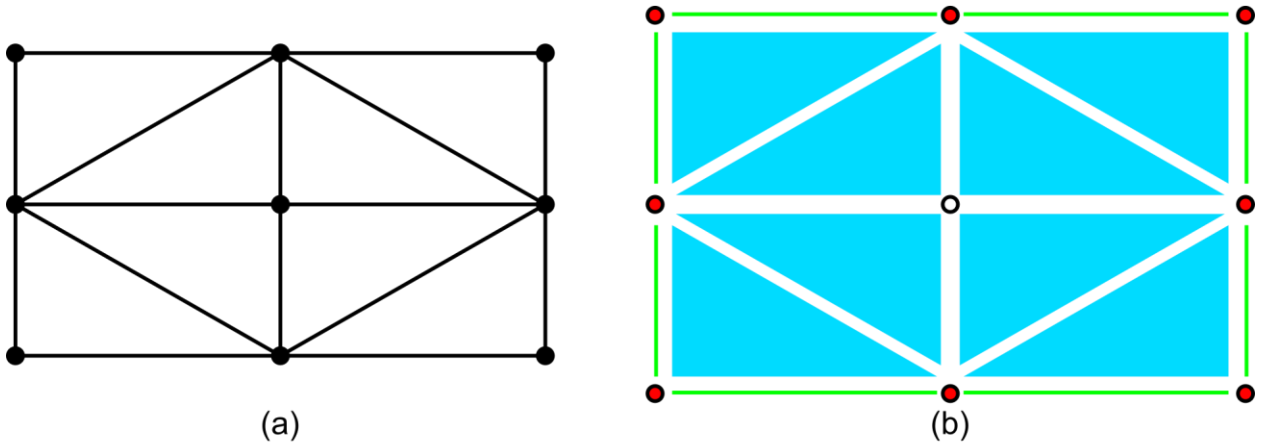
The virtual element method is exceptional in its element's geometrical versatility. Although the method works well when restricted to triangular geometries, this would be a poor use of its capabilities. A problem emerges: most mesh-generation software is based on Delaunay triangulations or quadrilateral tessellations, the FEM-friendly geometries.

The literature has taken many approaches to partition the domain in different ways: regular polygon tessellations, randomly distorted quadrilateral meshes, artistic tessellations, and Voronoi tessellations, to mention a few. For this work the meshes used are either Delaunay triangulations, generated by GMSH; or Voronoi tessellations, derived from these triangulations, obtained via author's own code. The triangulations allow for a stricter comparison of the method's, by sharing the same mesh. Whereas the Voronoi tessellations usually lead to a variety of convex polygons, usually ranging from quadrilaterals to octagons.

A triangular mesh can be thought of as a graph, where the nodes are the vertices, connected by edges, and the faces are the elements. In graph theory there is the concept of dual graph; this is a graph in which the faces of the primal graph are considered vertices. The vertices of the dual graph are connected by an edge wherever the corresponding faces of the primal graph share an edge. A Voronoi diagram associated with a point-set is the dual graph of the Delaunay triangulation of the same point-set.

This concept, with some adaptations, is what guided the algorithm that generates the Voronoi mesh associated with a given triangular mesh. Given the original Delaunay triangulation, illustrated in Figure 17(a). This triangulation is comprehended as a set of triangles (blue), boundary lines (green), boundary points (red), and internal points (white), in Figure 17(b). It is assumed that the triangular mesh is composed only of linear triangular elements, i.e., there are no nodes inside edges.

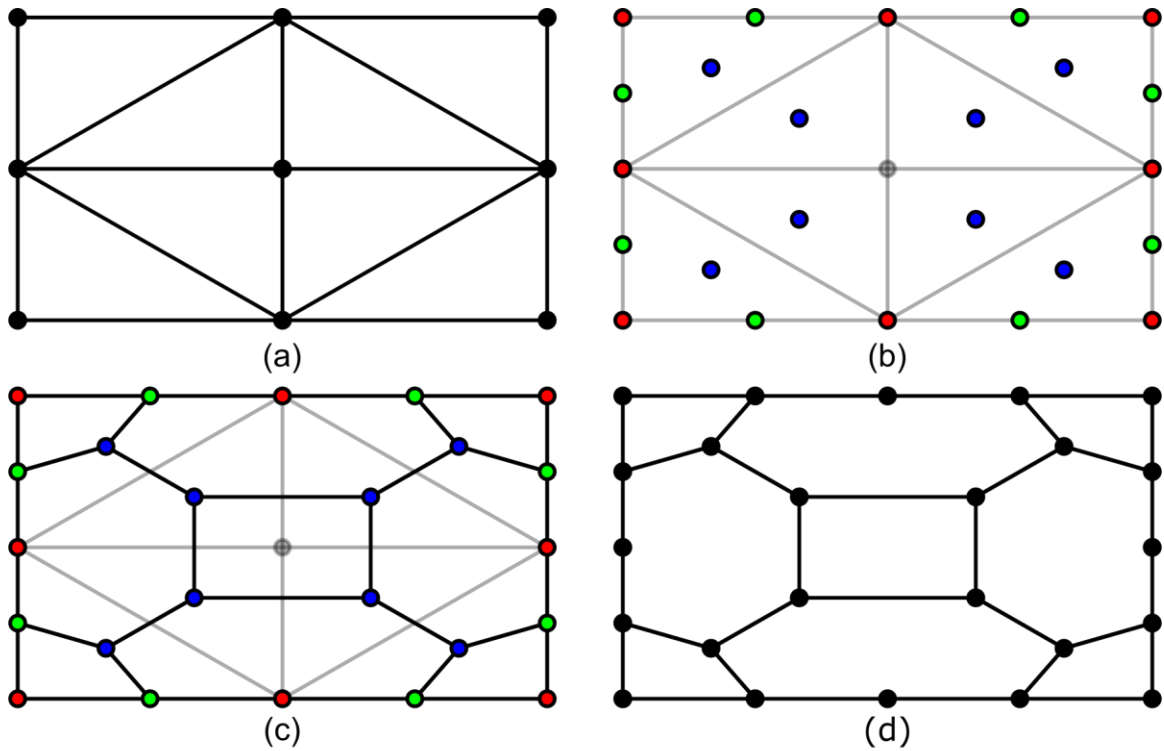
Figure 17. Original Delaunay triangulation.



Source: Author.

The steps to find the associated Voronoi mesh are illustrated in Figure 18.

Figure 18. Generation of Voronoi mesh from the Delaunay mesh.



Source: Author.

Starting from the original mesh, Figure 18(a), the first step is to create the vertices for the new mesh, as shown in Figure 18(b). The different situations in which a vertex is created are listed below, color-coded according to the referred figure:

- Boundary vertices (red): These are the only nodes that are preserved from the original mesh. They are necessary to ensure the shape of the domain is preserved. In the example in Figure 18, if those nodes were not preserved the resulting Voronoi mesh would have chamfered the original corners.
- Mid-point of the edges (green): The mid-points of the edges of the original mesh, become vertices of the edges of the Voronoi mesh.
- Centroid of the triangles (blue): The centroid of the triangles become internal nodes in the Voronoi mesh.

The second step, as illustrated in Figure 18(c), is to assemble the polygons from the generated vertices. Each polygon is associated with a node in the old mesh and should contain the vertices created from the geometric entities that were connected to this node. In Figure 18(c), the center node (A) in the old mesh is belongs to four triangles. Therefore, the polygon associated with it is composed of the centroids of those triangles. Whereas, the upper-right corner node (B) is a boundary vertex, originally connected to two edges and one triangle. Its polygon contains B itself, along with the mid-edge points of those edges and the centroid of the triangle.

At this point the new entities (polygons, edges and nodes) are defined. For the representation of the polygon, it is interesting that the vertices are stored in a list oriented counterclockwise. This can be achieved by computing a pseudo-centroid (average vertex position) and using polar coordinates, relative to it, for the ordering. Presently, a first order polygonal element mesh is effectively generated.

An additional step, not illustrated in the previous figures, is to add the additional nodes for a higher order mesh. For VEM this means adding the internal Gauss-Lobatto points on each edge (boundary and internal), as well as the representation of the degrees of freedom internal to the element.

The preservation of the original boundary vertices in the new mesh lead to a higher density of nodes in the boundary. Each edge in the original mesh is effectively split into two in the final mesh. And the polygons that border the boundary always have two colinear edges. This is important to observe as it will have consequences for the contact applications.

3.3.7. Adaptations for plane linear elasticity

The method has been presented in the context of Poisson's equation. Its use in the context of plane linear elasticity requires some adaptation, as was done in section 3.2.6 for the Finite Element Method.

The weak formulation for the problem at hand was expressed in (3.23). The key differences remain the same as stated before. The adaptation of the finite element approximation for two dimensions, expressed in (3.24) and (3.25), remains valid for the Virtual Element Method, only the basis functions are now the virtual ones. There are now two degrees of freedom for each in the one-field interpolation version. Each element in the virtual displacement space $\mathbf{V}_h = (V_h)^2$ is a vector with two fields, and each field contains a virtual function (in the sense explored in section 3.3.1). The polynomial subspace $\mathbf{P}_k(\Omega_e) = (P_k(\Omega_e))^2$ can be expressed as the span of a scaled monomial basis

$$\mathbf{P}_k(\Omega_e) = \text{span} \left(\left\{ \begin{matrix} m_\alpha \\ 0 \end{matrix} \right\}, \left\{ \begin{matrix} 0 \\ m_\alpha \end{matrix} \right\} \right), \quad \alpha = 0, \dots, n_k - 1, \quad (3.82)$$

and the virtual function space of the displacements as the span of the canonical basis

$$\mathbf{V}_h(\Omega_e) = \text{span} \left(\left\{ \begin{matrix} \phi_i \\ 0 \end{matrix} \right\}, \left\{ \begin{matrix} 0 \\ \phi_i \end{matrix} \right\} \right), \quad i = 0, \dots, n_{dof}^{1d} - 1, \quad (3.83)$$

where n_{dof}^{1d} is the number of degrees of freedom for a problem in one field given in (3.41), therefore $n_{dof} = \dim(\mathbf{P}_k) = 2n_{dof}^{1d}$ is the current number of degrees of freedom.

For the strain vector $\boldsymbol{\varepsilon}$ however, the expression must be different from the FEM's, because of the ignorance of the virtual functions and their derivatives. This is handled by the projection operator in what some have started calling the virtual element decomposition. The literature presents more than one way to define the projection for this problem. For example: Artioli, et al. [86] define the projection directly for a polynomial strain vector, not

including the constitutive matrix \mathbf{D} in the orthogonality condition; meanwhile Mengolini, Benedetto, and Aragón [87] define a projection into the polynomial space (including the constitutive matrix), and then finds the strain vector. This work follows the procedure presented by Artioli, et al.

In the original paper, the projection operator is denoted only by Π . To avoid confusion, in this work this specific projector will be denoted by Π^ε . Its definition is like that of Π^∇ presented in section 3.3.3. It is defined as a projection from the virtual function space of displacements into the space of symmetric gradients of polynomials written as the 3×1 vector $\boldsymbol{\varepsilon}$:

$$\Pi_{\Omega_e, k}^\varepsilon: \mathbf{V}_h(\Omega_e) \rightarrow \mathbf{P}_{k-1}(\Omega_e)_{sym}^{2 \times 2}. \quad (3.84)$$

The virtual element decompositions becomes:

$$\boldsymbol{\varepsilon}(\mathbf{v}_h) = \Pi^\varepsilon \mathbf{v}_h + (I - \Pi^\varepsilon) \mathbf{v}_h. \quad (3.85)$$

This projection uses the orthogonality condition:

$$(\boldsymbol{\varepsilon}(\mathbf{p}_k), (I - \Pi^\varepsilon) \mathbf{v}_h)_{0, \Omega_e} = 0. \quad (3.86)$$

The product of the matrix version of this projector $\Pi^\varepsilon \in \mathbb{R}^{3n_{k-1} \times n_{dof}}$ with the coordinates of \mathbf{v}_h in the virtual displacement space ($\tilde{\mathbf{v}}_h$) results in the coordinates in $(P_{k-1}(\Omega_e))^3$ for the strain vector $\hat{\boldsymbol{\varepsilon}}$. Thus, a covector field (\mathbf{N}^P) of the scaled monomial basis for this space,

$$\mathbf{N}^P = \begin{bmatrix} m_0 & 0 & 0 & \dots & m_{n_{k-1}-1} & 0 & 0 \\ 0 & m_0 & 0 & \dots & 0 & m_{n_{k-1}-1} & 0 \\ 0 & 0 & m_0 & \dots & 0 & 0 & m_{n_{k-1}-1} \end{bmatrix}, \quad (3.87)$$

is used to get the strain vector projection as a polynomial function:

$$\Pi^\varepsilon \mathbf{v}_h = \mathbf{N}^P \hat{\boldsymbol{\varepsilon}} = \mathbf{N}^P \Pi^\varepsilon \tilde{\mathbf{v}}_h. \quad (3.88)$$

Another matrix must be introduced, the change of basis from the polynomial subspace $\mathbf{P}_k(\Omega_e)$ to the virtual displacement space $\mathbf{V}_h(\Omega_e)$ will be denoted by \mathbf{A} (instead of \mathbf{D} as in the referred paper, to avoid confusion with the constitutive matrix), and is composed of the degrees of freedom of the basis vectors from the subspace

$$\mathbf{A} = \begin{bmatrix} dof_0^{1d}(m_0)\mathbf{I} & \dots & dof_0^{1d}(m_{n_k-1})\mathbf{I} \\ \vdots & \ddots & \vdots \\ dof_{n_{dof}}^{1d}(m_0)\mathbf{I} & \dots & dof_{n_{dof}}^{1d}(m_{n_k-1})\mathbf{I} \end{bmatrix}, \quad (3.89)$$

it is a $n_{dof} \times 2n_k$ matrix. The \mathbf{V}_h coordinates $\tilde{\mathbf{p}}$ of an element $\mathbf{p} \in \mathbf{P}_k$ represented by the coordinates vector $\hat{\mathbf{p}}$ in the usual scaled monomial basis can be written as

$$\tilde{\mathbf{p}} = \mathbf{A}\hat{\mathbf{p}}. \quad (3.90)$$

Introducing the decomposition into the main equation of the weak formulation yields:

$$\begin{aligned} \int_V (\Pi^\varepsilon \delta \mathbf{u})^T \mathbf{D} \Pi^\varepsilon \mathbf{u} \, dV + \int_V ((I - \Pi^\varepsilon) \delta \mathbf{u})^T \mathbf{D} (I - \Pi^\varepsilon) \mathbf{u} \, dV - \int_V \bar{\mathbf{b}} \cdot \delta \mathbf{u} \, dV - \\ \int_{S_F} \bar{\mathbf{t}} \cdot \delta \mathbf{u} \, dS = 0. \end{aligned} \quad (3.91)$$

The first two terms are the tangent stiffness matrix split as the sum of the consistency and stabilization terms, as in section 3.3.4.

The matrix form of the projection (3.88) is introduced in the stability term resulting in

$$\int_V (\Pi^\varepsilon \delta \mathbf{u})^T \mathbf{D} \Pi^\varepsilon \mathbf{u} \, dV = \delta \tilde{\mathbf{u}}^T \Pi^{\varepsilon T} \int_V \mathbf{N}^P \mathbf{D} \mathbf{N}^P \, dV \Pi^\varepsilon \tilde{\mathbf{u}} = \delta \tilde{\mathbf{u}}^T \mathbf{K}_c \tilde{\mathbf{u}}. \quad (3.92)$$

Therefore, the consistency stiffness matrix can be written as

$$\mathbf{K}_c = \Pi^{\varepsilon T} \int_V \mathbf{N}^P \mathbf{D} \mathbf{N}^P \, dV \Pi^\varepsilon. \quad (3.93)$$

The exact stability term

$$S^{\Omega_e}(\delta \mathbf{u}, \mathbf{u}) = \int_V ((I - \Pi^\varepsilon) \delta \mathbf{u})^T \mathbf{D} (I - \Pi^\varepsilon) \mathbf{u} \, dV, \quad (3.94)$$

cannot be computed exactly and is approximated under the same conditions as in section 3.3.4. The expression for the approximation is

$$S^{\Omega_e}(\delta \mathbf{u}, \mathbf{u}) \approx \delta \tilde{\mathbf{u}}^T \mathbf{K}_s \tilde{\mathbf{u}}, \quad (3.95)$$

and the stability stiffness matrix \mathbf{K}_s is given by

$$\mathbf{K}_s = \tau \text{tr}(\mathbf{K}_c) [\mathbf{I} - \mathbf{A}(\mathbf{A}^T \mathbf{A})^{-1} \mathbf{A}^T], \quad (3.96)$$

where τ is a positive real number and \mathbf{I} is the $n_{dof} \times n_{dof}$ identity matrix. According to the original paper the method is not sensitive to τ , and the chosen value was $\tau = 0.5$.

The procedure of computing the stiffness matrix elementwise and assembling the global matrix from the element counterparts remains in use.

The load term in the linear system is more direct. The term corresponding to the boundary integral is exactly computable as the virtual functions are known on the element's boundary. The term with the domain integral is usually added as a load on the internal degrees of freedom. For linear elements there is also an approximation for this volume load term in the referred paper.

For the total internal force, \mathbf{R}_{int} , advantage was taken of the linearity of this problem and it is computed by the element-wise product of stiffness matrix and the vector of degrees of freedom for the displacement solution.

3.4. Newton-Raphson method

The Newton-Raphson method (NR) is an iterative root-finding algorithm with quadratic convergence. Burden [95] calls it “one of the most powerful and well-known numerical methods for solving a root-finding problem”.

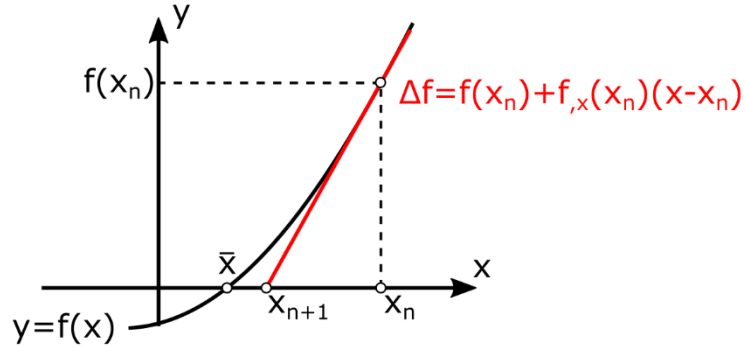
3.4.1. Procedure for one real variable

Let there be a function $f(x): \mathbb{R} \supset \Omega \rightarrow \mathbb{R}$, whose root \bar{x} , $f(\bar{x}) = 0$, is sought. Given an initial guess x_0 near this root, better subsequent guesses can be found by the expression:

$$x_{n+1} = x_n - \frac{f(x_n)}{f_x(x_n)}, \quad f_x(x_n) \neq 0. \quad (3.97)$$

There is a geometrical interpretation for this procedure. Given the point $(x_n, f(x_n))$, the line that passes through it and is tangent to f constitutes its linearization, $\Delta f|_{x_n}(x) = f(x_n) + f_x(x_n)(x - x_n)$, given by the procedure discussed in section 2.3.1. The root of this line constitutes the next approximation (x_{n+1}) , as illustrated in Figure 19.

Figure 19. Geometric interpretation of Newton-Raphson method.



Source: Author.

The expression presented in Eq. (3.97) can be interpreted as a sequence. Bartle and Sherbert [96] present proof of quadratic convergence by means of Taylor's theorem. The proof states that under certain hypotheses ($\exists M, m: |f_{,x}(x)| \geq m > 0$ and $|f_{,xx}| \leq M, x \in \Omega$), there exists a subinterval Ω^* of Ω such that for any $x_0 \in \Omega^*$ the sequence converges quadratically to \bar{x} :

$$|x_{n+1} - \bar{x}| \leq \frac{M}{2m} |x_n - \bar{x}|^2. \quad (3.98)$$

It might be difficult to establish, *a priori*, an interval for which the method will converge quadratically. For most practical applications this is managed by establishing stopping criteria. Some usual criteria are presented below:

- Maximum number of iterations ($n > n_{max}$).
- Tolerance for current iteration's function value, either absolute ($f(x_n) < tol$) or relative ($\frac{f(x_n)}{f(x_0)} < tol$).
- Tolerance for difference between guesses, which can also be either absolute ($|x_n - x_{n-1}| < tol$) or relative ($\frac{|x_n - x_{n-1}|}{|x_1 - x_0|} < tol$).

3.4.2. Generalization for more variables

The method can also be generalized for systems of nonlinear equations of many variables. The generalized procedure can be derived in similar manner, via finding root for the function's linearization:

$$\begin{aligned}\Delta F|_{x_n}(\mathbf{x}) &= \mathbf{F}(\mathbf{x}_n) + \frac{\partial \mathbf{F}}{\partial \mathbf{x}_n}(\mathbf{x}_n)[\mathbf{x} - \mathbf{x}_n] = \mathbf{0} \\ \therefore \mathbf{x} &= \mathbf{x}_n - \left(\frac{\partial \mathbf{F}}{\partial \mathbf{x}_n}\right)^{-1}(\mathbf{x}_n)\mathbf{F}(\mathbf{x}_n) = \mathbf{x}_n - \nabla \mathbf{F}^{-1}(\mathbf{x}_n)\mathbf{F}(\mathbf{x}_n) \\ \therefore \mathbf{x}_{n+1} &= \mathbf{x}_n - \nabla \mathbf{F}^{-1}(\mathbf{x}_n)\mathbf{F}(\mathbf{x}_n),\end{aligned}\tag{3.99}$$

where $\mathbf{F}(\mathbf{x}): \mathbb{R}^n \rightarrow \mathbb{R}^n$. For this form, the method's convergence is proved by Kantorovich's theorem. The stopping criteria in this form are analog to one variable but using the norm of the corresponding vectors.

An alternative way to write (3.99) is in terms of the increment

$$\Delta \mathbf{x}_n = (\mathbf{x}_{n+1} - \mathbf{x}_n) = -\nabla \mathbf{F}^{-1}(\mathbf{x}_n)\mathbf{F}(\mathbf{x}_n).\tag{3.100}$$

There are some problems for which this method is not recommended. One pertinent example in the context of elasticity is the snap-through instability. This problem has the region of interest near points where the gradient is not invertible. For this type of problem the arc-length method is indicated. For more on this method refer to Crisfield [97].

3.5. Node-to-Segment contact discretization

This section presents the Node-to-Segment (NTS) method for contact surface discretization. This method is a particularization of the Node-to-Surface method for planar problems. Given two candidate surfaces for the contact interaction, one is discretized continuously, i.e., as the segments that define the boundary of the finite or virtual elements mesh. This surface is commonly called the "master" surface. The other surface is discretized into a set of points, usually the nodes from the finite or virtual element mesh. This surface is commonly called the "slave" surface. The contact interaction is, thus, discretized into a set of contacts involving a node-segment pair. This method is classified as a "master-slave" method, due to the asymmetric treatment of the contact surfaces.

This section is organized as follows: the next paragraphs will summarize the main references used, as well as a brief review of other methods. The next four subsections will (in a general sense): introduce the basic kinematics between the discretized surfaces

(3.5.1); pose the local contact problem (3.5.2); show the contact contribution to the weak formulation (3.5.3); and perform the consistent linearization for the Newton-Raphson method, leading to the contact contribution to the problem's stiffness matrix (3.5.4). The following two particularize the formulation to the linear (3.5.5), and quadratic (3.5.6) elements. The next one (3.5.7) expands upon the solution algorithm. Finally, subsection (3.5.8) explores some of the method's interpretations and inherent problems.

There are two main sources for this review. The first one is the one by Wriggers [98] (1995): it presents an historical overview of the evolution of finite element algorithms for contact. Its review is split into different aspects of contact algorithms, one of those being contact surface discretization. De Lorenzis, Wriggers and Hughes [99] (2014) presents a review on isogeometric contact accompanied by a more up-to-date historical review of contact discretization methods. Refer to those for a more complete review.

Early works, e.g., Francavilla and Zienkiewicz [100] (1975), employ a Node-to-Node discretization suitable only for matching meshes. This approach is restricted to problems where the contact surface is known *a priori*, and the meshes are designed to allow nodes from both surfaces to coincide when contact happens, this implies linear elasticity, small displacements and rotations.

An early version of what is now the NTS discretization can be found in Hughes, et al. [101] from 1976. A thorough analysis of the classical version of the method for frictionless contact was published by Zavarise and De Lorenzis [102] in 2009. This method allows large deformations. Despite its inherent problems, this discretization is widely used, being present in commercial finite element analysis software such as ABAQUS, Ansys, LS-Dyna, and others. This method leads to the contact surface being a set of points, which can also be interpreted as a collocation approach for computing the contact integral.

Another family of methods are the Surface-to-Surface in 3D or Segment-to-Segment in 2D. These differ from NTS as the contact integral is not collocated at the nodes but integrated over the contact surface. This surface can be one of the bodies' or a new intermediate surface. There are many methods in this family, most of them fail to compute the integral exactly due to the piecewise discontinuous nature of the normal gap function for C^0 surfaces. El Abbasi and Bathe [103] (2001) presents an analysis of stability and

patch test performance for those available at the time, as well as a method that satisfies both conditions. Another example that will be explored in later section is the modified version of NTS which passes the patch test, proposed in Zavarise and De Lorenzis [104] (2009), which turns it into a Segment-to-Segment method.

Another family of discretization methods worth mentioning is that of the Mortar methods, the main reference used in this paragraph is the thesis by Popp [105]. Initially developed for mesh-tying purposes aimed at domain decomposition techniques (see Belgacem [106]), these methods have been repurposed for contact constraints (see Belgacem, Hild, and Laborde [107]). The method enforces the contact restriction in a weak sense by using continuous approximations for the Lagrange multipliers, effectively becoming a mixed formulation. Moreover, this formulation leads to a Saddle-point problem: the internal and external works must be minimized, whereas the contact term must be maximized. This type of problems leads to a linear system structure different than those for minimization problems, requiring specialized solvers. Dual Mortar methods (see Wohlmuth [108]) provide a specific choice of basis for the Lagrange multipliers that allow practical condensation of the Lagrange multipliers and even another set of surface degrees-of-freedom. This overcomes the increase in DOFs disadvantage of Lagrange multipliers and leads to a linear system with the same structure as a minimization problem. There are many works on the applications of such methods in contact mechanics, to provide a few examples: Mortar method for large deformations is found in Puso and Laursen [109], and an application of the Dual Mortar method for large deformations in Popp, et al. [110].

Recently, other approaches have been proposed such as the “master-master” class of formulations presented in Gay Neto and Wriggers [8], a Surface-to-Surface discretization with symmetric treatment of both surfaces with excellent results (Gay Neto and Wriggers [111]) for pointwise contact. The Virtual Element Method has allowed a resurgence of the Node-to-Node approach in the method first proposed by Wriggers, Rust and Reddy [9] for frictionless contact, but later expanded to frictional contact in large deformations by Wriggers and Rust [93], and for curvilinear elements in Aldhakeel, et al. [94]. This Node-to-Node approach is based on the cheap relocation of the nodes, a type of refinement that leads to great results, see Franke, et al. [112]. Another current research field for contact

discretization is that of isogeometric analysis for contact applications, a review of which is found in De Lorenzis, Wriggers, and Hughes [99], the more precise and smooth representation of surfaces leads to better results in contact problems, as those are highly dependent on geometry.

For more information on computational contact mechanics in general, the author indicates his primary source for the following sections: Wriggers [113] textbook on the subject.

3.5.1. Kinematics

Examining an individual node-segment pair. This generic segment is a straight line between the points $x_m^{start,R}$ and $x_m^{end,R}$ in the reference configuration. It is parameterized by a coordinate $\xi \in [0,1]$, such that the position of any point in the reference configuration is $x_m^R = \hat{x}_m^R(\xi)$. The convective coordinate $\xi = 0$ corresponds to the start position, and $\xi = 1$ to the end position. The node's position in the reference configuration is x_s^R . In the current configuration the positions are expressed by the same symbols, except that the superscript $(\cdot)^R$ is dropped. In this configuration the segment is treated as a curve, with its tangent vector $\boldsymbol{\tau}$ (oriented in the direction with increasing ξ)

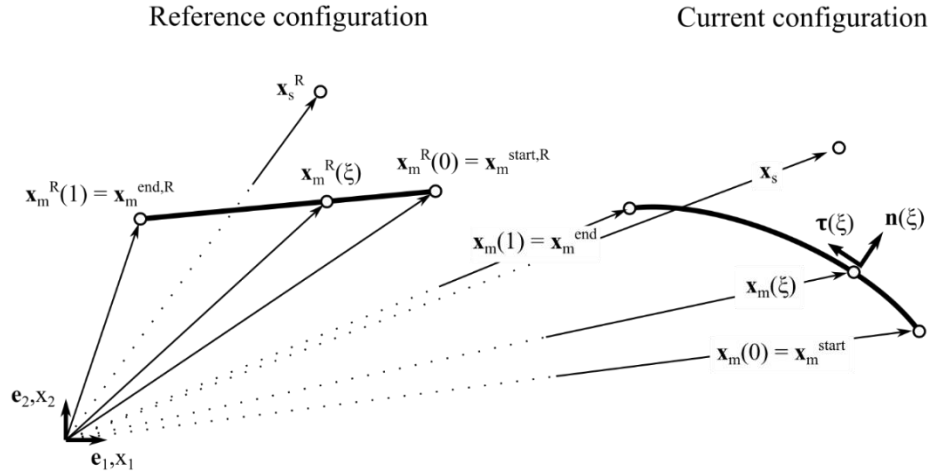
$$\boldsymbol{\tau}(\xi) = \frac{1}{\sqrt{\frac{\partial x_m}{\partial \xi}(\xi) \cdot \frac{\partial x_m}{\partial \xi}(\xi)}} \frac{\partial x_m}{\partial \xi}(\xi) = \frac{1}{\|x_{m,\xi}\|} x_{m,\xi}, \quad (3.101)$$

and external normal vector \boldsymbol{n} defined by a rotation of -90° of the tangent vector as

$$\boldsymbol{n}(\xi) = \begin{bmatrix} 0 & 1 \\ -1 & 0 \end{bmatrix} \boldsymbol{\tau}(\xi) = \boldsymbol{Q} \boldsymbol{\tau}(\xi), \quad (3.102)$$

depending on the convective coordinate. This is illustrated in Figure 20. The subscript $(\cdot)_m$, for the quantities associated with the segment, denotes the “master” moniker; whereas the subscript $(\cdot)_s$ for those associated with the node stands for “slave”.

Figure 20. Contact kinematics for a node-segment pair.



Source: Author.

Let \mathbf{u} be the vector that holds the degrees of freedom for all nodes in the contact pair. Two operators \mathbf{H}_s and $\mathbf{H}_m = \hat{\mathbf{H}}_m(\xi)$ are used to extract the components $\mathbf{u}_s = \mathbf{H}_s \mathbf{u}$ and $\mathbf{u}_m = \hat{\mathbf{u}}_m(\xi) = \mathbf{H}_m(\xi) \mathbf{u}$ from \mathbf{u} in the following way

$$\mathbf{x}_s = \mathbf{x}_s^r + \mathbf{H}_s \mathbf{u}, \quad (3.103)$$

$$\mathbf{x}_m(\xi) = \mathbf{x}_m^r(\xi) + \mathbf{H}_m(\xi) \mathbf{u}.$$

The same is done for the reference configuration coordinates with \mathbf{x}^r .

3.5.2. Local contact problem

The local contact problem is to find the point on the segment which is closest to the node in the current configuration, considered frozen for each NR iteration. It is formulated as the minimum of the squared distance between a point in the segment and the node, $\|\mathbf{x}_s - \mathbf{x}_m\|^2$, which is a function of the convective coordinate. The minimum can be found by finding a stationary point:

$$\begin{aligned} \delta(\|\mathbf{x}_s - \mathbf{x}_m\|^2) &= \frac{\partial}{\partial \xi} (\|\mathbf{x}_s - \mathbf{x}_m\|^2) \delta \xi = 0 \\ \Leftrightarrow \frac{\partial}{\partial \xi} (\|\mathbf{x}_s - \mathbf{x}_m\|^2) &= -2(\mathbf{x}_s - \mathbf{x}_m)^T \mathbf{x}_{m,\xi} = 0 \end{aligned}$$

$$\Leftrightarrow (\mathbf{x}_s - \mathbf{x}_m) \cdot \boldsymbol{\tau} = 0; \quad (3.104)$$

the variation was used to find the stationary point because, although treated as an independent variable, the convective coordinate of the solution depends on the displacements as the problem is formulated in the current configuration.

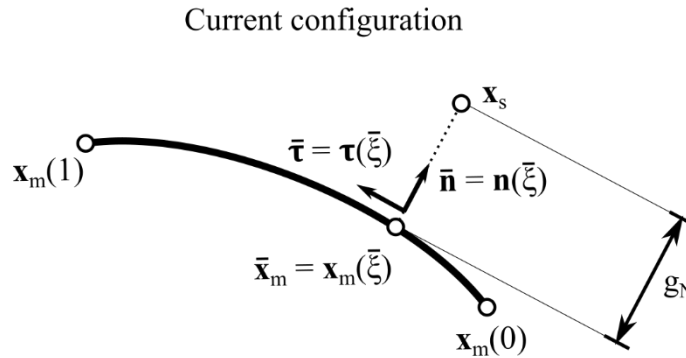
The expression in (3.104) is usually associated with the local contact problem. The distance must be orthogonal to the tangent vector, i.e., the closest point is the orthogonal projection of the node into the segment. Henceforth the solution to this problem will be denoted $\bar{\xi}$, and the quantities at this point will be denoted with $(\bar{\cdot})$, e.g., $\mathbf{x}_m(\bar{\xi}) = \bar{\mathbf{x}}_m$.

With the solution known, the distance vector to the solution $(\mathbf{x}_s - \bar{\mathbf{x}}_m)$ will be denoted the vector normal gap \mathbf{g}_n . Its intensity is the scalar normal gap g_n (from here on referred only as normal gap) and its direction is the normal direction at the solution point $\bar{\mathbf{n}}$, i.e.

$$\mathbf{g}_n = g_n \bar{\mathbf{n}}. \quad (3.105)$$

As illustrated in Figure 21.

Figure 21. Local contact problem solution.



Source: Author.

Now the normal gap referred to in the contact potential (2.67) in section 2.5 is formally presented.

3.5.3. Weak formulation

The weak formulation for linear elasticity with the contact constraint is that in (3.23) with the addition of the variation of the contact potential (2.68). The contact contribution to the

weak form depends on the variation of the normal gap δg_n . The normal gap is independent of the convective coordinate because it is defined for constant $\bar{\xi}$. Therefore, the variation is expressed as:

$$\delta g_n = \frac{\partial g_n}{\partial \mathbf{u}} [\delta \mathbf{u}] = (\delta \mathbf{u}_s - \delta \bar{\mathbf{u}}_m) \cdot \bar{\mathbf{n}}. \quad (3.106)$$

Even if ξ is considered a parameter of g_n , the resulting terms of the variation with respect to it are identically zero.

3.5.4. Consistent linearization

As the contact contribution is added to the weak formulation, its consistent linearization is required to solve the now nonlinear problem. The linearization is obtained by the procedure presented in section 2.3.1 and recontextualized in section 3.4:

$$\begin{aligned} \Delta \delta U_c|_{\mathbf{u}} &= \Delta \left(\epsilon \int_{S_c} g_n \delta g_n dS \right) = \epsilon \int_{S_c} \left(\frac{\partial g_n}{\partial \mathbf{u}} [\Delta \mathbf{u}] \delta g_n + g_n \frac{\partial \delta g_n}{\partial \mathbf{u}} [\Delta \mathbf{u}] \right) dS \\ &= \epsilon \int_{S_c} (\Delta g_n \delta g_n + g_n \Delta \delta g_n) dS. \end{aligned} \quad (3.107)$$

The consistent linearization of the normal gap Δg_n is analog to its variation:

$$\Delta g_n = \frac{\partial g_n}{\partial \mathbf{u}} [\Delta \mathbf{u}] = (\Delta \mathbf{u}_s - \Delta \bar{\mathbf{u}}_m) \cdot \bar{\mathbf{n}}. \quad (3.108)$$

The linearization of the variation of the normal gap $\Delta \delta g_n$ however, is a little more complicated. The full derivation process can be found in chapter 6 of Wriggers [113].

Summarizing:

$$\Delta \delta g_n = -(\delta \bar{\mathbf{u}}_{m,\xi} \Delta \xi + \Delta \bar{\mathbf{u}}_{m,\xi} \delta \xi + \bar{\mathbf{x}}_{m,\xi\xi} \delta \xi \Delta \xi) \cdot \bar{\mathbf{n}} + g_n \Delta \bar{\mathbf{n}} \cdot \delta \bar{\mathbf{n}}, \text{ where} \quad (3.109)$$

$$\delta \bar{\mathbf{u}}_{m,\xi} = \bar{\mathbf{H}}_{m,\xi} \delta \mathbf{u}, \text{ and } \Delta \bar{\mathbf{u}}_{m,\xi} = \bar{\mathbf{H}}_{m,\xi} \Delta \mathbf{u}, \quad (3.110)$$

$$\bar{\mathbf{x}}_{m,\xi\xi} = \bar{\mathbf{H}}_{m,\xi\xi} \mathbf{u}, \quad (3.111)$$

$$\delta \bar{\mathbf{n}} = -\frac{1}{\|\bar{\mathbf{x}}_{m,\xi}\|} [\bar{\mathbf{n}} \cdot (\bar{\mathbf{x}}_{m,\xi\xi} \delta \xi + \delta \bar{\mathbf{u}}_{m,\xi})] \bar{\mathbf{t}}, \text{ and} \quad (3.112)$$

$$\Delta \bar{\mathbf{n}} = -\frac{1}{\|\bar{\mathbf{x}}_{m,\xi}\|} \left[\bar{\mathbf{n}} \cdot (\bar{\mathbf{x}}_{m,\xi\xi} \Delta \xi + \Delta \bar{\mathbf{u}}_{m,\xi}) \right] \bar{\mathbf{t}}.$$

$$\Delta \bar{\mathbf{n}} \cdot \delta \bar{\mathbf{n}} = \frac{1}{\|\bar{\mathbf{x}}_{m,\xi}\|^2} (\bar{\mathbf{x}}_{m,\xi\xi} \delta \xi + \delta \bar{\mathbf{u}}_{m,\xi}) (\bar{\mathbf{n}} \otimes \bar{\mathbf{n}}) (\bar{\mathbf{x}}_{m,\xi\xi} \Delta \xi + \Delta \bar{\mathbf{u}}_{m,\xi}). \quad (3.113)$$

The convective coordinate depends on the displacements. Therefore, the variation and linearization of the convective coordinate can be expressed in terms of the variation and linearization of the displacements. The structure for both is similar, and therefore an auxiliary matrix \mathbf{D} is provided to mediate this relationship:

$$\Delta \xi = \mathbf{D} \delta \mathbf{u}, \text{ and } \delta \xi = \mathbf{D} \delta \mathbf{u}, \quad (3.114)$$

$$\mathbf{D} = \frac{1}{\|\bar{\mathbf{x}}_{m,\xi}\|^2 - g_n \bar{\mathbf{n}} \cdot \bar{\mathbf{x}}_{m,\xi\xi}} \left[\bar{\mathbf{x}}_{m,\xi}^T (\mathbf{H}_s - \bar{\mathbf{H}}_m) + g_n \bar{\mathbf{n}}^T \bar{\mathbf{H}}_{m,\xi} \right]. \quad (3.115)$$

The linearization of the variation of the normal gap can be expressed in terms of the variation and linearization of the displacement field as

$$\begin{aligned} \Delta \delta g_n = \delta \mathbf{u}^T & \left[\frac{g_n}{\|\bar{\mathbf{x}}_{m,\xi}\|^2} (\mathbf{D}^T \mathbf{u}^T \bar{\mathbf{H}}_{m,\xi\xi}^T + \bar{\mathbf{H}}_{m,\xi}^T) (\bar{\mathbf{n}} \otimes \bar{\mathbf{n}}) (\bar{\mathbf{H}}_{m,\xi} + \bar{\mathbf{H}}_{m,\xi\xi} \mathbf{u} \mathbf{D}) - \right. \\ & \left. (\bar{\mathbf{H}}_{m,\xi}^T \bar{\mathbf{n}} \mathbf{D} + \mathbf{D}^T \bar{\mathbf{n}}^T \bar{\mathbf{H}}_{m,\xi} + \mathbf{D}^T \bar{\mathbf{n}}^T \bar{\mathbf{H}}_{m,\xi\xi} \mathbf{u} \mathbf{D}) \right] \Delta \mathbf{u}. \end{aligned} \quad (3.116)$$

The consistent linearization of the variation of the contact potential (3.107) can thus be written as

$$\begin{aligned} \Delta \delta U_c = \delta \mathbf{u}^T \int_{S_c} \epsilon & \left[\frac{g_n^2}{\|\bar{\mathbf{x}}_{m,\xi}\|^2} (\mathbf{D}^T \mathbf{u}^T \bar{\mathbf{H}}_{m,\xi\xi}^T + \bar{\mathbf{H}}_{m,\xi}^T) (\bar{\mathbf{n}} \otimes \bar{\mathbf{n}}) (\bar{\mathbf{H}}_{m,\xi} + \bar{\mathbf{H}}_{m,\xi\xi} \mathbf{u} \mathbf{D}) - \right. \\ & g_n (\bar{\mathbf{H}}_{m,\xi}^T \bar{\mathbf{n}} \mathbf{D} + \mathbf{D}^T \bar{\mathbf{n}}^T \bar{\mathbf{H}}_{m,\xi} + \mathbf{D}^T \bar{\mathbf{n}}^T \bar{\mathbf{H}}_{m,\xi\xi} \mathbf{u} \mathbf{D}) + (\mathbf{H}_s - \bar{\mathbf{H}}_m)^T (\bar{\mathbf{n}} \otimes \bar{\mathbf{n}}) (\mathbf{H}_s - \\ & \left. \bar{\mathbf{H}}_m) \right] dS \Delta \mathbf{u}. \end{aligned} \quad (3.117)$$

This can also be interpreted in terms of a contact contribution to the tangent stiffness matrix of the form $\Delta \delta U_c = \delta \mathbf{u}^T \mathbf{K}_7^c \Delta \mathbf{u}$, where this contribution is defined as

$$\begin{aligned}
\mathbf{K}_C^T = \int_{S_c} \epsilon \left[\frac{g_n^2}{\|\bar{\mathbf{x}}_{m,\xi}\|^2} (\mathbf{D}^T \mathbf{u}^T \bar{\mathbf{H}}_{m,\xi\xi}^T + \bar{\mathbf{H}}_{m,\xi}^T) (\bar{\mathbf{n}} \otimes \bar{\mathbf{n}}) (\bar{\mathbf{H}}_{m,\xi} + \bar{\mathbf{H}}_{m,\xi\xi} \mathbf{u} \mathbf{D}) - \right. \\
g_n (\bar{\mathbf{H}}_{m,\xi}^T \bar{\mathbf{n}} \mathbf{D} + \mathbf{D}^T \bar{\mathbf{n}}^T \bar{\mathbf{H}}_{m,\xi} + \mathbf{D}^T \bar{\mathbf{n}}^T \bar{\mathbf{H}}_{m,\xi\xi} \mathbf{u} \mathbf{D}) + (\mathbf{H}_s - \bar{\mathbf{H}}_m)^T (\bar{\mathbf{n}} \otimes \bar{\mathbf{n}}) (\mathbf{H}_s - \\
\left. \bar{\mathbf{H}}_m) \right] dS. \quad (3.118)
\end{aligned}$$

Now comes in hand the contact surface discretization. The contact surface is a discrete set of points. Therefore, the integral over the contact surface becomes a collocation at each individual point. The contact stiffness matrix is computed locally for each contact pair, involving only the degrees of freedom for this pair, and is later assembled into a global contribution in the same process as for the local element-wise stiffness matrices for both the FEM and the VEM.

3.5.5. Linear element formulation

Particularizing this formulation for linear elements. The displacement field along each segment is interpolated by linear functions over ξ , therefore each segment remains a straight line in the current configuration. The linear functions adopted are the Lagrangian functions. Particularizing the quantities introduced in the kinematics section (3.5.1)

$$\mathbf{x}^r = [\mathbf{x}_s^r \quad \mathbf{x}_m^r{}^0 \quad \mathbf{x}_m^r{}^1]^T, \quad (3.119)$$

$$\mathbf{u} = [\mathbf{u}_s \quad \mathbf{u}_m^0 \quad \mathbf{u}_m^1]^T, \quad (3.120)$$

$$\mathbf{H}_s = [\mathbf{I} \quad \mathbf{0} \quad \mathbf{0}], \quad (3.121)$$

$$\mathbf{H}_m(\xi) = [\mathbf{0} \quad (1 - \xi)\mathbf{I} \quad \xi\mathbf{I}], \quad (3.122)$$

$$\mathbf{H}_{m,\xi} = [\mathbf{0} \quad -\mathbf{I} \quad \mathbf{I}]. \quad (3.123)$$

$$\mathbf{x}_s^r = \mathbf{H}_s \mathbf{x}^r, \text{ and } \mathbf{x}_m^r(\xi) = \mathbf{H}_m \mathbf{x}^r \quad (3.124)$$

The second derivatives in this case are null. In this section the superscripts $(\cdot)^0$ and $(\cdot)^1$ refer to the start and end nodes of the segment, respectively.

The LCP has analytic solution that can be obtained by substituting the defined quantities into (3.104) and rearranging terms:

$$\bar{\xi} = \frac{(x_s - x_m^0) \cdot (x_m^1 - x_m^0)}{(x_m^1 - x_m^0) \cdot (x_m^1 - x_m^0)}. \quad (3.125)$$

The auxiliary D operator is expressed as

$$D = \frac{1}{\|\bar{x}_{m,\xi}\|^2} [\bar{x}_{m,\xi}^T \quad -(1 - \bar{\xi})\bar{x}_{m,\xi}^T - g_n \bar{n}^T \quad -\bar{\xi}\bar{x}_{m,\xi}^T + g_n \bar{n}^T]. \quad (3.126)$$

And the contribution to the tangent stiffness matrix is limited to

$$K_C^T = \int_{S_c} \epsilon \left[\frac{g_n^2}{\|\bar{x}_{m,\xi}\|^2} (\bar{H}_{m,\xi}^T) (\bar{n} \otimes \bar{n}) (\bar{H}_{m,\xi}) - g_n (\bar{H}_{m,\xi}^T \bar{n} D + D^T \bar{n}^T \bar{H}_{m,\xi}) + \right. \\ \left. (H_s - \bar{H}_m)^T (\bar{n} \otimes \bar{n}) (H_s - \bar{H}_m) \right] dS. \quad (3.127)$$

3.5.6. Quadratic element formulation

The following formulation is a particularization of the general formulation presented earlier, for quadratic elements. The choice of parametrization functions was that of the usual Lagrangian functions. The interpolation of the reference configuration coordinates could have been done with a linear interpolation (for non-isoparametric elements) or with the same quadratic interpolation (isoparametric formulation). The latter (3.124) was adopted, as it is more general, working for straight elements (used in this work) and simplifies the notation. In this section the superscripts $(\cdot)^0$, $(\cdot)^1$, and $(\cdot)^2$ refer to the start, end, and mid nodes of the segment, respectively. Particularizing:

$$x^r = [x_s^r \quad x_m^r 0 \quad x_m^r 1 \quad x_m^r 2]^T, \quad (3.128)$$

$$u = [u_s \quad u_m^0 \quad u_m^1 \quad u_m^2]^T, \quad (3.129)$$

$$H_s = [I \quad 0 \quad 0 \quad 0], \quad (3.130)$$

$$H_m(\xi) = [0 \quad (2\xi^2 - 3\xi + 1)I \quad (2\xi^2 - \xi)I \quad 4\xi(1 - \xi)I], \quad (3.131)$$

$$H_{m,\xi}(\xi) = [0 \quad (4\xi - 3)I \quad (4\xi - 1)I \quad (4 - 8\xi)I], \quad (3.132)$$

$$H_{m,\xi\xi}(\xi) = [0 \quad 4I \quad 4I \quad -8I]. \quad (3.133)$$

The LCP becomes a little more complicated. Substituting the particularizations into (3.104), and denoting the quantity (to be annulated) expressed as g_τ , yields

$$g_\tau = (\mathbf{x}_s - \mathbf{x}_m) \cdot \mathbf{x}_{m,\xi} = (\mathbf{x}^r + \mathbf{u})^T (\mathbf{H}_s - \mathbf{H}_m)^T \mathbf{H}_{m,\xi} (\mathbf{x}^r + \mathbf{u})$$

$$g_\tau(\xi) = -2(\mathbf{c} \cdot \mathbf{c})\xi^3 - 3(\mathbf{b} \cdot \mathbf{c})\xi^2 - (\mathbf{b} \cdot \mathbf{b} + 2\mathbf{a} \cdot \mathbf{c})\xi - (\mathbf{a} \cdot \mathbf{b}), \text{ where} \quad (3.134)$$

$$\mathbf{a} = (\mathbf{x}_s - \mathbf{x}_m^0), \mathbf{b} = (3\mathbf{x}_m^0 + \mathbf{x}_m^1 - 4\mathbf{x}_m^2), \text{ and } \mathbf{c} = (-2\mathbf{x}_m^0 - 2\mathbf{x}_m^1 + 4\mathbf{x}_m^2).$$

This is a cubic equation on ξ , which is solved using Newton-Raphson method with initial guess $\xi_0 = 0.5$ (the center of the segment). Therefore, if there is a solution inside the segment, the method will find it. The NR procedure is

$$\xi_{n+1} = \xi_n - \frac{g_\tau(\xi_n)}{g_{\tau,\xi}(\xi_n)}, \text{ with} \quad (3.135)$$

$$g_{\tau,\xi} = -6(\mathbf{c} \cdot \mathbf{c})\xi^2 - 6(\mathbf{b} \cdot \mathbf{c})\xi - (\mathbf{b} \cdot \mathbf{b} + 2\mathbf{a} \cdot \mathbf{c}).$$

The stopping criteria adopted were $g_\tau \leq 10^{-6}$ and 20 as limit for number of iterations.

The \mathbf{D} operator is given by

$$\mathbf{D} = \frac{1}{\|\bar{\mathbf{x}}_{m,\xi}\|^2 - g_n \bar{\mathbf{n}}^T \bar{\mathbf{H}}_{m,\xi\xi} (\mathbf{x}^r + \mathbf{u})} [(\mathbf{x}^r + \mathbf{u})^T \bar{\mathbf{H}}_{m,\xi}^T (\mathbf{H}_s - \bar{\mathbf{H}}_m) + g_n \bar{\mathbf{n}}^T \bar{\mathbf{H}}_{m,\xi}]. \quad (3.136)$$

The contribution to the stiffness matrix becomes

$$\begin{aligned} \mathbf{K}_C^T = \int_{S_c} \epsilon \left[\frac{g_n^2}{\|\bar{\mathbf{x}}_{m,\xi}\|^2} (\mathbf{D}^T \mathbf{u}^T \bar{\mathbf{H}}_{m,\xi\xi}^T + \bar{\mathbf{H}}_{m,\xi}^T) (\bar{\mathbf{n}} \otimes \bar{\mathbf{n}}) (\bar{\mathbf{H}}_{m,\xi} + \bar{\mathbf{H}}_{m,\xi\xi} \mathbf{u} \mathbf{D}) - \right. \\ \left. g_n (\bar{\mathbf{H}}_{m,\xi}^T \bar{\mathbf{n}} \mathbf{D} + \mathbf{D}^T \bar{\mathbf{n}}^T \bar{\mathbf{H}}_{m,\xi} + \mathbf{D}^T \bar{\mathbf{n}}^T \bar{\mathbf{H}}_{m,\xi\xi} \mathbf{u} \mathbf{D}) + (\mathbf{H}_s - \bar{\mathbf{H}}_m)^T (\bar{\mathbf{n}} \otimes \bar{\mathbf{n}}) (\mathbf{H}_s - \right. \\ \left. \bar{\mathbf{H}}_m) \right] dS. \end{aligned} \quad (3.137)$$

3.5.7. Solution algorithm

There are many methods working together at this point. Establishing a robust procedure to solve this problem is not a trivial task. This section presents an overview of the algorithm constructed to solve the contact problems in sections 6 and 7. This is a crude approach in many aspects but is enough for the purposes of this work.

3.5.7.1. Load stepping

The nonlinearity of contact methods, even for linear elasticity, should be a little more evident now. The weak formulation of plane linear elasticity, without the contact contribution, depends linearly on the displacement field. This is the reason why a system of the form (3.11) is obtained when the finite element approximation is introduced, without need for linearization.

Whereas the nonlinearity of the contact contribution to the weak form is evident when its linearization leads to something as big as (3.117). Another reason for the nonlinearity of the contact contribution is the fact that it is only introduced when contact is active. This requires an active-set strategy to include only the contribution of node-segment pairs for which contact is happening.

The application of the Newton-Raphson method is not without its complications. There is a tradeoff between the robustness of the method regarding the intensity of prescribed loads and displacements, and the residual penetration left from the penalty method. If the penalty parameter is too high, the pressure generated from a small initial penetration will be enough for NR to diverge, leading to a small range of problems that can be solved. If the penalty parameter is too low, the method will converge to a solution for a wider variety of problems, however there will be significant persistent penetration in the solution, tainting it.

Compromise was found by introducing load-steps. The total prescribed load/displacement is divided and introduced by incremental steps. For every increment, a new problem is solved using the NR method, using the current solution as initial guess. This makes the method search for a solution that is much closer to the current state, improving convergence drastically. For this, an adaptive scheme was devised. An initial step-size may be doubled, maintained, or halved depending on whether the number of iterations required for convergence for the last step application was low, adequate, or high. With this, the method is no longer limited in intensity of prescribed loads/displacements, the tradeoff is now between step-size and residual penetration.

In practical implementation aspects, this work employed a load-stepping function that does this adaptive interpolation of the boundary conditions. At each step, a partial problem is formulated and passed on to a partial-solving function which, in turn, returns the number of iterations required or -1 if the problem diverged (resetting the initial solution). This information is used to adapt the step-size.

3.5.7.2. Solving the partial problems

Given the boundary conditions for the current load-step and the current solutions as initial guess, a partial problem is defined. This problem is put into terms of the total unbalanced force as the difference between total external (considered independent of the displacements) and internal forces:

$$\mathbf{R}_u(\mathbf{u}) = \mathbf{R}_{ext} - \mathbf{R}_{int}(\mathbf{u}). \quad (3.138)$$

The total external force is fully determined by the boundary conditions. The total internal force is dependent on the displacement field and is nonlinear due to contact. The objective is to find the displacement field that vanishes the total unbalanced force. The generalized version of Newton-Raphson method is employed. Equation (3.100) for this problem becomes

$$\Delta \mathbf{u}_n = - \left(\frac{\partial \mathbf{R}_u}{\partial \mathbf{u}}(\mathbf{u}_n) \right)^{-1} \mathbf{R}_u(\mathbf{u}_n) = \left(\frac{\partial \mathbf{R}_{int}}{\partial \mathbf{u}} \right)^{-1} \mathbf{R}_u = \mathbf{K}_T^{-1} \mathbf{R}_u. \quad (3.139)$$

To each iteration's solution, \mathbf{u}_n , there corresponds a set of active contact pairs. Part of the nonlinearity of the contact interaction is that there might be changes in this set from one iteration to the next. This is captured in a "contact-flag", a Boolean variable that is true if there were any changes from last iteration to the current one. This is an important criterion to be considered in the Newton-Raphson loop: if the active-set changed, another iteration is required.

The set should be updated before the current iteration's total internal force and tangent stiffness matrix are evaluated. The first determination of this set is done by a "contact search" function, and its update by a "contact check" function. Both functions return a

Boolean value with same meaning as the contact flag, this output is used to update said flag.

3.5.7.3. Contact search and check

The contact search procedure adopted is quite simple when compared to other options. A contact-pair object is created for each node in the slave surface. This object contains a “slot” for a segment and can compute a rough distance estimate (distance from node to segment midpoint), performs checks for contact validity, computes the total internal force contribution and the tangent stiffness matrix contribution. The search consists of a global search, where each contact pair object loops through the segments in the master surface storing the rough distance estimates into an array, looking for the closest segment; and a local validity check. In summary: for each node, the closest segment is found and checked for valid contact. After every node has been searched, if any pair became active, the “contact search” function returns True. If not, False.

The validity check for each pair consists of solving the Local Contact Problem and checking two conditions:

- i. If the solution lies within the boundaries of the segment;
- ii. If the normal gap is negative (there is penetration).

If only condition (i) is true, this means the correct pair is found, but there is no contact; the procedure goes on to the next node. If both conditions are satisfied, the contact is set as active for this node-segment pair, and the search goes on to the next node.

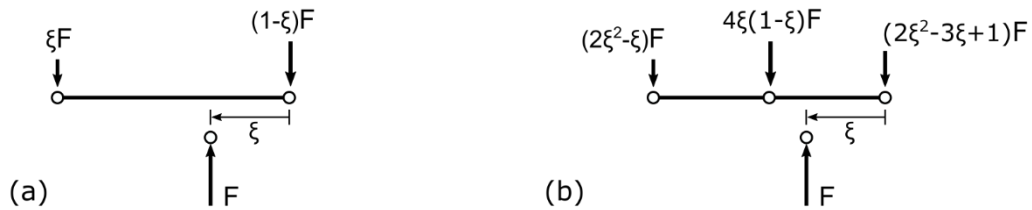
The contact check procedure is similar. For each node, if its contact pair is inactive, the search described earlier is performed. If it is active, the validity check is performed: if it remains active, nothing changes; if it becomes inactive due to condition (i), another search is performed; whereas if it becomes inactive due only to condition (ii), it becomes inactive. Again, if there were any changes, the function returns True. If not, False.

It bears remarking that there are more efficient ways to perform this search procedure. Usually, the global search is performed for subdomains to make it more efficient. More on search algorithms can be found in Wriggers [20].

3.5.8. Inherent problems and alternate interpretations

Up to this point the method was presented in its classical formulation and interpretation: one surface composed of nodes (points) and the other of segments. The penetration constraint is enforced at node-segment pairs. The contact surface is the intersection between points and segments, i.e., a set of points. Hence, the contact term in the weak formulation (2.68) is computed exactly by summing the integrand evaluated at those points. The contact forces are pointwise and concentrated on the slave nodes and represented by the equivalent nodal load in the master segments. These are obtained via the segment's shape functions, as shown in Figure 22. Any interpretation of those as a distributed contact pressure is outside the scope of the method and treated as post-processing procedure.

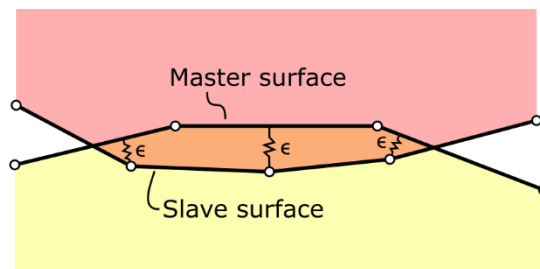
Figure 22. Equivalent nodal forces for the master segment. Linear (a) and Quadratic (b).



Source: Author.

In section 2.5, the physical interpretation of the penalty method was claimed to be that of springs acting on the penetration. The surface discretization gives a nice context to illustrate this claim. For each active pair, a spring of stiffness ϵ (penalty parameter) links the slave node and the master surface in the normal direction, as illustrated in Figure 23.

Figure 23. Interpretation of the Penalty method as springs.



Source: Author.

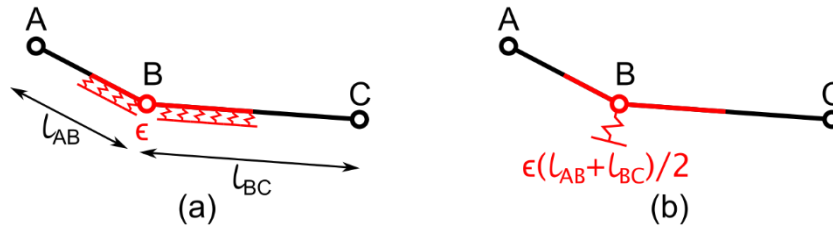
El-Abbasi and Bathe [103] presents two unrelated criteria in evaluating contact discretizations: stability and patch test performance. The first criterion is related to the LBB or inf-sup condition for the mixed formulation associated with Lagrange multipliers. This ensures the solvability and convergence, leading to robust formulations. Unstable discretizations, although frail, can still be used with the penalty method. The paper show that the Node-to-Segment discretization satisfies this condition and is robust. The second criterion is associated with the exact evaluation of the contact integral for constant contact pressures. The NTS discretization fails this test, as will be shown in practice in section 6. The consequence of this is solution errors in the contact surface that are not guaranteed to diminish with finer meshes. These oscillations in the results will become evident in said section.

Zavarise and De Lorenzis [104] dissects the reasons behind the patch test failure for the linear case, and propose a modified version that passes the test. The authors identify three main problems, whose expositions requires a shift on the method's interpretation. They also propose three independent solutions that, put together, form the modified version. The shift in interpretation requires considering the slave surface as a surface instead of a set of points. This would change the method from a node-to-segment into a segment-to-segment method, as is effectively done at the end. In this new framework, the contact surface is now a set of segments, and the contact integral is now being computed by collocation at the nodes. This resembles a Newton-Cotes integration, in the linear case the trapezoidal rule.

The first problem is the uniform use of the penalty parameter. In the node-to-segment interpretation, there is no reason to adopt different penalty parameters for different nodes. In the new interpretation, the Newton-Cotes rule requires weights depending on the length of the segment. Zavarise and De Lorenzis illustrate this as a change in the physical interpretation of the penalty parameter. Instead of pointwise springs (Figure 23), the parameter would represent the stiffness of a Winkler foundation (bed of springs), as in Figure 24(a), uniformly distributed along the slave surface. The penalty associated with each node would represent the equivalent stiffness, considering its width of influence (in

red), as in Figure 24(b). This matches the correct weights for the Newton-Cotes rule. This procedure is denoted as the area regularization of the penalty parameter.

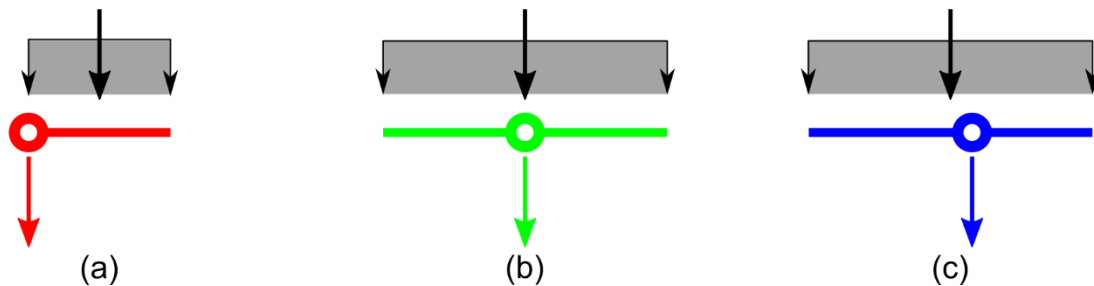
Figure 24. Bed of springs interpretation of the penalty parameter (a) and equivalent spring for node B (b).



Source: Author.

The second problem pointed out by Zavarise and De Lorenzis is that the contact force at the slave nodes is not mechanically equivalent to the uniform contact pressure. The contribution at each point in the Newton-Cotes rule should be equivalent to the integral over its area of contribution. This leads to the Newton-Cotes contribution for each slave node, its concentrated contact force, being mechanically equivalent to the pressure field inside its contribution width. This does not happen. Except in the case of a uniform mesh, the balance of moments is violated, as illustrated in Figure 25. Although the figure illustrates the case for uniform contact pressure, the same point can be made for general pressure distributions: mechanic equivalence in this formulation is the exception, not the rule.

Figure 25. Slave node and uniform pressure inequivalence. Corner node (a), uniform mesh exception (b), and general case (c).

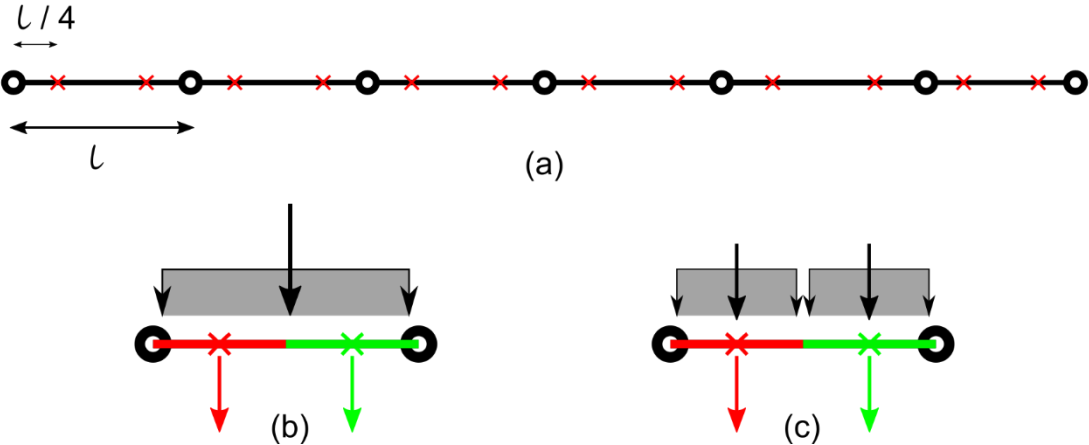


Source: Author.

The solution proposed by Zavarise and De Lorenzis is the choice of a different integration scheme. This is done in a way that the distribution of integration points inside each slave segment is always symmetric, and each integration point's width of influence is entirely

contained in one slave segment (Figure 26). This ensures mechanical equivalence in the case of uniform pressure. With this solution, the new slave points are now the integration points, not the nodes. Their kinematic is interpolated from the segment's nodes using the shape functions. The authors call these points virtual slave nodes, as they permit better discretization of the slave surface without introducing additional degrees of freedom.

Figure 26. Integration scheme proposed by Zavarise and De Lorenzis (a), mechanical equivalence on segment level (b) and on the level of each integration point influence width (c).

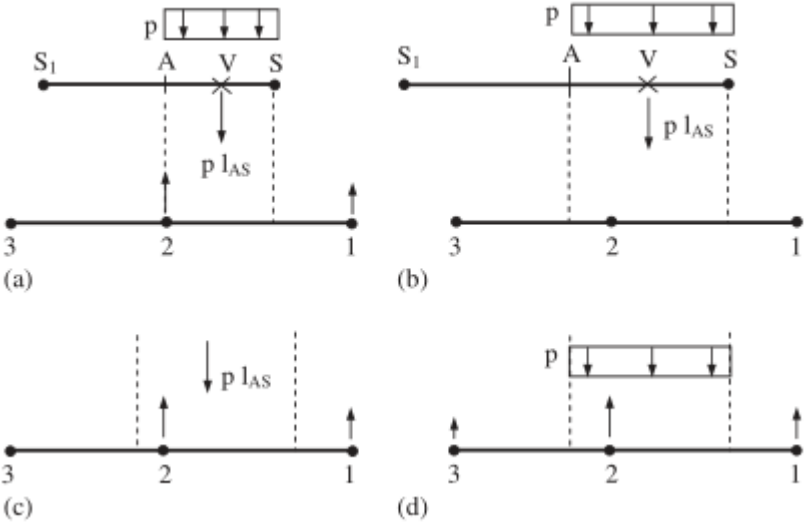


Source: Author.

The last problem is the transmission of force from the virtual slave node to the master surface. Ideally, the slave node should represent its area of competence, and the force transferred should have the same effect on the master surface as the uniformly distributed pressure in this area. In the general case, the projection of the area of competence of some slave nodes can overlap more than one master segment, see Figure 27(b). Therefore, the slave node should transfer part of the load to each master segment involved, Figure 27(d). This does not happen. Each integration point is paired only with one master segment, without regard to its area of competence. This leads to an incorrect transmission of forces between the two surfaces, Figure 27(c). In other words, the contact pressure that acts on the master surface is different from the one acting on the slave surface. To fix this, Zavarise and De Lorenzis present an algorithm that takes this into account, it finds all master segments in the projection of the slave node's area of competence, and couples them together in the formulation.

The three modifications presented above form the patch-test-passing modified node-to-segment algorithm. At this point, it is no longer a node-to-segment algorithm, but a segment-to-segment algorithm. These modifications fix, but also complicate, an algorithm whose place in commercial finite-element codes is preserved due its simplicity.

Figure 27. Problem of wrongful force transmission illustrated. (a) Normal case, (b) problematic case: its incurred force transfer (c) and the ideal force transfer (d).



Source: Zavarise and De Lorenzis [104].

All the problems and fixes explained previously were presented in the context of linear elements. Crisfield [114] states that the NTS is usually employed with linear elements, De Lorenzis, Wriggers, and Hughes [99] corroborates this by stating the reason as the exacerbation of this moment imbalance due to the non-uniform distribution of forces arising from a uniform pressure distribution (see Figure 28) when higher order functions are used. This makes the fulfilment of the patch test even more difficult for higher order shape functions.

Figure 28. Nodal forces equivalent to constant pressure. Linear element (a) and quadratic element (b).



Source: Author.

4. First application – St. Venant torsion

This application serves the purpose of a first practical exercise during the learning of the novel method. It is a simple problem to solve using the FEM and leads to equations of the same nature as those used to illustrate the VEM in the literature; it is also a problem inside the context of structural engineering and of great importance in other contexts, as mentioned in section 2.5.

Partial results of this study have been published, Moherdauí and Gay Neto [115], and presented in the XL Ibero-Latin-American Congress on Computational Methods in Engineering (CILAMCE 2019).

4.1. Goals

The general goal of this study is to use both the FEM and VEM for approximate solutions for uniform torsion problems. Providing context for a qualitative and quantitative comparison of the methods.

4.2. Methodology

The method is a comparative analysis for the torsion constant error (introduced in the following section). The varied parameters, topic of the following sections, are as follows:

- Problem formulation;
- numerical method;
- cross-section geometry;
- element geometry;
- element order;
- element size.

The quantitative comparison is established by means of the convergence curves, as presented in section 3.2.4. The results also include a qualitative appreciation of the numerical solutions.

4.2.1. Torsion constant error

The torsion constant is the scalar geometric property of the cross-section, which helps mediate the relationship between the twisting moment and corresponding twist rate (2.76) in St. Venant's torsion theory.

It is expressible in terms of the warping function (2.103), or Prandtl's function (2.106); it constitutes a global appraisal of the function from which it is calculated; and it has analytic solutions for simple geometric shapes. Because of these reasons, this quantity was elected as a quantitative measure of the success of the approximated solutions. The error (e) with respect to property, expressed as follows:

$$e = \frac{|I_T^{analytic} - I_T^{approximate}|}{I_T^{analytic}} \quad (4.1)$$

is the one, relative to which, the convergence curves are constructed.

4.2.2. Formulation

The implementation of both formulations was motivated by the variety of conditions necessary for the program. The warping function formulation requires the handling of the Neumann boundary condition, whereas Prandtl's formulation involves a constant distributed load and Dirichlet boundary condition.

Although the two functions lead to similar equations, the warping function is a displacement and Prandtl's function is related to the stresses. Their relationship with the torsion constant is also different: the warping function is related by an integral of its derivatives summed with a polynomial, whereas Prandtl's function is integrated by itself.

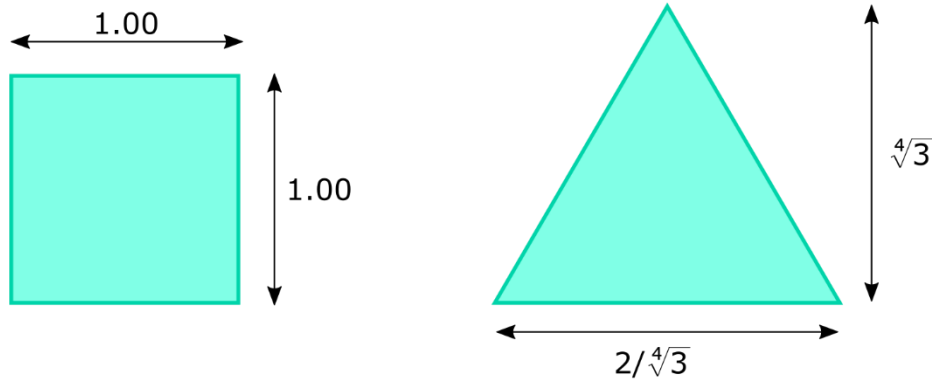
Each mesh is simulated twice, one time solving for the warping function, the other for Prandtl's function. The torsion constant is evaluated each time. The product ($G\theta'$) is adopted as constant and equal to 1 for this study.

4.2.3. Cross-section geometry

Two cross-section geometries were chosen (to avoid any unexpected bias particular to a single geometry), consisting of basic geometric shapes (for which there are analytic

solutions in the literature) of unit area (so that element-sizes are comparable from one to the other). The shapes are a square and equilateral triangle, illustrated with their corresponding dimensions in Figure 29.

Figure 29. Cross-section geometries.



Source: Author.

The analytic solution for the torsion constant of the square cross-section, from Timoshenko [18], is expressed by the following series, where l is the length of the side, in this case equal to one:

$$I_T^{\square} = l^4 \left[\frac{1}{3} - \frac{64}{\pi^5} \sum_{n=0}^{\infty} \frac{\tanh\left(\frac{(2n+1)\pi}{2}\right)}{(2n+1)^5} \right] = 0.140577 \dots \quad (4.2)$$

The solution for the equilateral triangle is:

$$I_T^{\Delta} = \frac{l^4 \sqrt{3}}{80} = 0.127323 \dots, \quad (4.3)$$

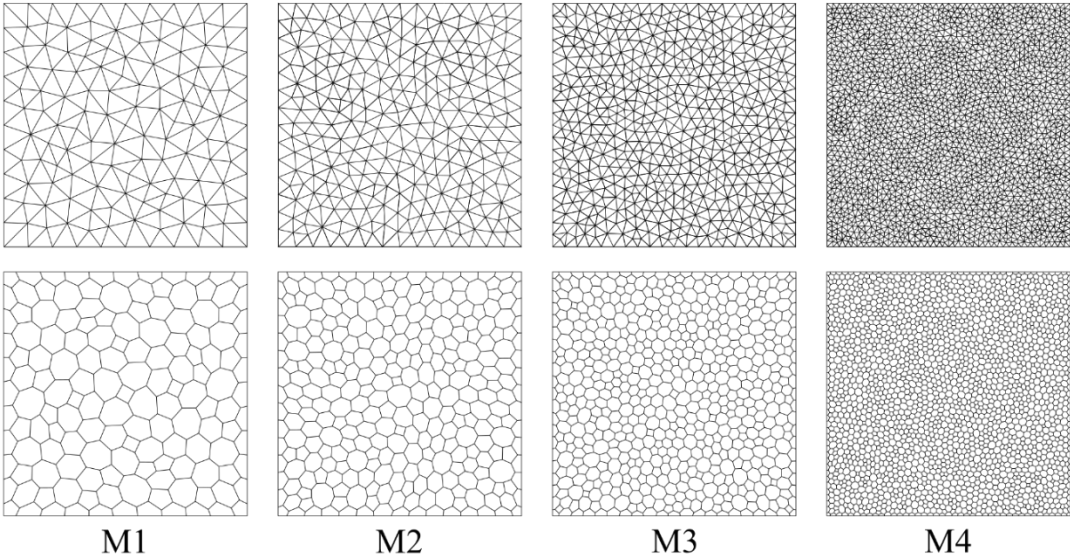
where l is the length of the side, in this case equal to $\frac{2}{\sqrt[4]{3}}$.

4.2.4. Element geometry, size, and order

For each cross-section geometry were generated four Delaunay triangulations of different levels of refinement. For each, the associated Voronoi tessellations was generated using the procedure mentioned in section 3.3.6. Each different level of refinement is associated,

for the purposes of this work, with an integer ranging from 1 to 4, coarsest to finest. The triangulations and polygonal tessellations are illustrated in Figure 30.

Figure 30. Domain partitions of different geometries and sizes.



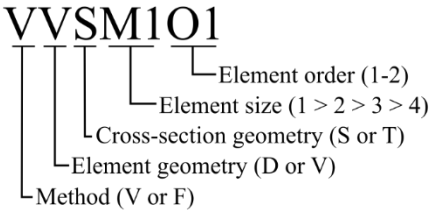
Source: Author.

The triangular partitions were used for first and second order, finite and virtual elements, i.e., for each triangulation four meshes were generated, forming all combinations of method and order. As for the Voronoi tessellations, two meshes originated from each partition; for first and second order virtual elements.

4.2.5. Meshes and simulations

A code was devised to identify the combination of parameters for each simulation. One instance of this codification is illustrated in Figure 31, where the positions associated with each parameter are shown.

Figure 31. Mesh codification example.



Source: Author.

The method character assumes V for virtual element method and F for finite element method. The element geometry assumes D for Delaunay triangulations and V for Voronoi tessellations. The cross-section geometry character assumes S for square and T for triangle. The element size pair range from M1 to M4, from coarsest to finest, as explained and illustrated. The element order assumes 1 for linear elements and 2 for quadratic elements, the implications of which were explained, for each method, in section 3.

A total of 48 meshes were produced by these combinations, and each is used twice: once for the warping function and once for Prandtl's function.

The mesh parameters associated with each combination are presented in Table 3.

Table 3. Mesh parameters.

Code	h	n _{dof}	Code	h	n _{dof}
FDSM1O1	1.37E-01	105	FDTM1O1	1.28E-01	124
FDSM2O1	9.67E-02	230	FDTM2O1	9.76E-02	225
FDSM3O1	6.62E-02	493	FDTM3O1	7.26E-02	496
FDSM4O1	3.43E-02	2057	FDTM4O1	3.58E-02	2014
FDSM1O2	1.37E-01	457	FDTM1O2	1.28E-01	541
FDSM2O2	9.67E-02	973	FDTM2O2	9.76E-02	960
FDSM3O2	6.62E-02	2049	FDTM3O2	7.26E-02	2074
FDSM4O2	3.43E-02	8385	FDTM4O2	3.58E-02	8236
VDSM1O1	1.37E-01	105	VDTM1O1	1.28E-01	124
VDSM2O1	9.67E-02	230	VDTM2O1	9.76E-02	225
VDSM3O1	6.62E-02	493	VDTM3O1	7.26E-02	496
VDSM4O1	3.43E-02	2057	VDTM4O1	3.58E-02	2014
VDSM1O2	1.37E-01	705	VDTM1O2	1.28E-01	835
VDSM2O2	9.67E-02	1487	VDTM2O2	9.76E-02	1471
VDSM3O2	6.62E-02	3113	VDTM3O2	7.26E-02	3157
VDSM4O2	3.43E-02	12657	VDTM4O2	3.58E-02	12445
VVSM1O1	1.44E-01	248	VVTM1O1	1.46E-01	294
VVSM2O1	1.09E-01	514	VVTM2O1	1.06E-01	511
VVSM3O1	7.41E-02	1064	VVTM3O1	7.63E-02	1083
VVSM4O1	3.89E-02	4272	VVTM4O1	4.13E-02	4209
VVSM1O2	1.44E-01	785	VVTM1O2	1.46E-01	931
VVSM2O2	1.09E-01	1599	VVTM2O2	1.06E-01	1597
VVSM3O2	7.41E-02	3273	VVTM3O2	7.63E-02	3343
VVSM4O2	3.89E-02	12977	VVTM4O2	4.13E-02	12811

Source: Author.

4.3. Results

The results are organized in different subsections, according to what type of result is shown. These types are the qualitative analysis of each interpolated function: warping function and Prandtl's function; the qualitative analysis of the stresses associated with these approximated functions; and the quantitative analysis of the torsion constants and torsion constant errors for each simulation.

For each different type of qualitative result there are four figures. Each figure corresponds to one combination of cross-section geometry and numerical method/element geometry. For conciseness, the results of the virtual element method on triangular partitions are not shown, only those of Voronoi tessellations. Therefore, all results shown for triangulations were obtained using the finite element method.

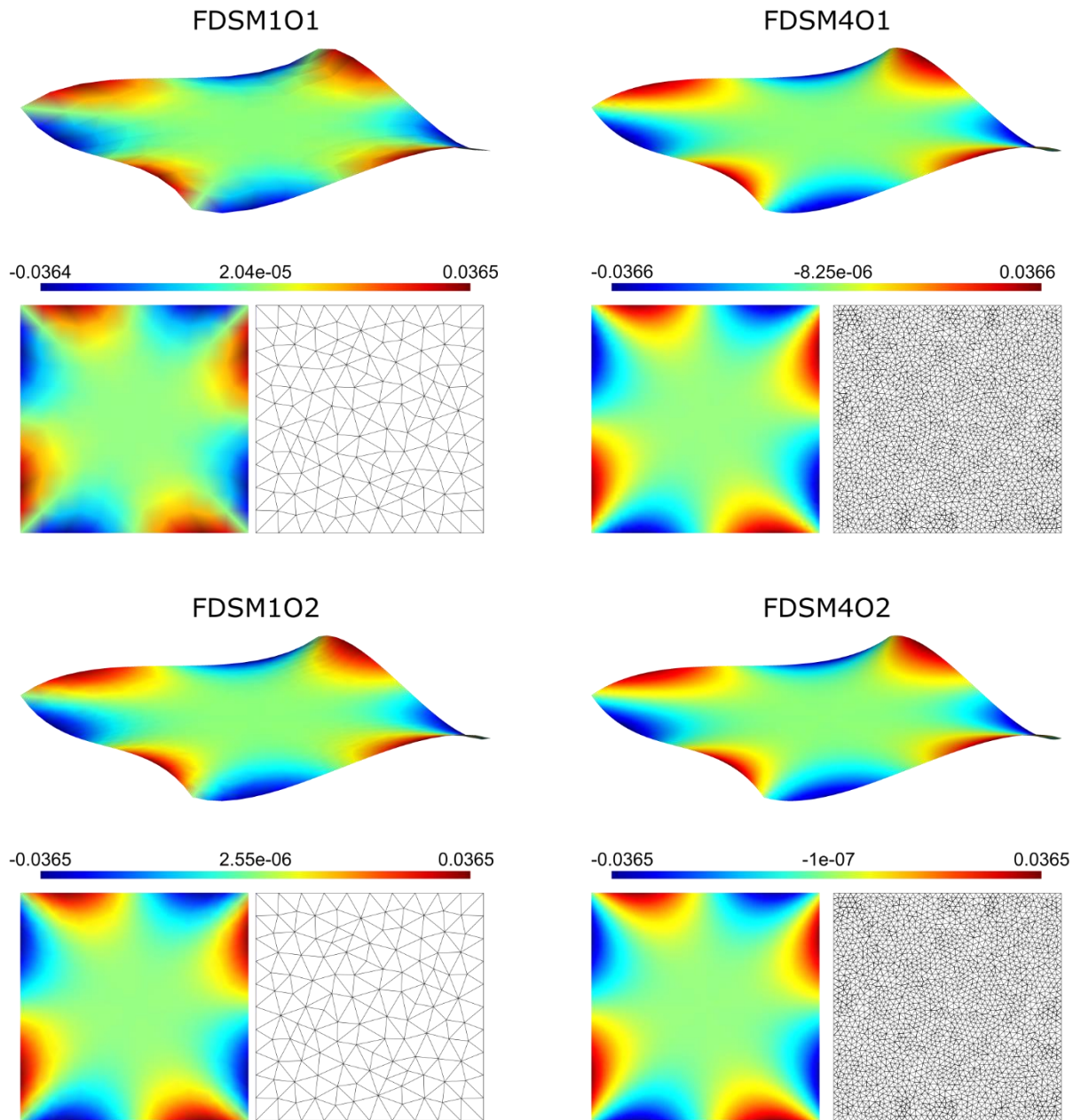
For each figure of qualitative results, only the coarsest (M1) and finest (M4) meshes are shown, to illustrate the impact of h-refinement, i.e., the refinement of the domain partition; the results of these meshes are shown for first order (O1) and second order (O2) elements, to illustrate the impact of p-refinement (increasing the polynomial order associated with the element space). Thus, each figure presents four different results, considering the extremes of each type of solution refinement.

The qualitative results were post-processed using the software GMSH. The results that show 3-dimensional surfaces are represented by collection of triangles in 3d space, colored by linear gradients of color associated with a scalar parameter associated with each vertex. This perfectly illustrates the results for first order FEM and VEM results on triangular meshes. For polygonal VEM and second-order results, there arise inherent imprecisions. The solution adopted for this was to show the linear interpolation of nodal results through these triangles. For the second-order triangular elements this means the decomposition into 4 sub-triangles which linearly interpolate the nodal results, not necessarily showing the approximated solution, which should take the shape functions into consideration for the color gradients. For polygonal elements, a similar solution is adopted, only decomposing every polygon into triangles which connect the center of the polygon (assuming as its value the average value of the nodes) with every two sequential edge nodes.

4.3.1. Warping function

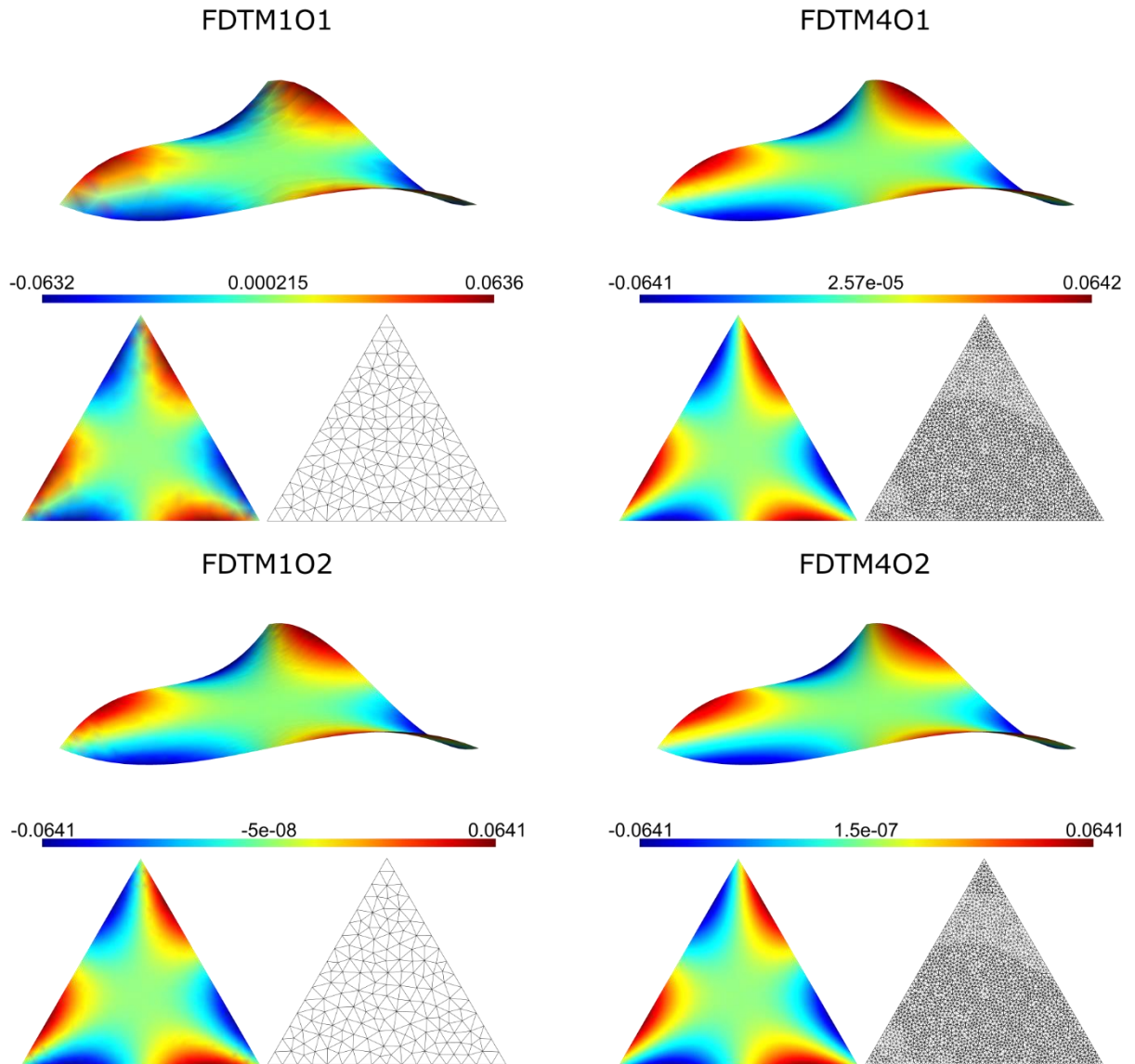
The results for the FEM-approximated warping function are presented in Figure 32 and Figure 33, for the square and triangle cross-section geometries, respectively.

Figure 32. FEM approximated warping functions for the square cross-section.



Source: Author.

Figure 33. FEM approximated warping function for triangle cross-section.

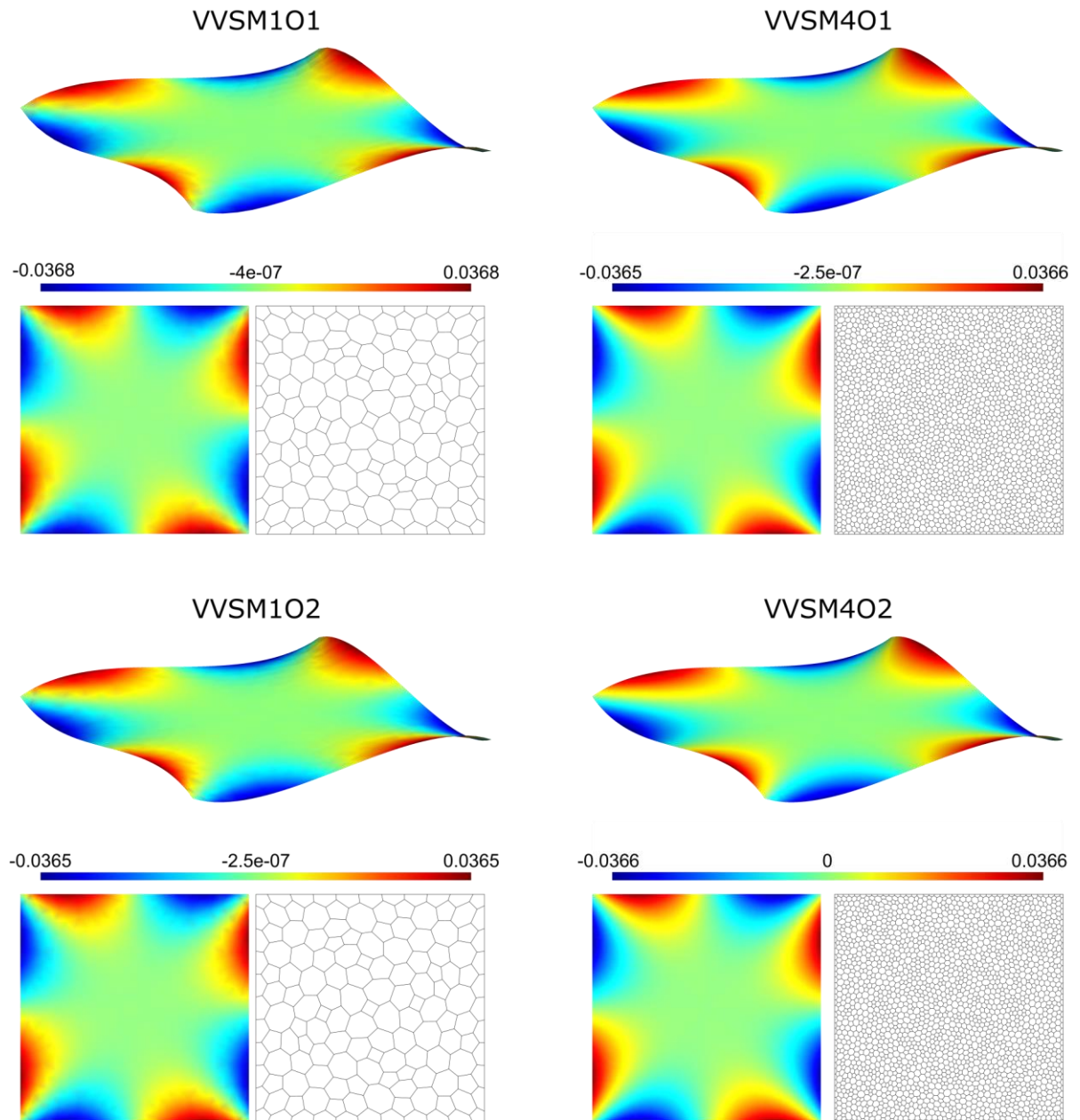


Source: Author.

The results for the VEM-approximated warping functions are presented in Figure 34 and Figure 35, for the square and triangle cross-sections, respectively.

The warping function shown in each figure is composed of its 3-dimensional colormap, illustrating the warping as a displacement; a 2-dimensional colormap to better illustrate the nodal interpolations (as explained in the beginning of the section) of the approximated solution; and the mesh from which the result originated.

Figure 34. VEM approximated warping function for square cross-section.

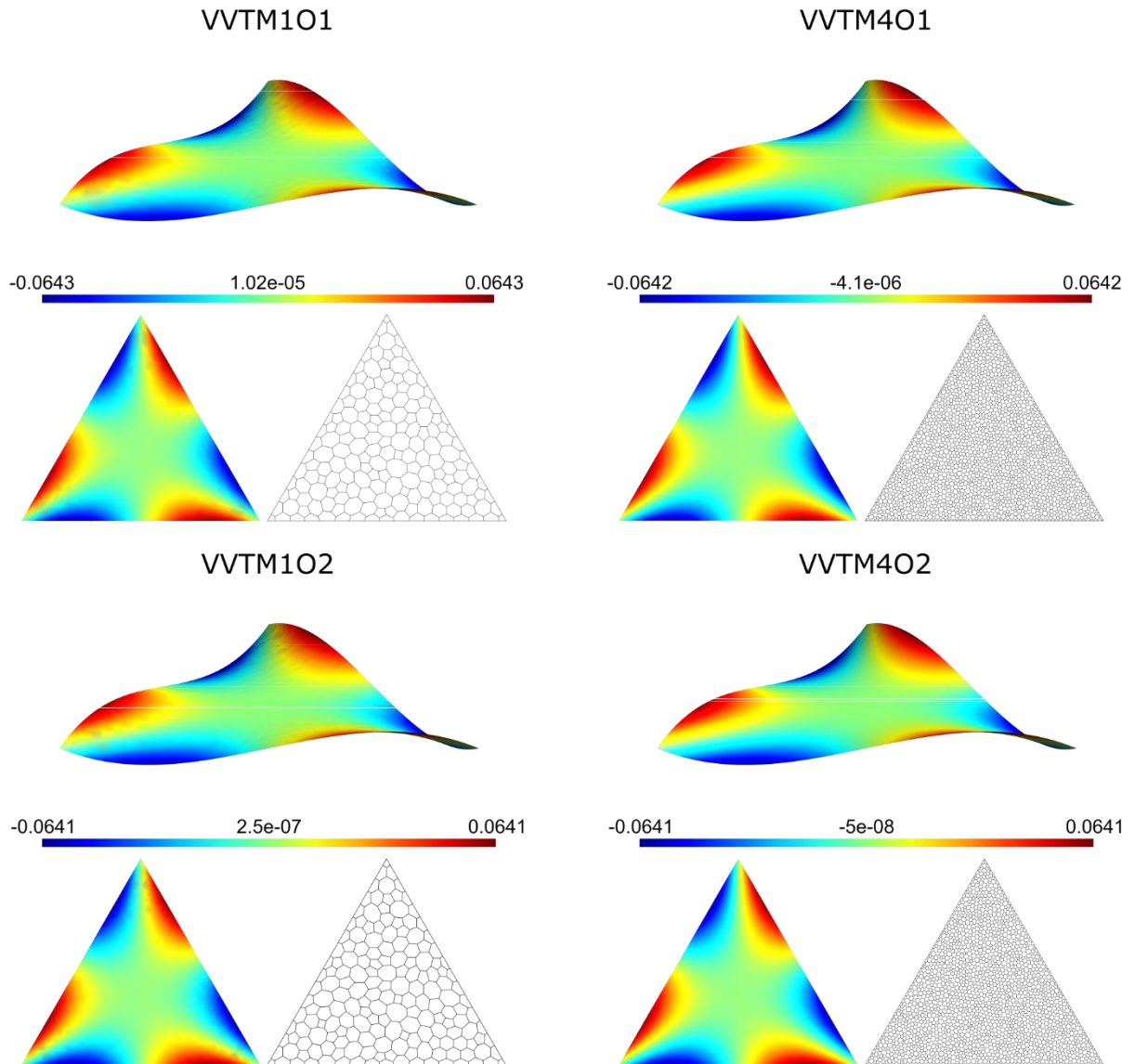


Source: Author.

In visual inspection, all solutions for the warping function are similar, showing internal coherence between results. Furthermore, the general shape also coincides with what the literature presents for the warping function of square and triangular cross-sections.

This concludes this first qualitative analysis of the approximated warping functions.

Figure 35. VEM approximated warping function for triangle cross-section.



Source: Author.

4.3.2. Prandtl's function

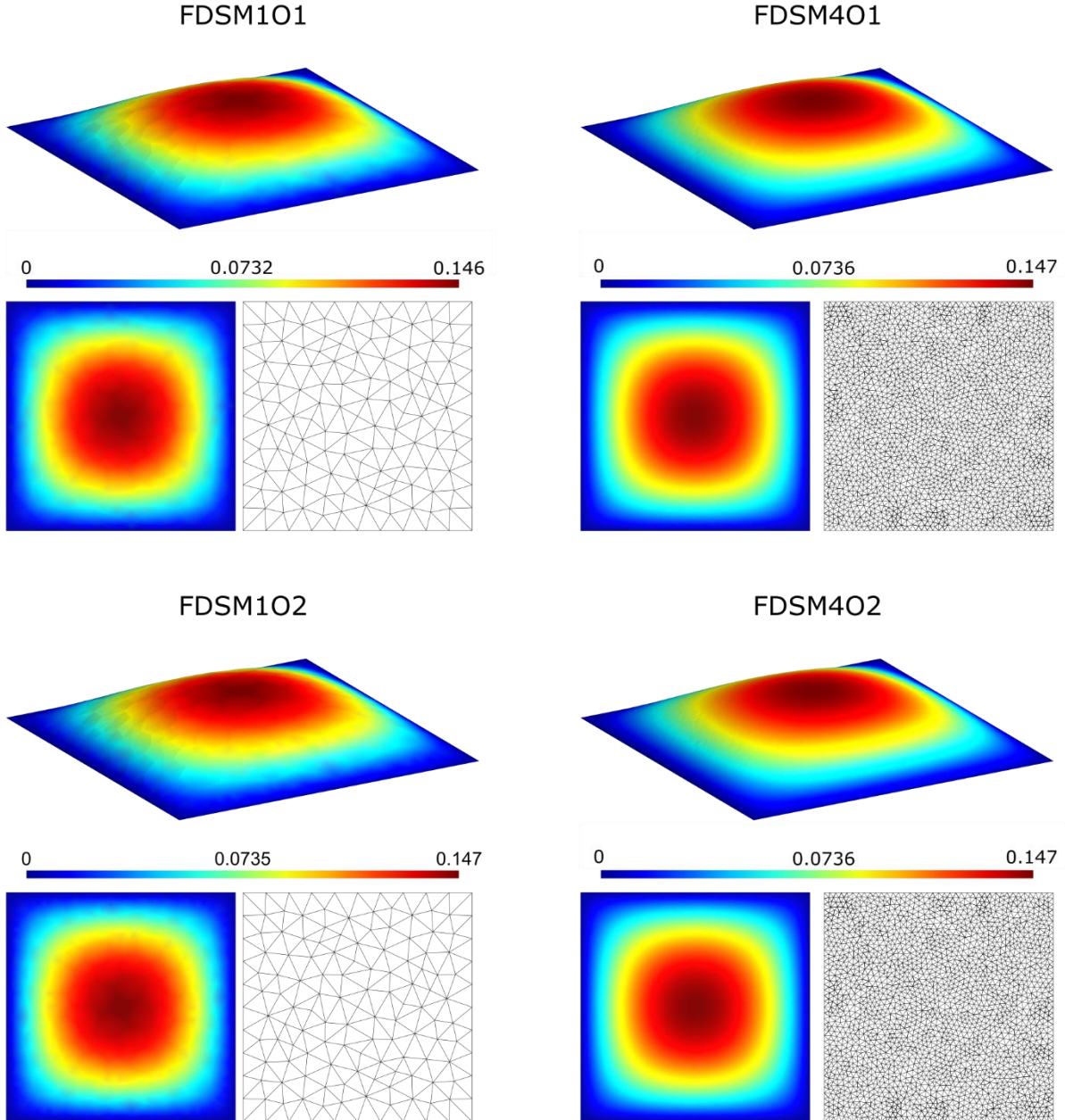
The results for the FEM-approximated Prandtl's functions are presented in Figure 36 and Figure 37, for the square and triangle cross-section geometries, respectively. Whereas those obtained via VEM are shown in Figure 38 and Figure 39, in similar manner.

The Prandtl's function results are easier to visually inspect, as they should resemble the vertical displacements of a membrane, of the same shape as the cross-section, fixed at

the boundaries and undergoing constant pressure. This is a result of the membrane analogy mentioned in section 2.7.4.

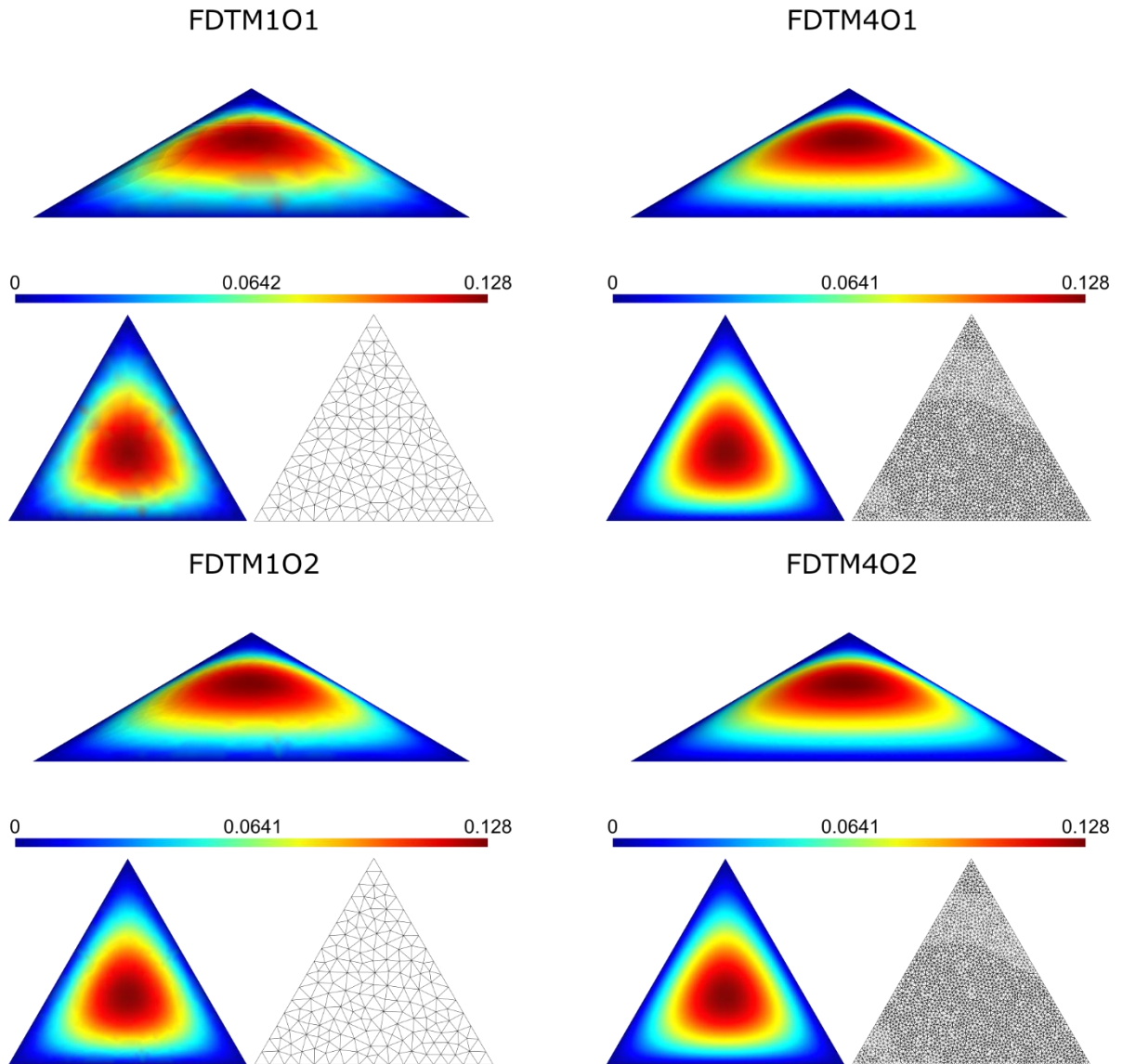
The conclusions of the visual inspection of these results are the same presented for the warping function results, last section.

Figure 36. FEM approximated Prandtl's function for square cross-section.



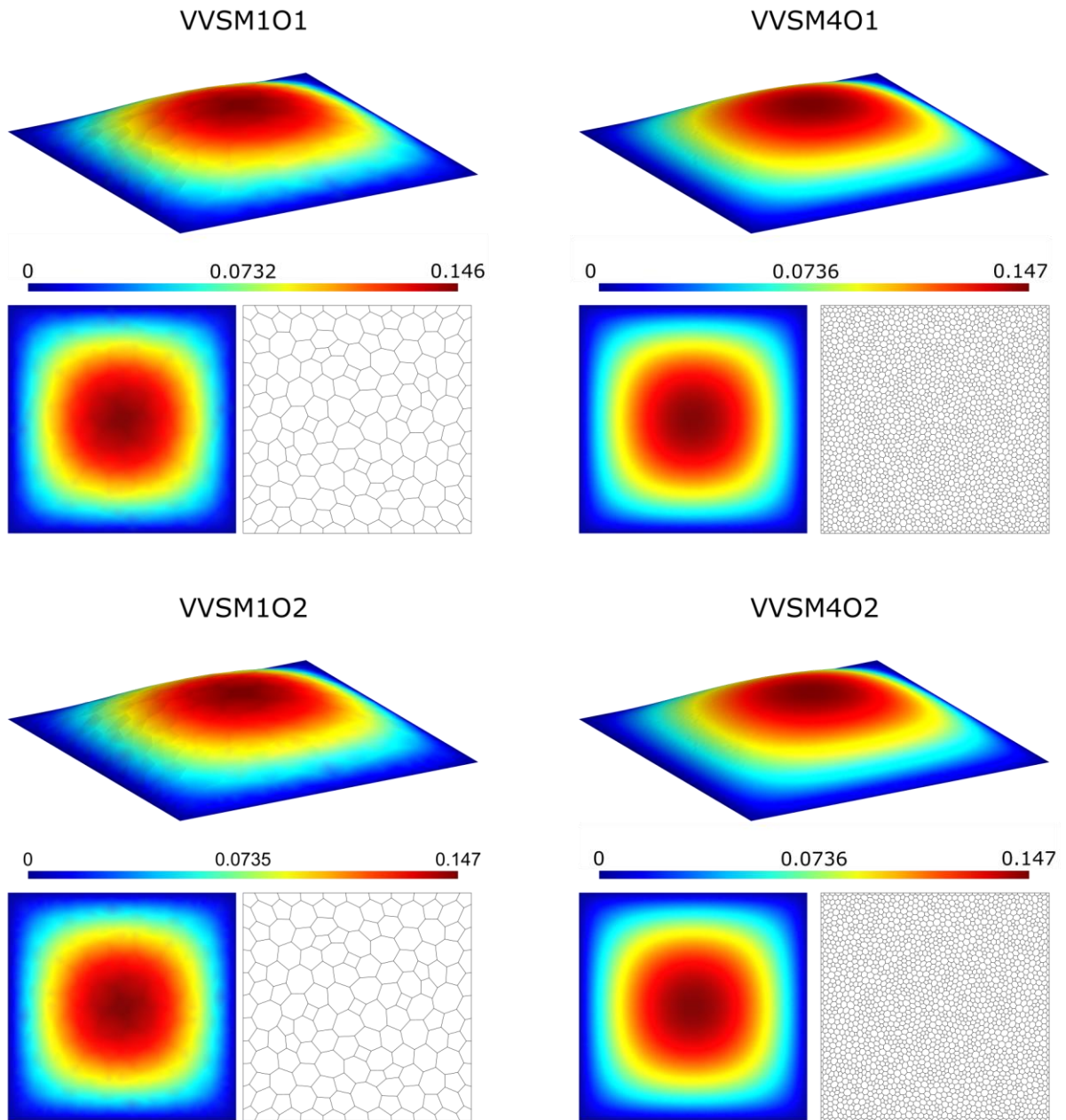
Source: Author.

Figure 37. FEM approximated Prandtl's function for triangle cross-section.



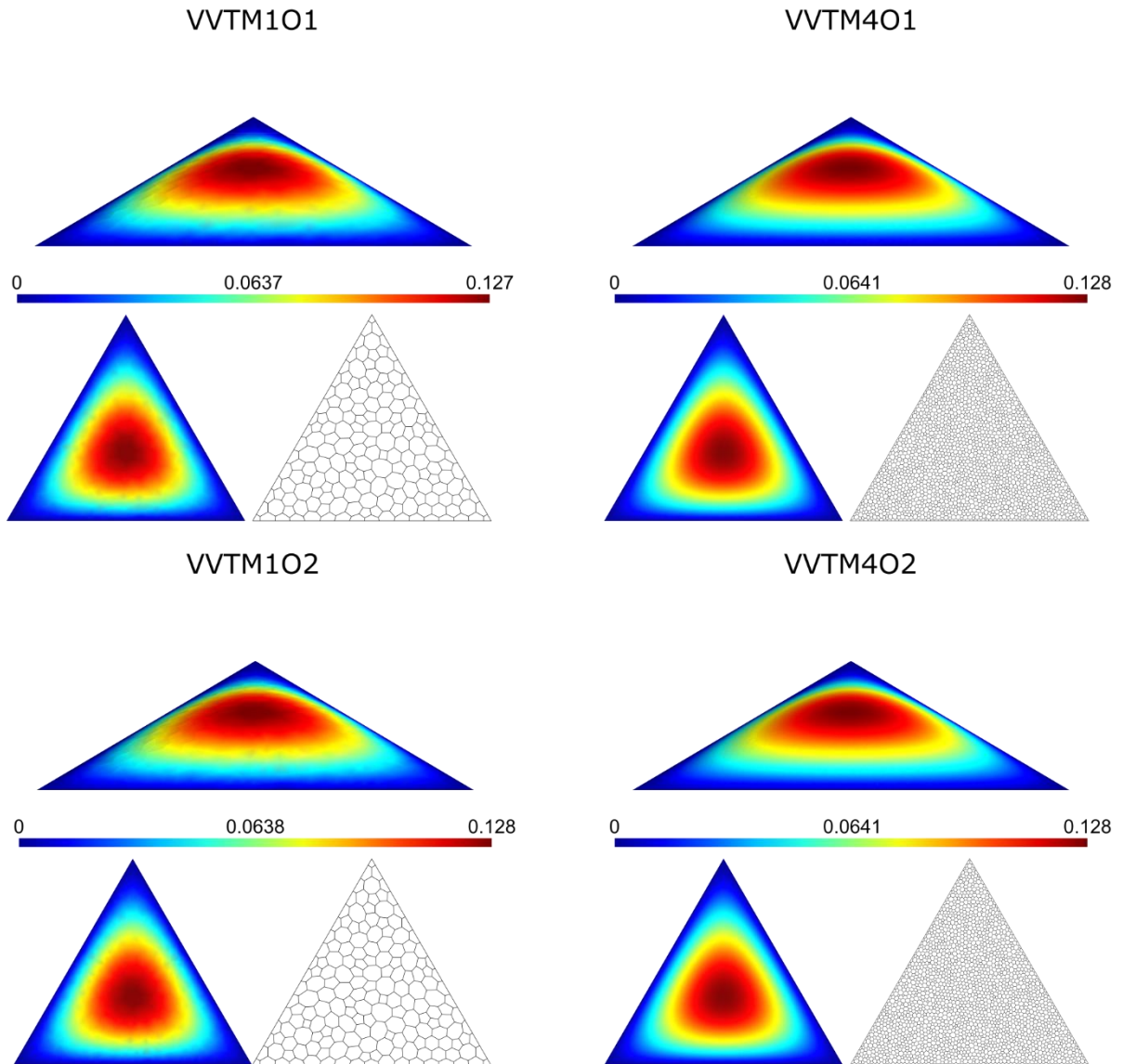
Source: Author.

Figure 38. VEM approximated Prandtl's function for square cross-section.



Source: Author.

Figure 39. VEM approximated Prandtl's function for triangle cross-section.



Source: Author.

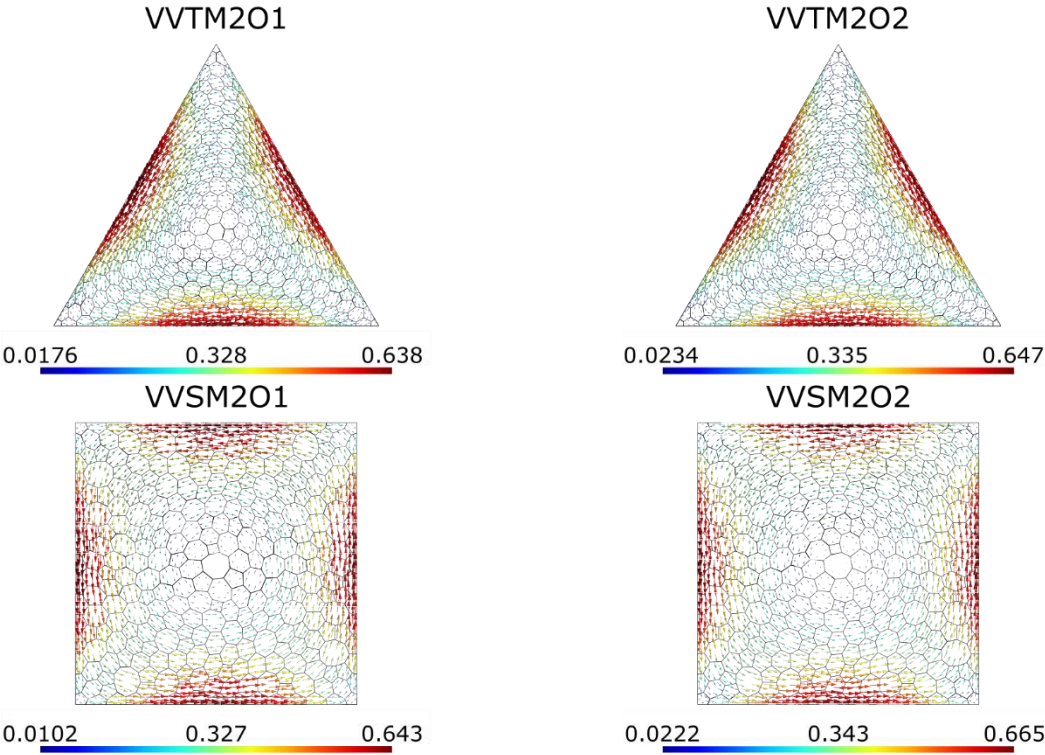
4.3.3. Stress distribution

The stresses are a tensorial quantity, as established in section 2.2.3. The stress tensor takes as input the vector normal to a plane and outputs the stress vector associated with that plane. For uniform torsion there are only 4 components of the symmetric stress tensor which are not null, by symmetry only two are independent; both are associated with the same plane: that of the cross-section. Therefore, the stresses for uniform torsion are possible to be represented as a vector field in the plane of the cross-section.

According to Zienkiewicz, Taylor and Zhu [36], the best approximation for the derivatives of the approximated function for the finite element method is located at the Gauss quadrature points. Therefore, for the vector representation of the stresses generated for the FEM results are taken at these points. The solution adopted to provide analog visualization for the VEM results is to choose the Gauss points for each triangle of the polygon triangulation described in section 4.3, with no guarantee for better quality.

This visualization provides means for intuitive interpretation of the stress field. Equilibrium implies that the stresses should balance the external load. This is clearly reflected in this vector representation: there is no clear resultant vector in any direction. The vectors indicate a circulating field, which counteracts the external torsional moment applied. This can be seen for VEM in Figure 40, and for FEM in Figure 41.

Figure 40. Vector plots of VEM stresses.

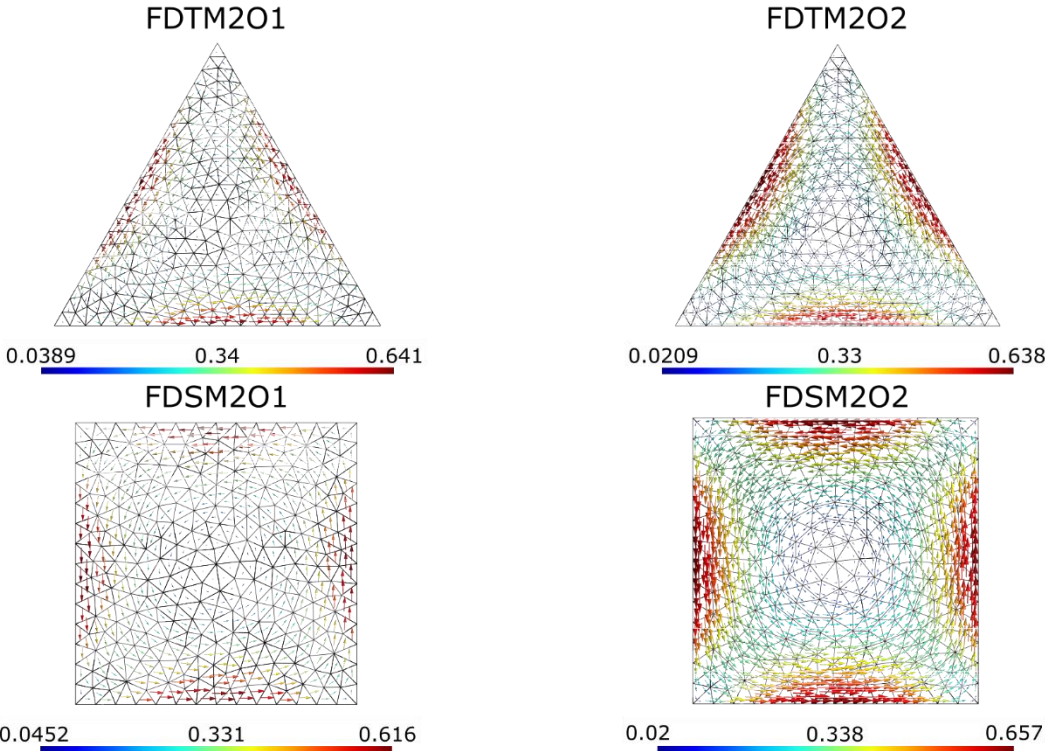


Source: Author.

The disadvantage of this visualization is that it easily becomes too polluted due to the excess of information. Because of this, only two mid-level refinement (M2) meshes are illustrated for each cross-section, numerical method, and polynomial order. As the results

are similar, the triangle cross-section results shown were restricted to those of the warping function, and the square cross-sections to those of Prandtl's function.

Figure 41. Vector plots of FEM stresses.

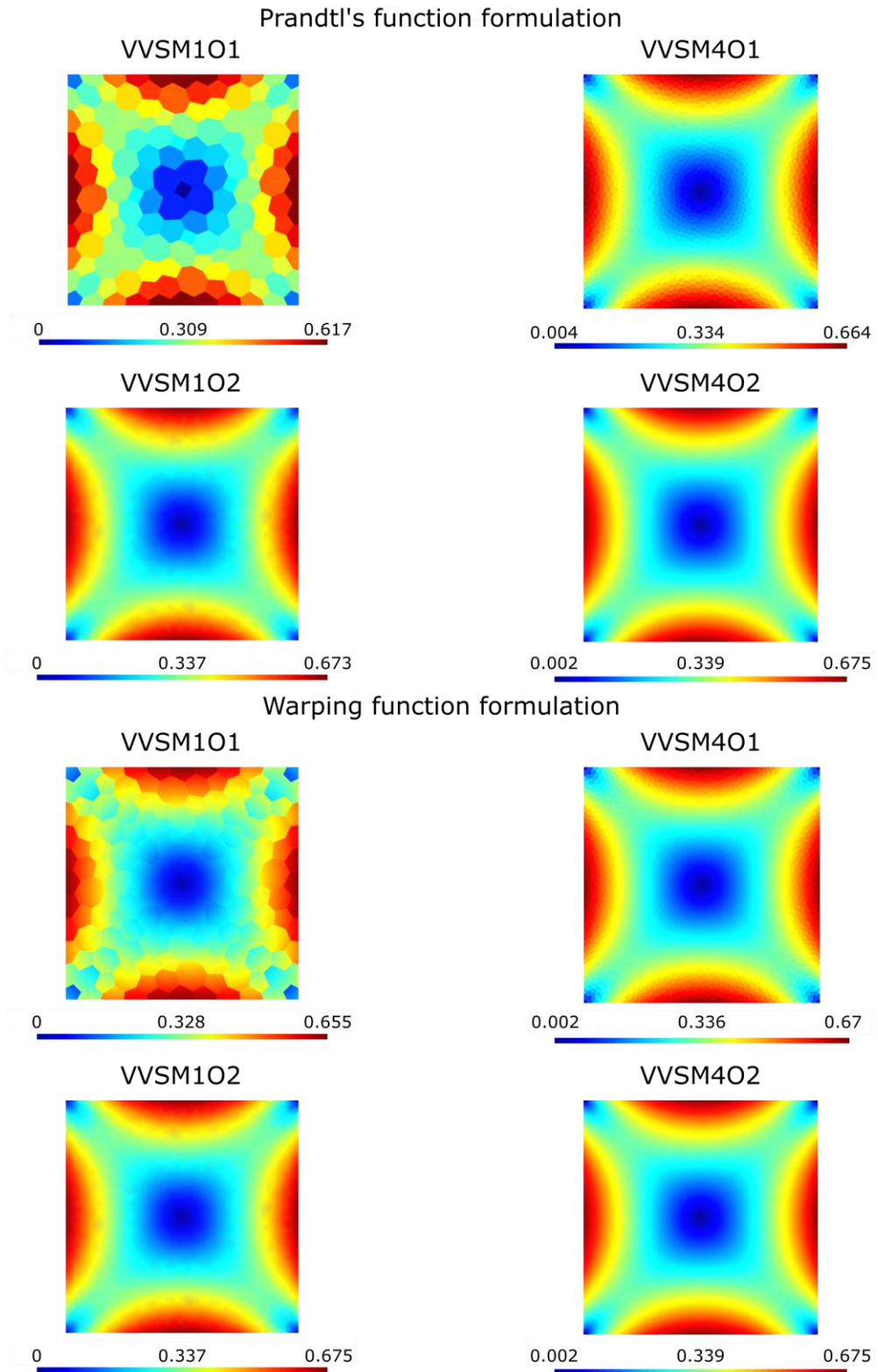


Source: Author.

A better way to show the stresses for this problem is to take the norm of the stress vector acting at each point. This can be illustrated as a colormap and brings richer information regarding the derivatives of the approximations of each method, and differences in the formulation of the problem. The figures representing the colormaps of the tangential stress norm are organized in similar way to those of the interpolated functions, showing the differences arising from h-refinement and p-refinement. For conciseness' sake, the square cross-sections are shown only for VEM results and the triangular cross-sections for FEM stresses. These are shown in Figure 42 and Figure 43, respectively.

All second-order results are similar, and some of the apparent inconsistencies in coarse meshes may still be a result of the nodal interpolation rather than of inaccurate results. This is due to the derivatives of the approximated function being linear and the discontinuities being rather small, giving the appearance of continuity.

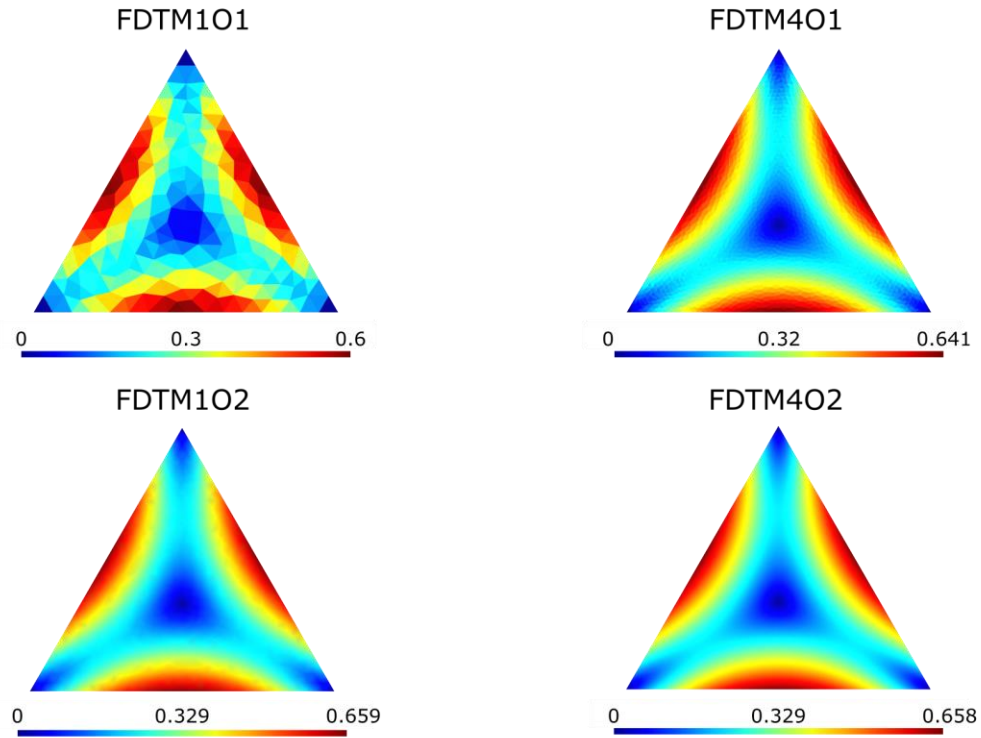
Figure 42. Tangential stress norm colormaps for VEM.



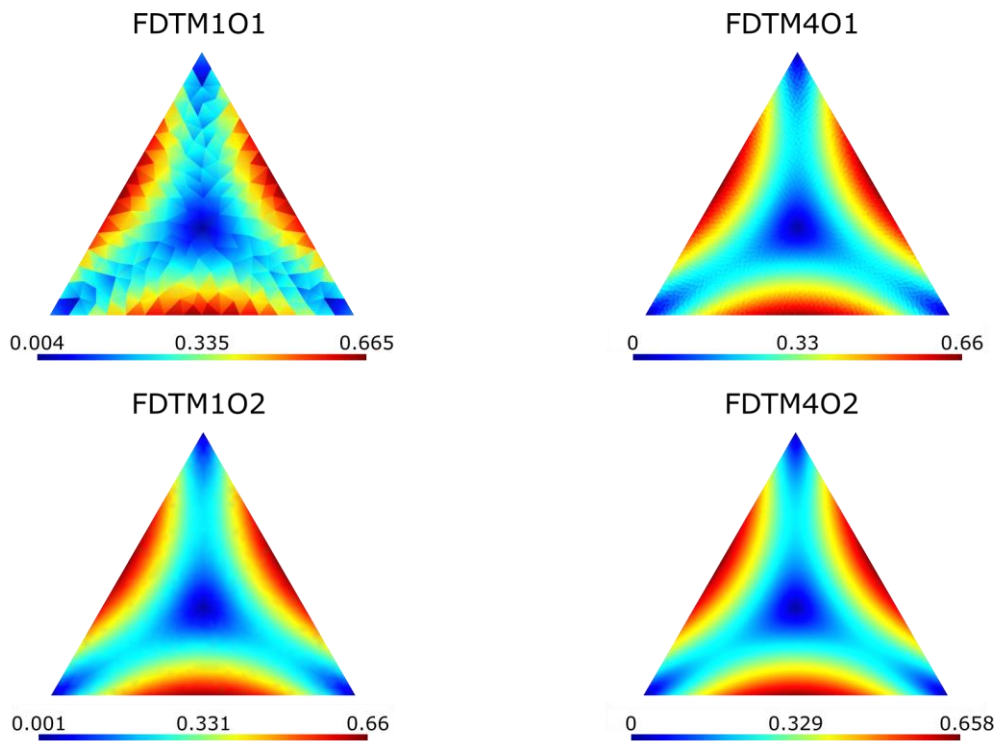
Source: Author.

Figure 43. Tangential stress norm colormaps for FEM.

Prandtl's function formulation



Warping function formulation



Source: Author.

For the linear interpolations, however, the derivatives are constant inside each element. This is more obvious in the results from Prandtl's formulation, as the stresses are the derivatives. For the warping function's formulation, the stresses are obtained by summing the derivatives with a linear polynomial (2.86), this gives the elementwise linear result, but the fact that the derivatives are constant lead to greater discontinuities between elements.

4.3.4. Torsion constant error

The values for the torsion constant, and the correspondent error, relative to each simulation are presented for St. Venant's formulation in Table 4 and Table 5, and for Prandtl's formulation in Table 6 and Table 7.

Table 4. Torsion constant results for square cross-section in St. Venant's formulation.

Code	h	n_{DOF}	I_T	e
FDSM1O1	1.37E-01	145	0.14217	1.13E-02
FDSM2O1	9.67E-02	286	0.14140	5.82E-03
FDSM3O1	6.62E-02	573	0.14102	3.15E-03
FDSM4O1	3.43E-02	2217	0.14067	6.97E-04
FDSM1O2	1.37E-01	537	0.14059	9.75E-05
FDSM2O2	9.67E-02	1085	0.14058	2.30E-05
FDSM3O2	6.62E-02	2209	0.14058	5.97E-06
FDSM4O2	3.43E-02	8705	0.14058	4.20E-07
VDSM1O1	1.37E-01	145	0.14217	1.13E-02
VDSM2O1	9.67E-02	286	0.14140	5.82E-03
VDSM3O1	6.62E-02	573	0.14102	3.15E-03
VDSM4O1	3.43E-02	2217	0.14067	6.97E-04
VDSM1O2	1.37E-01	785	0.14058	3.22E-05
VDSM2O2	9.67E-02	1599	0.14058	1.07E-05
VDSM3O2	6.62E-02	3273	0.14058	2.96E-06
VDSM4O2	3.43E-02	12977	0.14058	1.85E-07
VVSM1O1	1.44E-01	328	0.14081	1.68E-03
VVSM2O1	1.09E-01	626	0.14067	6.44E-04
VVSM3O1	7.41E-02	1224	0.14062	3.18E-04
VVSM4O1	3.89E-02	4592	0.14059	6.17E-05
VVSM1O2	1.44E-01	945	0.14058	2.92E-05
VVSM2O2	1.09E-01	1823	0.14058	6.26E-06
VVSM3O2	7.41E-02	3593	0.14058	1.59E-06
VVSM4O2	3.89E-02	13617	0.14058	1.37E-07

Source: Author.

Table 5. Torsion constant results for triangle cross-section in St. Venant's formulation.

Code	h	n_{DOF}	I_T	e
FDTM1O1	1.28E-01	172	0.11692	1.26E-02
FDTM2O1	9.76E-02	288	0.11633	7.41E-03
FDTM3O1	7.26E-02	589	0.11588	3.53E-03
FDTM4O1	3.58E-02	2197	0.11557	9.01E-04
FDTM1O2	1.28E-01	637	0.11547	1.23E-05
FDTM2O2	9.76E-02	1086	0.11547	3.93E-06
FDTM3O2	7.26E-02	2260	0.11547	9.22E-07
FDTM4O2	3.58E-02	8602	0.11547	6.01E-08
VDTM1O1	1.28E-01	172	0.11692	1.26E-02
VDTM2O1	9.76E-02	288	0.11633	7.41E-03
VDTM3O1	7.26E-02	589	0.11588	3.53E-03
VDTM4O1	3.58E-02	2197	0.11557	9.01E-04
VDTM1O2	1.28E-01	931	0.11547	6.16E-06
VDTM2O2	9.76E-02	1597	0.11547	2.04E-06
VDTM3O2	7.26E-02	3343	0.11547	4.24E-07
VDTM4O2	3.58E-02	12811	0.11547	2.75E-08
VVTM1O1	1.46E-01	390	0.11565	1.60E-03
VVTM2O1	1.06E-01	637	0.11556	7.52E-04
VVTM3O1	7.63E-02	1269	0.11551	3.04E-04
VVTM4O1	4.13E-02	4575	0.11548	7.02E-05
VVTM1O2	1.46E-01	1123	0.11547	8.73E-06
VVTM2O2	1.06E-01	1849	0.11547	3.59E-06
VVTM3O2	7.63E-02	3715	0.11547	6.49E-07
VVTM4O2	4.13E-02	13543	0.11547	5.02E-08

Source: Author.

Table 6. Torsion constant results for square cross-section in Prandtl's formulation.

Code	h	n_{DOF}	I_T	e
FDSM1O1	1.37E-01	105	0.13811	1.76E-02
FDSM2O1	9.67E-02	230	0.13931	9.00E-03
FDSM3O1	6.62E-02	493	0.13998	4.24E-03
FDSM4O1	3.43E-02	2057	0.14043	1.07E-03
FDSM1O2	1.37E-01	457	0.14056	1.19E-04
FDSM2O2	9.67E-02	973	0.14057	2.57E-05
FDSM3O2	6.62E-02	2049	0.14058	5.82E-06
FDSM4O2	3.43E-02	8385	0.14058	4.79E-07
VDSM1O1	1.37E-01	105	0.13811	1.76E-02
VDSM2O1	9.67E-02	230	0.13931	9.00E-03
VDSM3O1	6.62E-02	493	0.13998	4.24E-03
VDSM4O1	3.43E-02	2057	0.14043	1.07E-03
VDSM1O2	1.37E-01	705	0.14057	8.06E-05
VDSM2O2	9.67E-02	1487	0.14058	1.31E-05
VDSM3O2	6.62E-02	3113	0.14058	2.49E-06
VDSM4O2	3.43E-02	12657	0.14058	2.48E-07
VVSM1O1	1.44E-01	248	0.13844	1.52E-02
VVSM2O1	1.09E-01	514	0.13950	7.67E-03
VVSM3O1	7.41E-02	1064	0.14005	3.74E-03
VVSM4O1	3.89E-02	4272	0.14043	1.02E-03
VVSM1O2	1.44E-01	785	0.14058	1.92E-05
VVSM2O2	1.09E-01	1599	0.14058	3.08E-06
VVSM3O2	7.41E-02	3273	0.14058	1.06E-06
VVSM4O2	3.89E-02	12977	0.14058	7.01E-08

Source: Author.

Table 7. Torsion constant results for triangle cross-section in Prandtl's formulation.

Code	h	n_{DOF}	I_T	e
FDTM1O1	1.28E-01	124	0.11330	1.88E-02
FDTM2O1	9.76E-02	225	0.11418	1.12E-02
FDTM3O1	7.26E-02	496	0.11486	5.30E-03
FDTM4O1	3.58E-02	2014	0.11531	1.36E-03
FDTM1O2	1.28E-01	541	0.11547	1.30E-05
FDTM2O2	9.76E-02	960	0.11547	4.19E-06
FDTM3O2	7.26E-02	2074	0.11547	9.40E-07
FDTM4O2	3.58E-02	8236	0.11547	6.09E-08
VDTM1O1	1.28E-01	124	0.11330	1.88E-02
VDTM2O1	9.76E-02	225	0.11418	1.12E-02
VDTM3O1	7.26E-02	496	0.11486	5.30E-03
VDTM4O1	3.58E-02	2014	0.11531	1.36E-03
VDTM1O2	1.28E-01	835	0.11547	5.07E-06
VDTM2O2	9.76E-02	1471	0.11547	1.57E-06
VDTM3O2	7.26E-02	3157	0.11547	3.99E-07
VDTM4O2	3.58E-02	12445	0.11547	2.58E-08
VVTM1O1	1.46E-01	294	0.11367	1.56E-02
VVTM2O1	1.06E-01	511	0.11439	9.37E-03
VVTM3O1	7.63E-02	1083	0.11494	4.58E-03
VVTM4O1	4.13E-02	4209	0.11534	1.15E-03
VVTM1O2	1.46E-01	931	0.11547	2.87E-06
VVTM2O2	1.06E-01	1597	0.11547	8.17E-07
VVTM3O2	7.63E-02	3343	0.11547	2.64E-07
VVTM4O2	4.13E-02	12811	0.11547	1.68E-08

Source: Author.

All of this information is summarized by the convergence curves presented, in terms of the element size parameter (h), for St. Venant's formulation in Figure 44 and Figure 45; and for Prandtl's formulation in Figure 46 and Figure 47.

Note that for all curves the notation has been abbreviated, as the different meshes are explicitly represented by the different coordinates in the element size axis and the cross-section is explicit in the title of the chart; the legend entries consist only of the symbols associated with the numerical method, element geometry and element order. Furthermore, the legend entries separate the combinations of method and element geometry in different colors, and the markers are chosen to clearly indicate the element geometry: triangles for Delaunay triangulations and squares for Voronoi tessellations.

Results from linear elements are shown with hollow markers and quadratic elements with filled markers. All curves are shown together with a fitting of general form similar to (3.22), the equations for those fittings are provided next to the associated legend key.

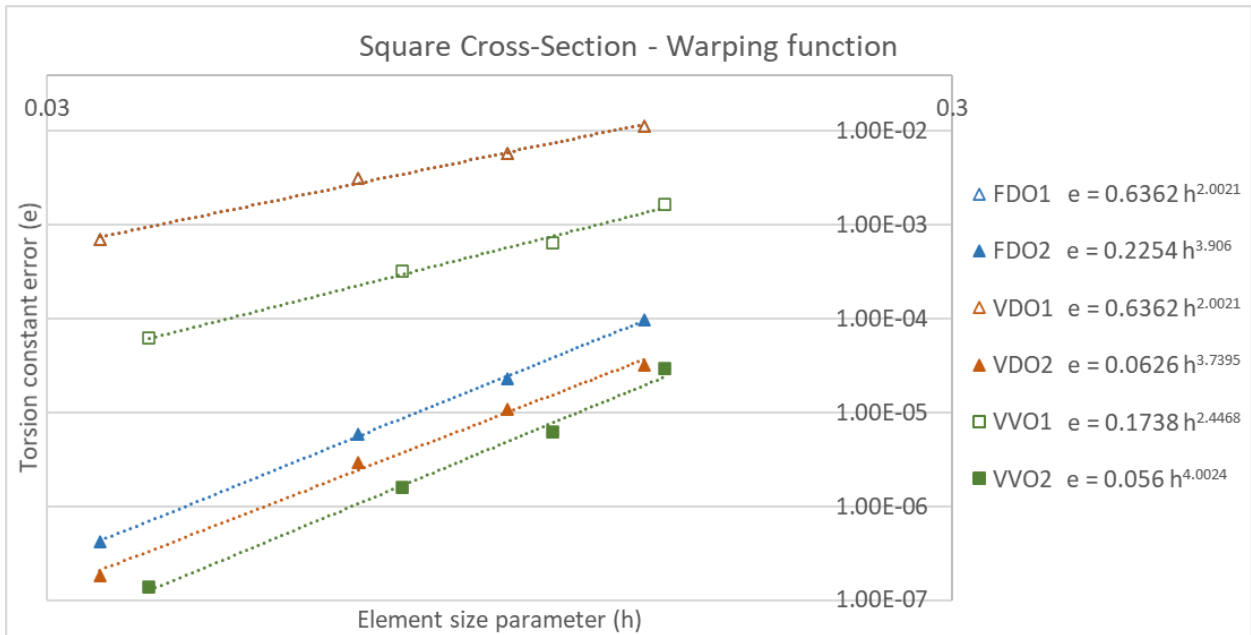
All curves show a clear tendency to convergence, i.e., the error tends to naught as the element size diminishes. The impact of the polynomial order of the interpolation is also pronounced and follows the general trend appointed in the literature for the usual *a priori* error measures, which consist of integer changes in the convergence rate p as the polynomial order is changed. This is visible in the different slopes of the fitting curves for different polynomial order interpolations.

In both formulations, the first order results in triangular meshes completely coincide, leading to a total overlap of the convergence curves, giving the impression that one of them is missing. This is a consequence of the virtual element space and finite element space (space of linear polynomials) completely coinciding. For triangular (3-sided) virtual element of first order the virtual element space has dimension $n_{dof} = 3$, according to (3.41); the space must include, by definition, the space of linear polynomials P_1 , as a subspace. This subspace, however, has the same dimension. This implies the two spaces coincide: the linear triangular virtual element being exactly the same as the linear triangular finite element.

These same curves are also presented in terms of the number of degrees of freedom, instead of the element size, in Figure 48 and Figure 49 for St. Venant's; and Figure 50 and Figure 51, for Prandtl's formulation.

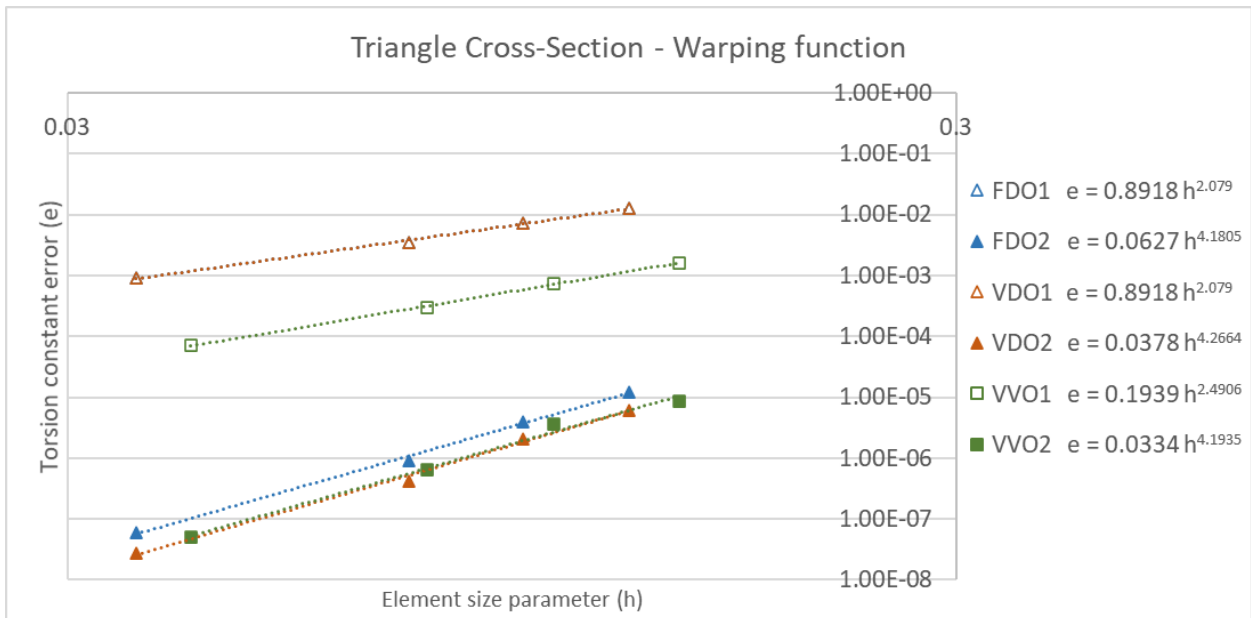
When presented in terms of the degrees of freedom the differences between the two methods are accentuated. Virtual elements have more degrees of freedom than finite elements, the only exception being linear triangular elements, which have the same number. The same observations regarding convergence and convergence rate are valid and visible in the different slopes of the fitting curves.

Figure 44. Convergence curve (log-log plot), for element size, of square cross-section and St. Venant's formulation.



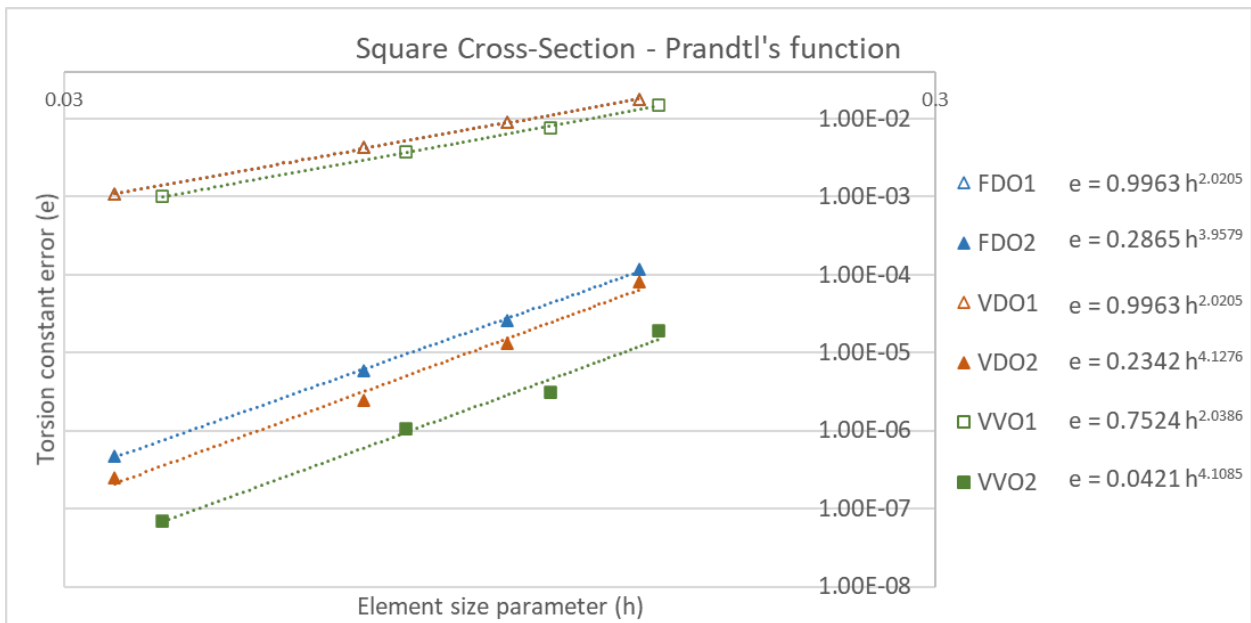
Source: Author.

Figure 45. Convergence curve (log-log plot), for element size, of triangle cross-section and St. Venant's formulation.



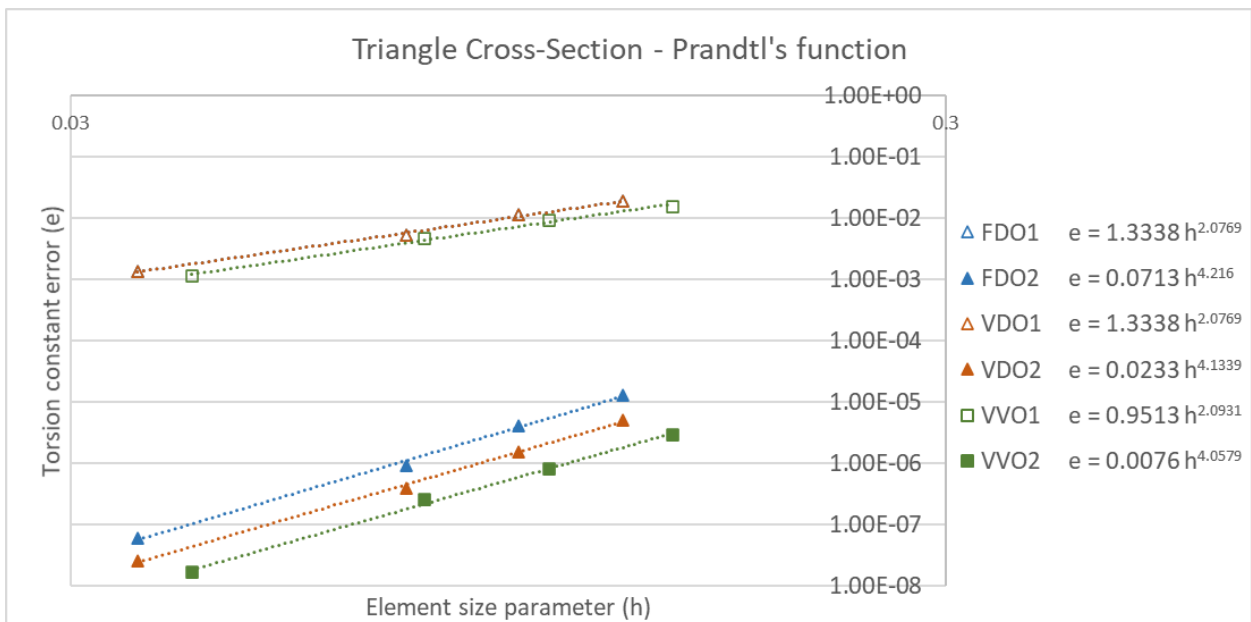
Source: Author.

Figure 46. Convergence curve (log-log plot), for element size, of square cross-section and Prandtl's formulation.



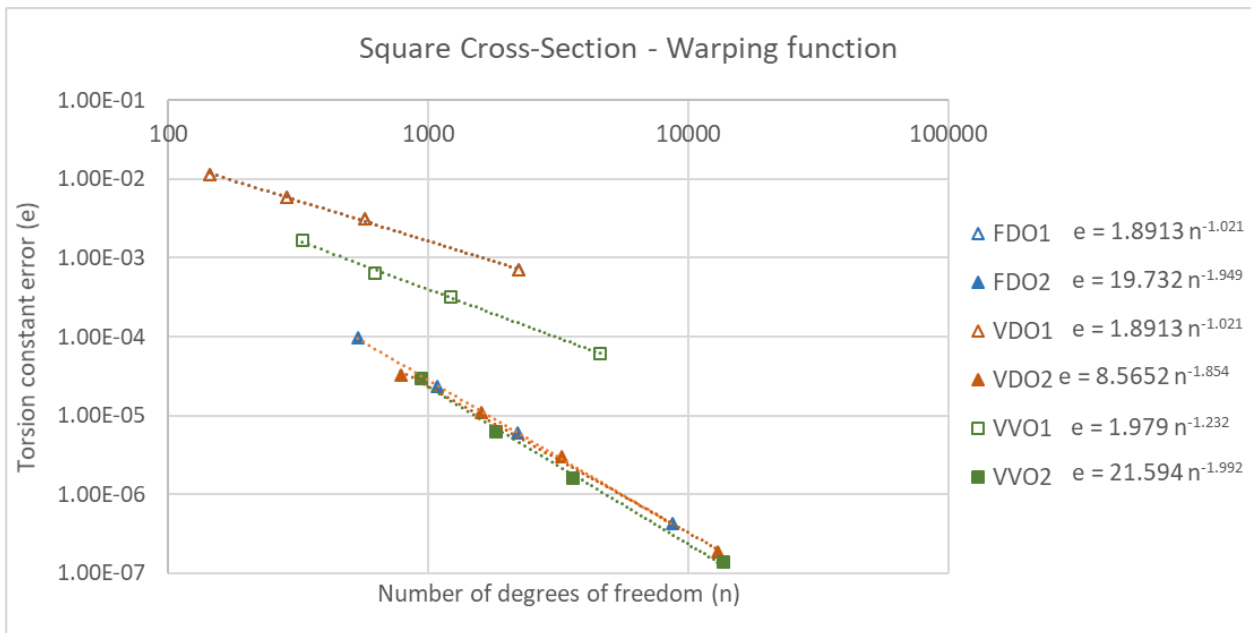
Source: Author.

Figure 47. Convergence curve (log-log plot), for element size, of triangle cross-section and Prandtl's formulation.



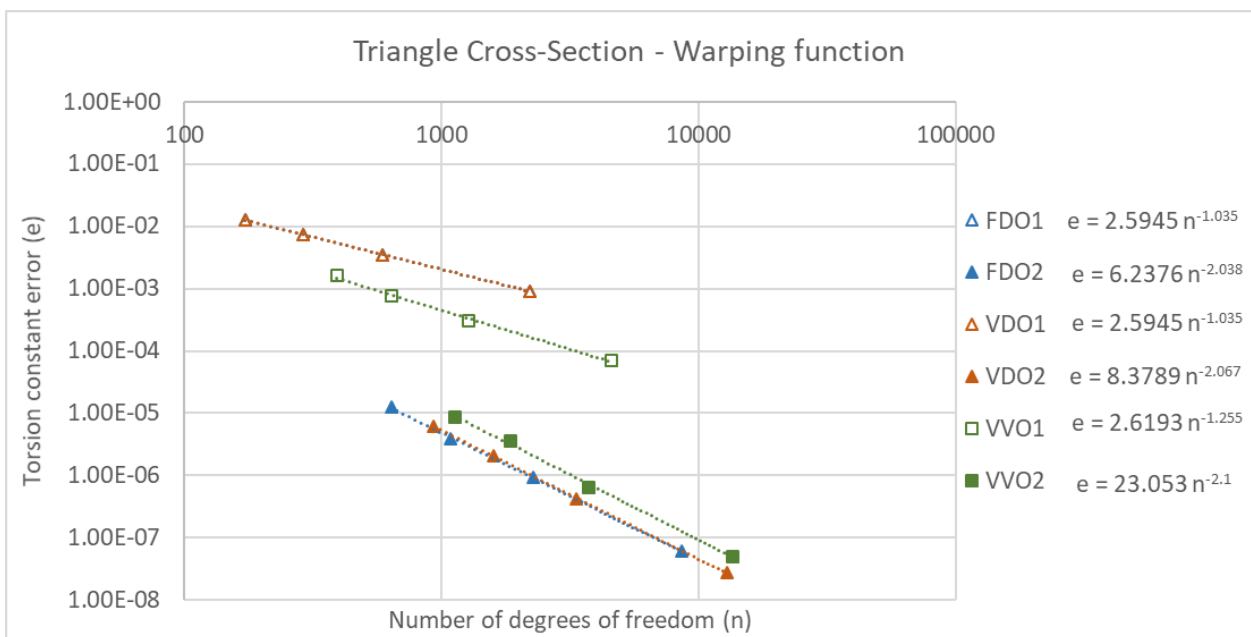
Source: Author.

Figure 48. Convergence curve (log-log plot), for number of degrees of freedom, of square cross-section and St. Venant's formulation.



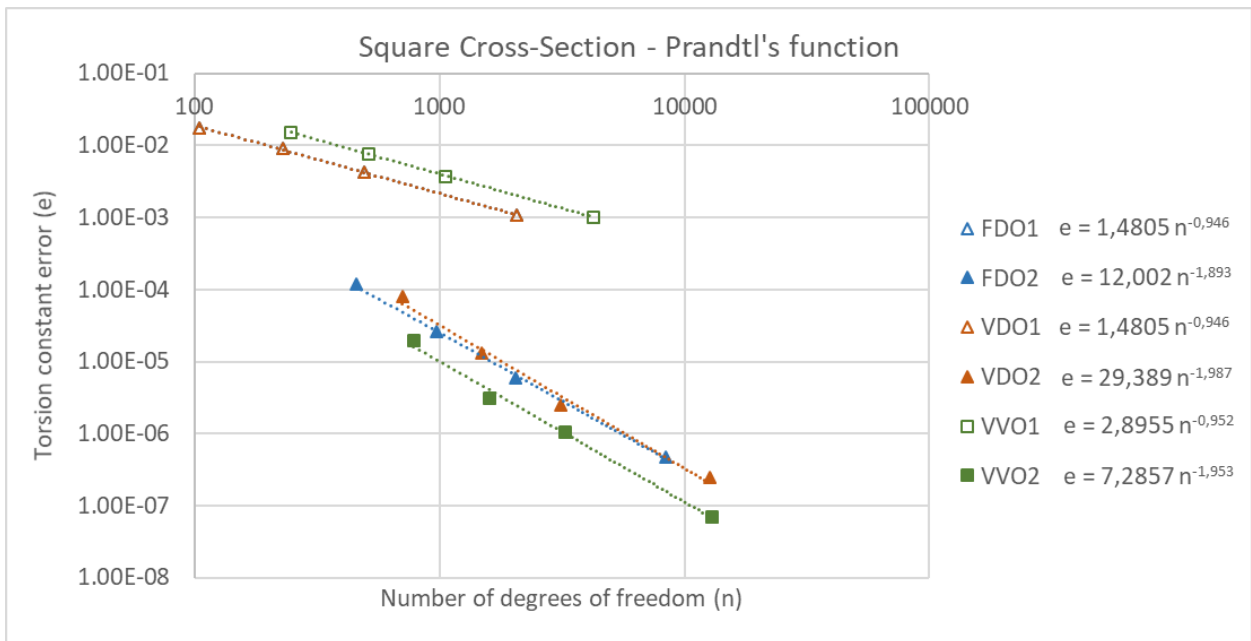
Source: Author.

Figure 49. Convergence curve (log-log plot), for number of degrees of freedom, of triangle cross-section and St. Venant's formulation.



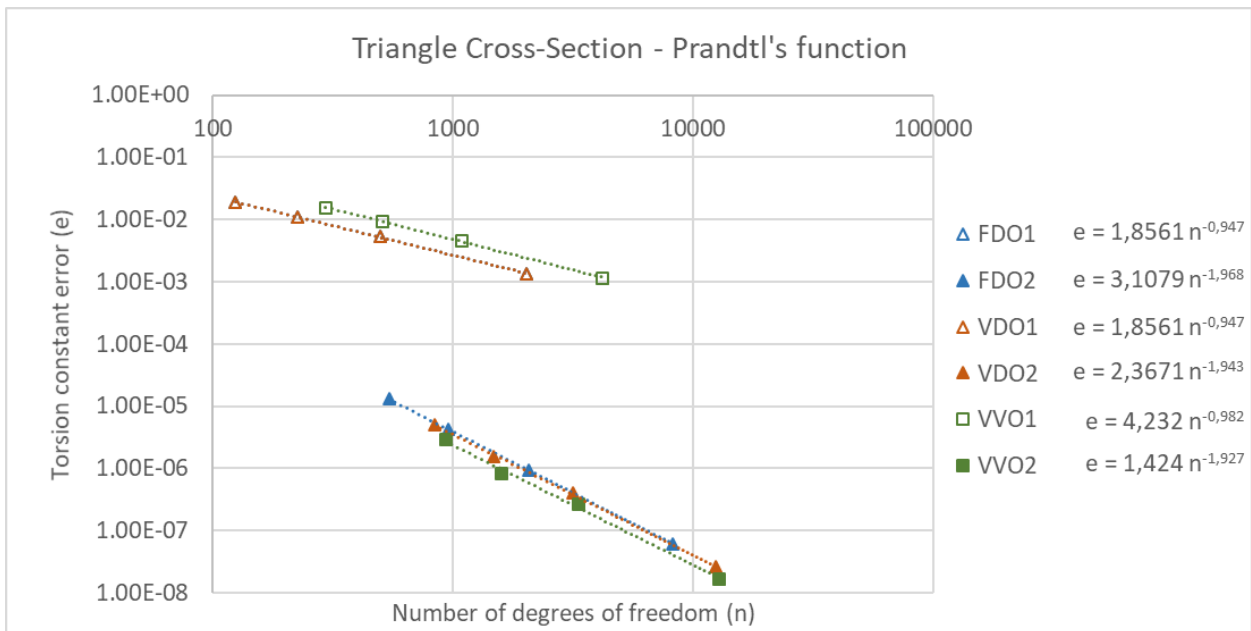
Source: Author.

Figure 50. Convergence curve (log-log plot), for number of degrees of freedom, of square cross-section and Prandtl's formulation.



Source: Author.

Figure 51. Convergence curve (log-log plot), for number of degrees of freedom, of triangle cross-section and Prandtl's formulation.



Source: Author.

4.4. Conclusions

The application was an overall success for comparing both methods.

All solutions produced seemed adequate in qualitative visual inspection, as well as the associated stresses.

Both numerical methods converged to the analytic answers with the coincidence of convergence properties presented in the literature. The element-size and element order parameters have provided the expected behavior regarding the torsion constant error of the numerically approximated solutions.

Different element geometries led to different curves, but no conclusion could be drawn regarding an overall advantage, as the number of degrees of freedom also increased and the convergence rates were not consistently better for any geometry.

As for the different formulations, each presented advantages and disadvantages. Prandtl's formulation provides easier boundary conditions, and the torsion constant is obtained in more direct manner. For domains containing holes, however, Prandtl's formulation requires the use of constraint imposition techniques, such as the penalty method or Lagrange multipliers, to enforce the constancy of the value of the internal boundary. Whereas for St. Venant's formulation this is just a matter of applying the same boundary conditions for two different boundaries.

The overall conclusion for the method comparison is that, for this specific problem, the virtual element method presents no clear advantage, leading instead, to a greater number of degrees of freedom. This was already expected, as the focus of this work consists in the advantages the method provides in another context: contact simulations.

5. Second application – Plane strain linear elasticity

This study serves the purpose of validating the implementation of the Virtual Element Method for plane linear elasticity, as presented in section 3.3.7.

In the first application, the validation was made through qualitative comparison of the results with the FEM's, and quantitative comparison via convergence curves. In that case, the torsion constant provided a convenient error measure.

In this application, the convergence curve analysis is left out due to Cook's membrane having a singularity on the upper left corner.

5.1. Goals

This application's objective is to ensure the adequate implementation of the method via two benchmark tests usual in this context: a simple traction patch test and Cook's membrane.

The goals are to show the exactness of the method for polynomial solutions (patch test) and a qualitative assessment of the results for a problem with non-polynomial solution (Cook's membrane).

5.2. Methodology

The methodology for this application is similar to that presented in section 4.2, leading to analog nomenclature for the different simulations performed. The main difference is that the triangular meshes have not been used for virtual elements, to reduce the number of results without loss of information. The element shape is now associated with the method. This is shown in Figure 52.

Figure 52. Illustrative example of the codification for the simulations of (a) the patch test and (b) Cook's membrane.

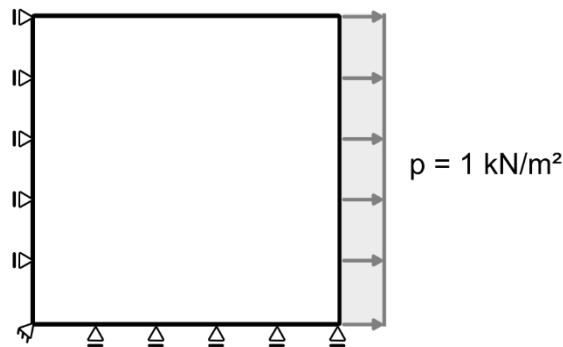


Source: Author.

5.2.1. Patch test

This test consists in modeling a solid of square cross-section subjected to uniform tension. This is achieved by the load and boundary conditions as illustrated in Figure 53. This is a simple problem, for which the displacements depend on the elastic parameters, but the stresses are constant for all the domain $T_{11} = p$ and $T_{12} = T_{22} = 0$. This test is considered successful for a given simulation if the numerical results correspond to the analytic ones, up to the usual residue of floating-point operations.

Figure 53. Patch test configuration.



Source: Author.

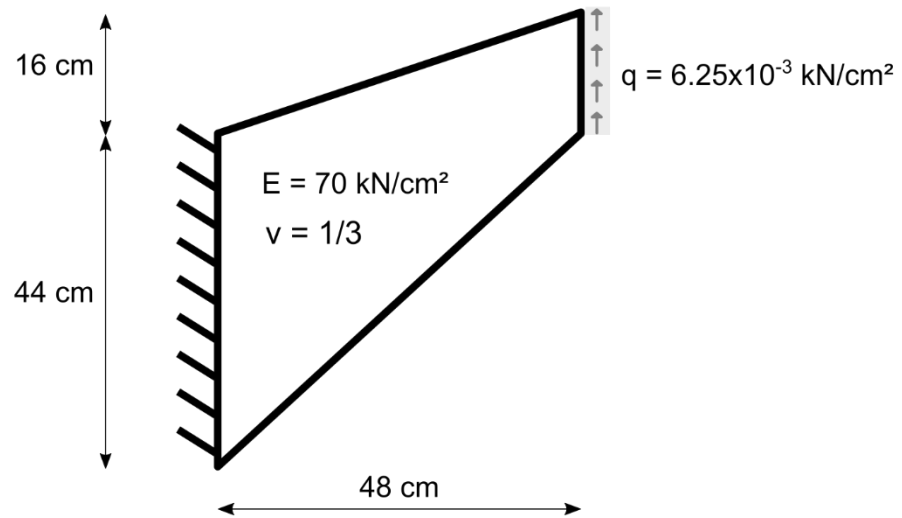
This test is conducted for one level mesh refinement, thus the lack of element size identifier in the codification examples of Figure 52. Therefore, the only free parameters are the method, element geometry (as explained in section 4.2.4) and element order.

5.2.2. Cook's membrane

This is a problem dominated by shear and bending, commonly used as benchmark for plane elasticity problems. The problem configuration is shown in Figure 54. The elastic parameters and load were taken from Artioli, et al. [86].

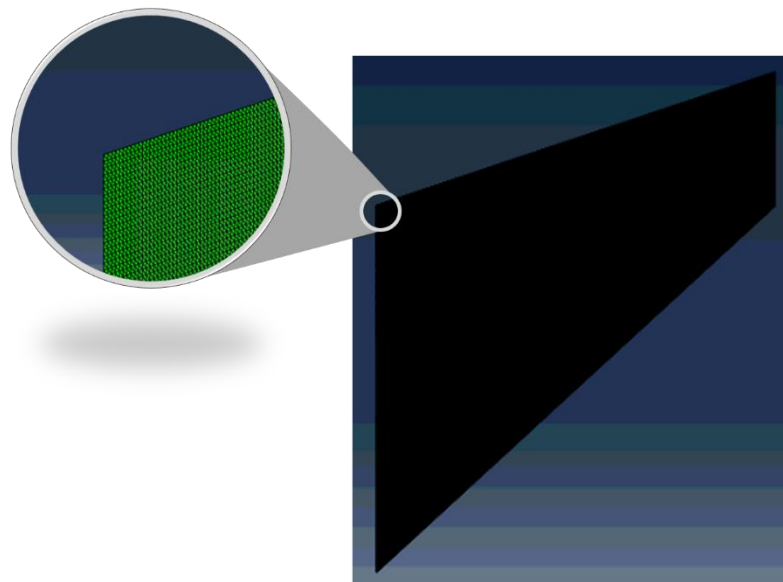
This problem does not have analytic solution; therefore, the basis of comparison is established via an overkilled solution. This solution was established with the use of commercial finite element analysis software ABAQUS Standard 2018 [116]. The problem was solved using an extremely refined mesh, with over 300.000 quadratic triangular elements, as illustrated in Figure 55.

Figure 54. Cook's membrane problem configuration.



Source: Author.

Figure 55. Mesh for the overkilled solution using ABAQUS Standard 2018.



Source: Author.

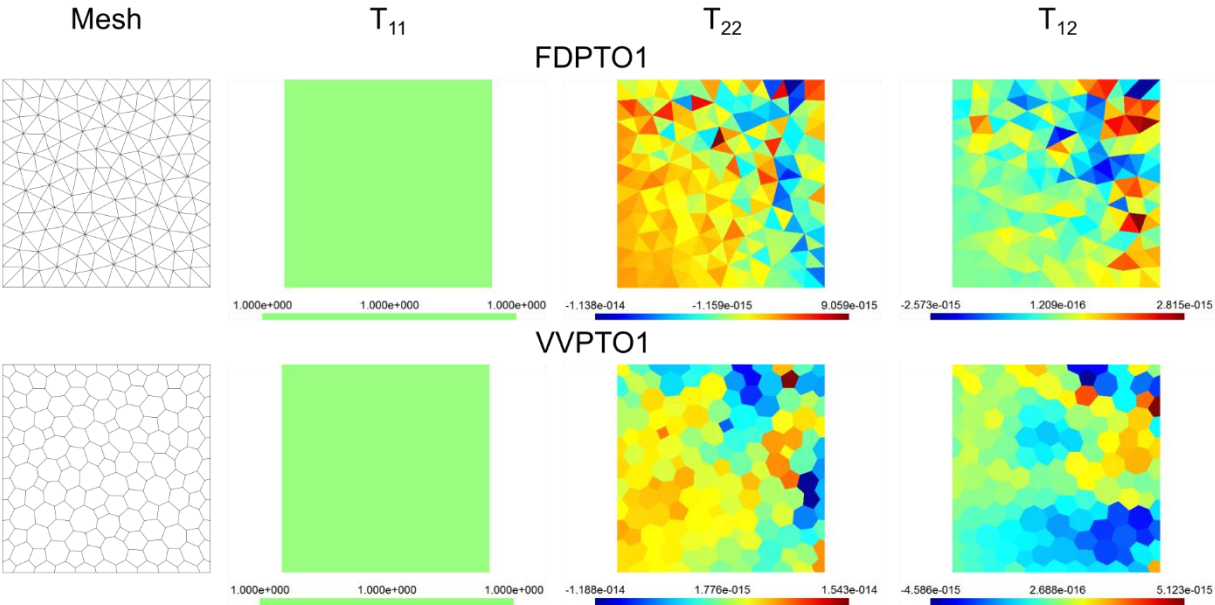
5.3. Results

5.3.1. Patch test

The results for the patch test simulations were all successful and virtually identical, the only variation being the numerical error on the stresses that should be null. To avoid

repetition, the mesh and stresses are shown for only two simulations: FDPTO1 and VVPTO1. These are presented in Figure 56.

Figure 56. Patch test results for FDPTO1 and VVPTO1 in kN/cm^2 .



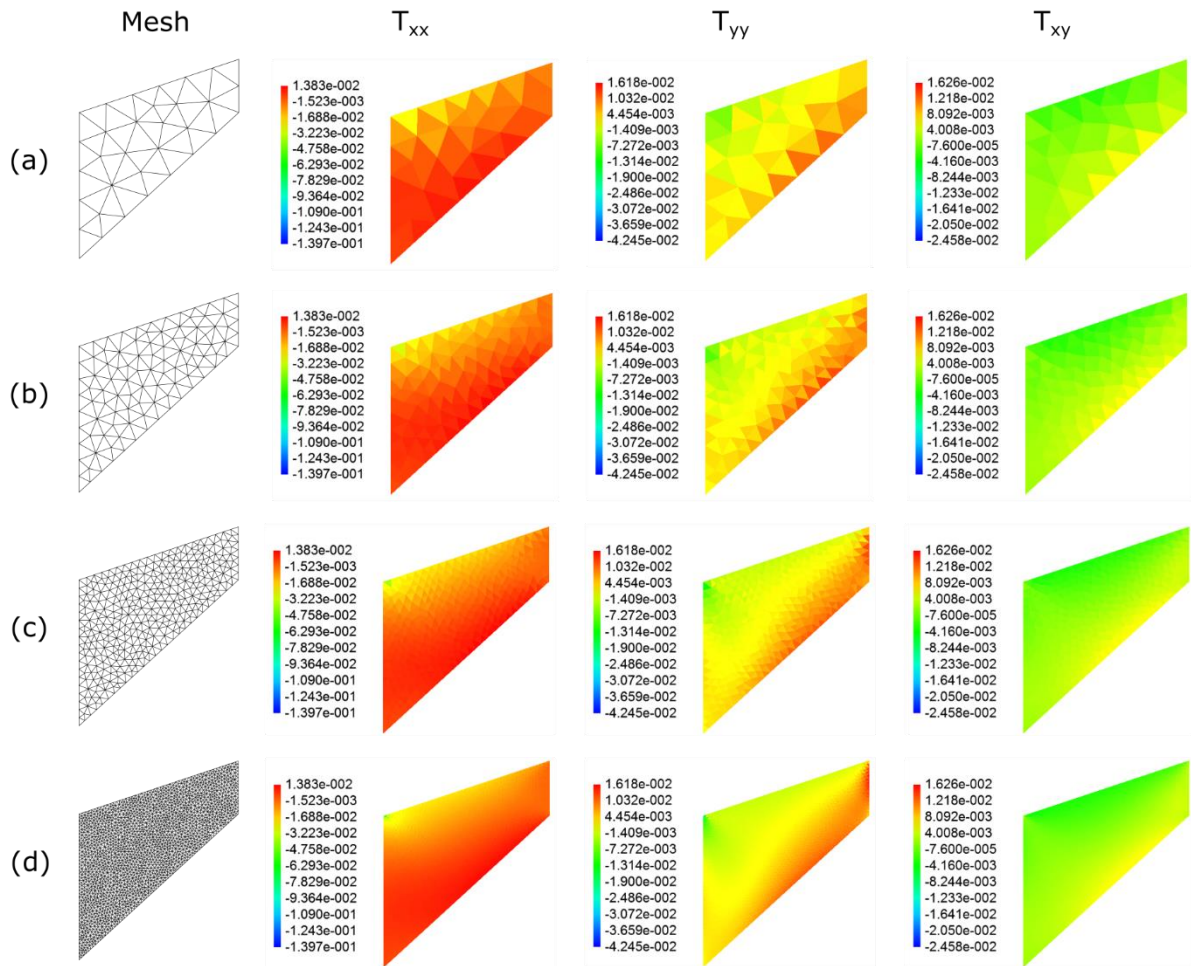
Source: Author.

5.3.2. Cook’s membrane

The results are presented in a series of figures. The first four figures show the results for the four mesh variations for linear finite elements (Figure 57), quadratic finite elements (Figure 58), linear virtual elements (Figure 59), and quadratic virtual elements (Figure 60). These illustrate a clear convergence tendency.

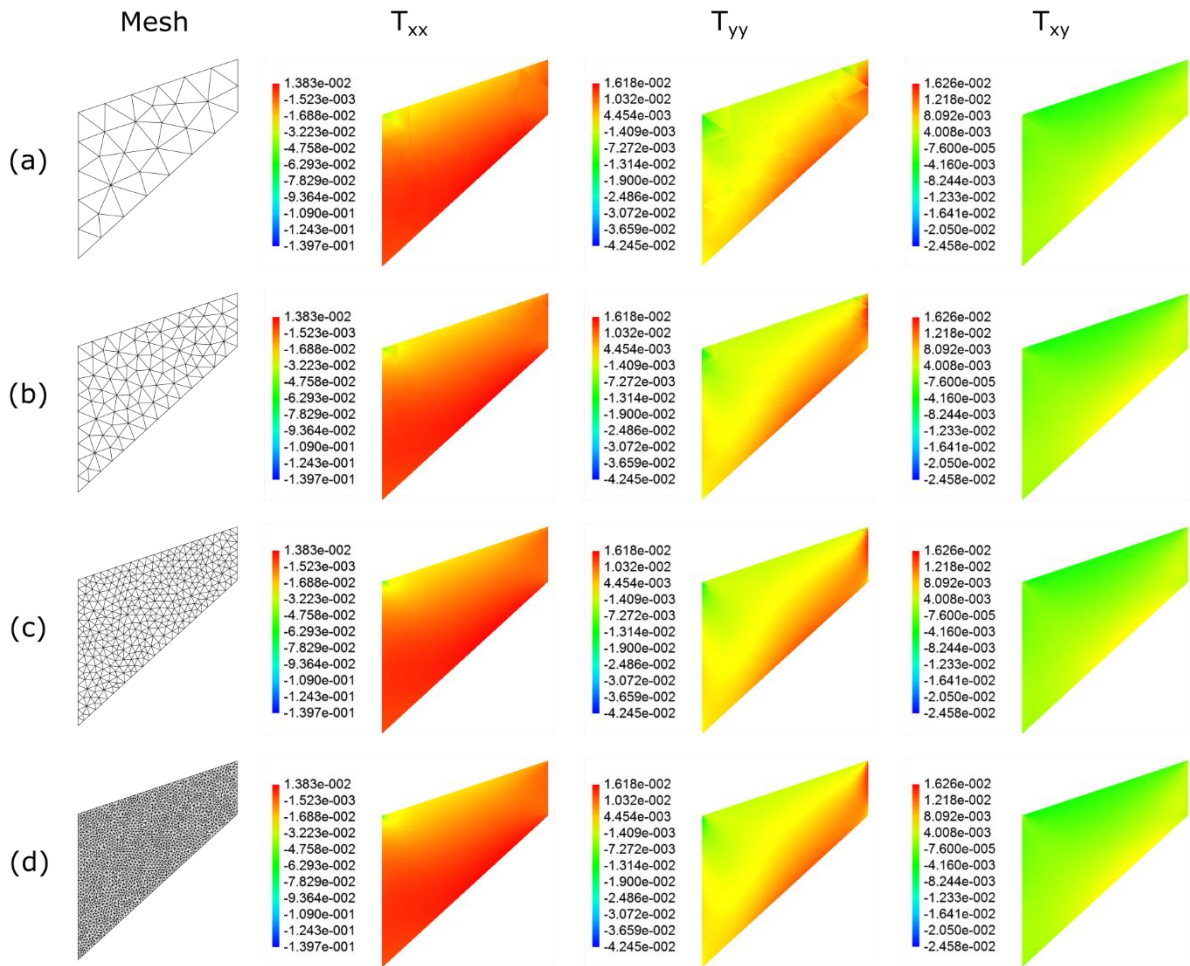
The fifth figure (Figure 61), shows a comparison between the most refined quadratic solutions for the finite (b) and virtual (c) element methods and the overkilled ABAQUS solution (a), to show that the convergence is indeed to the solution.

Figure 57. Cook's membrane solutions with linear finite elements for the meshes: (a) M1, (b) M2, (c) M3, and (d) M4, in kN/cm^2 .



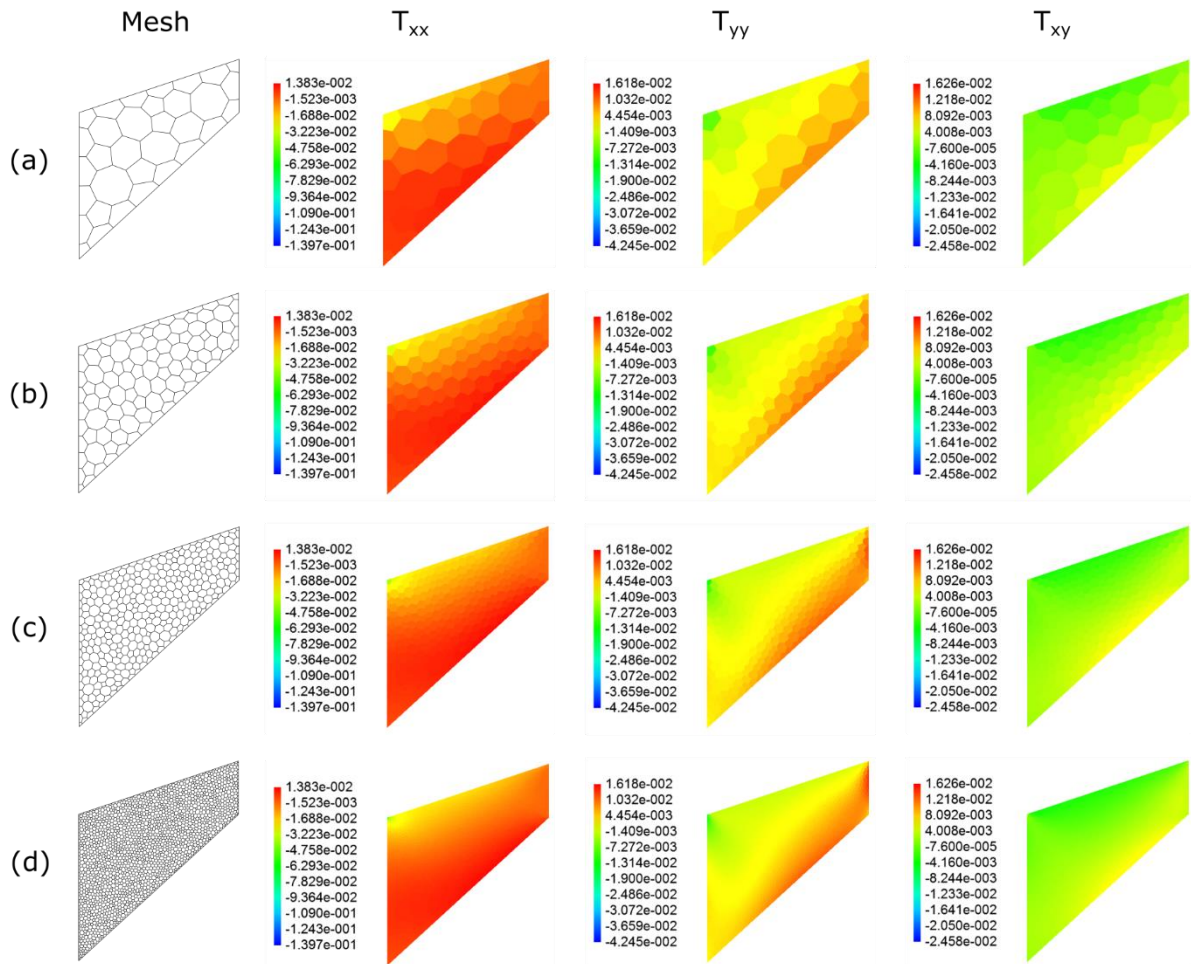
Source: Author.

Figure 58. Cook's membrane solutions with quadratic finite elements for the meshes: (a) M1, (b) M2, (c) M3, and (d) M4, in kN/cm^2 .



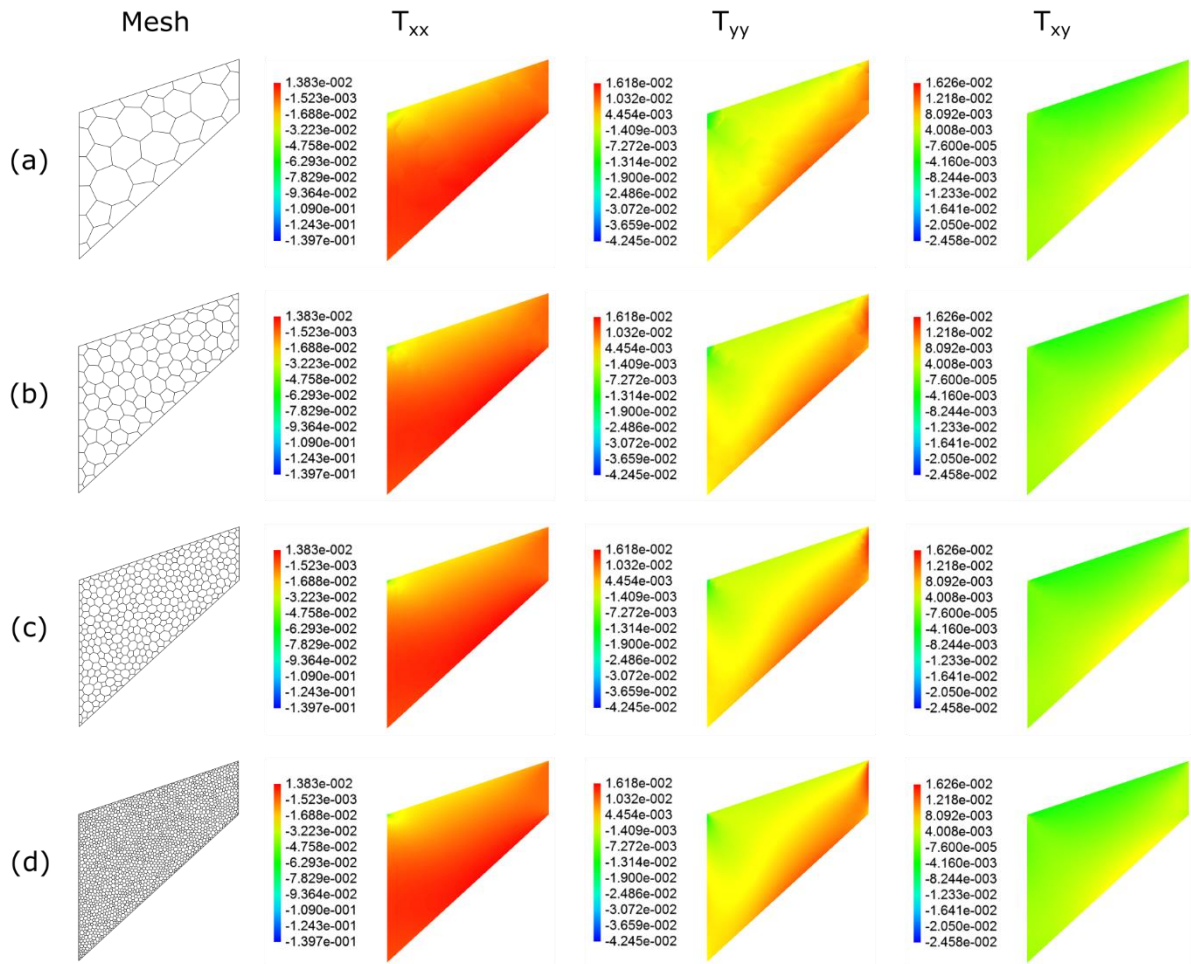
Source: Author.

Figure 59. Cook's membrane solutions with linear virtual elements for the meshes: (a) M1, (b) M2, (c) M3, and (d) M4, in kN/cm^2 .



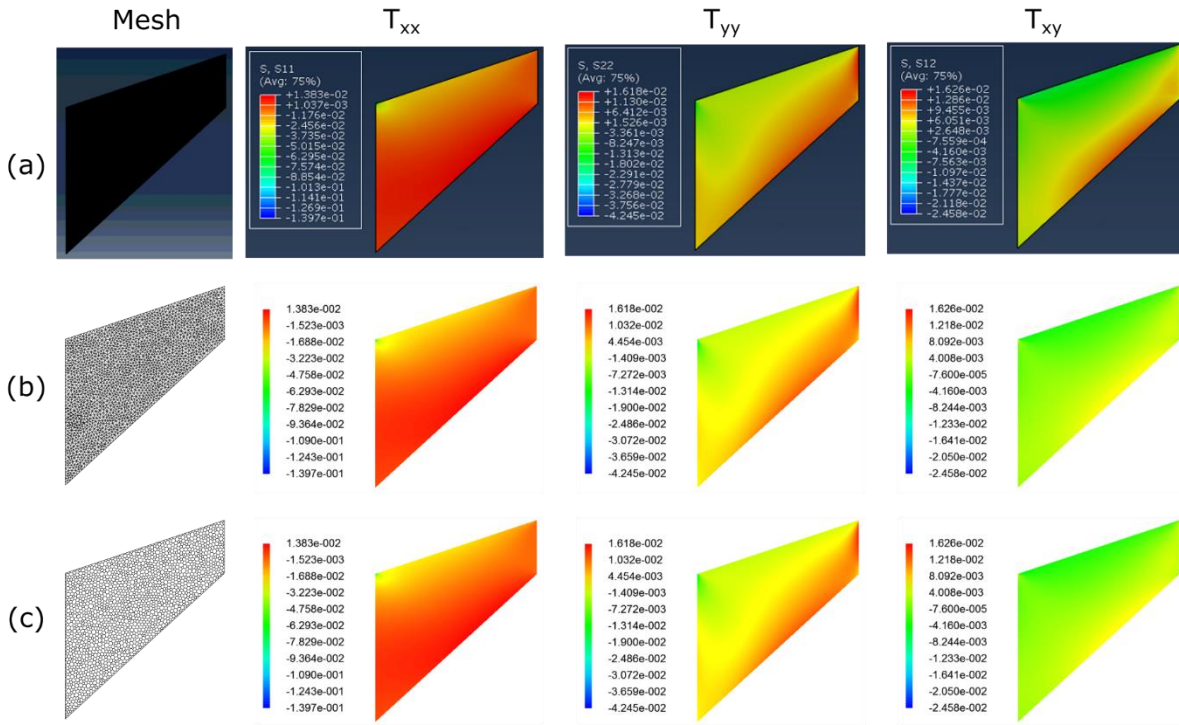
Source: Author.

Figure 60. Cook's membrane solutions with quadratic virtual elements for the meshes: (a) M1, (b) M2, (c) M3, and (d) M4, in kN/cm^2 .



Source: Author.

Figure 61. Cook's membrane results for (a) ABAQUS, (b) FCM4O2, (c) VCM4O2, in kN/cm^2 .



Source: Author.

5.4. Conclusions

Both problems seem to indicate a successful implementation of the method for plane linear elasticity problems.

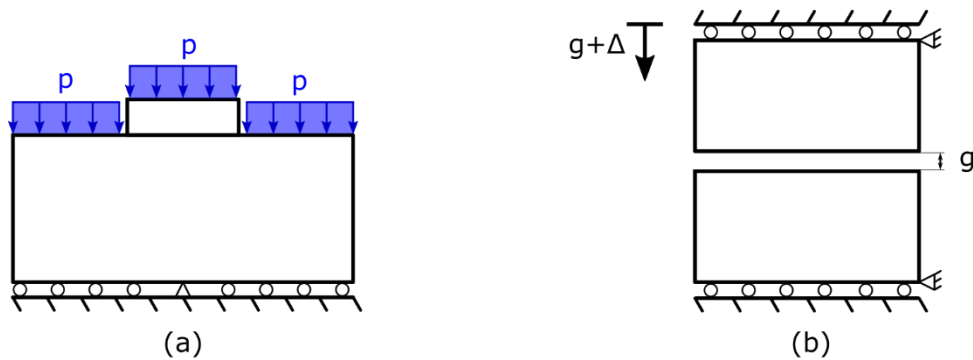
The patch test was passed flawlessly, a good indicator of a correct implementation. In Cook's membrane, the results from FEM and VEM were practically the same, and both were remarkably similar to the overkilled solution.

6. Third application – Contact benchmarks

This application uses two important contact benchmarks to validate the Node-to-Segment and Penalty method contact implementation.

The first benchmark is the modified version of the contact patch test. This version was proposed by Crisfield [114] as a modification on the original version by Taylor and Papadopoulos [117]. The original version has bodies of different sizes and is based on the application of distributed forces, whereas the modified version has two equal bodies and is based on prescribing displacements. Both versions are illustrated in Figure 62.

Figure 62. Contact patch tests. Original version (a) and modified version (b).



Source: Author.

Any patch test has, by definition, a polynomial solution. For a method to pass the patch test, it should match the exact polynomial answer. El Abbasi and Bathe [103] have shown that, albeit stable under the inf-sup condition, the Node-to-Segment discretization does not pass this test. Zavarise and De Lorenzis [104] does a thorough investigation on this in the case of linear elements, a brief recount of their findings can be found in section 3.5.8.

The second benchmark, herein denoted Hertz problem, is a problem designed to have analytical solution in Hertz's contact theory. This problem consists in the contact between two parallel cylinders, which in the plane strain framework are modelled as two semi-circles. The theory, previously discussed in section 2.6, and particularized for this specific problem in subsection 2.6.2, provides analytical solutions for this benchmark.

6.1. Goals

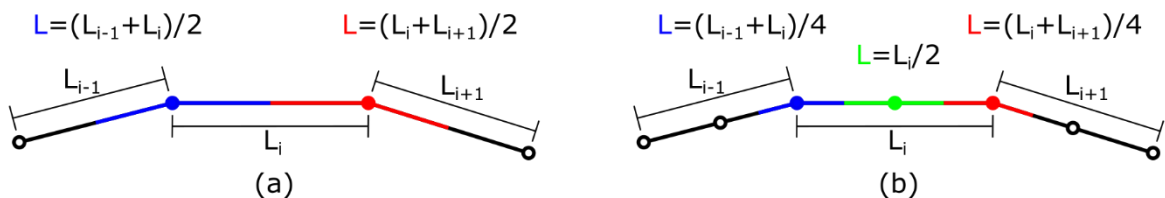
This application will simulate two problems widely used in the literature to compare contact formulations. The objective is to ensure the author's implementation is working correctly, leading to results like those found in the literature, analytic solutions, and commercial software.

6.2. Methodology

This application follows a similar structure to the previous ones. For both benchmarks a series of simulations are performed with varying parameters such as: the numerical method, element shape, element-size parameter, order of polynomial interpolation, etc. The element orders for contact and structural elements are always the consistent.

Another procedure common to both problems is the estimation of the contact pressure. The recovery of a pressure distribution from the contact forces can be tricky, especially for interpolations using polynomial using second or higher order polynomials. The weak form contribution from each contact pair consists in a contact force in the slave node, and a set of contact forces on the master segment nodes. The master segment information may present oscillations due to the shape functions adopted, as explained in section 3.5.8. The contact forces on slave nodes are used to present an approximation of the contact pressure distribution, by considering that each node's force is the equivalent to a constant pressure distribution over an influence width. This influence width is considered as indicated in Figure 63.

Figure 63. Influence width for each type of slave node: Linear elements (a) and quadratic elements (b).



Source: Author.

Although the slave surface is treated as an unbiased set of nodes, the weights induced by the high order shape functions in the master surface will generate some oscillations on

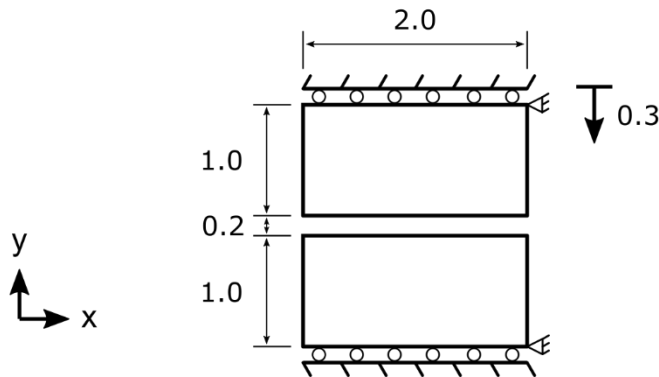
the results for the slave surface. Nevertheless, the slave side shows smaller oscillations, and is used to estimate the contact pressure.

The following two subsections address each of the benchmark problems individually. In them, a more in-depth explanation of the problem is found, along with the varied parameters and codification employed for this section. The methodology for the contact patch test is presented in subsection 6.2.1, and for the Hertz problem in subsection 6.2.2.

6.2.1. Contact patch test

The general configuration for this test was presented in Figure 62, however a more informative version is presented in Figure 64. The two rectangles are free to move in the horizontal direction except for one point each. The upper rectangle is pressed against the bottom one by a prescribed displacement which would lead to a total penetration $\Delta = 0.1 \text{ cm}$.

Figure 64. Contact patch test configuration, dimensions in *cm*.



Source: Author.

Both bodies are made of the same material, emulating the properties of steel, with units consistent with kilonewtons and centimeters, i.e., $E = 20,000 \frac{\text{kN}}{\text{cm}^2}$, $\nu = \frac{1}{3}$.

Due to the freedom in the horizontal direction and lack of friction in the contact model, only vertical normal stresses appear. The analytical solution corresponds to a constant value for this stress as presented in (6.1).

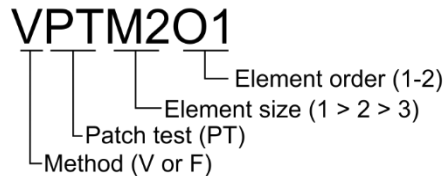
$$T_{yy} = -\frac{E}{1-\nu^2} \frac{\Delta}{2} = -1125 \frac{\text{kN}}{\text{cm}^2}, \quad T_{xx} = T_{xy} = 0 \frac{\text{kN}}{\text{cm}^2}. \quad (6.1)$$

For this problem, the varying parameters on the simulations are:

- Numerical method – Finite (F) or Virtual (V) elements. Element shape is implied, triangulations are used for finite elements and Voronoi meshes for virtual elements.
- Element size – Three variations, where M1 is the coarsest and M3 is the finest. The meshes will be illustrated along with the results.
- Element order – Linear (O1) or quadratic (O2).

These are also summarized in the codification adopted for the simulations, illustrated in Figure 65.

Figure 65. Codification for simulations of the contact patch test.



Source: Author.

The element-size is homogeneous, but different on each rectangle. This is done to avoid matching meshes, which lead to a special case in which the method may have trouble converging. This special case consists in a slave node changing its master segment every iteration, instead of settling for their shared point. Even though a small tolerance has been introduced to avoid this, it is best to employ nonmatching meshes to avoid this altogether. The meshes are shown along with the results in section 6.3.1.

The top of the lower box is chosen as the master surface, and the bottom of the upper box as the slave surface. A penalty parameter $\epsilon = 10^6$ was adopted for all meshes.

As this test has a well-defined coordinate system orientation, the stresses shown in the results section are the components associated with the directions illustrated in Figure 64.

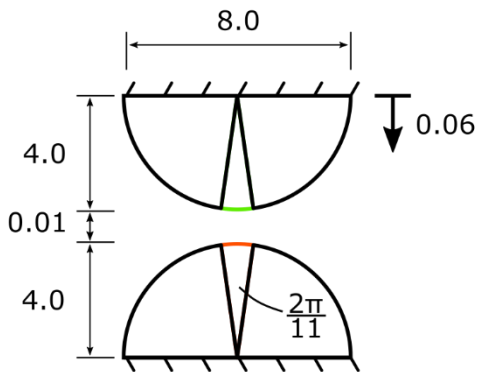
6.2.2. Hertz problem

The problem consists of two parallel cylinders being pushed against each other. It fits the criteria for plane strain modelling, leading to a two-dimensional problem involving the cross-sections of the cylinders (circles). The symmetrical nature of the shapes allows

modelling each body as a semi-circle, this facilitates the prescription of the boundary conditions and displacements.

For this application only one geometric configuration is adopted, with the two cylinders sharing the same radius of 4 units, as illustrated in Figure 66. The displacement is prescribed such that the total penetration, were contact not considered, would amount to $\Delta = 0.05$. The material adopted is the same as for the contact patch test ($E = 20,000 \frac{kN}{cm^2}$, $\nu = \frac{1}{3}$).

Figure 66. Hertz problem configuration. Colors in boundary refer to the triangulation algorithm's element-size parameter. Dimensions in *cm*.



Source: Author.

As stated in section 2.6, Hertz's theory is of a local nature, and the results it provides are restricted. This leads to two problems: first, there is no formula relating the prescribed displacement to quantities that determine the contact pressure; and second, the analytical results for the stresses are restricted to one line (the axis of symmetry of the contact pressure). The solution provided for both these problems is the use of the commercial Finite Element Analysis (FEA) software to get a reliable solution. Which, in turn, provides the missing parameter to fully determine analytical expressions for the contact pressure and the stresses along the symmetry line, as explained in section 2.6.2.

The chosen commercial FEA software is ABAQUS [116]. The problem is modelled using its segment-to-segment contact algorithm, which provides a solution free of contact-algorithm-induced oscillations. The mesh employed for this reference model is exceptionally refined, to generate a reliable overkilled solution. This reference numerical

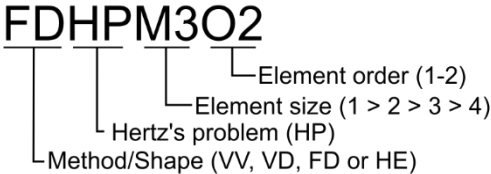
solution also serves to provide stress solutions along the bulk of the two bodies, complementing the analytical results along the symmetry line. These serve as basis for comparison with analog results from the Node-to-Segment contact with FEM and VEM.

Regarding the simulations in author’s code. For this problem, the varied parameters are:

- Numerical method: Finite elements (F), Virtual elements (V) or Hybrid (H), the last one being both types of elements used in the same mesh.
- Element shape: Delaunay triangulations (D), their associated Voronoi meshes (V) and a special case of a Delaunay triangulation with an edge refinement (E), which will be explained further in this section.
- Element size: Four variations are adopted with increasing refinement, M1 is the coarsest and M4 is the finest.
- Element order: Linear (O1) or quadratic (O2) elements.

The codification (Figure 67) summarizes the configuration of parameters adopted for each simulation. The combinations of method and order are summarized in Table 8 below.

Figure 67. Codification for simulations of Hertz’s problem.



Source: Author.

Table 8. Numerical method used relative to element shape and order.

Element Shape/Order	Linear (O1)	Quadratic (O2)
Triangulation (D)	F	F and V
Voronoi polygons (V)	V	V
Edge-refined triangles (E)	-	H

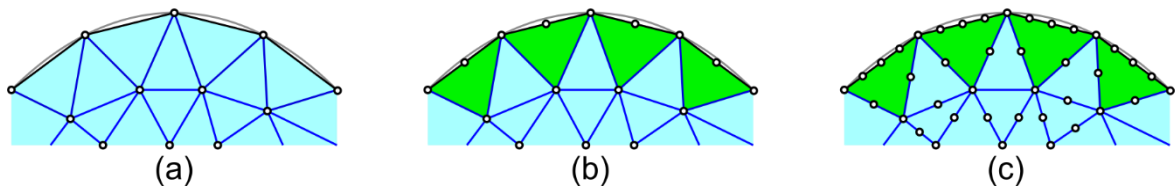
Source: Author.

The meshes used are not homogenous. They are much finer in the region predicted for contact, roughly estimated as an angle of $\frac{2\pi}{11}$. This is done to minimize the impact of approximating a circle by straight segments, while being able to capture the local effects of the contact interaction, without requiring solving an unnecessarily large linear system

of equations at each step, i.e., maintaining a reasonable number of degrees of freedom for the problem at hand. The element sizes in fine regions of both semi-circles are also slightly different to avoid the matching of the meshes in contact.

This wider exploration of method and element shape combinations requires some explaining. Originally the combinations were the same as those for the contact patch test in the previous section (6.2.1), i.e., triangles for finite elements and polygons for virtual elements. As will be seen in the following sections, the results for quadratic elements showed important differences for the more refined meshes. This led to an investigation on the reasons for this. Adopting quadratic virtual elements of triangular shape (VD combination) should indicate an influence of the internal degree of freedom. The edge-refined mesh (Figure 68) should provide means to test if more nodes on the contact boundary are the source for this difference. The use of both numerical methods at once in this case is meant to avoid additional internal degrees of freedom in the bulk of the bodies, whereas only the influence of additional nodes on the surface is being evaluated. Additionally, this served as a proof of concept for fully integrating both methods for surface-based interactions, in this case contact. The inspiration for this edge-refinement came from the two aligned edges resulting from the Voronoi mesh generation, illustrated in Figure 69, and explained in the following paragraphs in the context of explaining the choice of penalty parameter for each mesh. This refinement transforms each triangle on the boundary into a quadrilateral with two aligned edges.

Figure 68. Edge refinement illustration. Original mesh (a), linear refined mesh (b) and quadratic refined mesh (c). Finite elements in blue, virtual elements in green.



Source: Author.

The triangulation algorithm used in GMSH takes as input an element-size parameter associated with each point that generates the geometry. For the coarse region, black in Figure 66, the parameter is $els = 0.5$ for all meshes. For the regions in orange (els_{master}) and green (els_{slave}), the parameters vary for each mesh and are presented in Table 9. For

the Voronoi meshes, although not generated with GMSH, a parameter with the same interpretation (size of individual edge of the element) is provided.

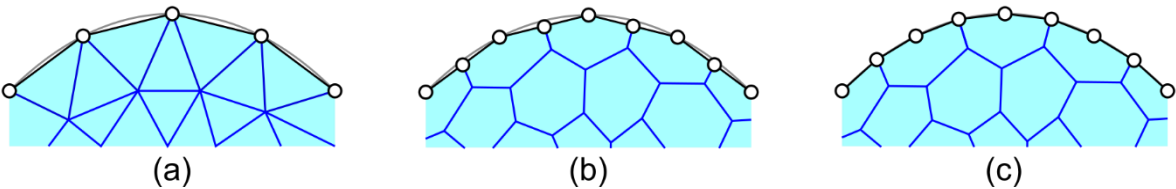
Table 9. Mesh element-size parameters.

Mesh	$els_{master}^{Delaunay}$	$els_{slave}^{Delaunay}$	$els_{master}^{Voronoi}$	$els_{slave}^{Voronoi}$
1	6.00e-02	5.00e-02	3.00e-02	2.50e-02
2	3.00e-02	2.50e-02	1.50e-02	1.25e-02
3	1.50e-02	1.25e-02	7.50e-03	6.25e-03
4	7.50e-03	6.25e-03	3.75e-03	3.13e-03

Source: Author.

The element-size parameters associated with the Voronoi meshes are shown as half the value of the associated Triangulation because the Voronoi tessellations are generated using the procedure presented in section 3.3.6. This algorithm inserts new nodes in the middle of the edges while retaining the boundary nodes of the input mesh to preserve its full outline. Therefore, each boundary segment in the input Delaunay mesh becomes two segments, each with half of the original length. This leads to another caveat in this polygonal mesh generation procedure, which is that straight segments continue straight even when representing curved surfaces. Although there is a gain in boundary resolution (twice as many segments), it does not imply a better representation of the intended geometry (in this case a circle). This, as illustrated in Figure 69 (a) and (b), is another potential source for variations in the results. However, upon later experimentation with manually corrected meshes, Figure 69 (c), it was found to be of no impact on the results.

Figure 69. Illustration of triangular mesh (a), generated Voronoi mesh (b), and manually fixed Voronoi mesh (c).



Source: Author.

The penalty parameter is arbitrary, and its choice must take into consideration the trade-offs explained in section 3.5.7.1. The range for this parameter that leads to satisfying results are correlated with the size of the partition in the slave surface, such that fine

meshes are more sensitive to the penalty parameter. Therefore, this is reflected in the penalty parameters adopted for each mesh/method for this application, i.e., the penalty for the virtual elements is always half the one for finite elements. The parameters adopted are shown in Table 10.

Table 10. Penalty parameters [kN/cm].

Mesh	$\epsilon_{Delaunay}$	$\epsilon_{Voronoi}$
1	1.00e+05	5.00e+04
2	8.00e+04	4.00e+04
3	6.40e+04	3.20e+04
4	5.12e+04	2.56e+04

Source: Author.

One result of interest is the contact pressure distribution. Its evaluation when the Node-to-Segment discretization is employed, however, is a problem on its own. As stated in section 3.5.8, the discretization treats one surface as a set of points, finding an equivalent pressure field requires reinterpreting that surface as continuous. This falls out of the scope of the method.

For the linear case, an estimation of the pressure distribution is easily computed as the point's contact force divided by an estimated width of contribution. In this case, this width of contribution is the same as shown in Figure 24. Furthermore, this can be done for either surface (master or slave), leading to good results.

For quadratic elements, the analog estimation does not perform so well. The two surfaces' forces behave in different ways due the different nature of their discretization. The forces in the master surface will tend to follow the pattern dictated by the weighting of the nonlinear shape functions and the variation in the shape of the pressure field. Whereas the slave surface is considered as a set of individual points, it still presents considerable oscillation because of the reasons exposed in section 3.5.8, as well as the induced oscillation in the penetrations due to the higher order shape functions in the master surface. Nevertheless, in the absence of a better procedure, this estimation method was employed using the slave surface contact forces in both cases.

Another result of interest is the stress distribution resulting from the contact interaction. The elected stress results to be shown are the minimum principal stress (σ_3), the Von Mises stress (σ_{vm}) and the maximum tangential stress (τ_1). The first shows the maximum compressive stress in the contact interface. The second is the distortional stress, a result of interest for inelastic analyses such as plasticity. The last one is the shear stress, its maximum another result predicted in Hertz's theory (2.75).

6.3. Results

In the following subsections the results and their discussion are presented for each benchmark.

6.3.1. Contact patch test

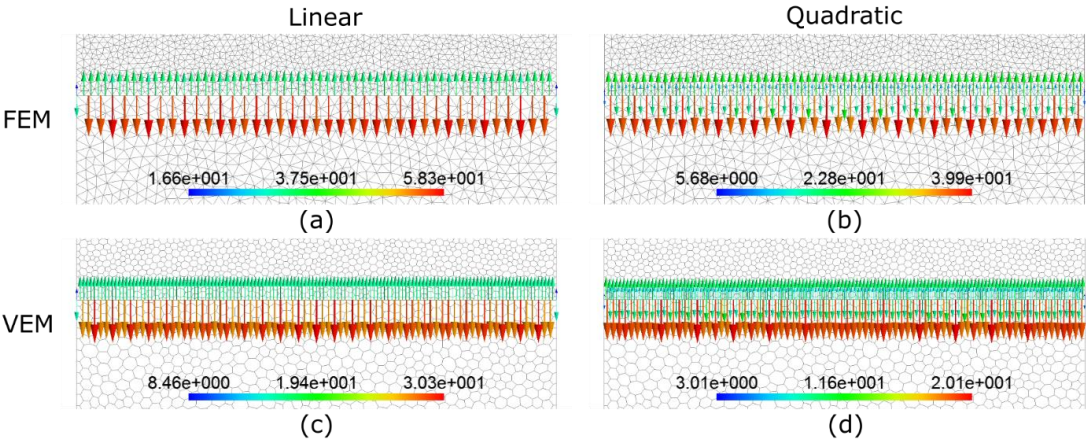
The results are segregated by method and order (the structural and contact elements being always of the same order). The results for contact forces are illustrated in Figure 70 for the finest meshes and summarized for all configurations in Figure 71. Next come the stress results in the following four figures: in Figure 72 and Figure 73 are the results for linear finite and virtual elements, respectively; whereas those for quadratic finite and virtual elements are in Figure 74 and Figure 75.

As expected, in no simulation the patch test was satisfied exactly. Oscillations appeared both in the stresses and the contact forces. The discretization leads to loads in the slave surface that are mechanically inequivalent to the uniform pressure this problem induces. Furthermore, these loads are transferred only to one master element per node, which might lead to incorrect transference. These reasons have been explored more in depth in section 3.5.8.

In the case of quadratic methods, the node-asymmetric nature of the equivalent load (due to quadratic shape functions) coupled with the asymmetric treatment of the surfaces (one as a set of isolated points, and the other as segments under the influence of those shape functions), aggravate this situation. However, the oscillations on the contact forces originated from the shape functions do not necessarily amplify the oscillations in the stresses.

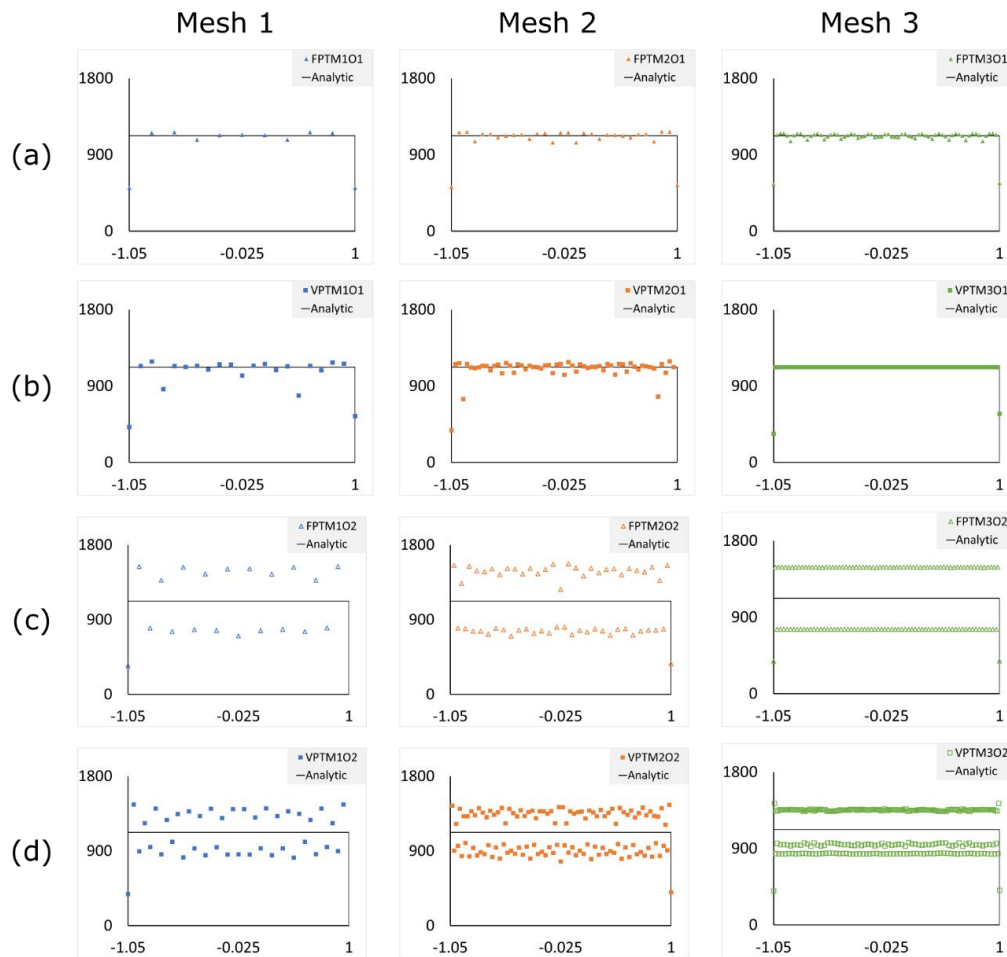
In general, all oscillations seem to diminish as the meshes get more refined. This difference is more noticeable with quadratic elements than linear ones. Another relevant disparity is that of the amplitude of oscillations between finite and virtual elements. The former method leads to a wider amplitude, whereas the latter to a smaller one, these can be noticed in the limits of the color scale.

Figure 70. Contact forces [kN] detail for: (a) FPTM3O1, (b) FPTM3O2, (c) VPTM3O1, and (d) VPTM3O2.



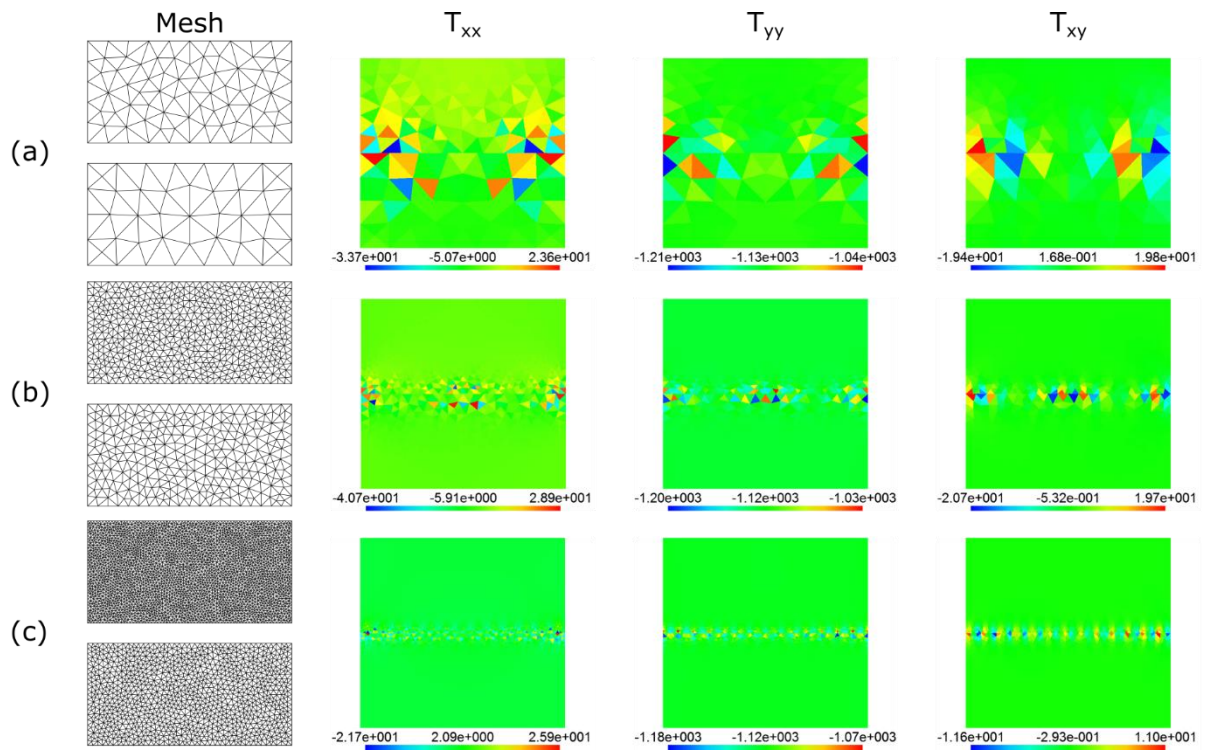
Source: Author.

Figure 71. Estimated contact pressure [kN/cm^2] for Linear (a) and Quadratic (c) Finite Elements, and for Linear (b) and Quadratic (d) Virtual Elements.



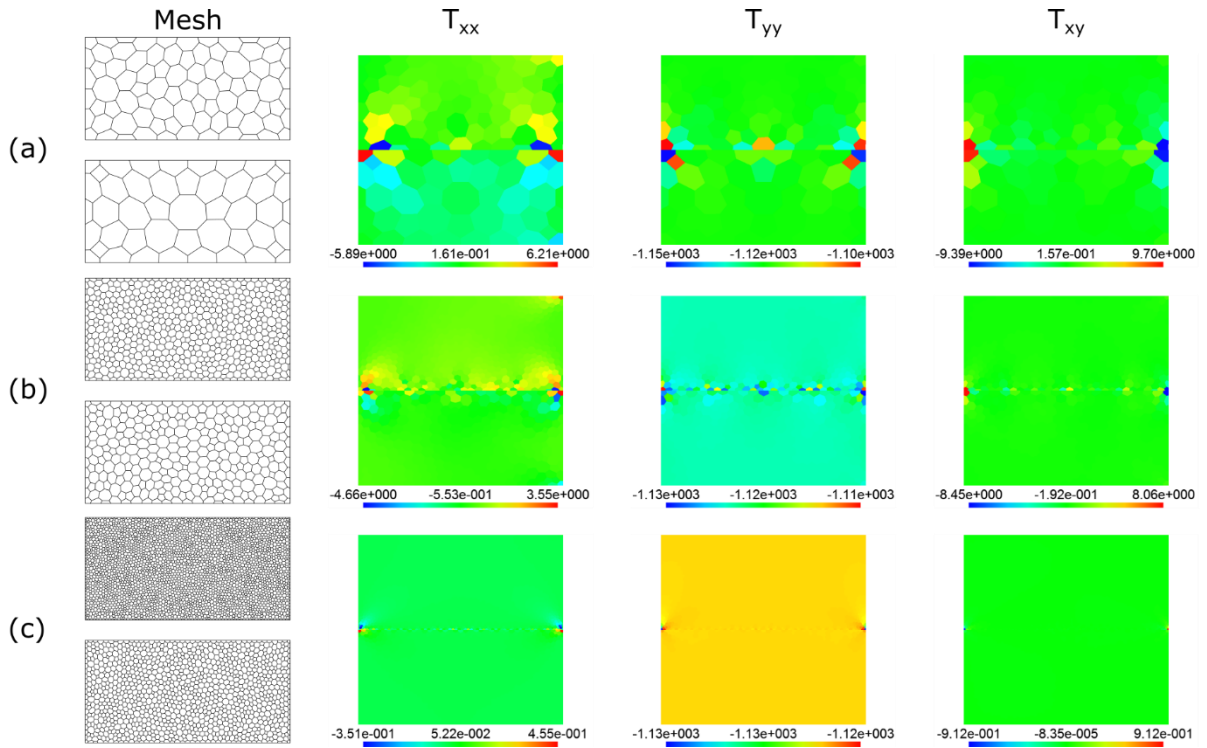
Source: Author.

Figure 72. Contact patch test results [kN/cm^2] for linear finite elements: M1 (a), M2 (b) and M3 (c). The bottom box is the master surface, and the top box is the slave one.



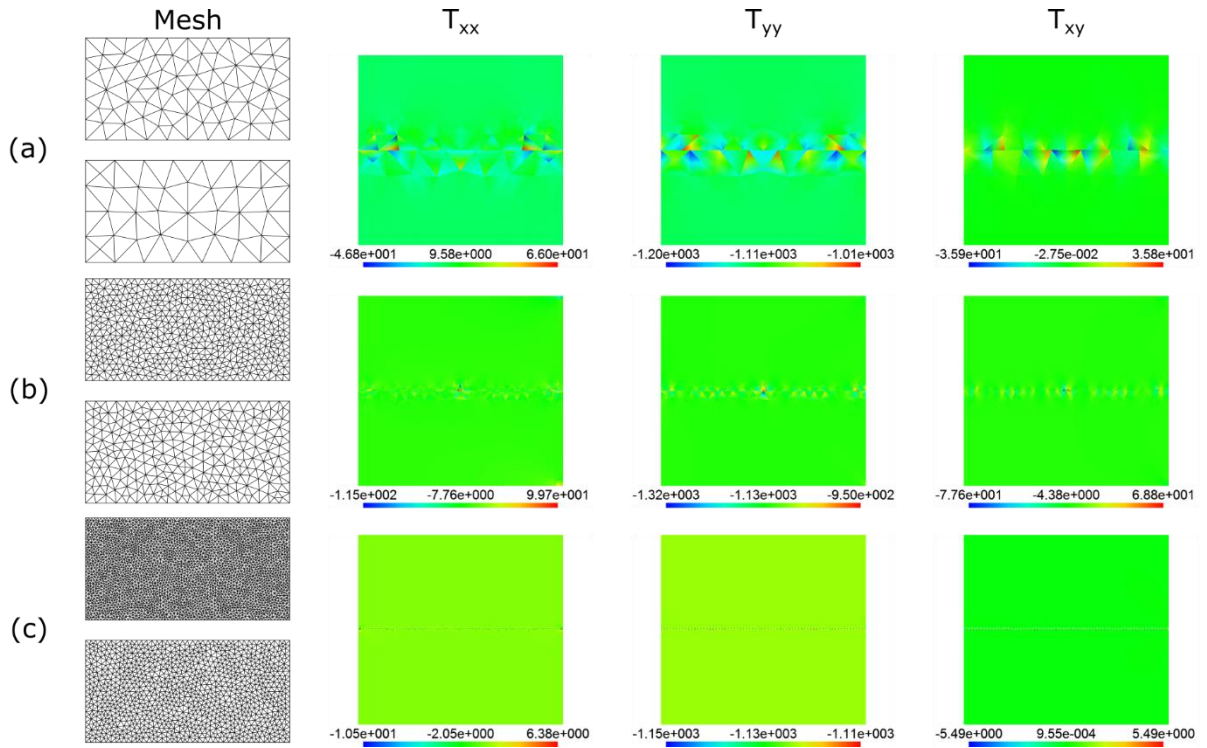
Source: Author.

Figure 73. Contact patch test results [kN/cm^2] for linear virtual elements: M1 (a), M2 (b) and M3 (c). The bottom box is the master surface, and the top box is the slave one.



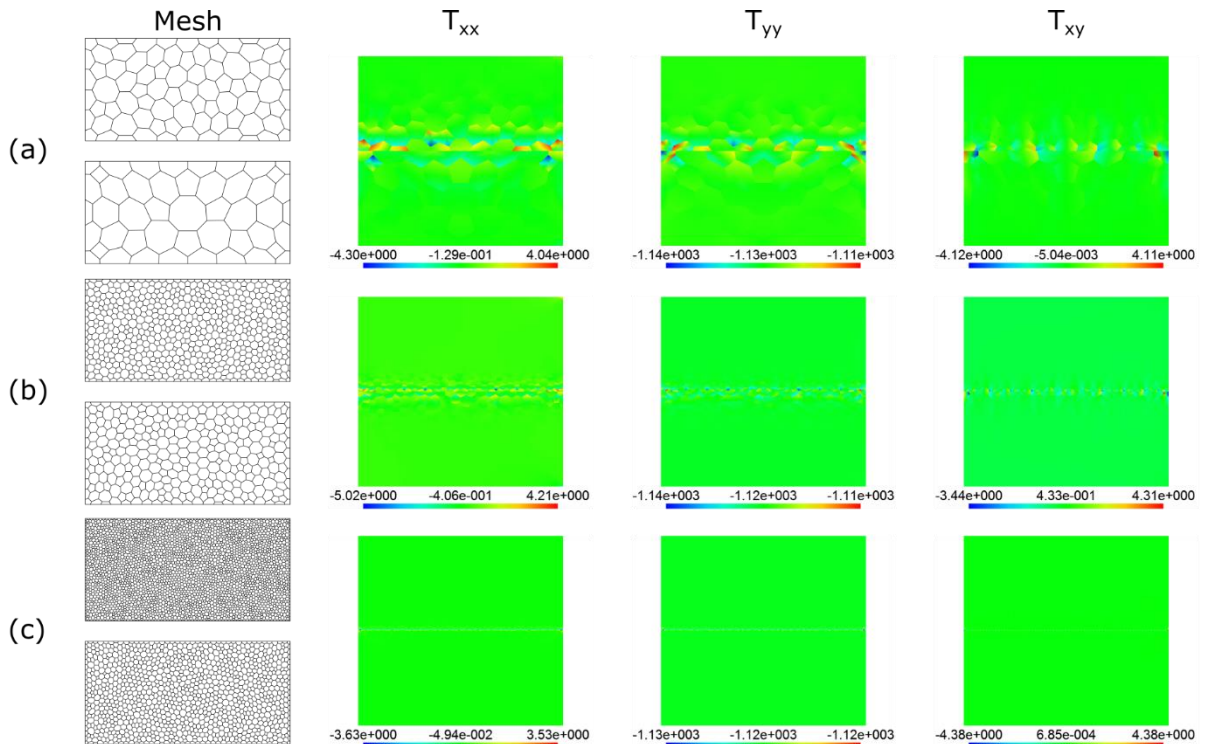
Source: Author.

Figure 74. Contact patch test results [kN/cm^2] for quadratic finite elements: M1 (a), M2 (b) and M3 (c).
 The bottom box is the master surface, and the top box is the slave one.



Source: Author.

Figure 75. Contact patch test results [kN/cm^2] for quadratic virtual elements: M1 (a), M2 (b) and M3 (c).
The bottom box is the master surface, and the top box is the slave one.



Source: Author.

6.3.2. Hertz problem

This section is structured as follows. First, reference solutions are established. These are composed of the numerical solution from the ABAQUS simulation and the analytical expressions for the quantities of interest induced by this solution. Once these reference scenarios are defined, begin the analyses of the author's results. These analyses are ordered from the more local results (where the analytical solution serves as reference) to the more global ones (where comparison is established using the ABAQUS' numerical solution). The first analysis regards the contact pressure distribution and the second one concerns the stresses in the symmetry line of the problem. Both have analytical predictions. The third analysis inspects the stress results in general, then examines their extrema to evaluate the amplitude of oscillations in each case.

As explained in the methodology section, the analytical solution is not fully determined by the problem configuration. The local nature of Hertz's theory requires knowledge of either the total transferred force, the maximum pressure, or the size of the contact area. As this

problem is displacement-based, neither quantity is known *a priori*. The solution is to obtain this defining parameter from the numerical solution of reference performed using ABAQUS.

The ABAQUS model used a very refined mesh comprising 45.122 nodes and 22.264 quadratic triangular elements. The easiest result to extract from the numerical solution that fully characterizes the Hertzian model is the maximum contact pressure, which coincides with the maximum compressive stress in the contact region ($p_0 = |\min \sigma_3| = 671.51 \text{ kN/cm}^2$). With this quantity determined, the other two are computed from the expressions in Table 2. Those are summarized in Table 11. This scenario is used as a reference Hertz model for the results denoted as analytical.

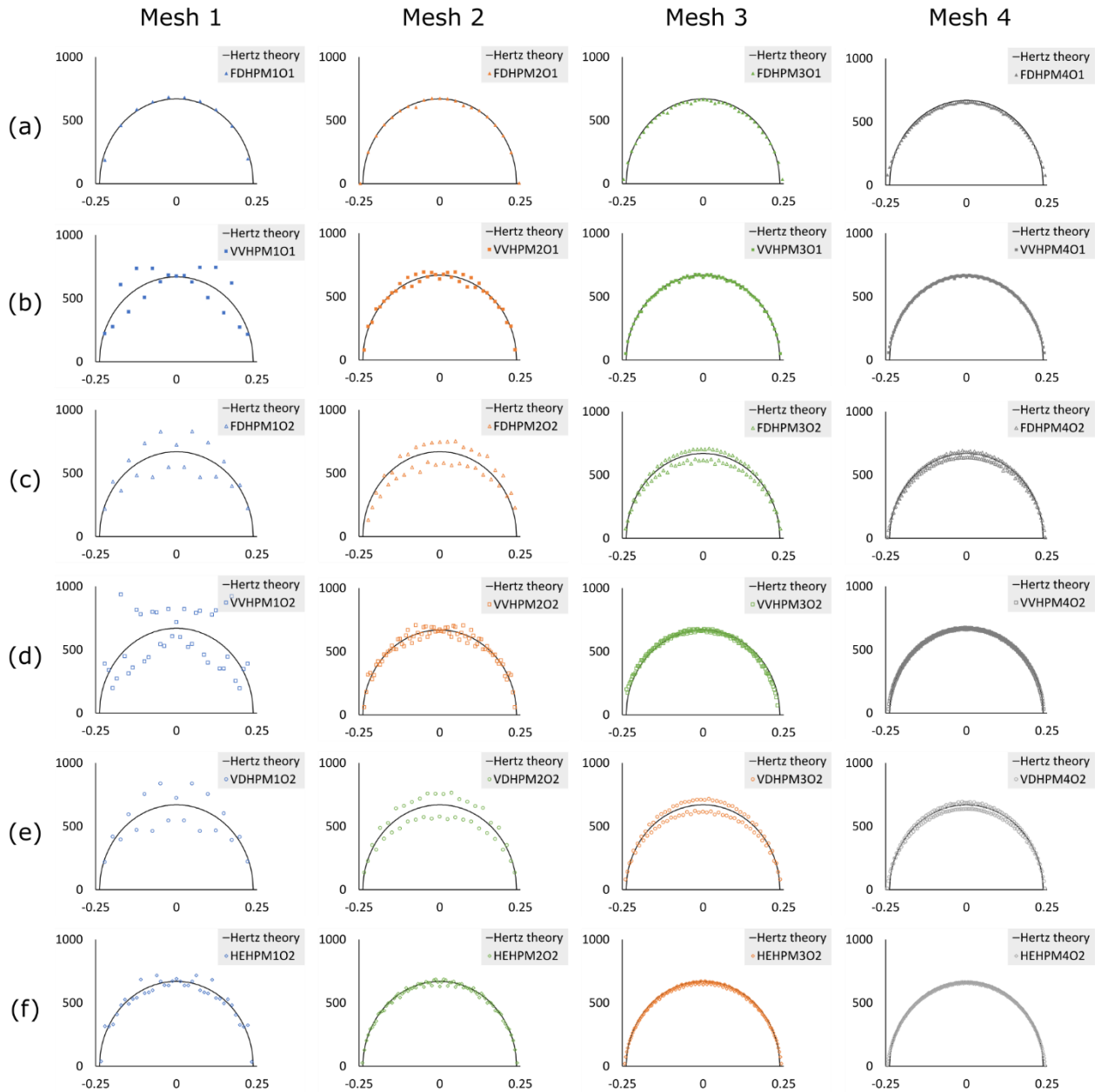
Table 11. Reference results for the Hertz problem.

Configuration	$p_0 \left[\frac{kN}{cm^2} \right]$	$P [kN]$	$a [cm]$
Reference Hertz model	671.51	251.84	0.239

Source: Author.

The contact pressure estimates for all the configurations explored, along with the analytical contact pressure, are illustrated in Figure 76.

Figure 76. Contact pressure estimates [kN/cm^2] for all configurations along with Hertz theoretic reference. Linear FEM (a), Linear VEM with polygons (b), Quadratic FEM (c), Quadratic VEM with polygons (d) and triangles (e), and the Hybrid approach with edge refined mesh (f).



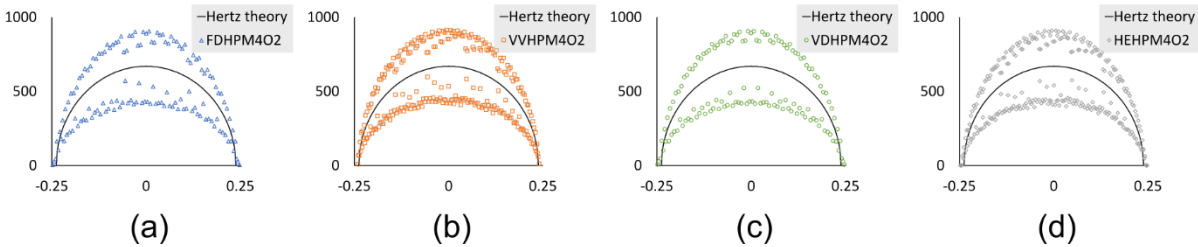
Source: Author.

Linear FEM, Figure 76(a), shows the results closest to the analytical solution for the coarser meshes (1, 2). Nonetheless, some small measure of oscillation can be seen for the finer meshes (3, 4) which seems to be associated with the causes studied by Zavarise and De Lorenzis [104], and already discussed in section 3.5.8. It is worth noting that this method/order combination is the fastest of all those tested. Linear VEM with polygonal

meshes, item (b), leads to some considerable oscillation in the coarser meshes, which vanishes in the finer ones, leading to results like Linear FEM's.

The quadratic methods have the additional problem of the weights induced by the high-order shape functions exacerbating the inherent differences in the discretization of both surfaces. These make the recovery of the pressure distribution much harder, if possible. Nevertheless, the method adopted (described in section 6.2.2) to produce the estimates shown in Figure 76 produces acceptable results, especially for the more refined meshes. To make clearer the reason for estimating the pressure from the forces on the slave surface, the same estimation applied to those of the master surface is shown for the quadratic methods in Figure 77.

Figure 77. Contact pressure estimates [kN/cm^2] based on master-surface forces. Quadratic FEM (a), Quadratic VEM with polygons (b) and triangles (c), and the Hybrid approach with edge refined mesh (d).



Source: Author.

The estimates for quadratic FEM, Figure 76(c), show an oscillation pattern akin to linear VEM's in the coarsest mesh. This similarity is likely to be unrelated. Despite the oscillations' persistence with the mesh refinement, its pattern becomes more homogeneous. Quadratic VEM for polygonal meshes, Figure 76(d), show a similar, yet more intense, oscillation in the coarsest mesh. Yet, as the meshes become finer, the oscillations not only become homogeneous, but they also diminish significantly. This, along with similar behavior in the stress oscillations, was what prompted the additional method/element shape combinations as further investigation.

Quadratic VEM with triangular elements differs from quadratic FEM with the same mesh only by the presence of the internal degrees of freedom. This was hypothesized to be a candidate reason for the different oscillation behavior. This hypothesis was discarded with

the almost identical results both in the pressure estimation and the stresses, as is shown later in this section. These are depicted in Figure 76(e).

Last comes the hybrid approach in the edge-refined mesh. Recall that this mesh consists of triangular quadratic finite elements except on the layer bordering the contact boundary. In this layer are virtual elements with four nodes, consisting of triangular shapes with two aligned edges on the contact boundary. This investigates the hypothesis that the decrease in oscillations came from using elements with more degrees of freedom, i.e., increasing the number of shape functions available. The results in Figure 76(f) show a clear difference, abating even the oscillations in the coarsest mesh, and leading the results that adhere closest to the analytical curve with exception, perhaps, of linear FEM.

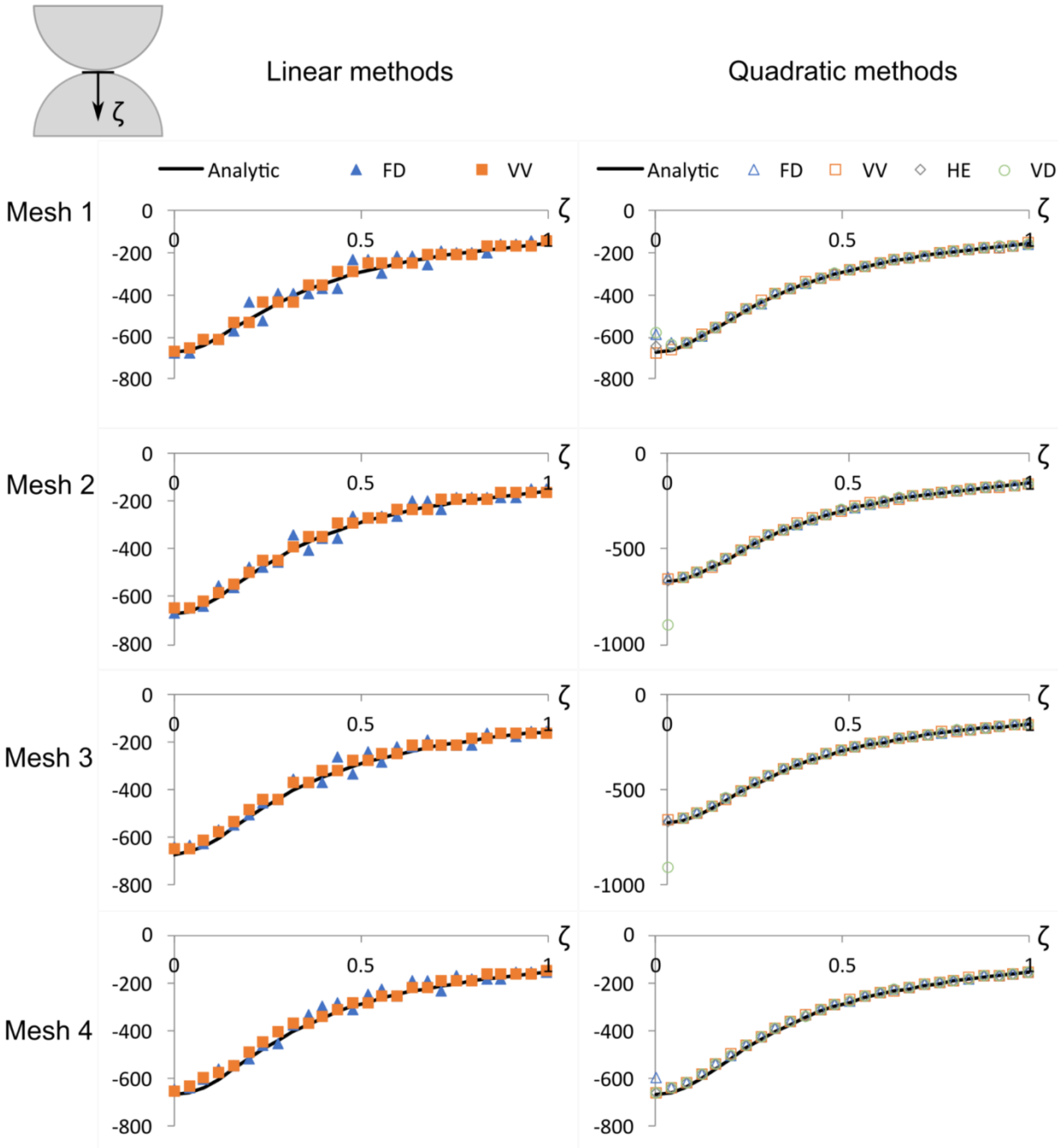
In the vein of reference results provided by the numerically calibrated analytical solution, the next ones analyzed are the stresses predicted by Hertz's theory for the symmetry line of the problem. These results were sampled using the probe function for GMSH's API over equally spaced points along the symmetry line, starting in the contact point and ending 1 cm inside the bulk of the lower circle. Figure 78 depicts the vertical normal stress σ_y in this problem's basis, but which corresponds to σ_z in that adopted in the theory's presentation in section 2.6. Its analytical expression is found in Eq. (2.73), considering the swap of coordinates y and z . Figure 79 presents the horizontal normal stress σ_x , the analytical expression for which is found in Eq. (2.74). Finally, the maximum shear stress τ_1 is shown in Figure 80, and its analytical expression is Eq. (2.75). The problem-related parameters for the analytical curves shown in all cases are those in Table 11.

Overall, the results agree among themselves and are considerably close to the analytical solution. The linear results for coarser meshes seem to follow a ladder-pattern, which is a consequence of the stresses being piecewise constant inside the elements, more than one sample may be taken from the same element. Another observation is that, despite showing some of the best results in the contact pressure estimation, the linear methods do not perform so well for the stress results.

As for the quadratic methods, the results are practically coincident for most of the curve. The exception being the first sampled point, where the FEM and triangular meshes VEM seem to present more noticeable oscillations in all cases. These results show that the

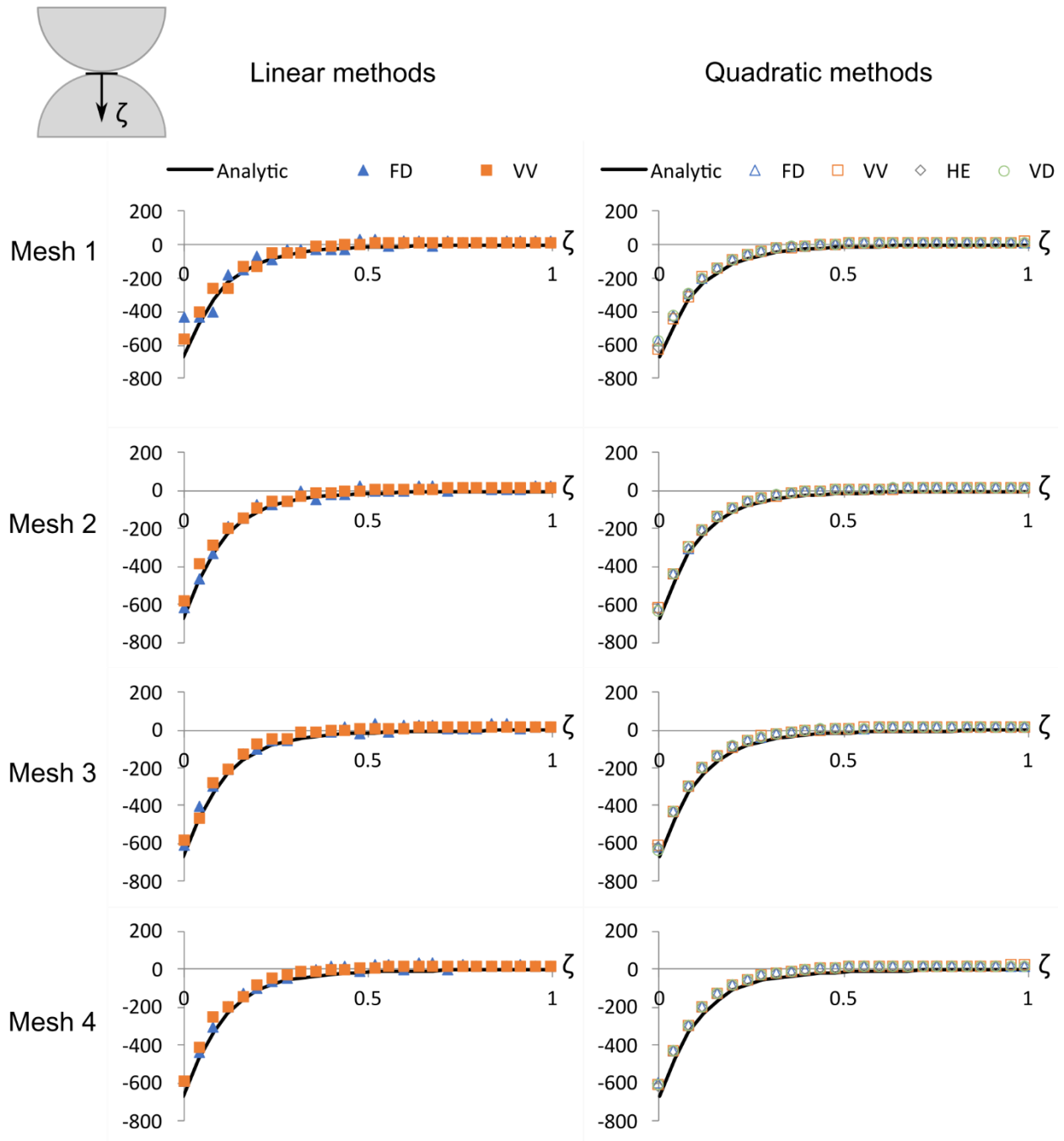
stress oscillations seem to be concentrated on a close neighborhood of the contact surface. The results even a small distance inside the bulk agree with those predicted by the theory.

Figure 78. Vertical normal stress (σ_y [kN/cm^2]) results along the symmetry line coordinate ζ [cm].



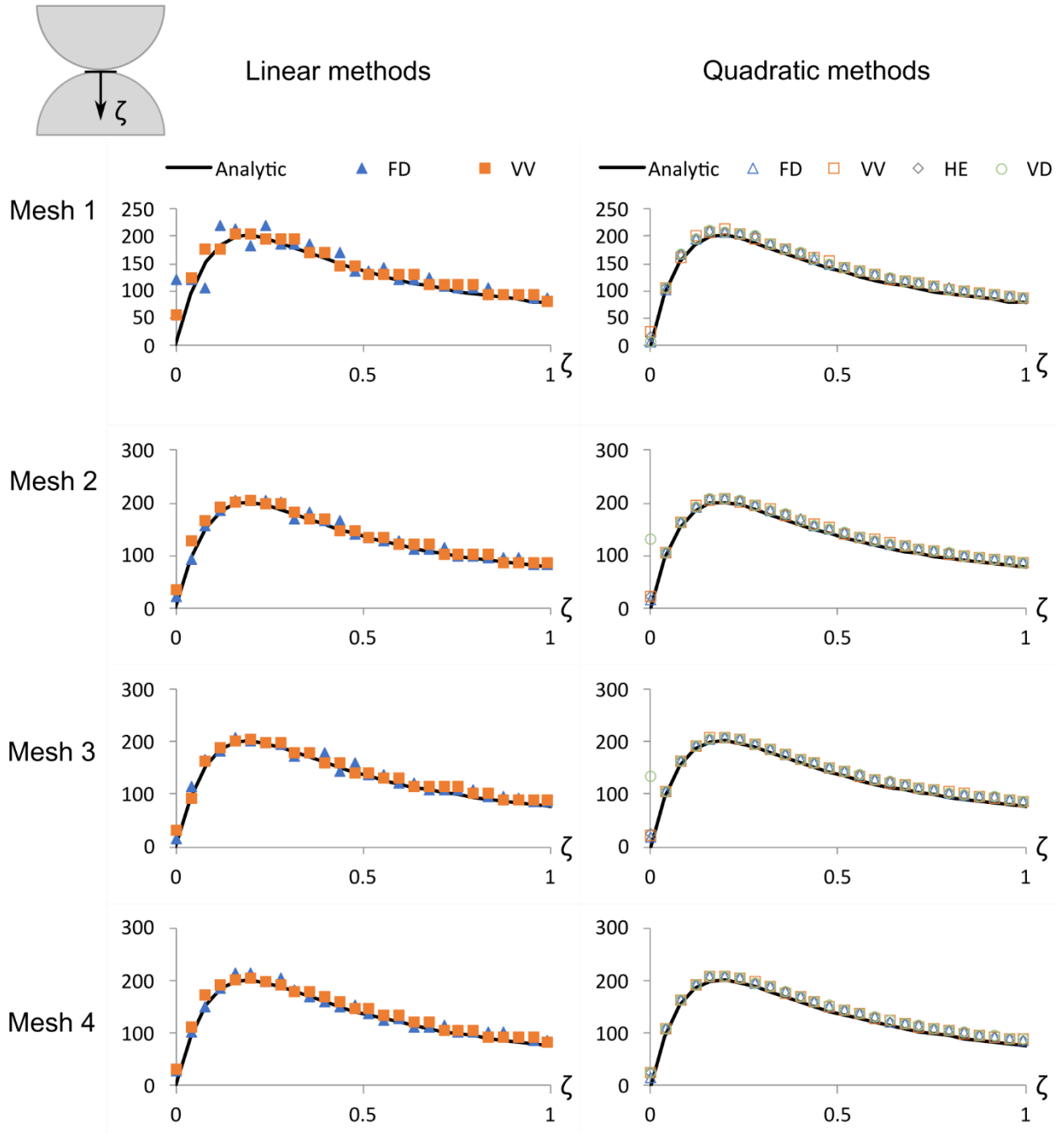
Source: Author.

Figure 79. Horizontal normal stress (σ_x [kN/cm^2]) results along the symmetry line coordinate ζ [cm].



Source: Author.

Figure 80. Maximum shear stress (τ_1 [kN/cm^2]) results along symmetry line coordinate ζ [cm].

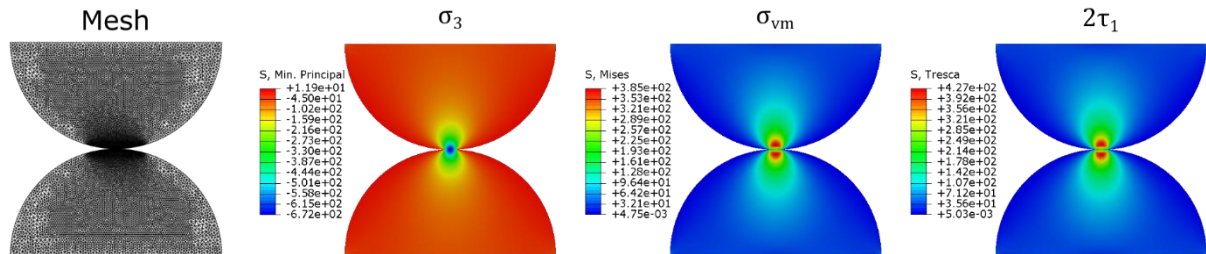


Source: Author.

The next analyses concern the global stress results. The illustration of the results obeys the following sequence: Mesh, Minimum Principal Stress (σ_3), Von Mises Stress (σ_{vm}), and Maximum Shear Stress (τ_1). The only exception lies in the reference ABAQUS results

in Figure 81. There is no preset configuration to show the maximum shear stress, and instead its Tresca stress is shown, which is twice the sought quantity.

Figure 81. Reference stress results from ABAQUS, in kN/cm^2 .



Source: Author.

The analysis of these results revolves around two aspects: the qualitative analysis of general distribution of the stresses, which can be seen by the general color distribution (especially near the contact surface). The second is the quantitative comparison of relevant extremum value for each illustrated stress. For the Minimum Principal Stress, the interest resides in its minimum value ($\min \sigma_3$), which indicates the maximum compression. For both the Von Mises stress and Maximum Shear Stress, the focus is their maximum value ($\max \sigma_{vm}$ and $\max \tau_1$). The first of these values serves as an indicator of the oscillations in the stresses. The Maximum Shear Stress has value zero at the contact surface (in the frictionless case) and its maximum value predicted by Hertz's theory at a distance $y = 0.78a$ from the contact point, where a is the half-width of the contact area. The Von Mises stress can be formulated in terms of the principal stresses and maximum shear stress. It was observed that the Maximum Shear Stress seems to be not as affected by the oscillations in principal stresses as the Von Mises Stress.

From Figure 82 to Figure 87 are displayed the results, for every mesh, for a particular combination of method and element shape. The figures correspond to Linear FEM (FDO1), Linear VEM with polygons (VVO1), Quadratic FEM (FDO2), Quadratic VEM with polygons (VVO2), Quadratic VEM with triangles (VDO2), and Hybrid quadratic method with edge refined meshes (HEO2), respectively. The results are plotted in their own value scale, i.e., no scale homogenization was performed. This is done to avoid loss of information in the distribution of the colors. To accompany the illustrated results, the

following three tables summarize the extremum values of interest for each method/shape (row) and mesh (column), along with those from ABAQUS' reference result.

Table 12. Minimum of the Minimum Principal Stress ($\min \sigma_3$) in kN/cm^2 .

	M1	M2	M3	M4
ABAQUS			-672.51	
FDO1	-699.4	-677.2	-710.6	-676.3
VVO1	-667.5	-667.7	-669.5	-662.9
FDO2	-891.7	-927.1	-1024.4	-1081.6
VVO2	-690.6	-686.3	-686.1	-682.5
VDO2	-870.2	-902.6	-988.9	-1039.3
HEO2	-746.4	-749.8	-770.4	-782.5

Source: Author.

Table 13. Maximum of Maximum Shear Stress ($\max \tau_1$) in kN/cm^2 .

	M1	M2	M3	M4
ABAQUS			213.70	
FDO1	228.21	224.52	216.32	214.43
VVO1	205.61	206.35	204.21	204.16
FDO2	219.33	212.56	209.51	210.60
VVO2	215.76	212.79	209.74	208.67
VDO2	219.20	212.60	209.53	214.24
HEO2	219.73	212.69	209.61	209.09

Source: Author.

Table 14. Maximum of Von Mises Stress ($\max \sigma_{vm}$) in kN/cm^2 .

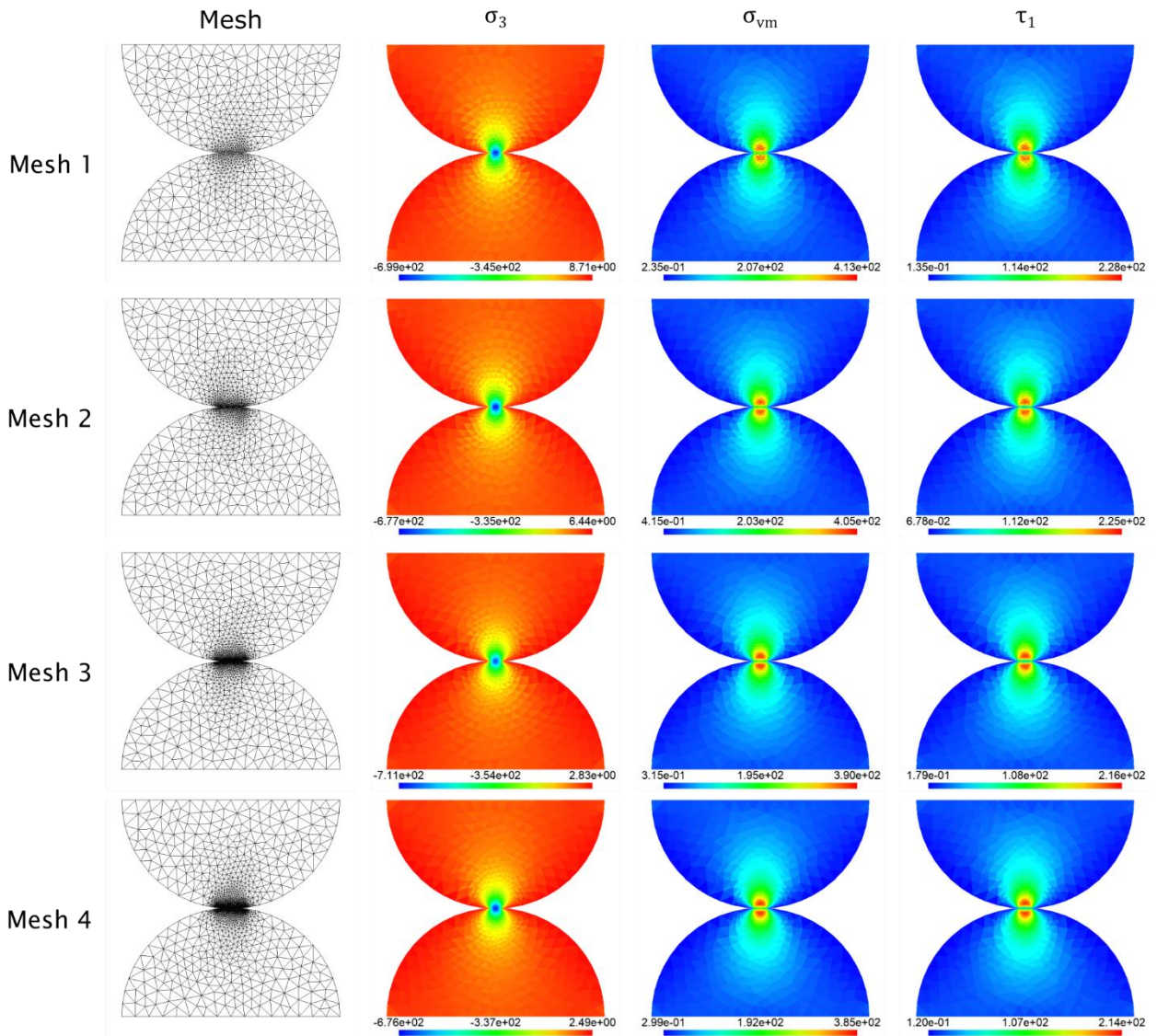
	M1	M2	M3	M4
ABAQUS			385.46	
FDO1	413.11	404.68	389.95	384.65
VVO1	370.68	372.32	369.43	368.26
FDO2	395.49	383.38	429.40	460.31
VVO2	389.85	384.63	378.20	376.02
VDO2	395.27	383.45	402.76	432.72
HEO2	396.18	383.62	377.81	376.37

Source: Author.

The results for linear methods are, in general, close to the reference. Both Linear FEM and Linear VEM lead to stress extrema close to the reference ones, especially if compared to some of the quadratic methods. The general distribution of the stresses, shown in Figure 82 (FEM) and Figure 83 (VEM), are also similar to those provided by ABAQUS in

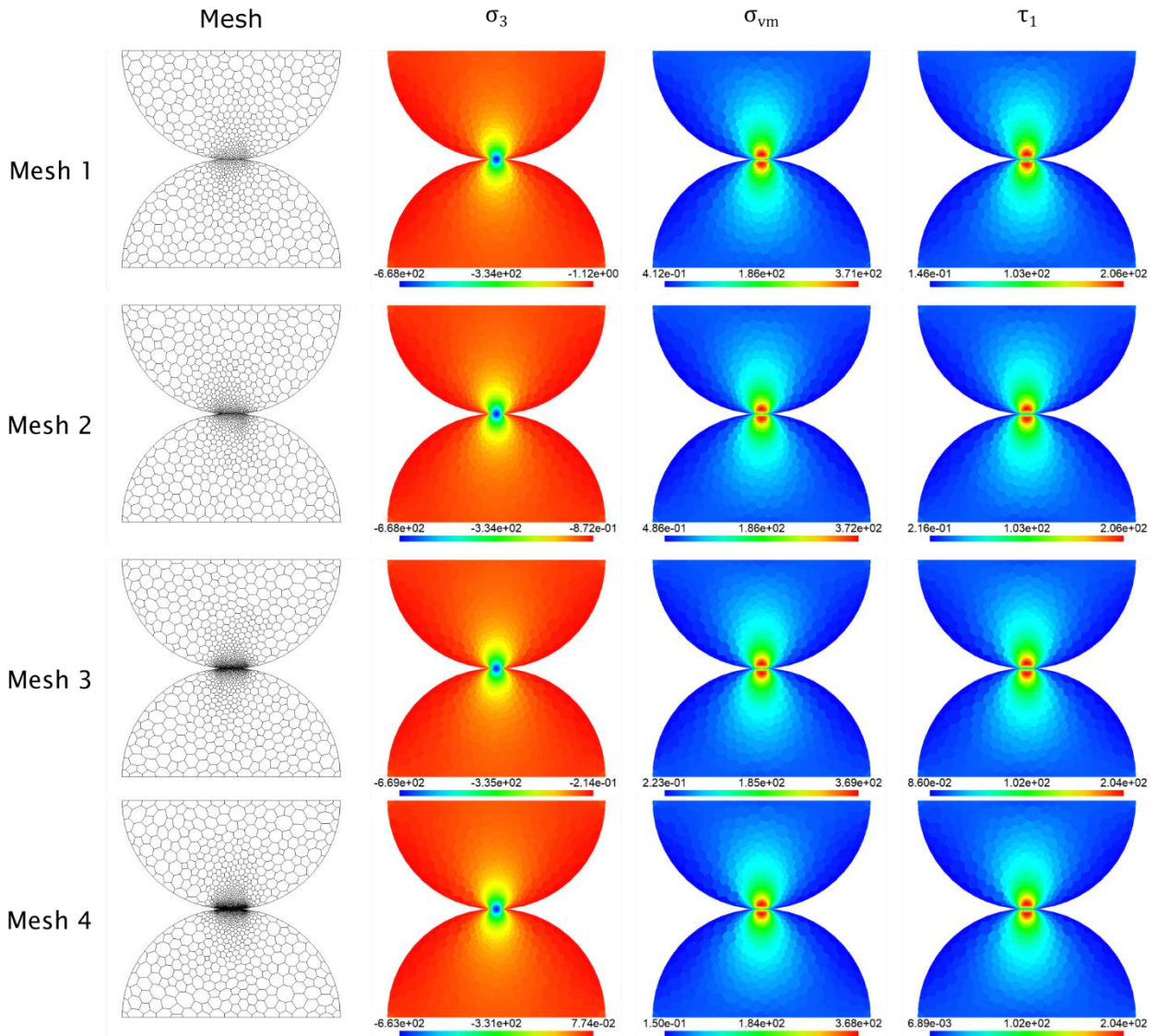
Figure 81. The main difference is their elementwise constant characteristic, direct consequence of the piecewise linear shape functions. The relationship between the polynomial order and quality of the results is known and inherent for these numerical methods They do not show as much oscillation as the quadratic methods because the linear shape functions do not exacerbate the asymmetry in the contact surface treatment.

Figure 82. Stress results for linear FEM meshes (FDO1), in kN/cm^2 .



Source: Author.

Figure 83. Stress results for linear VEM with polygonal meshes (VVO1), in kN/cm^2 .

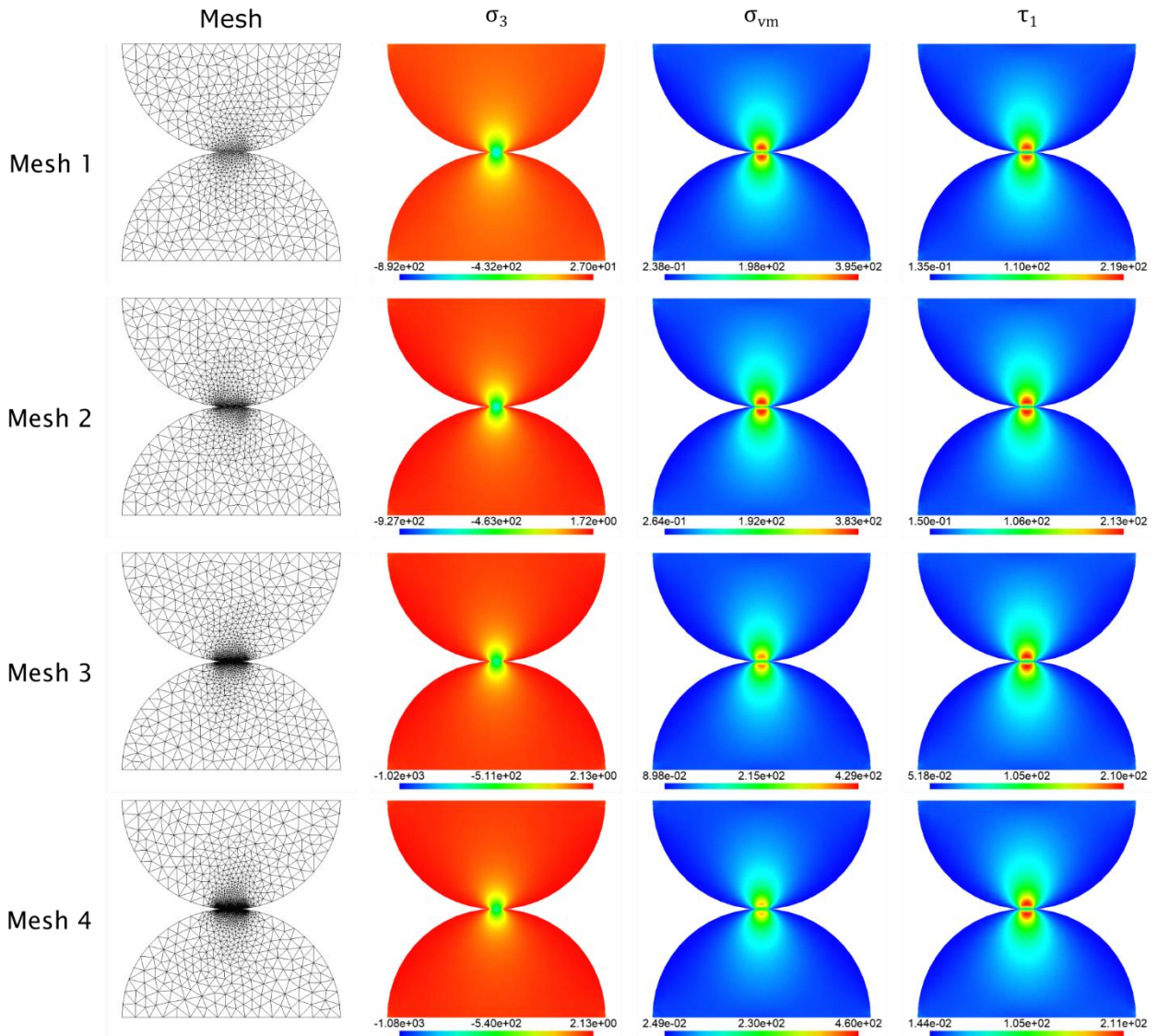


Source: Author.

The results for Quadratic FEM show more explicitly the effects of higher oscillations. As these oscillations lead to great increase of the extrema values for the Minimum Principal Stress in a barely noticeable region around the contact surface. The result of these oscillations with high values and extremely localized nature is to throw off the colorscale, leading to noticeable changes in the color distribution in Figure 84. These oscillations seem to grow in amplitude with finer meshes, this can be seen both in the extremum values of interest and the disappearance of the darker blue core in the Minimum Principal Stress results and the darker red core in the Von Mises Stress results. As the Maximum

Shear Stress is null in the contact surface, it is not as affected by the oscillations and its results show no remarkable difference with the refinement of the meshes.

Figure 84. Stress results for quadratic FEM meshes (FDO2), in kN/cm^2 .

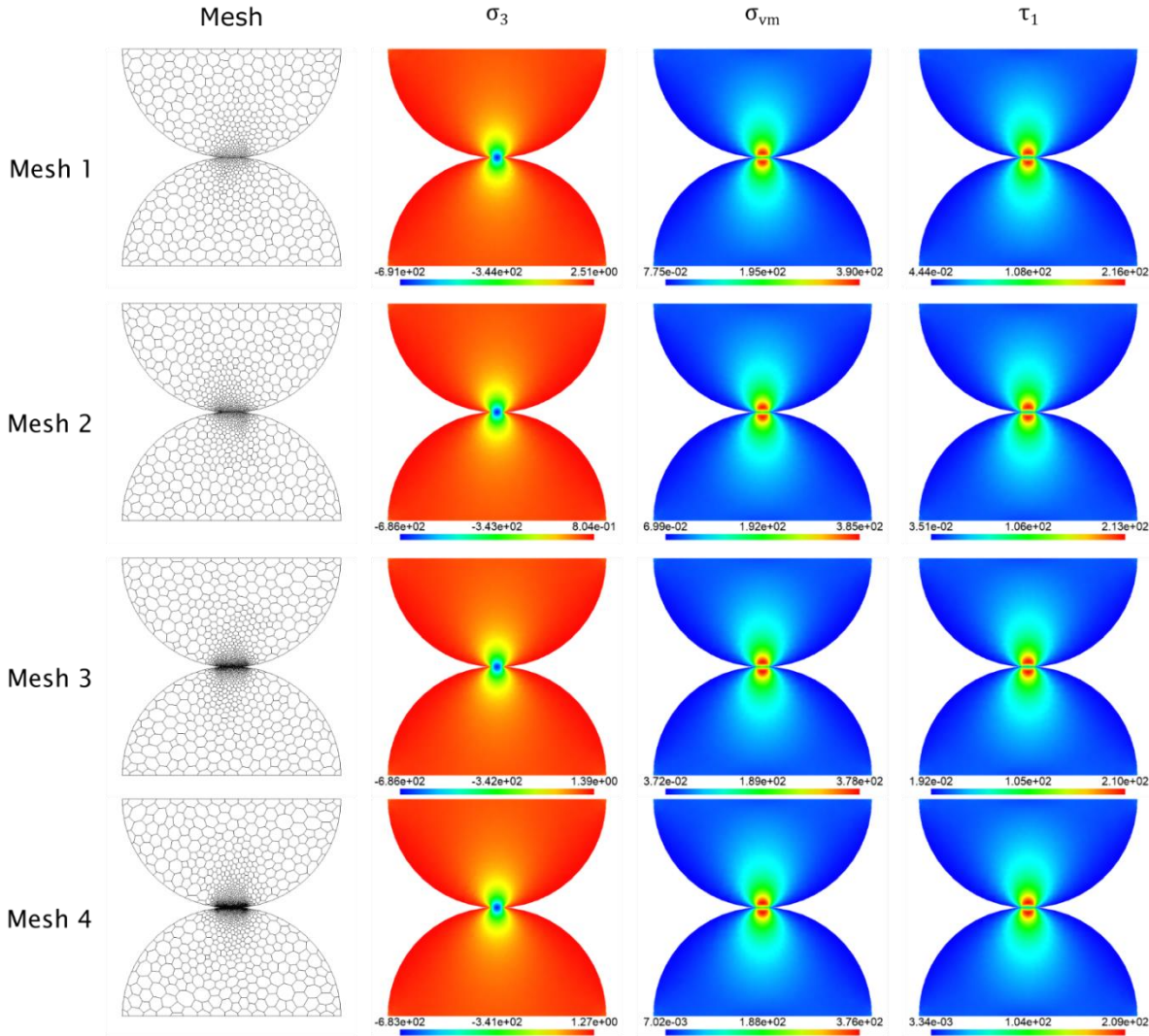


Source: Author.

Quadratic VEM for polygonal meshes (Figure 85) shows much smaller oscillations. The general stress distribution shows the same color pattern as those in the reference solution (Figure 81). The extremum value for the Minimum Principal Stress stays much closer to the reference value. This result is the other reason, along with the estimated pressure distribution, which led to a wider exploration of method and element shape combinations.

The VEM introduces internal degrees of freedom for associated orders two and higher, and the polygonal meshes lead to solutions in higher dimensional virtual function spaces that are later projected into polynomial approximations for the stresses. These were the two main candidates to explain the differences generation of oscillations in the two cases just presented. The VEM in triangular meshes combination (VDO2) tests the effect of the internal degree of freedom alone. Whereas the edge refined approach (HEO2) tests the contribution of a one-side-increase strategically positioned in the contact surface, and the hybrid approach serves to test this effect without burdening the system with additional internal degrees of freedom for the rest of the elements.

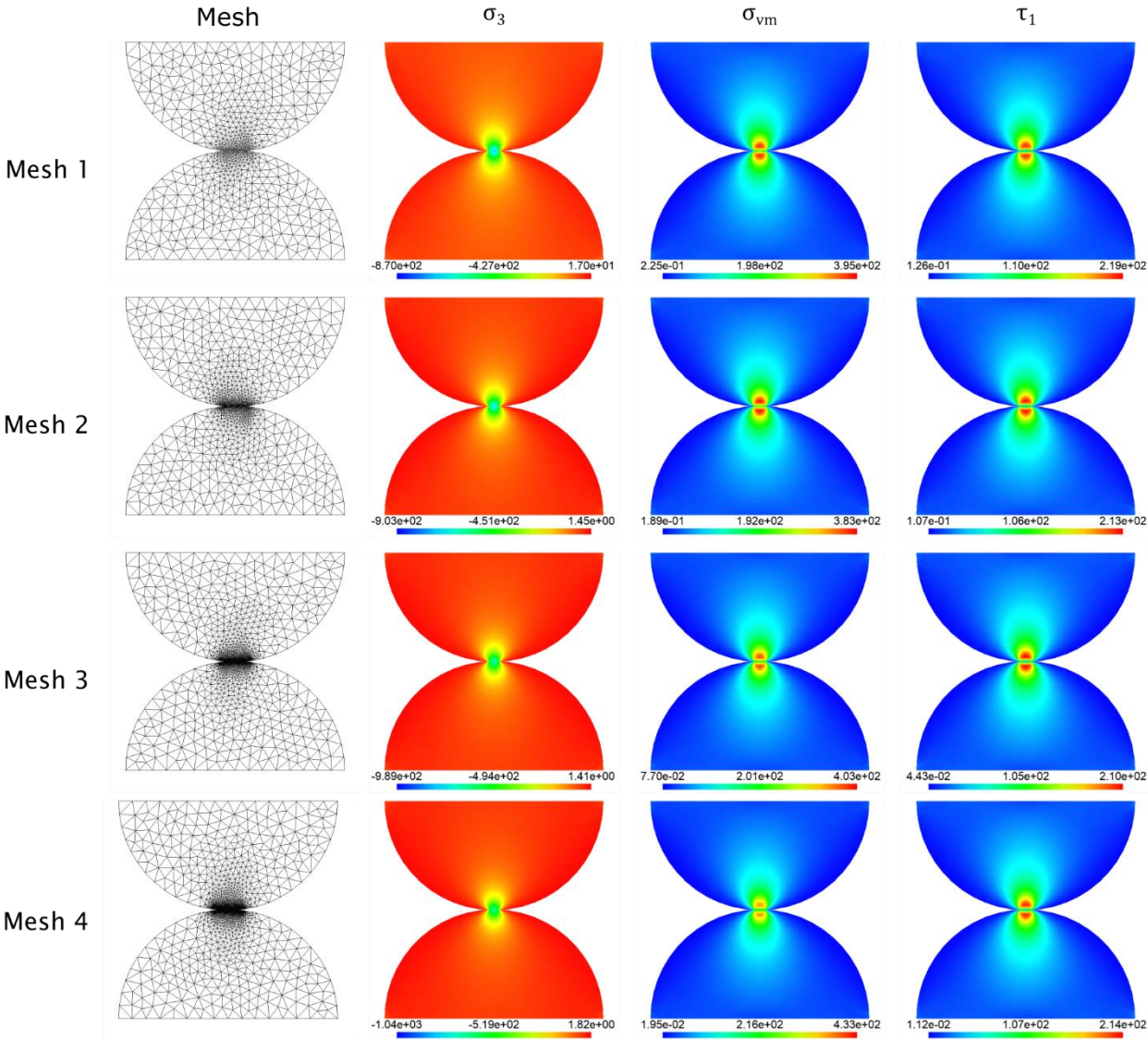
Figure 85. Stress results for quadratic VEM with polygonal meshes (VVO2), in kN/cm^2 .



Source: Author.

The output from VEM in triangular meshes (Figure 86) confirms that the internal degree of freedom has an effect, which is practically negligible. The Minimum Principal Stress is -1039 kN/cm^2 for the finest mesh, instead of the -1081 kN/cm^2 for the Quadratic FEM. It also follows the same tendency to increase the oscillations with the refinement of the mesh. The change in the color distribution of σ_3 and σ_{vm} is qualitatively the same as for Quadratic FEM.

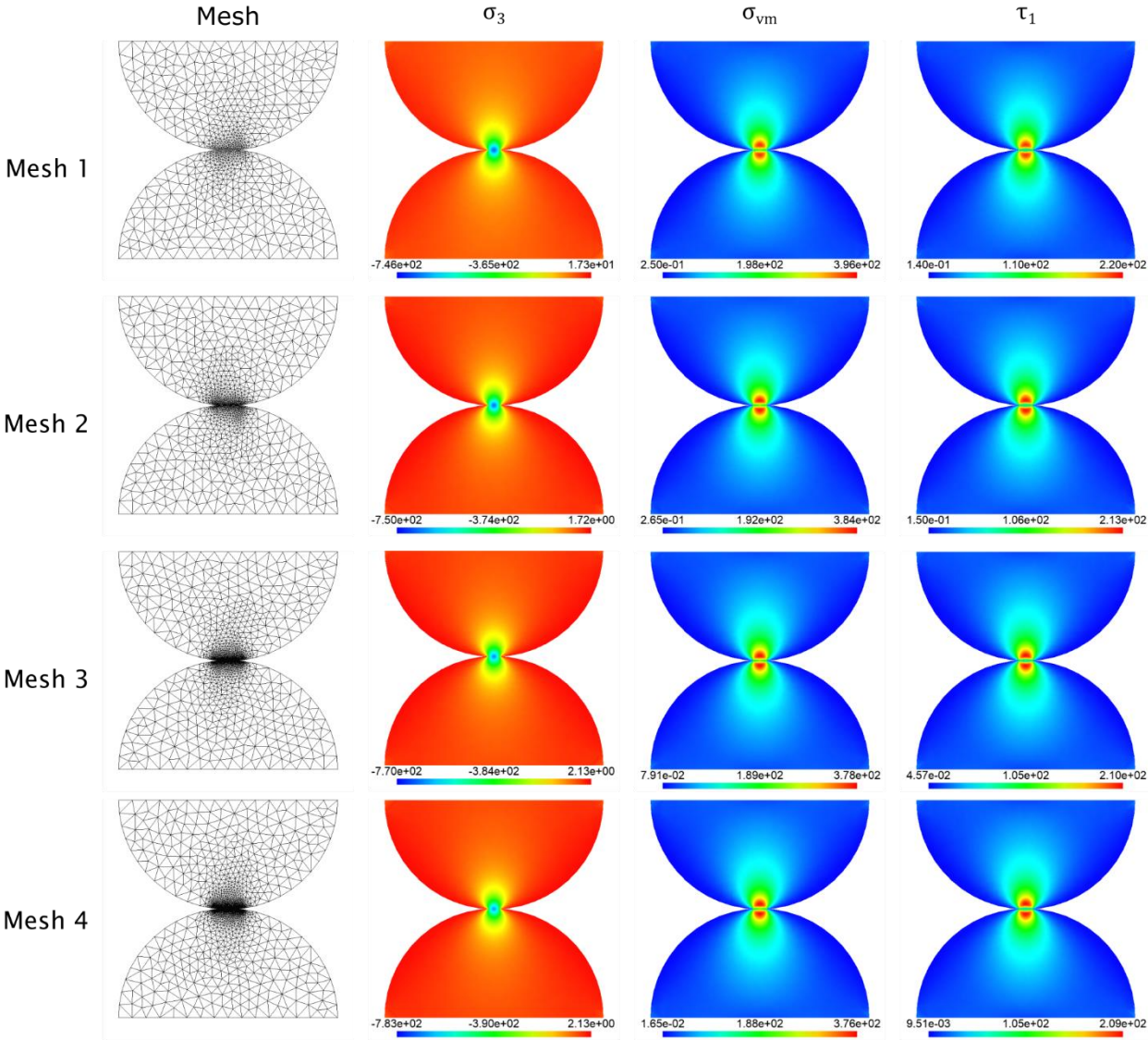
Figure 86. Stress results for quadratic VEM with triangular meshes (VDO2), in kN/cm^2 .



Source: Author.

The Hybrid approach shows results somewhere in between VEM with polygonal meshes and FEM. The oscillations are much smaller, yet still quite noticeable in the Minimum Principal Stress. However, these are not high enough to affect the maximum Von Mises Stress, as happens for Quadratic FEM and VEM with triangular meshes. There is appreciable effect of the oscillations in the color distribution of the Minimum Principal Stress, yet the darker blue core remains visible, if smaller.

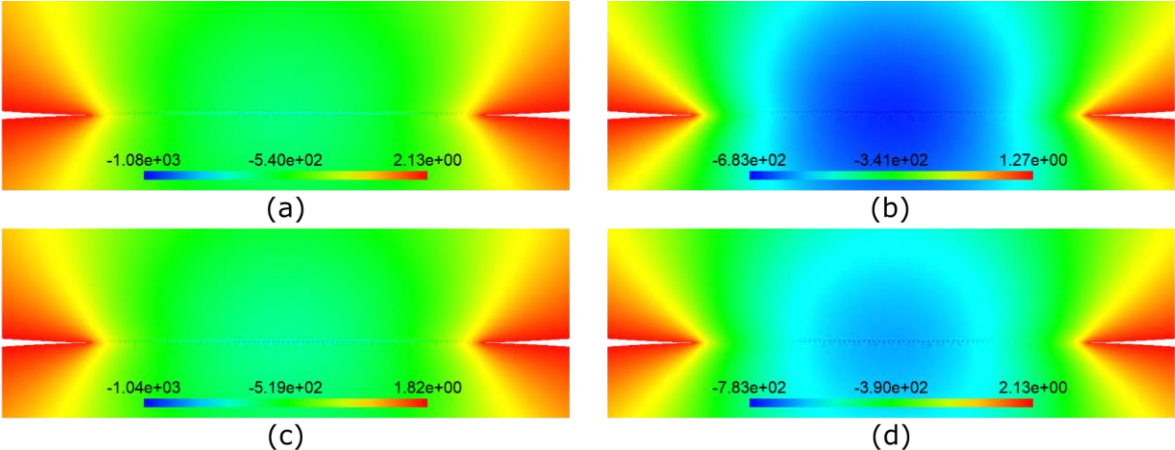
Figure 87. Stress results for the hybrid approach in the edge-refined meshes (HEO2), in kN/cm^2 .



Source: Author.

To conclude this section, a better visualization comparing the oscillations from each quadratic configuration is found in Figure 88. For FEM (a) and VEM with triangular meshes (c), the elements bordering the contact surface are in a lighter blue that stands out against the almost green background. These triangles have a barely noticeable darker blue vertex on the contact surface, which is where the oscillations reach the highest value. For the Hybrid approach (d), the triangles in the boundary are almost whole in darker blue, which stands out against a light blue background, indicating the smaller oscillations. Whereas the VEM with polygonal meshes has the edges coincident with the contact surface of the bordering polygons in darkest blue, which is barely noticeable against the deep blue background, indicating small oscillations.

Figure 88. Comparison of Minimum Principal Stresses [kN/cm^2] on the contact surface for quadratic methods. FEM (a), VEM with polygonal meshes (b), VEM with triangular meshes (c), and Hybrid approach with Edge refinement (d).



Source: Author.

Conclusion

This application illustrated much of what was discussed in section 3.5. The contact patch test was not passed, as expected. Nevertheless, it served to evidence the effects of the Node-to-Segment’s asymmetrical discretization of the surfaces, and how this is exacerbated when higher order shape functions are employed.

The discretization’s lack of procedure to recover the contact pressure distribution made the choice of estimators necessary. The one chosen for the linear methods produced good estimations for the contact pressure, but more noticeable oscillations on the stress results.

The one for quadratic methods produced contact pressure estimations with amplitudes close to the weighting induced by the quadratic shape functions. Their stress results, however, show barely noticeable oscillations for the finer meshes if compared to the linear methods.

Whereas the contact patch test represents a simple contact pressure field, the Hertz problem tests the method for a more complex scenario. This leads to a more complex and richer analysis. The problem was setup with prescribed displacements so that it could be solved with static analysis. However, Hertz's theory does not make predictions based on displacements, the need arose to produce a numerical result to calibrate the analytical ones. Therefore, the reference results should not be taken as the absolute truth, but as a relatively good reference for the comparisons.

The estimator for contact pressure distribution behaved somewhat differently for this application than for the patch test. For the linear methods it behaved the same, leading to estimations very close to the analytical curve. For the quadratic methods, however, the oscillations have diminished significantly for all methods with the finer meshes, practically vanishing for the VEM in polygonal meshes and for the Hybrid approach. Additionally, even the oscillations for the coarser meshes were greatly reduced for the latter approach. The oscillations have persisted, although much reduced, for both methods in triangular meshes.

The resulting stress fields for the Hertz problem have also shown different behavior. Whereas the oscillations tended to diminish with finer meshes for the patch test, for the Quadratic FEM and VEM with triangular meshes the opposite occurred. For the Hybrid approach the oscillations also increased with mesh refinement, though in much less drastic manner. And for the Quadratic VEM with polygonal meshes the oscillations were practically indifferent to mesh refinement, even diminishing an almost imperceptible amount.

The first quadratic configurations studied were those for FEM and VEM with polygonal meshes, and their contrasting behavior motivated the inclusion of the other two configurations to investigate further. The Quadratic VEM with triangular meshes was devised to test the influence of the internal degrees of freedom in isolated manner. Once

the results came almost identical to those of Quadratic FEM's, the hypothesis arose that the use of larger virtual functions spaces to obtain the solution, later projected into polynomial stresses, could be the reason for the better results. This was tested by introducing the virtual elements only on the contact boundary and performing one iteration of the edge refinement, leading to the Hybrid approach. Virtual elements were not used in the whole mesh for this approach to avoid unnecessary internal degrees of freedom, as the oscillations to be damped were extremely localized. The hypothesis was confirmed when the results came showing considerable decrease in the oscillations.

The current hypothesis, and candidate conclusion of this work, is that the employment of larger virtual function spaces allows the capturing of the oscillations, and their projection onto the smaller polynomial space effectively dampens them. The Voronoi polygonal meshes leads to elements with 4 to 8 sides in general, and the boundary elements usually have around 6 or 7 edges (counting the two aligned ones). This leads to a wider function space, which better captures the actual solution, and then the optimal projection onto polynomial space for the stresses filters some of the oscillations. The presence of the two aligned edges may also have some influence in this effect.

The quadratic Voronoi polygonal meshes tend to have more degrees of freedom than their source quadratic triangular mesh. This happens because of an increased number of nodes and for the presence of internal degrees of freedom. The Hybrid approach sought to introduce the advantages found from using virtual elements, while maintaining a lightweight method as is the intention of using Node-to-Segment discretization. The use of virtual elements only on the estimated contact boundary significantly diminishes the number of additional degrees of freedom, in comparison to using fully virtual element meshes. The edge refinement brings both hypothesized sources of oscillation dampening to its location: an additional node (leading to larger virtual function space), and its location on the contact surface (better local description of the solution). This lead to intermediate behavior between that found in Quadratic FEM and Quadratic VEM with polygonal meshes.

The mechanism for the damped oscillations and the better estimation of the contact pressure field is still not clear. However, the results seem to indicate a direction to lessen

this fault of the Node-to-Segment discretization using this relatively new, powerful, and more complex method (VEM), in a way that does not stray too much from the lightweight characteristic that ensures its presence in commercial software in the face of more precise methods.

7. Fourth application – Wheel-Rail contact problem

This application employs the techniques tested in the last section to a practical context in railway engineering. The general motivation for this context is found in section 1.2.

First, let it be clear that phenomena in the wheel-rail interface are more complex than shown here. The individual elements are made of steel alloys and usually undergo high intensity effort; adequate modeling should consider polycrystal plasticity and take into account steel phase transformations, fracture mechanics, thermic effects on material properties, as well as possible residual stresses from welding and manufacturing processes, etc. This work merely borrows this context as a practical application of contact between more complicated geometries. Nevertheless, some measure of coherence with this practical approach is maintained by setting conditions for the analyses that are suitable for heavy-haul operations. The conditions for this section were chosen to represent a wagon loaded with 120 *tonnes*. These are split into its four wheelsets equally, leading to 30 *tonnes* per wheelset.

The motion of a train, as a mechanical problem, is dynamic in nature. The wheels are turning, and the point of contact is always changing for both the wheel and rail. Even on a segment with straight tracks, the train presents small lateral oscillations around a central position. The methodology here proposed is inspired by that in Higa, Kina, and Gay Neto [6]: a steady state approach to characterize the contact for this central position around which the train oscillates; two-dimensional, to find the stresses on a representative cross-section during the contact interaction. These simplifications together restrict the usefulness of modelling friction which, although important, requires 3D analysis and motion for its more relevant effects to be captured. Therefore, the additional simplification of a frictionless contact model is included. The resulting model should lead to the normal contact forces arising on this central position, which serves as indicator for defect prone regions.

The key differences between this work's method, and that of Higa, Kina, and Gay Neto are the use of deformable body mechanics, a pure static approach instead of a quasi-static one, and different contact discretization method. While the first one represents a model refinement, the second one is a shortcoming to be surpassed in future works; the

third is hard to qualify (as the master-master is specialized for pointwise contact) but clearly subject to improvement by employment of better contact discretization schemes. The static approach is combined with some trial and error to find the prescribed displacements that lead to whole system's static equilibrium, i.e., a displacement-controlled solution.

7.1. Goals

The goal of this application is to apply the techniques tested in the previous application (in section 6) to wheel-rail contact inspired situations.

7.2. Methodology

This section starts with some of the problem's mechanical and geometrical aspects in subsection 7.2.1, leading to a more complete explanation on the quantities being balanced, as well as the presentation of wheel and rail profiles used. In the following subsection (7.2.2), are the definitions regarding the numerical methods and configurations, like in previous applications.

7.2.1. Mechanical and geometric aspects

Two rails are considered fixed at their base. They each have a local inclination, towards the inside of the tracks, called *cant* and illustrated in blue in Figure 89. In this inclined position, they are placed with a horizontal distance, between inner faces, called *track gauge*. If this track section is a curve, an additional rotation is performed on both, such that the height difference between the two sides is that of a prescribed *superelevation*. The additional rotation for the superelevation is illustrated in red in Figure 90. The rails are modeled in their full cross-section.

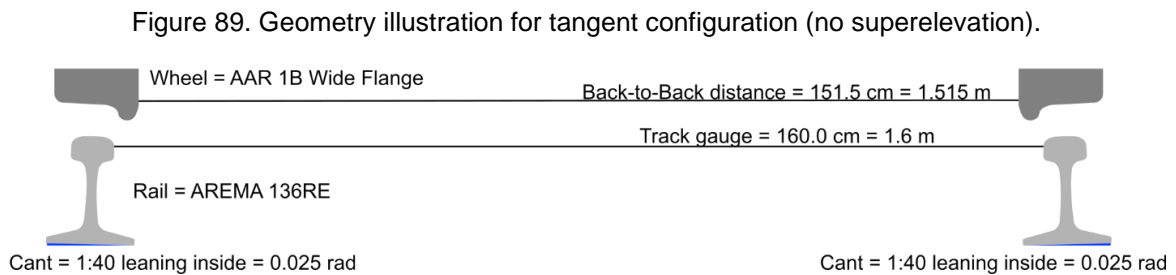
The elected rail geometry is called 136RE, taken from the recommendations of the American Railway Engineering and Maintenance-of-way Association's (AREMA) Manual for Railway Engineering [118]. The *track gauge* is the broad gauge (1,600.0 mm), used in some of the Brazilian railroads (Carajás railroad, Ferronorte railroad, Transnordestina railroad, and others). Each rail has a *cant* of 1:40 (approximately 0.025 radians) leaning to the inside of the tracks. In curves a superelevation is introduced to better distribute the

forces between both rails, this is determined according to the Brazilian standard NBR 16810:2019 [119].

The counterpart for the rail is the wheel. Each wheel is a solid of revolution with its associated *radius*. A pair of wheels is joined together by an axle, forming a wheelset. The distance between the two internal faces of the wheels is called the *back-to-back* distance. Two wheelsets are put together in a bogie, along with other equipment such as springs, bolsters, bearings, and brakes. A typical rail car is supported by two bogies. Most of the systems mass is in the cargo, therefore the inertial forces are considered as acting on the barycenter of the car (important for the balance of moments). As this is a static and two-dimensional model to represent local contact effects, the wheels are represented by the region of their profile closest to the rails. This is illustrated in Figure 89.

The wheel geometry chosen is the AAR 1B with wide flange, found in the Association of American Railroads' (AAR) Manual of Standards and Recommended Practices [120]. The chosen wheelset's *back-to-back* distance is 1,515.0 *mm*, adequate for broad gauge railroads. The elected *radius* is of 500 *mm*, measured from the farthest point from the axle. The height of the car barycenter relative to the center of the wheelset axle is 1,457.7 *mm*.

An illustration of most dimensions and profiles is shown in Figure 89.



Source: Author.

This work will consider two situations: a tangent (straight path) and a curve. The forces acting on the system are the weight of the cargo and centrifugal force (curve only). The adopted car bears a load of 120 *tonnes*. Considering it evenly shared among the four supporting wheelsets, each is loaded with 30 *tf* \approx 300 *kN*. For the curve, information about speed and curvature radius becomes important. A curve of radius of 400 *m* is considered, and the train speed adopted is of 70 *km/h*. This leads to a total centrifugal

force of 28.4 kN , corresponding to a superelevation of 3 cm according to the standard mentioned earlier. The geometrical configurations for both cases are depicted in Figure 90. The base inclination (blue) and superelevation (red) are indicated.

Figure 90. Geometry for (a) Tangent and (b) Curve configurations.



Source: Author.

These forces are considered acting of the car barycenter and are transferred to the rails exclusively via contact. The global system is equivalent to the association of two subsystems: one consisting of the external forces acting on the car barycenter, balanced by the contact forces as perceived by the wheels; and the other consisting of the rails, loaded with their perceived contact forces, which are balanced by the reactions at their fixed bases. Only the first of these subsystems is critical in defining the contact solution that balances the external forces. The second subsystem is merely the transference of a load already defined by the first subsystem. Therefore, balance can be satisfied considering only the first subsystem, i.e., the contact forces perceived by the wheel and the external forces. Furthermore, the balance is always computed in the current configuration.

This work uses a static model with only Dirichlet boundary conditions. The solution for the contact problem are the boundary conditions such that the resulting contact forces balance the forces and moments from the external loading. These boundary conditions are characterized by three degrees of freedom corresponding to the rigid-body motions of the barycenter of the wheelset. These are converted into a linear field of displacements prescribed in the upper boundary of both wheels.

The tangent situation is entirely symmetrical and leads to a simple solution. However, for the curve situation, an external reference model is used to provide basis for comparison. The chosen model is simulated with the software GIRAFFE (sites.poli.usp.br/p/alfredo.gay/giraffe.html), following the methodology in Higa, Kina, and Gay Neto [6]. This methodology aims at the same steady-state solution through dynamic relaxation. This model uses three dimensional surfaces for the wheels and rails but restricts movement to the three rigid body motions in the plane in question. The wheels and rails are treated as rigid bodies and represented by a set of revolutionized and extruded arcs, respectively. A master-master contact discretization uses analytic expressions to find the contact between each pair of arcs. The time integration is performed with Newmark's method with $\beta = 0.3$ and $\gamma = 0.5$, introducing a small numerical damping.

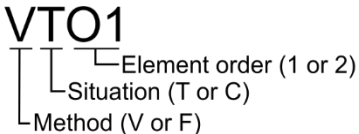
The model consists of a rigid-body element representing the car with artificial inertial properties. This rigid-body element is rigidly linked with a node representing the wheelset barycenter, to which the wheels' contact surfaces (revolutionized arcs) are associated. This block representing the wheelset and car has its movements restricted to the three rigid body motions associated with the plane being studied. Each rail surface (extruded arcs) is associated with its own pair of nodes (start and end of extrusion), these are completely fixed. A pair of dampers is introduced connecting the rails to the wheelset/car block to assist the problem convergence. Contact is configured between each side's wheel and rail, introducing a penalty parameter for normal contact and a damping constant to accelerate the problem's convergence. These dampers serve only numerical purpose during the dynamic relaxation, the same as the inertial properties of the rigid body element. Those need to resemble the actual dynamic properties of the train.

7.2.2. Numerical aspects

This application employs the same techniques featured in the previous application for a more complex scenario. The problem is modeled using plane-strain linear elasticity, restricting the wheel geometry only to the region closest to the contact. The two hypothetical circumstances typical of railway transport, tangent and curve, were presented in the last subsection.

Regarding the configurations adopted for the numerical simulations: only two combinations of method and element shape are used. Finite elements are used with triangular meshes, and Virtual elements with polygonal ones. This covers the two extremum behaviors found in section 6. Only one mesh is adopted for each element shape, employing fine sizes in the candidate contact regions and coarse elements elsewhere (Figure 92). The two methods are used with both linear and quadratic polynomials. The codification for these configurations is presented in Figure 91.

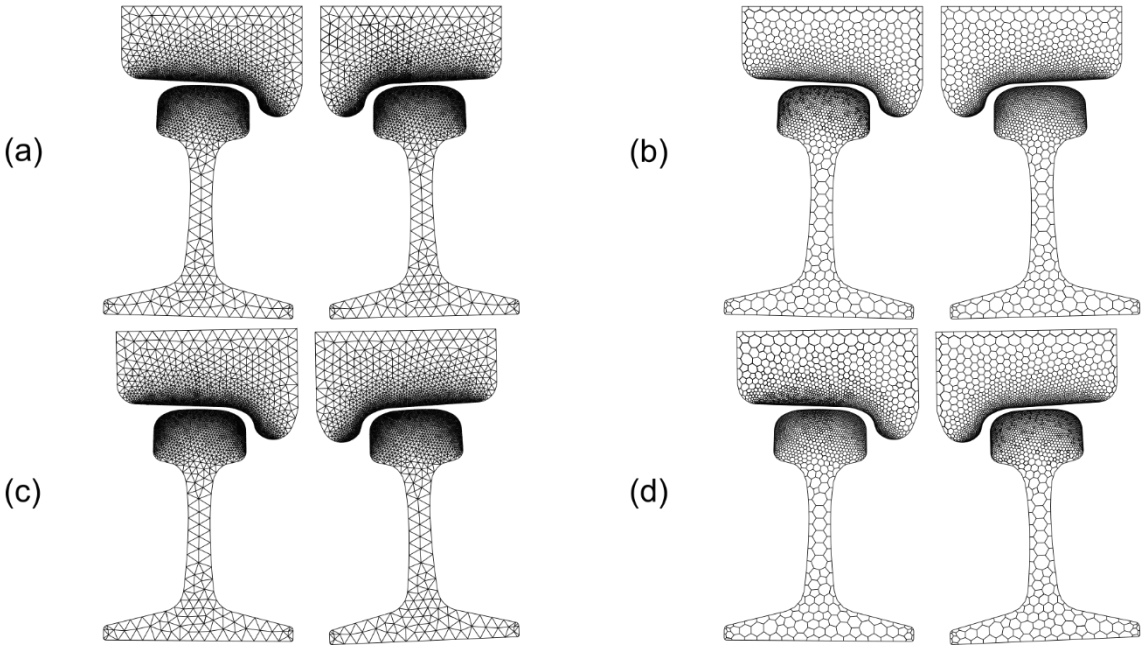
Figure 91. Codification for wheel-rail contact simulations.



Source: Author.

One additional observation: the author’s code is restricted to two bodies at a time. Because of this, each side (left and right) is simulated separately using consistent boundary conditions. The results, be them total forces/moments or post-processed images, are later joined.

Figure 92. Tangent: Delaunay (a) and Voronoi (b). Curve: Delaunay (c) and Voronoi (d).



Source: Author.

The criterion for acceptance of a contact solution is based on a quantity referred as the resulting error. The balance residuals of the moment and two forces are computed for each trial simulation. The relative error for each balanced quantity is defined as its residual over a reference quantity. For the vertical force, this reference quantity is the external vertical force (-300 kN), whereas for the horizontal one, it is horizontal force in the curve case (28.4 kN) for both cases; for the moment, the resulting moment from one side is elected as reference. The resulting error is the square root of the sums of squares of the individual relative errors. The cutoff value for the resulting error adopted for the tangent situation is 10^{-5} and for the curve situation 10^{-4} . The different values were adopted to reflect the difference in difficulty to achieve convergence.

7.3. Results

This section contains the discussion of results for this application. These are split into two subsections, one for each situation simulated (Tangent and Curve). Inside each subsection the results are presented for all configurations, along with a table summarizing the errors found in the balance of forces and moments and discussed in the light of the conclusions from the last section. For the curve situation a comparison with the results from the GIRAFFE model is also shown and discussed.

The main results are presented in templated figures for ease of reading. Each figure represents all results for one configuration. The first two subfigures show the Von Mises stress (a) and the maximum tangential stress (b), these are related and important for evaluating inelastic material behavior. Although there is some redundancy in showing both, the last section has shown that the contribution of the principal stresses in the Von Mises stress lead to it being affected by the oscillations from the contact discretization, whereas the value of the maximum shear stress being null at the region of contact leads to an apparent immunity to those. Subfigure (c) shows the global minimum principal stress, which best represents the maximum compression at contact and its effect throughout the wheel and rail. This is accompanied with a magnified version for each side, left (d) and right (e). Similarly, the contact forces are shown in subfigure (f) with the minimum principal stresses as background, along with magnifications (g) and (h).

7.3.1. Tangent situation

The results for this situation for Linear FEM, Linear VEM, Quadratic FEM, and Quadratic VEM are found in Figure 93, Figure 94, Figure 95, and Figure 96, respectively.

The tangent situation is symmetric, a naïve approach for the search of boundary conditions that balance the external force would apply only vertical displacements. This approach was initially taken and led to residuals in horizontal forces and moments that, although small, were not enough to satisfy the criterion established in the methodology. Starting from the results of this approach, small changes in the horizontal displacement and rotation produced solutions that passed the defined criterion. All rotations and displacements are relative to the reference configuration shown in Figure 92. The rigid body motions for the solutions are presented along with their relative errors and the resulting error in Table 15. In it one can see that the variations from the naïve approach are very small, probably caused by asymmetries in the mesh generation. The maximum horizontal translation and rotation differ from their counterparts in the Curve situation (Table 16) by three to four orders of magnitude.

Table 15. Boundary conditions and errors for Tangent situation.

Config.	Vertical Translation [cm]	Horizontal Translation [cm]	Rotation	Vertical Force Error	Horizontal Force Error	Moment Error	Resulting Error
FO1	-3.285E-01	1.00E-06	2.45E-07	-1.32E-07	1.92E-06	1.63E-06	2.52E-06
VO1	-3.285E-01	0.00E+00	5.00E-08	-3.11E-06	-6.93E-06	1.72E-06	7.79E-06
FO2	-3.291E-01	2.50E-06	7.50E-09	8.73E-06	-8.16E-08	4.86E-06	9.99E-06
VO2	-3.289E-01	-3.75E-05	1.60E-09	-3.93E-06	6.76E-06	6.22E-06	9.99E-06

Source: Author.

Looking at the common tendencies throughout the different results, the expected symmetry of the two sides of the problem is present. Analyzing each side, the direct effects of the contact interaction can be seen: a bulb. Each rail seems to be experiencing a slight bending inward, resulting from the eccentricity of the load with respect to the rail's web. This is interesting because it leads to considerable Von Mises and shear stresses in this region, rivaling with those in the contact interface.

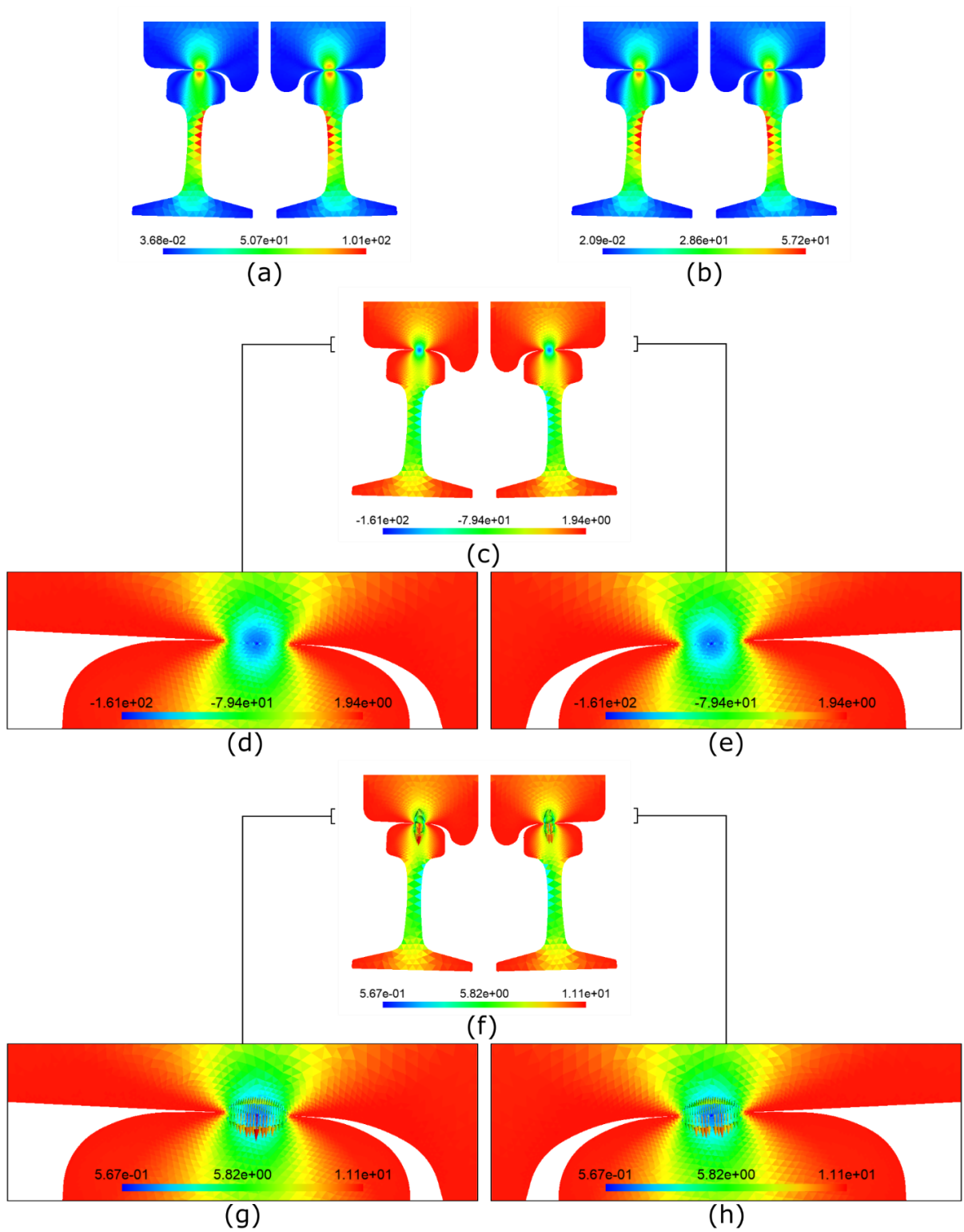
These results should be taken warily. The plane strain model assumes the hypothesis that the bodies are prismatic and that the loads are constant along the prism axis. This models

exactly the case of the last application (contact between aligned cylinders), the same cannot be said for this wheel-rail context. The situation effectively modeled is that of the rails entering contact with an extruded version of the wheel profiles. In this, the rails are uniformly loaded with the contact forces along their axis, instead of locally loaded as the real interaction is. Furthermore, the plane strain analysis represents the state away from the borders, where the boundary conditions are. In the wheel-rail situation, the contact is pointwise, the effects of the boundaries around the contact region are important. It is the author's belief that the boundary effects should lead to less relevant bending displacement/stresses. This small bending displacement might also affect the contact solution. A full assessment of the differences should require a 3D model, which is outside the scope proposed for this work. Nevertheless, this bending behavior (even if less intense in reality) is an example of secondary effect from the contact forces that would not be captured in a rigid-body model coupled with analytic hertzian results.

Focusing on the differences: the Linear FEM results (Figure 93) showed some atypical oscillations in the contact results. These are observed directly in the contact forces (g, h), and in their impact on the minimum principal stresses (d, e), which show a different color distribution than what was expected, i.e., something more similar to what is shown for Linear VEM (Figure 94) and Quadratic VEM (Figure 96). The Linear VEM results (Figure 94) adhere more closely to those of the hertzian theory. The mesh resolution in the contact region seems to be sufficient to avoid the oscillations shown in the previous application, see Figure 76 (b).

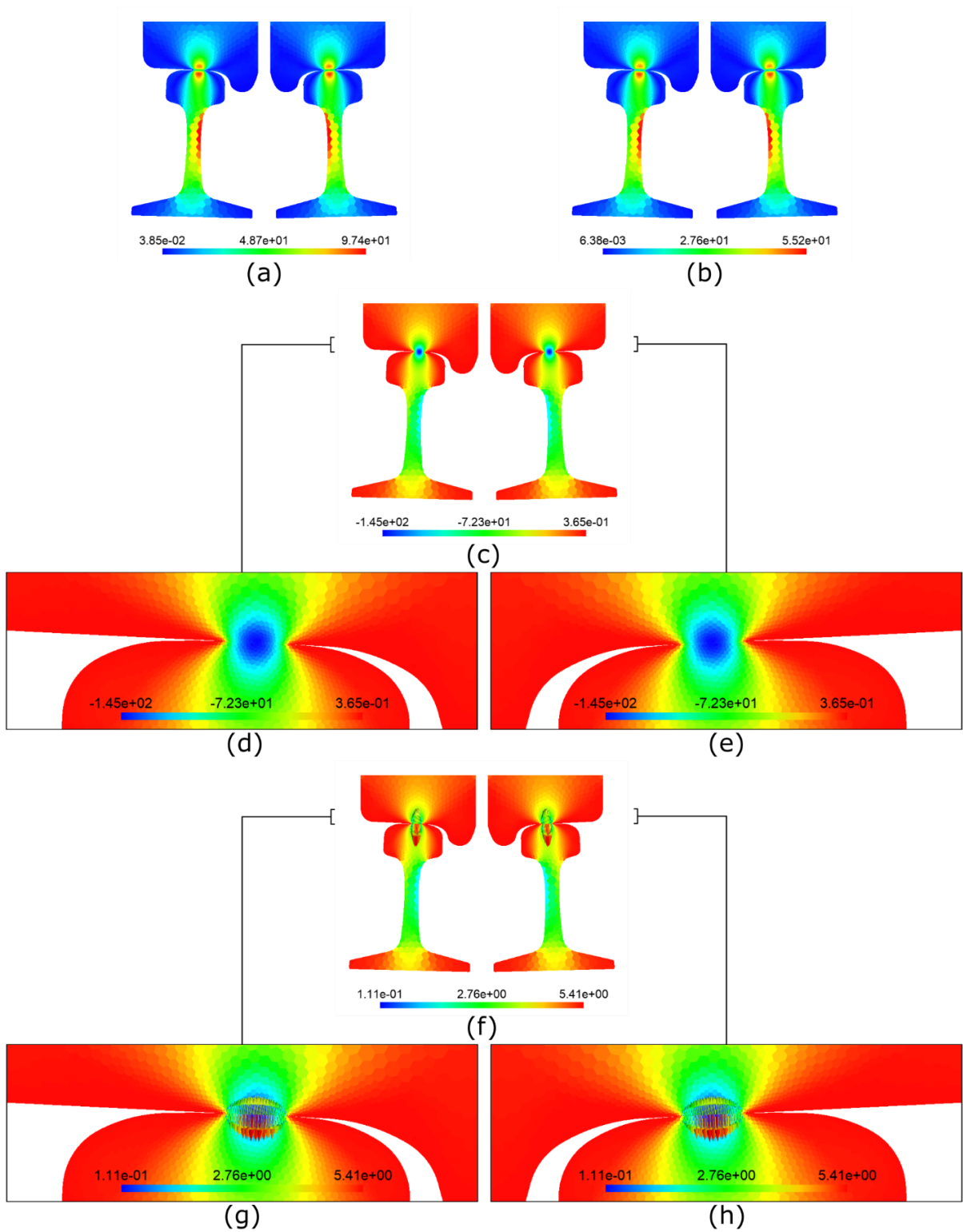
The Quadratic FEM results (Figure 95) show the considerable oscillations of stresses in the contact region (d, e), as was to be expected according to the last application. These oscillations are noticeable by the lighter-blue prevalence the contact region, whereas the higher values of those happen only at a few elements bordering the contact, barely visible. These oscillations affect the scale for the minimum principal stress visualization. The results for Quadratic VEM (Figure 96) seem to corroborate those found in the previous application of presenting reduced oscillations when compared to those in Quadratic FEM.

Figure 93. Linear FEM results for Tangent situation. Von Mises stress (a), maximum shear stress (b), minimum principal (c) with left (d) and right (e) zooms, in kN/cm^2 . Contact forces (f) with left (g) and right (h) zooms, in kN .



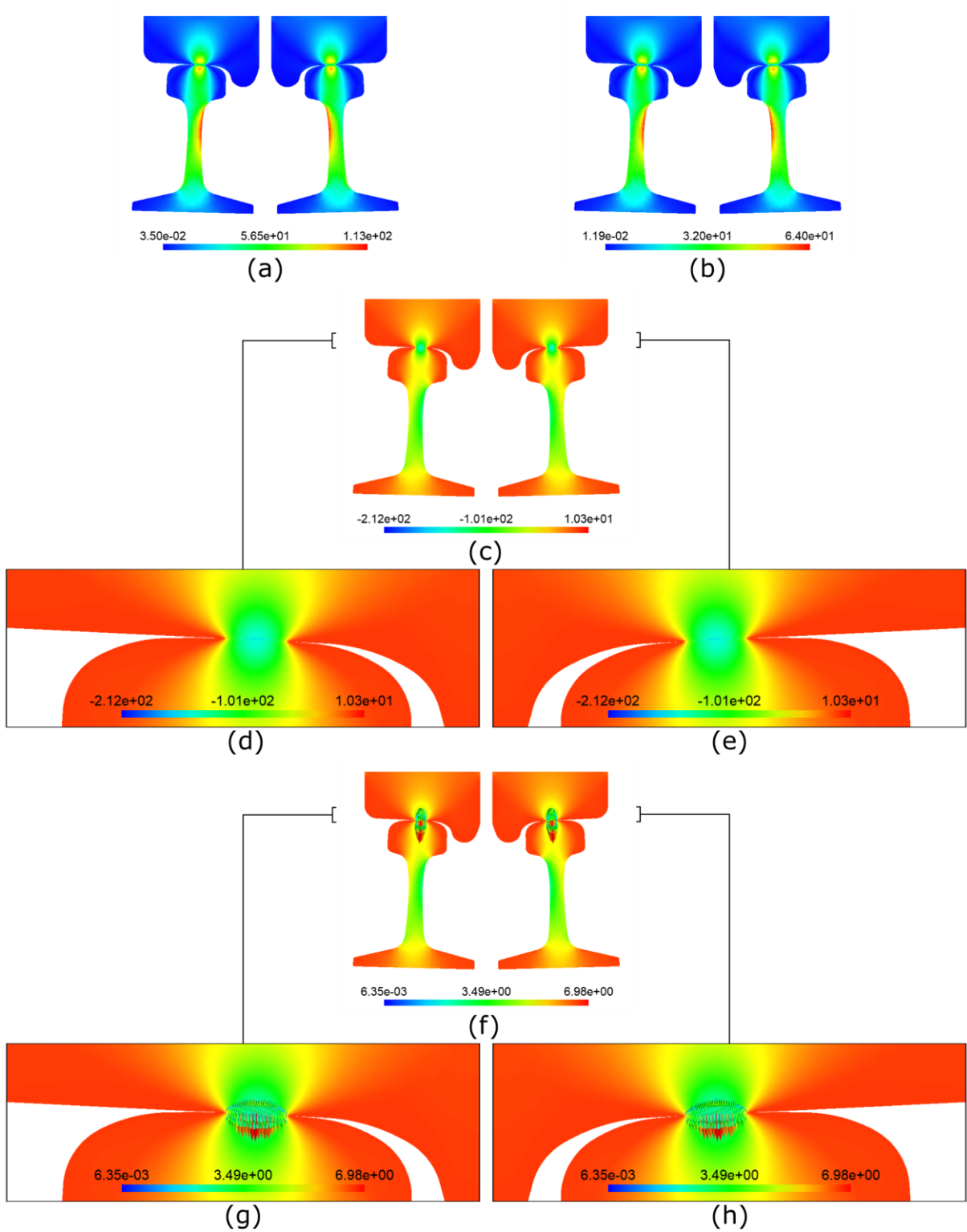
Source: Author.

Figure 94. Linear VEM results for Tangent situation. Von Mises stress (a), maximum shear stress (b), minimum principal (c) with left (d) and right (e) zooms, in kN/cm^2 . Contact forces (f) with left (g) and right (h) zooms, in kN .



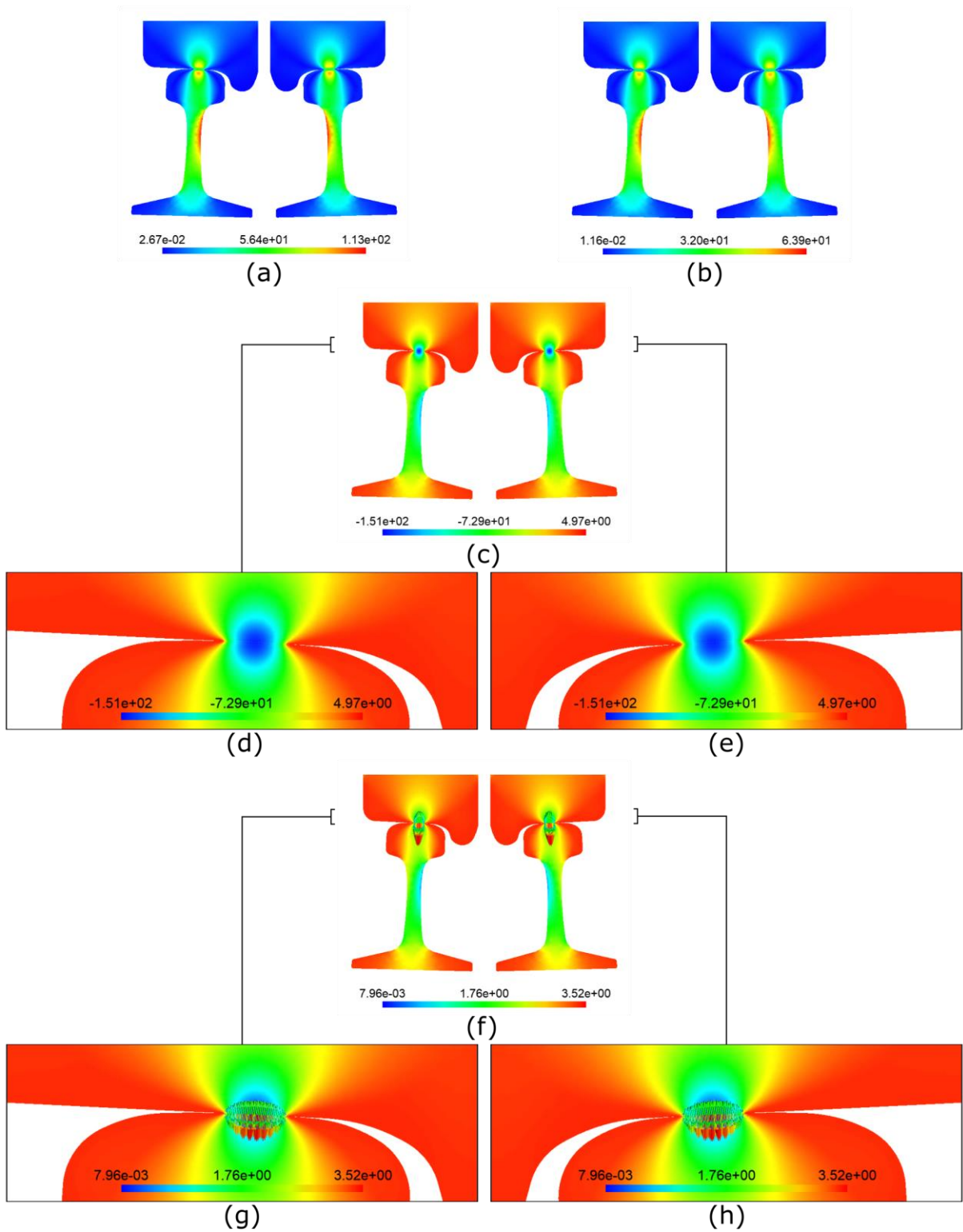
Source Author.

Figure 95. Quadratic FEM results for Tangent situation. Von Mises stress (a), maximum shear stress (b), minimum principal (c) with left (d) and right (e) zooms, in kN/cm^2 . Contact forces (f) with left (g) and right (h) zooms, in kN .



Source: Author.

Figure 96. Quadratic VEM results for Tangent situation. Von Mises stress (a), maximum shear stress (b), minimum principal (c) with left (d) and right (e) zooms, in kN/cm^2 . Contact forces (f) with left (g) and right (h) zooms, in kN .



Source: Author.

7.3.2. Curve situation

The results for this situation for Linear FEM, Linear VEM, Quadratic FEM, and Quadratic VEM are found in Figure 97, Figure 98, Figure 99, and Figure 100, respectively.

The search for the boundary conditions that satisfy the equilibrium was more difficult for this situation. The lack of symmetry in the problem requires all three rigid body motions to be varied from the outset, to balance the external loads. Although there appears to be a direct correspondence between some motions and resulting quantities (e.g., translations and total force in their direction; rotation and total moment), the geometries involved in contact lead to couplings that make the task more difficult.

The trial-and-error process is aggravated as the time required for each simulation increases. Linear FEM is the fastest method, leading to times around a minute per simulation. Linear VEM and Quadratic FEM lead to similar times, something between 10 to 20 minutes. Whereas Quadratic VEM can sometimes take up to a couple of hours. Because of this, the requirement to consider the solution acceptable was alleviated: the resulting error being smaller than 10^{-4} instead of 10^{-5} as in the Tangent situation. The boundary conditions that satisfied the requirement are summarized in Table 16.

Table 16. Boundary conditions and errors for Curve situation

Config.	Vertical Translation [cm]	Horizontal Translation [cm]	Rotation	Vertical Force Error	Horizontal Force Error	Moment Error	Resulting Error
FO1	-3.122E-01	7.025E-01	3.273E-04	2.7E-06	-5.7E-06	-1.8E-06	6.6E-06
FO2	-3.126E-01	7.330E-01	3.404E-04	-1.8E-06	-1.1E-06	2.3E-06	3.1E-06
VO1	-3.122E-01	7.073E-01	3.291E-04	8.1E-07	-6.1E-06	5.4E-06	8.2E-06
VO2	-3.125E-01	7.309E-01	3.395E-04	-7.4E-07	8.5E-05	-7.2E-06	8.6E-05

Source: Author.

An overall analysis of commonalities across the results leads to observations in the same line as those for the Tangent situation. The solution is more evidently asymmetric, mirroring the problem's asymmetry. The left side presents a contact solution and stress distribution similar to that seen earlier: the straight part of the wheel touching the top of the rail, leading to a slight bend inwards due to a small eccentricity of the contact forces relative to the rail's web. On the right-side is where the differences between curve and tangent situation becomes more evident. Whereas the external vertical force and moment

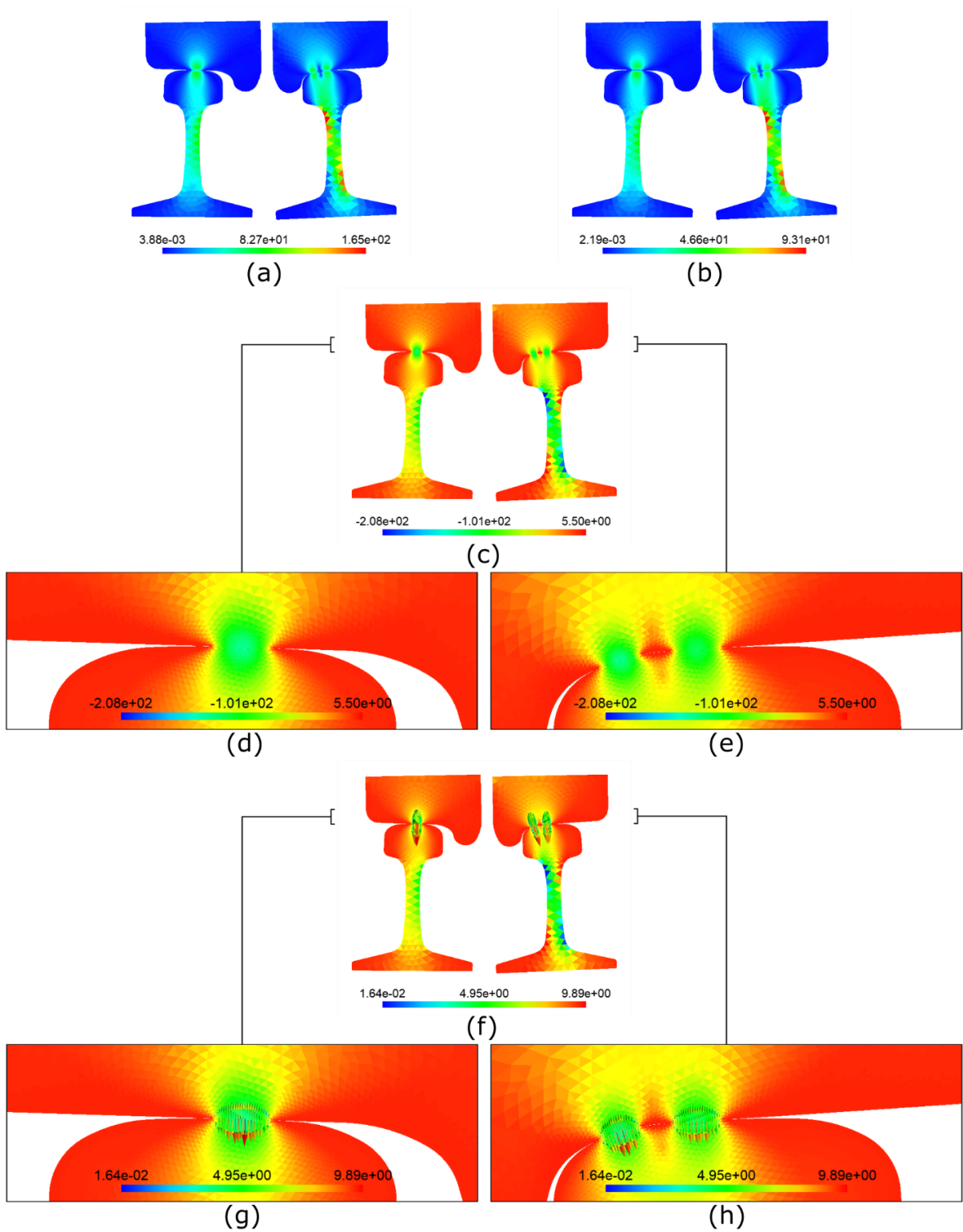
are mostly balanced by the almost-vertical contact forces on the top of the rail and their binary, the horizontal external force leads to a second contact region more to the inside of the rail. This second contact region leads to overall smaller contact stresses on the right side, as well as to a change in the bending behavior.

The criticism for the previous situation, regarding the plane strain model choice and its effect on the bending part of the solution, still applies. The plane strain state might be adequate for the local effects around the contact but exaggerates the bending part of the rail's response. However, in contrast with the tangent situation where the bending is not a focus of the analysis, for curves it can be a relevant aspect. Curves with high lateral loads sometimes suffer problems like *gauge widening* and ultimately *wheel climb derailment*. A more in-depth study of the various defects and problems that assail the wheel-rail interaction should indicate the typical mechanisms to pay more attention.

The comparative analysis between the methods for this case is the same as the tangent situation, basically corroborating the conclusions of the preceding application.

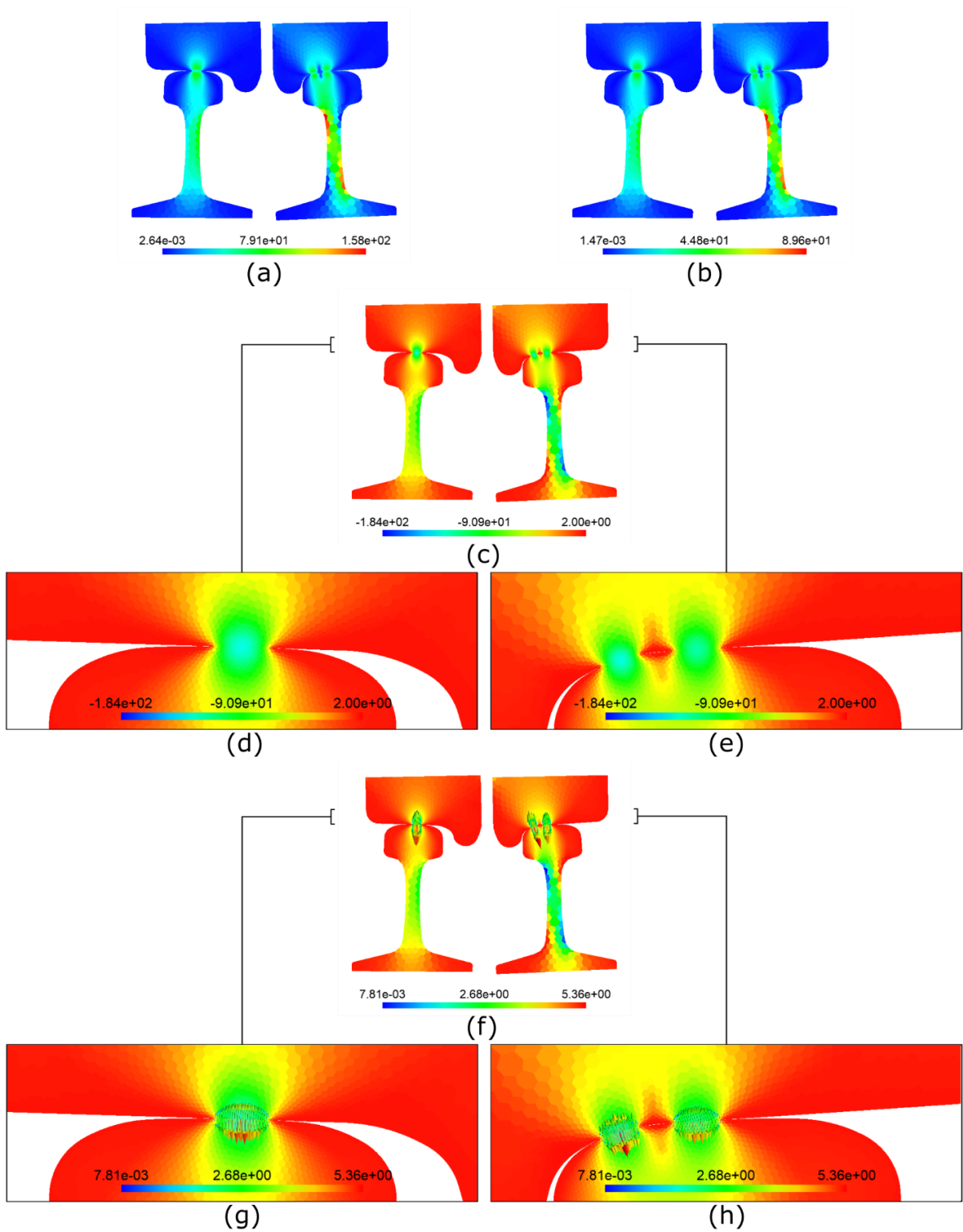
This situation is also modelled using the software GIRAFFE. Figure 101 shows the overlap of the GIRAFFE results over each combination of the author's results. The GIRAFFE results are opened and formatted using the free software Paraview. The contact surfaces are simplified to their outlines and overlapped by matching the wheel profiles in both results. The difference seen between the top of the rails in the GIRAFFE solution and the author's corresponds to the bending displacement. This displacement is thought to be the reason behind the slight difference in the contact positions in the left side. Overall, there seems to be agreement between the two models.

Figure 97. Linear FEM results for Curve situation. Von Mises stress (a), maximum shear stress (b), minimum principal (c) with left (d) and right (e) zooms, in kN/cm^2 . Contact forces (f) with left (g) and right (h) zooms, in kN .



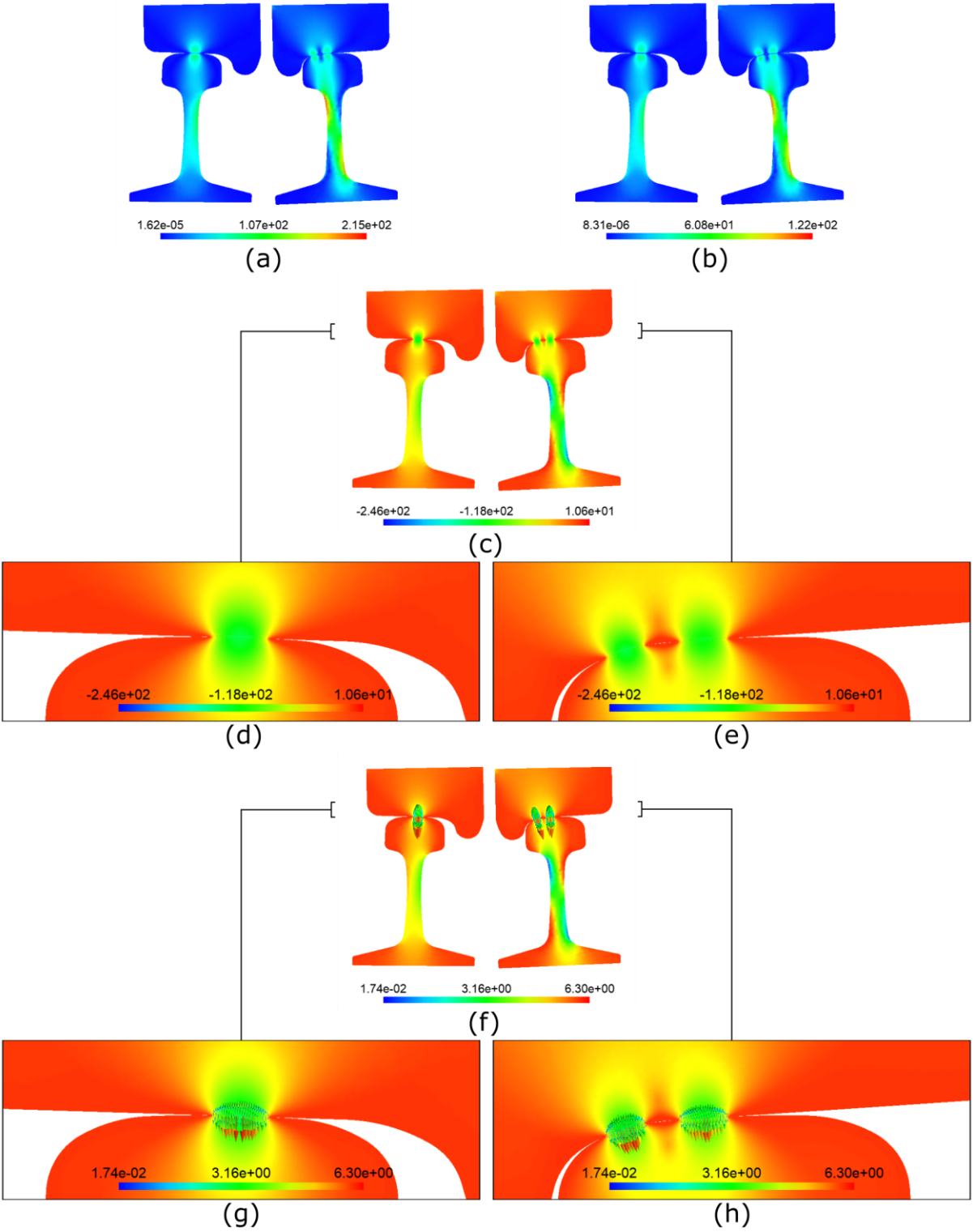
Source: Author.

Figure 98. Linear VEM results for Curve situation. Von Mises stress (a), maximum shear stress (b), minimum principal (c) with left (d) and right (e) zooms, in kN/cm^2 . Contact forces (f) with left (g) and right (h) zooms, in kN .



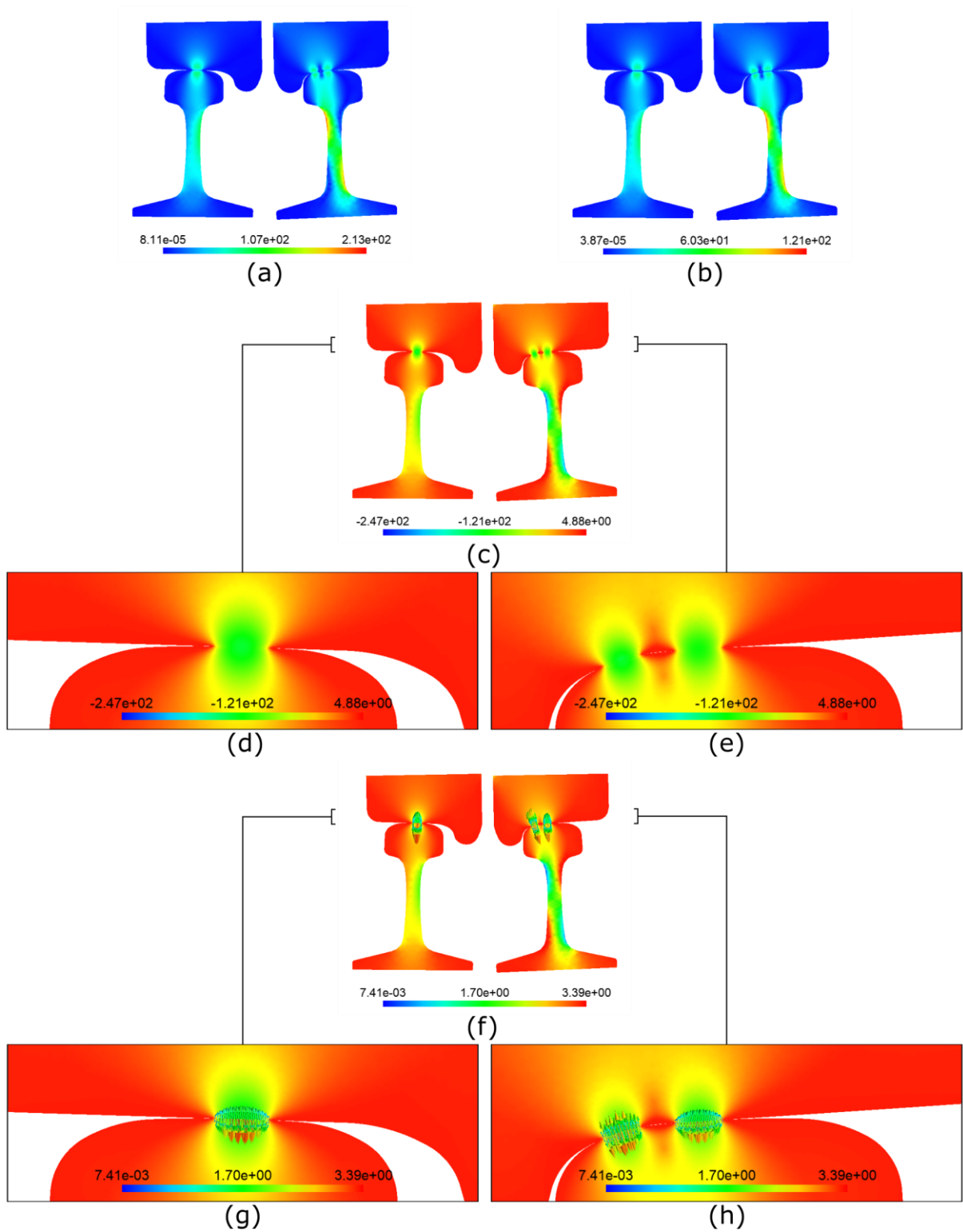
Source: Author.

Figure 99. Quadratic FEM results for Curve situation. Von Mises stress (a), maximum shear stress (b), minimum principal (c) with left (d) and right (e) zooms, in kN/cm^2 . Contact forces (f) with left (g) and right (h) zooms, in kN .



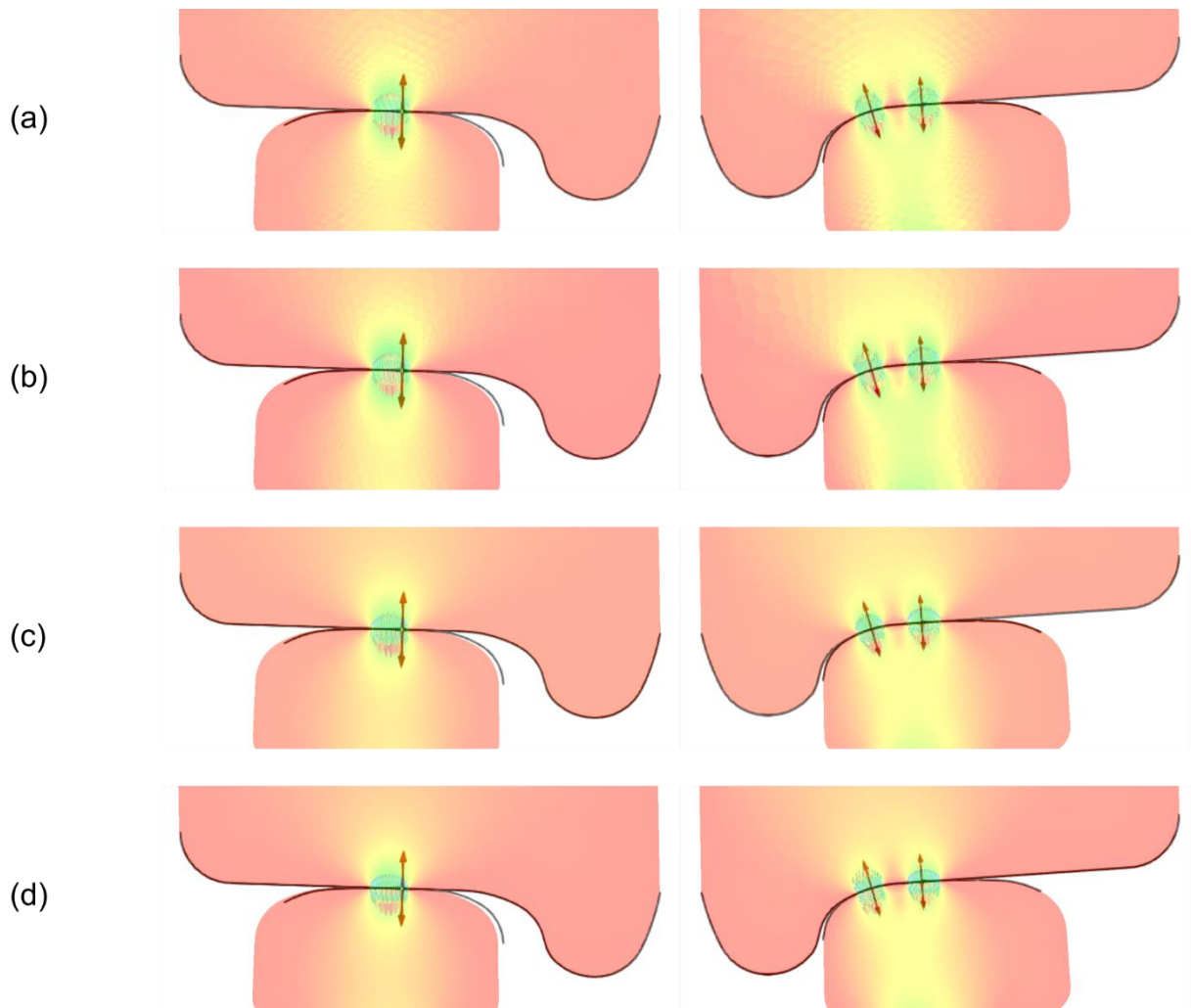
Source: Author.

Figure 100. Quadratic VEM results for Curve situation. Von Mises stress (a), maximum shear stress (b), minimum principal (c) with left (d) and right (e) zooms, in kN/cm^2 . Contact forces (f) with left (g) and right (e) zooms, in kN .



Source: Author.

Figure 101. Overlap of GIRAFFE's result over: (a) Linear FEM, (b) Linear VEM, (c) Quadratic FEM, and (d) Quadratic VEM.



Source: Author.

7.4. Conclusions

The wheel-rail contact is a mechanically complex problem. Modeling it in its full extent is a Herculean task, and therefore simplified models are required to make it more manageable. Nevertheless, simplifications come at the cost of neglecting or misrepresenting certain aspects of the underlying reality. This should always be kept in mind when using any modelling tool.

In this application, the goal was to apply the tools developed in this work to model a problem in this context. The delimitation of the work's scope to two dimensional models

led to the choice of a plane strain state as the more adequate representation for the contact between wheel and rail. Nevertheless, it is far from a perfect.

For both studied situations the stresses resulting from the rail bending were close or higher than those closest to the contact. As discussed in subsection 7.3.1, the model represents both bodies as prismatic, i.e., the contact forces are considered uniformly distributed along the axis of the rails, instead of restricted to the elliptic contact area (or something close to it) as indicated by Hertz's theory.

This misrepresentation can be harmless for the local contact stresses but leads to larger bending-related displacements and stresses. The degree to which these amplified displacements affect the overall contact solution is not explored in this work. It is the author's impression that for tangents and mild curves these could be neglected, and the local contact stresses can be of use. A full 3D model of different situations could help get a grasp at the size of this effect for different situations. Yet, for narrow curves such as the one adopted for this application, the real bending is a relevant effect as it may lead to problems such as *gauge widening* which can ultimately lead to a *wheel climbing derailment*. The augmentation of the bending due to a bad model choice can lead to exaggerated bending stresses, as well as a change in the overall contact solution due to the increased displacements, possibly rendering even the local contact solutions useless.

In this work, the Curve situation is where this effect is more pronounced. The comparison with the reference rigid-body formulation solution shows the possible amplitude of this bending effect. The author's solution represents an upper bound to the bending effect, while the reference solution represents a lower bound. In Figure 101, one can see that the contact solutions are quite similar. Therefore, the global contact solution seem acceptable and the local contact stresses should be reliable up to the errors involved in the Node-to-Segment oscillations, discussed in sections 3.5.8 (in theory) and 6 (in practice). The stresses arising from bending are not yet validated, requiring a more complex model to assess. Nevertheless, the presence of relevant bending in this model can be taken as an indicator that a more complex model may be required.

8. Final considerations

This work is a study of the Virtual Element Method (VEM), focusing on its application to problems in Contact Mechanics. Due its close relation with the Finite Element Method (FEM), the comparison of both is ever present throughout the work. Both methods were implemented (from scratch) by the author, and free software is used to generate meshes and for result visualization.

The study was divided into four applications, each with a specific focus, building up to the main objective of simulating wheel-rail contact problems. Each application includes an external reference solution to compare the two methods. This is either an analytic solution or one from tried-and-tested software. The mathematical models for each problem and a presentation of all numerical methods used can be found in their dedicated sections.

The first application focused on the simplest possible implementation of the methods: a scalar field solution. This application showcased the similarities in the methods' convergence rates, as well as their capabilities in exploring the two common types of boundary conditions in mechanical problems (Neumann and Dirichlet boundary conditions). As most VEM papers introduce concepts using the Poisson problem, the choice of St. Venant's torsion theory as background was good choice to remain inside the mechanics of deformable bodies theme. The presence of the torsion constant as basis to assess both methods' convergence rates enriched the. This application validated the author's comprehension and implementation of both methods.

In the second application, an enhanced implementation of both methods solved problem in plane strain linear elasticity. The validation comes from two benchmark problems comparing the author's solutions to the external reference: analytic solution in the case of the Patch Test, and that coming from the commercial Finite Element Analysis software ABAQUS for Cook's membrane. As contact problems require solving the elasticity equations along with the contact interaction itself, performing a validation for the VEM as implemented by the author allows the following application to focus on the contact aspect of the problem. The two methods led to results sufficiently alike to validate the implementation.

The third application introduces contact problems. Requiring a contact discretization method along with those already employed, this type of problem leads to a nonlinear system of equations, prompting the use of Newton-Raphson's method. The simplest contact discretization was chosen, as the focus of the work's complexity is the Virtual Element's Method, despite its known faults (see 3.5.8). Two common benchmarks for contact problems were elected to assess the correctness of the implementation, taking as reference a mix of analytic solutions and results from reliable software. The FEM led to results flawed in the same way the literature described. The VEM's shared in those flaws, as expected with their nature being more associated with the contact discretization than the method chosen to solve the underlying elasticity problem. Nevertheless, their macule differed considerably for the quadratic order, VEM's results showing smaller oscillations than those from the FEM. The exact mechanism behind this is not yet clear. The Newton-Raphson quadratic convergence is only partly achieved, as the integrated gap function is only piecewise continuous due to non-smooth boundary of the meshes. Quadratic convergence is only achieved once the contact pairings are the same for consecutive steps.

In the fourth application, the methods so far shown are employed for a couple of wheel-rail-interface-like problems. The problems tackled in this application differed significantly from those in the previous one, as they seek the configuration that balances external forces instead of that resulting from a known boundary condition, leading to a more dynamic-like problem. Instead of introducing a dynamic or quasi-static approach, a manual trial-and-error is performed, leading to satisfactory results. The external comparison in this case is the methodology established by the author's research group, using the software GIRAFFE. The solution found with the author's code almost coincided with GIRAFFE's, as far as their underlying model differences allow. The plane strain hypothesis for this model is not ideal, and many of its potential faults were pointed out. Nevertheless, considering this work's restriction to two-dimensional problems, it is considered sufficient for the intended purposes.

Throughout this work, the Virtual Element Method is shown to be a good competitor with the Finite Element Method, and even a good complement as in the hybrid mesh in section

6. Their similarities are nothing new, on the contrary, it is quite expected as one method is a generalization of the other and well documented in the literature. Yet, their differences may show up even when not directly exploited. The Node-to-Segment method does not explore their differences directly as the method presented in Wriggers, Rust, and Reddy [9] does, yet they have shown to still be relevant for this use. There is still much to be learned about this method.

Regarding the wheel-rail contact side of this work, the model used in the last application is composed of many different methods put together. Many of those were picked for their convenience, to keep an already too long work from becoming even longer, while still being able to adequately compare the two methods on which it focused. Other choices of two-dimensional formulations could be considered, such as the plane stress, axisymmetric elements, or a combination of the three, if not three-dimensional models themselves. There are many other contact discretization methods that can be used with both FEM and VEM, as well as the one designed specifically for VEM mentioned in the previous paragraph. Even keeping the Node-to-Segment discretization, other restriction enforcing methods common to contact problems could be used, other than the Penalty method, such as Lagrange Multipliers, Augmented Lagrangian method and the Barrier method. The use of hybrid meshes is another possibility to be explored, as the contact interaction would only affect the elements at the border, allowing the more computationally cheap finite elements to be used in the bulk of the model. The choice of the trial-and-error approach was contingent to avoid the additional complexity of time-integration. Nevertheless, other avenues should be explored in this respect.

8.1. Further work

During the development of this work came some ideas that, for a variety of reasons, were not pursued. This section lists some of them.

Many of the problems associated with the Node-to-Segment discretization were related with the choice of the Penalty method to enforce the restriction. This method was chosen for its simplicity, conservation of the number of degrees of freedom, and physical interpretation. Other methods could be explored to enforce it, possibly leading to different conclusion in the comparison between finite and virtual elements, such as: Lagrange

Multipliers, Augmented Lagrangian method, and Barrier methods, to mention some of the usual methods for contact problems.

Another avenue usually explored with contact methods is the description of the surface. In this work all elements' edges were initially straight, but there are already published works using virtual elements with curved edges. The possibility of better initial description of the problem such as the isoparametric or the isogeometric approaches could lead to a more precise contact solution. In addition, another avenue often approach is that of the surfaces' continuities. The use of C^1 -continuous finite and virtual element methods, ensuring the continuity of the first derivative in the solutions, should lead to overall better solutions, at the cost of a great increase in the problem's size.

Other contact discretization methods could be explored. There are Segment-to-Segment methods, as mentioned in section 3.5, that pass both the patch test and stability criteria, and are shown to correctly evaluate the contact integral. The VEM-based Node-to-Node discretization is another interesting avenue to explore in this sense.

Although there is widespread use of serendipity virtual elements and Guyan reduction (static condensation) to cut down the impact of internal degrees of freedom in the size of the problem. The use of hybrid approaches of virtual and finite elements might help delimitate the use of virtual elements to where their geometric versatility is required, allowing the computationally cheaper finite elements to take over elsewhere. These could inspire VEM-based local refinement approaches for contact to better describe conformal contact solutions.

Considering the wheel-rail applications, the next steps would be to implement the two methods for three-dimensional problems, as well as some additional material model to better capture the formation of defects.

9. References

- [1] A. A. Shabana, *Dynamics of multibody systems*, vol. 9781107042. 2013.
- [2] IHHA, *Guidelines to Best Practices For Heavy Haul Railway Operations: Management of the Wheel and Rail Interface*. Omaha: Simmons-Boardman Books, Inc., 2015.
- [3] E. E. Magel, "Rolling contact fatigue: a comprehensive review," U.S. Department of Transportation. Federal Railroad Administration, 2011. doi: 10.4224/23000318.
- [4] E. E. Magel and J. Kalousek, "The application of contact mechanics to rail profile design and rail grinding," *Wear*, vol. 253, no. 1–2, pp. 308–316, 2002, doi: 10.1016/S0043-1648(02)00123-0.
- [5] K. L. Johnson, *Contact Mechanics*. Cambridge: Cambridge University Press, 1985.
- [6] D. N. Higa, E. J. Kina, and A. Gay Neto, "Wheelset-rail mechanical model for a steady-state dynamic condition and prediction of rolling contact fatigue locci," *Veh. Syst. Dyn.*, 2020, doi: 10.1080/00423114.2020.1814960.
- [7] P. R. Refachinho de Campos and A. Gay Neto, "Rigid body formulation in a finite element context with contact interaction," *Comput. Mech.*, vol. 62, no. 6, pp. 1369–1398, 2018, doi: 10.1007/s00466-018-1569-6.
- [8] A. Gay Neto and P. Wriggers, "Computing pointwise contact between bodies: a class of formulations based on master–master approach," *Comput. Mech.*, vol. 64, no. 3, pp. 585–609, 2019, doi: 10.1007/s00466-019-01680-9.
- [9] P. Wriggers, W. T. Rust, and B. D. Reddy, "A virtual element method for contact," *Comput. Mech.*, vol. 58, no. 6, pp. 1039–1050, 2016, doi: 10.1007/s00466-016-1331-x.
- [10] J. N. Reddy, *An Introduction to Continuum Mechanics*, 1st ed. Cambridge: Cambridge University Press, 2007.
- [11] W. M. Lai, E. Krempl, and D. Rubin, *Introduction to Continuum Mechanics*, 3rd ed. Woburn: Butterworth-Heinemann, 2014.

- [12] C. Truesdell and W. Noll, *The non-linear field theories of mechanics*, 3rd ed., no. v. 2. Berlin: Springer-Verlag, 1992.
- [13] R. W. Ogden, *Non-linear Elastic Deformations*, 2nd ed. Toronto: Dover Publications, 1997.
- [14] J. M. Ball, "Convexity conditions and existence theorems in nonlinear elasticity," *Arch. Ration. Mech. Anal.*, vol. 63, no. 4, pp. 337–403, 1976, doi: 10.1007/BF00279992.
- [15] D. Y. Gao, N. Ruan, and V. Latorre, "Canonical Duality-Triality Theory: Bridge Between Nonconvex Analysis/Mechanics and Global Optimization in Complex Systems," *Math. Mech. Solids*, vol. 21, no. 3, pp. 1–43, 2014.
- [16] D. Y. Gao, "Analytic Solutions to Large Deformation Problems Governed by Generalized Neo-Hookean Model," in *Canonical Duality Theory: Unified Methodology for Multidisciplinary Study*, D. Y. Gao, V. Latorre, and N. Ruan, Eds. Cham: Springer International Publishing, 2017, pp. 49–67.
- [17] L. C. Evans, *Partial Differential Equations*, 1st ed. Berkeley: American Mathematical Society, 1998.
- [18] S. Timoshenko, *Theory of Elasticity*. New York: McGraw-Hill, 1951.
- [19] R. J. Roark, W. Young, and R. Budynas, *Roark's Formulas for Stress and Strain*, 7th ed. New York: McGraw-hill, 2002.
- [20] P. Wriggers, *Computational contact mechanics*, Second. Springer Berlin Heidelberg, 2006.
- [21] V. Vlasov, *Thin-walled elastic beams*, 2nd ed. Jerusalem: Israel Program for Scientific Translations, 1961.
- [22] N. S. Trahair, "Nonlinear Elastic Nonuniform Torsion," *J. Struct. Eng.*, vol. 131, no. 7, pp. 1135–1142, 2005, doi: 10.1061/(asce)0733-9445(2005)131:7(1135).
- [23] E. J. Sapountzakis and V. J. Tsipiras, "Nonlinear inelastic uniform torsion of composite bars by BEM," *Comput. Struct.*, vol. 87, no. 3–4, pp. 151–166, 2009, doi:

10.1016/j.compstruc.2008.11.005.

- [24] G. Romano, A. Barretta, and R. Barretta, "On torsion and shear of Saint-Venant beams," *Eur. J. Mech. A/Solids*, vol. 35, pp. 47–60, 2012, doi: 10.1016/j.euromechsol.2012.01.007.
- [25] H. F. Silva, "Formulação do problema da torção uniforme em barras de seção transversal maciça.," Universidade de São Paulo, São Paulo, 2005.
- [26] V. Thomée, "From finite differences to finite elements," *J. Comput. Appl. Math.*, vol. 128, no. 1–2, pp. 1–54, 2001, doi: 10.1016/s0377-0427(00)00507-0.
- [27] R. Courant, K. Friedrichs, and H. Lewy, "On the Partial Difference Equations of Mathematical Physics," *IBM J. Res. Dev.*, vol. 11, no. 2, pp. 215–234, Mar. 1967, doi: 10.1147/rd.112.0215.
- [28] J. Singer, "On the Equivalence of the Galerkin and Rayleigh-Ritz Methods," *J. R. Aeronaut. Soc.*, vol. 66, no. 621, pp. 592–592, 1962, doi: 10.1017/s0368393100077403.
- [29] R. W. Clough, "Early history of the finite element method from the view point of a pioneer," *Int. J. Numer. Methods Eng.*, vol. 60, no. 1, pp. 283–287, 2004, doi: 10.1002/nme.962.
- [30] O. C. Zienkiewicz, "The birth of the finite element method and of computational mechanics," *Int. J. Numer. Methods Eng.*, vol. 60, no. 1, pp. 3–10, 2004, doi: 10.1002/nme.951.
- [31] M. J. Turner, R. W. Clough, H. C. Martin, and L. J. Topp, "Stiffness and Deflection Analysis of Complex Structures," *J. Aeronaut. Sci.*, vol. 23, no. 9, pp. 805–823, Sep. 1956, doi: 10.2514/8.3664.
- [32] P. G. Ciarlet, *The Finite Element Method for Elliptic Problems*, 2nd ed. New York: SIAM, 2002.
- [33] S. C. Brenner and L. R. Scott, *The Mathematical Theory of Finite Element Methods*, 3rd ed., vol. 15. New York, NY: Springer New York, 2008.

- [34] K.-J. Bathe, *Finite Element Procedures*, 2nd ed. Watertown: Klaus-Jürgen Bathe, 2006.
- [35] P. Wriggers, *Nonlinear Finite Element Methods*. Berlin: Springer, 2008.
- [36] O. C. Zienkiewicz, R. L. Taylor, and J. Z. Zhu, “The Finite Element Method: Its Basis and Fundamentals,” in *The Finite Element Method: its Basis and Fundamentals (Seventh Edition)*, Seventh Ed., O. C. Zienkiewicz, R. L. Taylor, and J. Z. Zhu, Eds. Oxford: Butterworth-Heinemann, 2013, p. iii.
- [37] T. Strouboulis, I. Babuška, and K. Copps, “The design and analysis of the Generalized Finite Element Method,” *Comput. Methods Appl. Mech. Eng.*, vol. 181, no. 1–3, pp. 43–69, 2000, doi: 10.1016/S0045-7825(99)00072-9.
- [38] A. R. Khoei, *Extended Finite Element Method: Theory and Applications*. Chinchester: Wiley, 2015.
- [39] D. Boffi, F. Brezzi, and M. Fortin, *Mixed Finite Element Methods and Applications*. Berlin: Springer Berlin Heidelberg, 2013.
- [40] P. Wesseling, *Principles of Computational Fluid Dynamics*, 1st ed., vol. 29. Berlin, Heidelberg: Springer Berlin Heidelberg, 2001.
- [41] F. Brezzi, G. Manzini, D. Marini, P. Pietra, and A. Russo, “Discontinuous Galerkin approximations for elliptic problems,” *Numer. Methods Partial Differ. Equ.*, vol. 16, no. 4, pp. 365–378, 2000, doi: 10.1002/1098-2426(200007)16:4<365::AID-NUM2>3.0.CO;2-Y.
- [42] M. Ihmsen, J. Orthmann, B. Solenthaler, A. Kolb, and M. Teschner, “SPH Fluids in Computer Graphics,” in *Eurographics 2014 - State of the Art Reports*, 2014, no. 2, pp. 1–2, doi: 10.2312/egst.20141034.
- [43] A. Stomakhin, C. Schroeder, L. Chai, J. Teran, and A. Selle, “A material point method for snow simulation,” *ACM Trans. Graph.*, vol. 32, no. 4, 2013, doi: 10.1145/2461912.2461948.
- [44] J. Korelc and P. Wriggers, *Automation of Finite Element Methods*, 1st ed. Cham:

Springer International Publishing, 2016.

- [45] A. Logg, K.-A. Mardal, and G. Wells, *Automated Solution of Differential Equations by the Finite Element Method*, vol. 84. Berlin, Heidelberg: Springer Berlin Heidelberg, 2012.
- [46] A. Oishi and G. Yagawa, “Computational mechanics enhanced by deep learning,” *Comput. Methods Appl. Mech. Eng.*, vol. 327, pp. 327–351, 2017, doi: 10.1016/j.cma.2017.08.040.
- [47] G. Capuano and J. J. Rimoli, “Smart finite elements: A novel machine learning application,” *Comput. Methods Appl. Mech. Eng.*, vol. 345, pp. 363–381, 2019, doi: 10.1016/j.cma.2018.10.046.
- [48] C. Cecka, A. J. Lew, and E. Darve, “Assembly of finite element methods on graphics processors,” *Int. J. Numer. Methods Eng.*, vol. 85, no. 5, pp. 640–669, Feb. 2011, doi: 10.1002/nme.2989.
- [49] C. Geuzaine and J.-F. Remacle, “A three-dimensional finite element mesh generator with built-in pre- and post-processing facilities,” *Int. J. Numer. Meth. Engng.*, vol. 79, no. 11, pp. 1309–1331, 2017, [Online]. Available: http://gmsh.info/doc/preprints/gmsh_paper_preprint.pdf<http://gmsh.info/>.
- [50] L. Beirão da Veiga, F. Brezzi, A. Cangiani, G. Manzini, L. D. Marini, and A. Russo, “Basic Principles of Virtual Element Methods,” *Math. Model. Methods Appl. Sci.*, vol. 23, no. 01, pp. 199–214, 2013, doi: 10.1142/S0218202512500492.
- [51] L. Beirão da Veiga, F. Brezzi, and L. D. Marini, “Virtual Elements for Linear Elasticity Problems,” *SIAM J. Numer. Anal.*, vol. 51, no. 2, pp. 794–812, 2013, doi: 10.1137/120874746.
- [52] F. Brezzi and L. D. Marini, “Virtual Element Methods for plate bending problems,” *Comput. Methods Appl. Mech. Eng.*, vol. 253, pp. 455–462, 2013, doi: 10.1016/j.cma.2012.09.012.
- [53] F. Brezzi, “The Great Beauty of VEMs,” 2014.

- [54] L. Beirão da Veiga, F. Brezzi, L. D. Marini, and A. Russo, “H(div) and H(curl)-conforming virtual element methods,” *Numer. Math.*, vol. 133, no. 2, pp. 303–332, 2016, doi: 10.1007/s00211-015-0746-1.
- [55] L. Beirão Da Veiga, F. Brezzi, L. D. Marini, and A. Russo, “Virtual Element Method for general second-order elliptic problems on polygonal meshes,” *Math. Model. Methods Appl. Sci.*, vol. 26, no. 4, pp. 729–750, 2016, doi: 10.1142/S0218202516500160.
- [56] G. Vacca and L. Beirão da Veiga, “Virtual Element Methods for Parabolic Problems on Polygonal Meshes,” *Numer. Methods Partial Differ. Equ.*, vol. 31, no. July 2015, pp. 2110–2134, 2015, doi: 10.1002/num.21982.
- [57] G. Vacca, “Virtual Element Methods for hyperbolic problems on polygonal meshes,” *Comput. Math. with Appl.*, vol. 74, no. 5, pp. 882–898, 2017, doi: 10.1016/j.camwa.2016.04.029.
- [58] F. Brezzi, R. S. Falk, and L. D. Marini, “Basic principles of mixed Virtual Element Methods,” *ESAIM Math. Model. Numer. Anal.*, vol. 48, no. 4, pp. 1227–1240, 2014, doi: 10.1051/m2an/2013138.
- [59] L. Beirão da Veiga, F. Brezzi, L. D. Marini, and A. Russo, “Mixed Virtual Element Methods for general second order elliptic problems on polygonal meshes,” pp. 1–26, 2015, doi: 10.1051/m2an/2015067.
- [60] L. Beirão da Veiga, F. Brezzi, L. D. Marini, and A. Russo, “Serendipity Nodal VEM spaces,” *Comput. Fluids*, vol. 141, pp. 2–12, 2016, doi: 10.1016/j.compfluid.2016.02.015.
- [61] L. Beirão da Veiga, F. Brezzi, L. D. Marini, and A. Russo, “Serendipity face and edge VEM spaces,” *Rend. Lincei - Mat. e Appl.*, vol. 28, no. 1, pp. 143–180, 2017, doi: 10.4171/RLM/756.
- [62] L. Beirão Da Veiga, F. Brezzi, F. Dassi, L. D. Marini, and A. Russo, “Serendipity Virtual Elements for General Elliptic Equations in Three Dimensions,” *Chinese Ann. Math. Ser. B*, vol. 39, no. 2, pp. 315–334, 2018, doi: 10.1007/s11401-018-1066-4.

- [63] L. Beirão da Veiga and G. Manzini, “A virtual element method with arbitrary regularity,” *IMA J. Numer. Anal.*, vol. 34, no. 2, pp. 759–781, 2014, doi: 10.1093/imanum/drt018.
- [64] L. Beirão da Veiga, A. Russo, and G. Vacca, “The Virtual Element Method with curved edges,” no. November 2017, 2017, doi: 10.1051/m2an/2018052.
- [65] P. Wriggers, B. Hudobivnik, and F. Aldakheel, “A virtual element formulation for general element shapes,” *Comput. Mech.*, no. August, 2020, doi: 10.1007/s00466-020-01891-5.
- [66] E. Artioli, L. Beirão da Veiga, and F. Dassi, “Curvilinear Virtual Elements for 2D solid mechanics applications,” *Comput. Methods Appl. Mech. Eng.*, vol. 359, no. xxxx, p. 112667, Feb. 2020, doi: 10.1016/j.cma.2019.112667.
- [67] B. Ahmad, A. Alsaedi, F. Brezzi, L. D. Marini, and A. Russo, “Equivalent projectors for virtual element methods,” *Comput. Math. with Appl.*, vol. 66, no. 3, pp. 376–391, 2013, doi: 10.1016/j.camwa.2013.05.015.
- [68] L. Beirão da Veiga, C. Lovadina, and A. Russo, “Stability Analysis for the Virtual Element Method,” 2016, doi: 10.1142/S021820251750052X.
- [69] S. C. Brenner and L. Sung, *Virtual Element Methods on Meshes with Small Edges or Faces*, vol. 28, no. 7. 2017.
- [70] L. Mascotto, “Ill-conditioning in the virtual element method: Stabilizations and bases,” *Numer. Methods Partial Differ. Equ.*, vol. 34, no. 4, pp. 1258–1281, 2018, doi: 10.1002/num.22257.
- [71] S. Berrone and A. Borio, “Orthogonal polynomials in badly shaped polygonal elements for the Virtual Element Method,” *Finite Elem. Anal. Des.*, vol. 129, no. February, pp. 14–31, 2017, doi: 10.1016/j.finel.2017.01.006.
- [72] L. Beirão da Veiga, F. Dassi, and A. Russo, “High-order Virtual Element Method on polyhedral meshes,” *Comput. Math. with Appl.*, vol. 74, no. 5, pp. 1110–1122, 2017, doi: 10.1016/j.camwa.2017.03.021.

- [73] F. Dassi and L. Mascotto, “Exploring high-order three dimensional virtual elements: Bases and stabilizations,” *Comput. Math. with Appl.*, vol. 75, no. 9, pp. 3379–3401, 2018, doi: 10.1016/j.camwa.2018.02.005.
- [74] S. C. Brenner, Q. Guan, and L. Sung, “Some Estimates for Virtual Element Methods,” vol. 17, no. 4, pp. 553–574, 2017, doi: 10.1515/cmam-2017-0008.
- [75] L. Chen and J. Huang, “Some error analysis on virtual element methods,” *Calcolo*, vol. 55, no. 1, p. 5, Mar. 2018, doi: 10.1007/s10092-018-0249-4.
- [76] L. Beirão da Veiga and G. Manzini, “Residual *a posteriori* error estimation for the Virtual Element Method for elliptic problems,” *ESAIM Math. Model. Numer. Anal.*, vol. 49, no. 2, pp. 577–599, 2015, doi: 10.1051/m2an/2014047.
- [77] A. Cangiani, E. H. Georgoulis, T. Pryer, and O. J. Sutton, “A posteriori error estimates for the virtual element method,” *Numer. Math.*, vol. 137, no. 4, pp. 857–893, Dec. 2017, doi: 10.1007/s00211-017-0891-9.
- [78] S. Berrone and A. Borio, “A residual *a posteriori* error estimate for the Virtual Element Method,” *Math. Model. Methods Appl. Sci.*, vol. 27, no. 8, pp. 1423–1458, 2017, doi: 10.1142/S0218202517500233.
- [79] E. Artioli, S. de Miranda, C. Lovadina, and L. Patruno, “An equilibrium-based stress recovery procedure for the VEM,” *Int. J. Numer. Methods Eng.*, vol. 117, no. 8, pp. 885–900, 2019, doi: 10.1002/nme.5983.
- [80] A. M. D’Altri, S. de Miranda, L. Patruno, E. Artioli, and C. Lovadina, “Error estimation and mesh adaptivity for the virtual element method based on recovery by compatibility in patches,” *Int. J. Numer. Methods Eng.*, pp. 1–41, 2020, doi: 10.1002/nme.6438.
- [81] H. Guo, C. Xie, and R. Zhao, “Superconvergent gradient recovery for virtual element methods,” *Math. Model. Methods Appl. Sci.*, vol. 29, no. 11, pp. 2007–2031, 2019, doi: 10.1142/S0218202519500386.
- [82] H. Chi, L. Beirão da Veiga, and G. H. Paulino, “A simple and effective gradient recovery scheme and a posteriori error estimator for the Virtual Element Method

- (VEM),” *Comput. Methods Appl. Mech. Eng.*, vol. 347, pp. 21–58, 2019, doi: 10.1016/j.cma.2018.08.014.
- [83] T. F. Moherdau and A. G. Neto, “Virtual Element Method : Who are the virtual functions?,” in *Proceedings of the Ibero-Latin-American Congress on Computational Methods in Engineering*, 2020, pp. 1–7, [Online]. Available: <https://cilamce.com.br/arearestrita/apresentacoes/180/7675.pdf>.
- [84] L. Beirão da Veiga, F. Brezzi, L. D. Marini, and A. Russo, “The Hitchhiker’s Guide to the Virtual Element Method,” *Math. Model. Methods Appl. Sci.*, vol. 24, no. 08, pp. 1541–1573, 2014, doi: 10.1142/S021820251440003X.
- [85] O. J. Sutton, “The virtual element method in 50 lines of MATLAB,” *Numer. Algorithms*, vol. 75, no. 4, pp. 1141–1159, 2017, doi: 10.1007/s11075-016-0235-3.
- [86] E. Artioli, L. Beirão da Veiga, C. Lovadina, and E. Sacco, “Arbitrary order 2D virtual elements for polygonal meshes: part I, elastic problem,” *Comput. Mech.*, vol. 60, no. 3, pp. 355–377, Sep. 2017, doi: 10.1007/s00466-017-1404-5.
- [87] M. Mengolini, M. F. Benedetto, and A. M. Aragón, “An engineering perspective to the virtual element method and its interplay with the standard finite element method,” *Comput. Methods Appl. Mech. Eng.*, vol. 350, pp. 995–1023, 2019, doi: 10.1016/j.cma.2019.02.043.
- [88] G. H. Paulino and A. L. Gain, “Bridging art and engineering using Escher-based virtual elements,” *Struct. Multidiscip. Optim.*, vol. 51, no. 4, pp. 867–883, 2015, doi: 10.1007/s00158-014-1179-7.
- [89] L. Beirão da Veiga, C. Lovadina, and D. Mora, “A Virtual Element Method for elastic and inelastic problems on polytope meshes,” *Comput. Methods Appl. Mech. Eng.*, vol. 295, pp. 327–346, 2015, doi: 10.1016/j.cma.2015.07.013.
- [90] P. Wriggers, B. D. Reddy, W. Rust, and B. Hudobivnik, “Efficient virtual element formulations for compressible and incompressible finite deformations,” *Comput. Mech.*, vol. 60, no. 2, pp. 253–268, 2017, doi: 10.1007/s00466-017-1405-4.
- [91] M. L. De Bellis, P. Wriggers, and B. Hudobivnik, “Serendipity virtual element

- formulation for nonlinear elasticity,” *Comput. Struct.*, vol. 223, p. 106094, Oct. 2019, doi: 10.1016/j.compstruc.2019.07.003.
- [92] D. van Huyssteen and B. D. Reddy, “A virtual element method for isotropic hyperelasticity,” *Comput. Methods Appl. Mech. Eng.*, vol. 367, p. 113134, 2020, doi: 10.1016/j.cma.2020.113134.
- [93] P. Wriggers and W. T. Rust, “A virtual element method for frictional contact including large deformations,” *Eng. Comput.*, vol. 36, no. 7, pp. 2133–2161, Aug. 2019, doi: 10.1108/EC-02-2019-0043.
- [94] F. Aldakheel, B. Hudobivnik, E. Artioli, L. Beirão da Veiga, and P. Wriggers, “Curvilinear virtual elements for contact mechanics,” *Comput. Methods Appl. Mech. Eng.*, vol. 372, no. September, p. 113394, 2020, doi: 10.1016/j.cma.2020.113394.
- [95] L. R. Burden and J. D. Fairs, *Numerical Analysis*, 9th ed. Boston, 2010.
- [96] R. G. Bartle and D. R. Sherbert, *Introduction to Real Analysis*, 4th ed. John Wiley & Sons Incorporated, 2011.
- [97] M. A. Crisfield, “A fast incremental/iterative solution procedure that handles ‘snap-through,’” *Comput. Struct.*, vol. 13, no. 1–3, pp. 55–62, Jun. 1981, doi: 10.1016/0045-7949(81)90108-5.
- [98] P. Wriggers, “Finite element algorithms for contact problems,” *Arch. Comput. Methods Eng.*, vol. 2, no. 4, pp. 1–49, 1995, doi: 10.1007/BF02736195.
- [99] L. De Lorenzis, P. Wriggers, and T. J. R. Hughes, “Isogeometric contact: A review,” *GAMM Mitteilungen*, vol. 37, no. 1, pp. 85–123, 2014, doi: 10.1002/gamm.201410005.
- [100] A. Francavilla and O. C. Zienkiewicz, “A note on numerical computation of elastic contact problems,” *Int. J. Numer. Methods Eng.*, vol. 9, no. 4, pp. 913–924, 1975, doi: 10.1002/nme.1620090410.
- [101] T. J. R. Hughes, R. L. Taylor, J. L. Sackman, A. Curnier, and W. Kanoknukulchai, “A finite element method for a class of contact-impact problems,” *Comput. Methods*

Appl. Mech. Eng., vol. 8, no. 3, pp. 249–276, 1976, doi: 10.1016/0045-7825(76)90018-9.

- [102] G. Zavarise and L. De Lorenzis, “The node-to-segment algorithm for 2D frictionless contact: Classical formulation and special cases,” *Comput. Methods Appl. Mech. Eng.*, vol. 198, no. 41–44, pp. 3428–3451, 2009, doi: 10.1016/j.cma.2009.06.022.
- [103] N. El-Abbasi and K. J. Bathe, “Stability and patch test performance of contact discretizations and a new solution algorithm,” *Comput. Struct.*, vol. 79, no. 16, pp. 1473–1486, 2001, doi: 10.1016/S0045-7949(01)00048-7.
- [104] G. Zavarise and L. De Lorenzis, “A modified node-to-segment algorithm passing the contact patch test,” *Int. J. Numer. Methods Eng.*, vol. 79, no. 4, pp. 379–416, Jul. 2009, doi: 10.1002/nme.2559.
- [105] A. Popp, “Mortar Methods for Computational Contact Mechanics and General Interface Problems,” Technische Universität München, 2012.
- [106] F. Ben Belgacem, “The Mortar finite element method with Lagrange multipliers,” *Numer. Math.*, vol. 84, no. 2, pp. 173–197, 1999, doi: 10.1007/s002119900100.
- [107] F. B. Belgacem, P. Hild, and P. Laborde, “The mortar finite element method for contact problems,” *Math. Comput. Model.*, vol. 28, no. 4–8, pp. 263–271, 1998, doi: 10.1016/S0895-7177(98)00121-6.
- [108] B. I. Wohlmuth, “A mortar finite element method using dual spaces for the Lagrange multiplier,” *SIAM J. Numer. Anal.*, vol. 38, no. 3, pp. 989–1012, 2001, doi: 10.1137/S0036142999350929.
- [109] M. A. Puso and T. A. Laursen, “A mortar segment-to-segment contact method for large deformation solid mechanics,” *Comput. Methods Appl. Mech. Eng.*, vol. 193, no. 6–8, pp. 601–629, 2004, doi: 10.1016/j.cma.2003.10.010.
- [110] A. Popp, M. Gitterle, M. W. Gee, and W. A. Wall, “A dual mortar approach for 3D finite deformation contact with consistent linearization,” *Int. J. Numer. Methods Eng.*, vol. 83, no. 11, pp. 1428–1465, Sep. 2010, doi: 10.1002/nme.2866.

- [111] A. Gay and N. Peter, “Master - master frictional contact and applications for beam - shell interaction,” *Comput. Mech.*, vol. 0, no. 1, 2020, doi: 10.1007/s00466-020-01890-6.
- [112] D. Franke, A. Düster, V. Nübel, and E. Rank, “A comparison of the h-, p-, hp-, and rp-version of the FEM for the solution of the 2D Hertzian contact problem,” *Comput. Mech.*, vol. 45, no. 5, pp. 513–522, 2010, doi: 10.1007/s00466-009-0464-6.
- [113] P. Wriggers, *Computational Contact Mechanics*, 2nd ed. Berlin: Springer Berlin Heidelberg, 2006.
- [114] M. A. Crisfield, “Re-visiting the contact patch test,” *Int. J. Numer. Methods Eng.*, vol. 48, no. 3, pp. 435–449, 2000, doi: 10.1002/(SICI)1097-0207(20000530)48:3<435::AID-NME891>3.0.CO;2-V.
- [115] T. F. Moherdau and A. Gay Neto, “Virtual Element Method vs Finite Element Method for Prandtl’s Solution of St. Venant’s Torsion Problem,” 2019.
- [116] M. Smith, *ABAQUS/Standard User’s Manual, Version 6.9*. Providence, RI: Dassault Systèmes Simulia Corp, 2009.
- [117] R. L. Taylor and P. Papadopoulos, “On a patch test for contact problems in two dimensions,” *Nonlinear Computational Mechanics*. pp. 690–702, 1991.
- [118] AREMA, “Rail,” in *Manual for Railway Engineering*, Landover: American Railway Engineering and Maintenance-of-Way Association, 2007, p. 216.
- [119] Associação Brasileira de Normas técnicas, *ABNT NBR 16810: Via férrea - Superelevação em curvas*. Rio de Janeiro, 2019.
- [120] AAR, “Wheels and Axles,” in *Manual of Standards and Recommended Practices*, Washington: Association of American Railroads, 2004, p. 122.